Investigating the nakhlite source volcano on Mars via electron backscatter diffraction

Thesis submitted in fulfilment of the requirements for the degree of

Doctor of Philosophy
by
Sammy Griffin

School of Geographical and Earth Sciences
College of Science and Engineering

October 2021

Abstract

The overarching science question being addressed by this thesis is: what can the nakhlite meteorites tell us about their source volcano on Mars? To answer the overriding scientific question I have utilised the crystallographic technique of electron backscatter diffraction (EBSD) to answer several secondary questions: 1) Can EBSD be used to distinguish and identify different igneous units within the nakhlite Martian meteorites; 2) What does the micro-structural information reveal about the individual nakhlites emplacement on Mars; and 3) What crystallographic relationship patterns can be revealed from assessing a significant proportion of the currently identified nakhlite group. Answering these questions can provide critical insight into understanding Amazonian volcanism on Mars and provide further constraints towards locating the nakhlite source location on Mars.

Twenty-one thick sections representing sixteen of the twenty-six (currently identified) nakhlites were analysed in this thesis. The nakhlites represent a series of igneous rocks formed as either several extrusive flows or a series of shallow intrusive sills/dykes during the early-mid Amazonian. The rocks have a basaltic chemical composition, exhibiting high proportions of augite (high Ca-clinopyroxene), and express cumulate shape preferred orientation (SPO). They are the second largest class of identified Martian meteorites and represent the largest group or rocks sourced from a singular unknown location on Mars. Geochemical and isotopic investigations of the nakhlites identify a common parental magma source for all samples. This common parental magma source coupled with a shared ejection age had led to the current hypothesis of the nakhlites forming from a singular unidentified volcano on Mars.

Stitching together multiple electron backscatter (EBSD) maps is a method of EBSD analysis that is becoming more popular with advancing technology. This method enables the collection of statistically relevant datasets [sample dependent but sits at ~300 crystals for the nakhlites (this thesis)] at high spatial resolution (≤4 μm) enabling microstructural analysis to be assessed on the cm scale. However, the stitching of multiple panels can generate artifacts within the dataset. The EBSD data collected in this thesis was used to investigate SPO, crystallographic preferred orientation (CPO), and plastic deformation micro-structure parameters in the form of intra-crystalline misorientation patterns within augite (the dominant mineral phase in all samples).

Results from this thesis indicate that:

1) Microstructural analysis indirectly assessing slip-systems using a statistically relevant number of crystals can distinguish variation in emplacement and subsequent deformation environments between the nakhlite samples. Identifying eight unique environments, ranging from low temperature/high pressure to high temperature/low pressure, where a large proportion of the samples exhibited deformation related to low-moderate temperatures and moderate pressures.

2) Assessment of CPO and SPO within the nakhlites showed common CPO development within all nakhlite samples which varied slightly in strength. These CPO were dominated by low intensity and of weak to moderate strength S (foliation dominated) to LS (a combination of foliation

and lineation) CPO often with some expression of weak lineation. These types of CPO are commonly associated with gravity settling environments such as lava lakes, stagnant lava, sills and dykes, where the initial lineation within the magma is overprinted by crystal settling.

3) Modelling of emplacement mechanism endmembers showed crystal settling to be the dominant emplacement mechanism for all assessed nakhlites, agreeing with CPO observations. The crystal settling calculations resulted in unit thicknesses ranging two orders of magnitude from less than one metre to several tens of metres, enabling two distinct groups to be identified: group one being those with magma body thicknesses <10 m and group two with magma body thicknesses <10 m. When considered within the context of known nakhlites ages and the restriction to a localised ejection site on Mars indicate the thickness of the magma bodies to vary randomly over time. When considered against published geochemical data and reported CPO, the calculated magma body thicknesses showed no trends overall showing inherent randomness to the dataset.

Compiling the observed micro-structural CPO and SPO data from the 16 analysed nakhlite meteorites show that the nakhlites source location on Mars represents a diverse magmatic environment, where there are multiple units of variable magmatic thickness formed via a common emplacement process which is dominated by gravitational settling.

Acknowledgement

Firstly, I would like to thank my family for supporting and encouraging me to follow my dreams no matter how crazy they might appear. Your unending love, belief, and support mean the world to me.

To my Glasgow family, you have really made living on the other side of the world a real joy (leaky buildings and all). Neither this project nor my mental sanity would not have turned out the way it has without you. Know that I appreciate all you have done and continue to do for me.

To my supervisors for welcoming this crazy kiwi, encouraging, and enabling me to become the researcher I am today. A simple thank you will never be enough.

To my co-authors and collaborators. Thank you for all of your help and wisdom. I have learnt so much from all of you. Thank you for your time, critique, and support. I consider myself a better researcher because of you.

Finally, to all of you obliged/brave/mad enough to read this thesis, you poor souls. I hope you learn something. I know I did.

Author’s declaration

I declare that this dissertation is the result of my own work and has not been submitted for any other degree at the University of Glasgow or any other institution.

Sammy Griffin

Table of Contents

List of Tables

List of Figures

Preface

Definitions/Abbreviations

Acronym	Definition
A aka 'A-Type'	Component of the BA-Index referring to girdle CPO in the crystallographic [100] aka [*a*] axis
ALH 84001	Allan Hills meteorite number 84001; a Martian orthopyroxenite.
AU	Astronomical unit: a measurement based on distance from the sun.
B aka 'B-Type'	Component of the BA-Index referring to lineation CPO in the crystallographic [010] aka [*b*] axis
BA-Index	the A and B crystallographic axes index; Shows the relationship between the perpendicular <*a*> and <*b*> crystallographic axes where 1 = indicates complete $P_{(010)}$ CPO (B-type) and 0 = complete $G_{(100)}$ CPO (A-type).
BC	Band contrast: Assesses the indexing of EBSP.
BSE	Backscattered electron: electrons emitted from a sample after interaction in the coulomb field.
CIPW normative	Cross, Iddings, Pirsson, Washington normative; A calculation used to convert a chemical composition of an igneous rock to an ideal mineral composition.
CRA	Crystal rotation axes plots.
CSD	Crystal size distribution; a quantitative image processing technique
CPO	Crystallographic preferred orientation.
CU	Curtin University.
D_{conv}	Unit thickness for crystal convection; gives the maximum expected length of the unit.
D_{diff}	Unit thickness for thermal diffusion; gives the minimum expected length of a unit.
D_{sett}	Unit thickness for crystal/gravitational settling; gives an intermediary length of a unit.
EETA 79001	Elephant Moraine meteorite number 79001; a Martian shergottite.
EBSD	Electron backscatter diffraction.
EBSP	Electron backscatter patterns a.k.a. Kikuchi diffraction patterns
EDS	Energy dispersive X-ray spectroscopy.
ESEM	Environmental scanning electron microscope.
FEG-VP-SEM	Field emission gun-variable pressure-scanning electron microscope.
GAU	Geochemical Analysis Unit; a lab at Macquarie University.
GOS	Grain orientation spread; the average angle deviation from the mean measured grain orientation.
GROD	Grain reference orientation distribution angle, also known as mis2mean; the change in orientation relative to the mean orientation within a given crystal.
IPF	Inverse pole figure.
ISAAC	Imaging spectroscopy and Analysis Centre; a lab at the University of Glasgow.
J-Index	A type of CPO index which uses the second moment of an ODF, where the ODF is the distribution of discrete crystal orientation data in Euler angle space.
JEOL JXA-8900	Model of microprobe.
L aka "L-type"	Component of the LS-Index, referring to lineation or point CPO within the crystallographic [010] aka [*b*] axis
LocMis	Local average misorientation angle.
LPO	Lattice preferred orientation, a synonym for CPO.
LS-Index	the B and C crystallographic axes index; Shows the relationship between the perpendicular <*b*> and <*c*> crystallographic axes where 1 = indicates complete $P_{(010)}$ CPO (L-type) and 0 = complete $G_{(001)}$ CPO (S-type).
LV-SEM	Low vacuum scanning electron microscope
M-Index	Misorientation index. A CPO index based on the misorientation angle *i.e.*, the angle of rotation around a common axis required for the alignment of two crystal lattice orientations.

MAD	Mean angular deviation, refers to the quality of Kikuchi band indexing for EBSD, where values below X are considered sufficient.
mIPF	Misorientation index inverse pole area. A in the form of a crystal's fundamental region used to assess slip-system patterns.
Mg#	Magnesium number.
MIL 03346	Miller Range meteorite 03346, a nakhlite.
MIL 090030	Miller Range meteorite 090030, a nakhlite.
MIL 090032	Miller Range meteorite 090032, a nakhlite.
MIL 090136	Miller Range meteorite 0090136, a nakhlite.
Mis2Mean	Also referred to as GROD; the change in orientation relative to the mean orientation within a given crystal.
MOS	Maximum orientation spread; maximum angle deviation angle from the mean crystal orientation
MU	Mariequarie University
MUD	Multiples of uniform density.
Nikon LV100POL	Model of reflective light polarised microscope
NWA 817	Northwest Africa meteorite 817; a nakhlite.
NWA 998	Northwest Africa meteorite 998; a nakhlite.
NWA 5790	Northwest Africa meteorite 5790; a nakhlite.
NWA 8694	Northwest Africa meteorite 8964; a chassignite.
NWA 10153	Northwest Africa meteorite 10153; a nakhlite.
NWA 11013	Northwest Africa meteorite 11013; a nakhlite.
NWA 12542	Northwest Africa meteorite 12542; a nakhlite.
ODF	Orientation distribution function.
OIN	Oxford Instruments Nano-analysis, High Wycombe.
OPPG	One point per grain, a type of data reduction where one crystallite is used to represent a grain/crystal.
PGR	Point (a.k.a. lineation), girdle (a.k.a. foliation), random ternary endmembers of Eigenvalue analysis (a type of CPO index).
REE	Rare earth elements
S or "S-type"	Component of the LS-Index, referring to "schistose" or girdle CPO within the crystallographic [001] aka [*c*] axis
SE	Secondary electrons
SEM	Scanning electron microscope.
SDP	Spatial distribution pattern: the assessment of crystal population ordering and framework.
SPO	Shape preferred orientation: A micro-structural metric assessing the grain-shape alignment within a sample.
TKD	Transmission Kikuchi diffraction.
UNLV	University of Nevada Las Vegas.
UofG	University of Glasgow.
Y 000593	Yamato meteorite number 000593, a nakhlite.
Y 000749	Yamato meteorite number 000749, a nakhlite.
Y 000802	Yamato meteorite number 000802, a nakhlite.

Table 0.1. *Instruments used for EBSD analysis.*

SEM	**Emission Source**	**Institution**	**Sections analysed**
Zeiss Sigma FEG-VP-SEM	Field emission gun	ISAAC imaging centre, University of Glasgow	Governador Valadares (BM.1975,M16,P8469) Lafayette (USNM 1505-5) MIL 03346 (118) MIL 090032 (108) MIL 090136 (50) NWA 998 (T1; UG-1) NWA 11013 (UG-1) NWA 12542 (F83-1) Y 000593 (106-A; 127-A) Y 000749 (64-A; 72-A) Y 000802 (36-A)
Carl Zeiss EVO-SEM with HKL NordlysNano high Sensitivity EBSD detector	Thermal emission	Geochemical Analysis Unit, Macquarie University	Governador Valadares (BM.1975,M16,P19783) Nakhla (WAM 12965)
Hitachi SU70 FEG-SEM with Symmetry CMOS detector	Field emission gun	Oxford Instruments Nanoanalysis HQ, High Wycombe	NWA 817 (N8-1)
Tescan MIRA3 VP-FEG-SEM	Field emission gun	John de Laeter Centre, Curtin University	Caleta el Cobre 022 (CEREGE) MIL 090030 (62) NWA 10153 (SH65 T-2, 2) Nakhla (USNM 426-1)

1 Introduction

1.1 Mars

Mars (Fig. 1.1), the so-called 'red planet' of our Solar System, is a rocky planet circled by two moons (Phobos and Deimos). Its relative position as the fourth planet from the Sun and potential for hosting evidence of life due to evidence of previous surficial liquid water (Fig. 1.2; Cousin et al. 2017; Jackson et al. 2016; Tornabene et al. 2006) has led to 56 years' worth of Mars exploration science. Forty-nine exploration missions have been sent to Mars, 26 missions experienced setbacks or failure, 13 have been considered successful, while 11 are currently classified as operational (Carr & Head, 2010; M & Annavarapu, 2020; Malaya Kumar Biswal & Annavarapu, 2020, 2021). Mars 2020, consisting of the Perseverance Rover and Ingenuity helicopter, is the most recent mission to the red planet and is the first step towards Martian sample return (Farley et al., 2020). The numerous scientific Martian lander, rover, and orbital missions have led to the planet being the second best understood terrestrial body within our Solar System - after Earth. However, until we receive return samples being cached by Perseverance, Martian meteorites are currently the only physical specimens of Mars available for study on Earth (Udry et al., 2020).

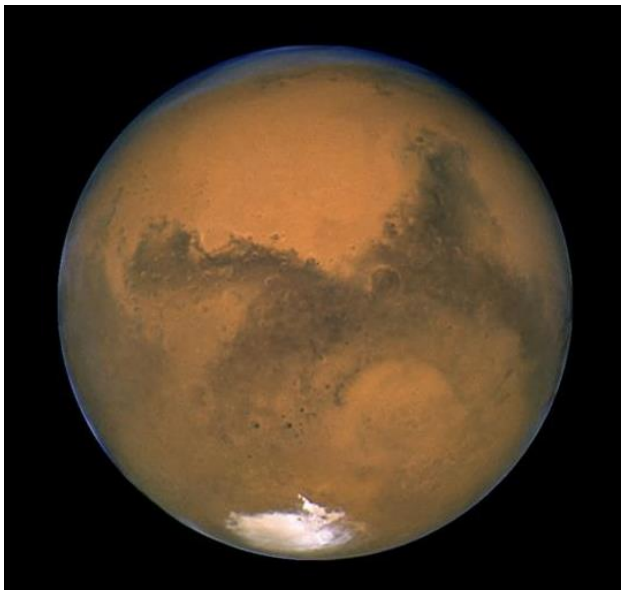

Figure 1.1. *The planet Mars. Image from www.nationalgeographic.com/science/photos/mars. The reddish-brown colour indicates Martian dust, formed from erosion of the various volcanic lithology. The dust covers majority of the planet, with the large darker brown regions having a thinner covering. The faint bluish tinge around the planet is Mars' thin atmosphere. The white region at the bottom is the frozen CO_2 southern polar cap. Small circular dark spots are large impact craters, which are common features on the Martian surface and are used to derive the different ages of the geological units using crater counting.*

Mars differentiated (*i.e.*, separated into crust mantle and core) within the first couple of tens of millions of years post Solar System formation (Carr & Head, 2010). With a diameter of 6,779 km and equatorial radius of 3,396.2 ± 1.6 km, Mars is the second smallest planet within our Solar System sitting at half the size of Earth with ~$^1/_3$ of Earth's surface area (1.44 x 10^8 km^2; Smith et al. 1999a). The ~1.5 Astronomical unit (AU) mean distance from the Sun and its highly elliptical orbit, results in different rhythms on Mars compared to Earth (J. W. Morgan & Anders, 1979). A Martian year

consists of 686.98 Earth days, yet one sol (Martian day) lasts 24 hr 37 min 36 sec which is similar to Earth's (Chamberlain et al., 1976). Mars' relative mass of 6.417 x 10^{23} kg, mean density of 3.39 g/cm^3 results in a surface gravity of 3.72 m/sec (~$^1/_3$ of Earth's) requiring a minimum velocity of 5.03 km/sec for objects, such as meteorites, to escape Mars' current atmosphere (0.61 kPa - ~0.6% of Earth's atmospheric pressure at sea level; Artemieva and Ivanov 2004; Bowling et al. 2020; Fritz et al. 2005a; Hirt et al. 2012; McKenzie et al. 2002; Smith et al. 1999b).

Although there are signs of surficial liquid water in Mars' early history (Fig. 1. 2), current atmospheric conditions and mean surface temperatures (~215 K) do not support surficial liquid water (Carr & Head, 2010). Presently frozen water is restricted to permafrost within the shallow crust (Harrison & Grimm, 2005; McCubbin et al., 2010; Nazari-Sharabian et al., 2020; Scott et al., 1986) with majority of the Martian surface being comprised of underlying igneous rocks (relatively pristine) covered by bright dust and soils formed from oxidised weathering and erosion products (Zuber, 2001). Glaciation, previous flowing water, volcanism, and hypervelocity impact cratering have all played a significant role in the development of today's observed geomorphic features (Carr et al., 1973; Carr & Head, 2010; Greeley & Guest, 1987). Martian geological history has been divided into three major time periods: the Noachian (4.5-3.7 Ga), Hesperian (3.7-3.1 Ga) and Amazonian (3.1 Ga-present; Carr and Head, 2010). The Noachian is defined by the formation of valley(s)/valley networks and most of Tharsis volcanic region, widespread weathering products particularly phyllosilicates, and high cratering rates. The Hesperian is defined by extensive lava plains, formation of canyons, large outflow channels into lakes/seas, localised sulphate-rich deposits, lower rates of cratering, with lower rates of erosion and valley formation. Lastly, the Amazonian is defined by modest volcanism, cratering, even lower erosion rates than both the Noachian and Hesperian, with ice activity (or evidence of) within the mid-high latitudes (Carr & Head, 2010).

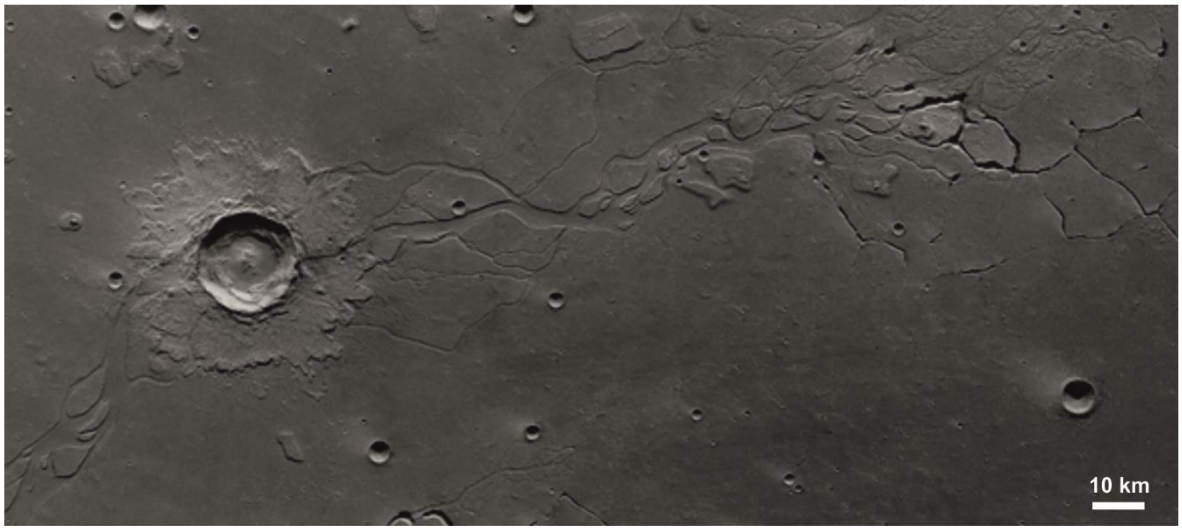

Figure 1.2. *Mars Express Orbiter image of Hephaestus Fossae. Hephaestus Fossae is a crater and river system which extends 604 km. The crater (¬20 km in diameter) and river system is located on the western flank of Elysium Mons within the Utopia Planitia region at ~21/126°. Smaller surrounding craters span 0.8-2.8 km in diameter. Image sourced from https://www.esa.int/Science_Exploration/Space_Science/Mars_Express/Craters_and_channels_in_Hephaestus_Fossae.Published June 2009*

This thesis will be focussing on volcanic samples sourced from the Amazonian period, which despite being the most recent and longest time period (two-thirds of Mars' geological history) represents only ~11% of Martian terrain. This lower volume of Amazonian outcrop is currently hypothesised as a reflection of both the decrease in the planet's active volcanism and other terrain building events coupled with low erosion rates and the reworking of the older Amazonian terrain as a result of extensive ice deposits (Carr et al., 1973; Carr & Head, 2010; Hepburn et al., 2020; Kenneth L. Tanaka, 1986). However, although there has been a notable decrease in Martian volcanism during the Amazonian, orbital studies have identified evidence of volcanic activity extending until very recent portions of Martian History with the most recent event approximated to have occurred around 50,000 years ago (Brož et al., 2015, 2017; Carr & Head, 2010; Hauber et al., 2011; Horvath et al., 2021; Mangold et al., 2010).

1.1.1 Martian volcanism

The study of volcanism provides important information with respect to a planet's formation and evolution. Current understanding of planetary evolution (including Earth) indicates that volcanism is one of the initial drivers of planetary differentiation. Volcanism and volcanic processes are also ubiquitous between different planetary bodies creating a common factor by which individual planets can be assessed and compared. By investigating volcanism of planets, such as Mars, better insight can be gained into how the Solar System formed, what critical factors need to occur during early planetary formation for life to subsequently evolve and be sustained, as well as whether current planetary conditions suitable for long-term terra forming.

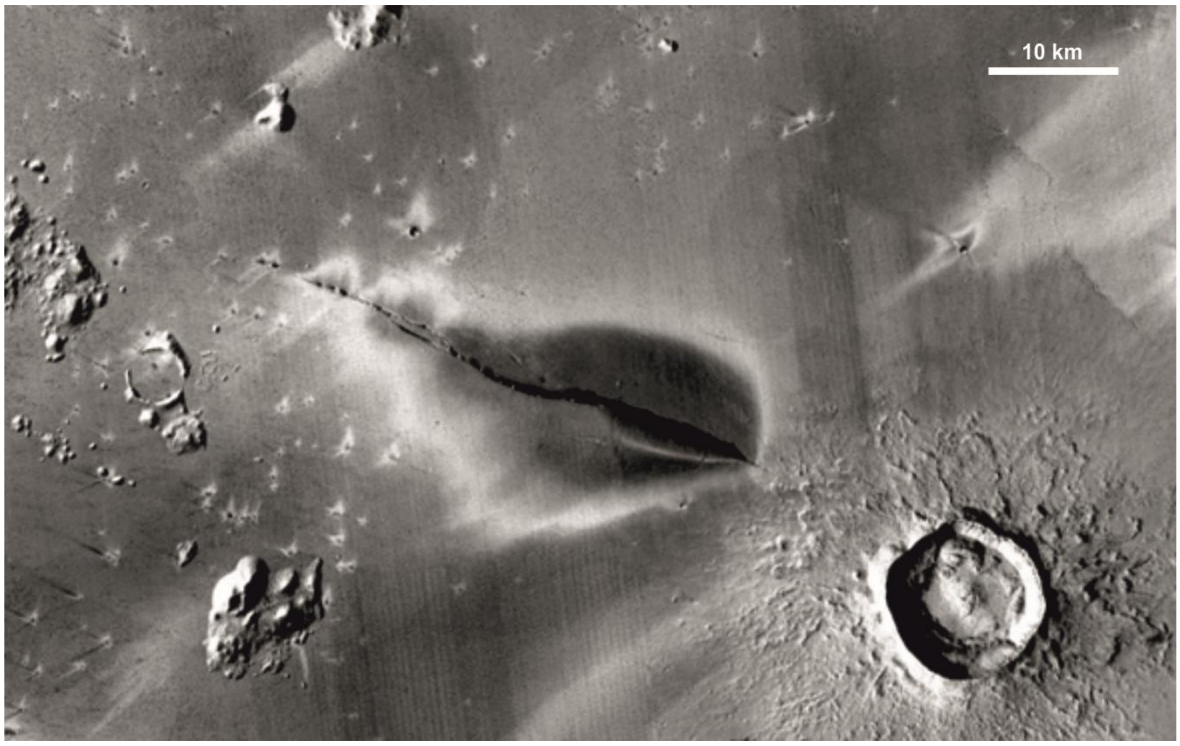

Figure 1.3. *Evidence of the most recent volcanic activity (Cereus Fossae mantling unit) within Elysium Planitia on Mars approximated to have occurred 50,000 years ago* (Horvath et al., 2021). *The dark region in the centre of the image depicts the Cereus Fossae mantling unit, which is hypothesised to be a fission fracture pyroclastic deposit.*

Volcanism has played a significant contribution to the development of Mars, although humans are yet to observe any active volcanism in the 56 years of monitoring the planet. The development of large volcanic edifices such as Olympus Mons (Fig. 1.4), the largest known volcano in the Solar System with eruption dates (determined via surface cratering) at various times over the last 3 Ga, demonstrates that Mars has long-lived volcanism (Carr & Head, 2010). The Martian crust, an important factor in the expression and development of volcanoes, is currently considered to have a thick and rigid outer shell consisting of a single tectonic plate (Zuber, 2001). Observed long-lived and static volcanism resulting in the large volcanic edifices such as Olympus Mons, Elysium, Pavonis, Alba Patera, Astraeus, and Arsia alongside the lack of observed subduction zones and seafloor ridges has led to the current hypothesis of plate tectonics not functioning on Mars. Lack of plate tectonics implies that partial melting from mantle plumes is the most feasible way for volcanism to function on the planet (Belleguic et al., 2005; Day et al., 2018a; McKenzie et al., 2002).

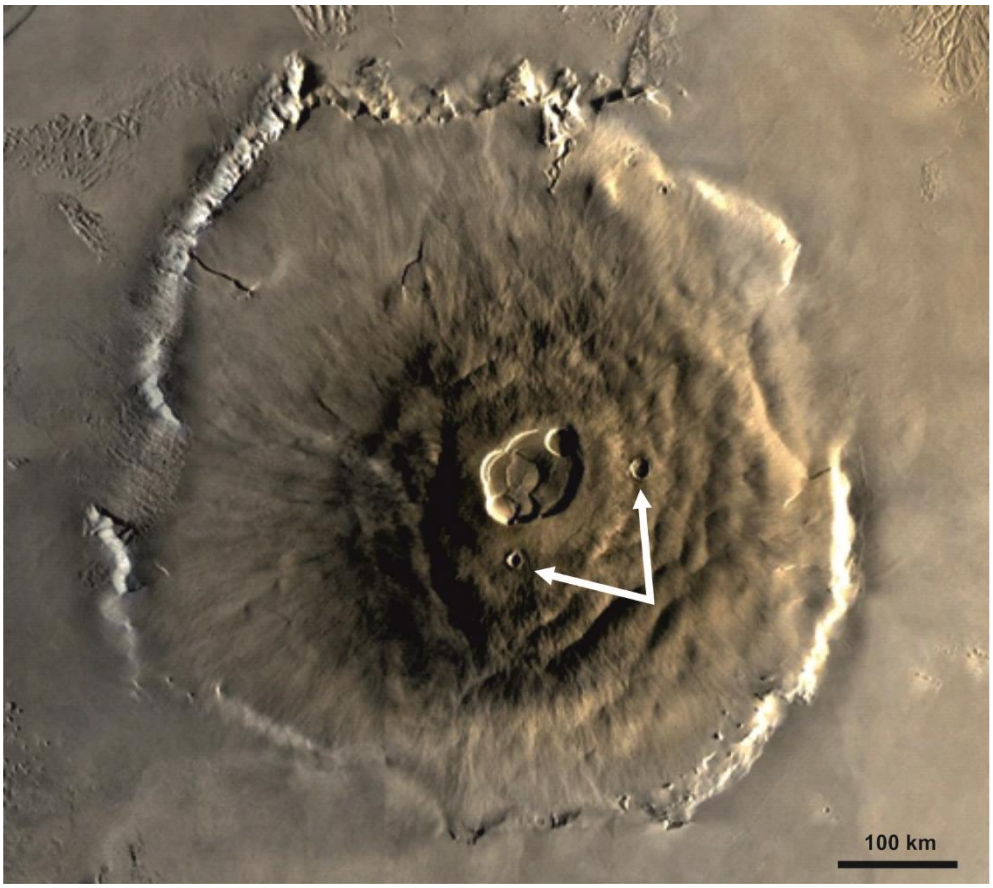

Figure 1.4. *Olympus Mons, 624 km in diameter, the largest volcano on Mars and the Solar System. A basaltic shield volcano, which is a typical type of volcano observed on Mars. The summit has a series of nested calderas, while the texture on the flanks is due to numerous lava flows. The relative paucity of impact craters (two notable examples arrowed) indicate that the edifice was active well into the late Amazonian* (Isherwood et al., 2013). *Image from olympus_mons.jpg (1124×1040) (nasa.gov).*

Amazonian volcanic activity is predominantly observed around the Tharsis and Elysium regions (Carr & Head, 2010; Hauber et al., 2011; K. L. Tanaka et al., 2014). Averaged eruption rates for the Amazonian shield volcanoes and lava plains are suggested to have lower eruption rates (~0.1 km^3/yr) and more episodic compared to earlier periods (Carr & Head, 2010; Grott et al., 2013; Hauber et al., 2011). The Amazonian lava fields are distinguishable from earlier fields by their

dominance of primary flow structures (*e.g.*, lava channels, flow fronts, skylights at lava ridge crests *etc.*) and lower abundances of wrinkle ridges compared to earlier fields which are wrinkle ridge dominated. This change in dominant structures reflects a change in eruption conditions, lava properties, or a combination of the two on Mars (Carr & Head, 2010).

Analysing the volcanic activity of Mars provides insight into the development and diversity of the Martian crust and mantle. Until the first Mars sample return mission succeeds there are three ways in which Martian volcanic activity can be directly analysed: 1) using remote sensing data gathered from orbiter missions; 2) direct sampling from lander and rover missions; and 3) analysis of Martian meteorites (Belleguic et al., 2005; Carr & Head, 2010; Cousin et al., 2017; Eigenbrode et al., 2018; McSween, 2002; Nazari-Sharabian et al., 2020; K. L. Tanaka et al., 2014; Udry et al., 2020). Option one provides contextual data but only for the surface of Mars and is at a broader scale and lower resolution than physically analysing samples from outcrops. Option two enables direct contextualised analysis. However, the types and range of the analyses are limited by the scope of equipment that can be included on a lander/rover, and the data obtained is often by nature lower in analytical resolution than what can be achieved using the same instruments in laboratories on Earth. Option three, the focus of this thesis, enables the analysis of physical specimens in Earth laboratories. However, the samples themselves lack geological context, as the meteorite ejection sites are not yet known, and are biased in terms of their sampling of the Martian crust, representing ~11 sites on Mars, all of which are from the Amazonian (Udry et al., 2020).

1.2 Martian meteorites

It was long considered impossible to transport meteorites from Mars to Earth, due to the high velocity required to escape Martian gravity (5.03 km/s; McEwen et al. 2005). However, the 'prevailing wisdom' changed after it was realised that the atmospheric gases trapped within the impact glass of Elephant Moraine (EETA) 79001 (Bogard & Johnson, 1983) matched the composition of the Martian atmosphere, as measured by the 1976 Viking landers. Today, we routinely identify a meteorite's Martian heritage using its $\Delta^{17}O$ isotopic composition. For Martian rocks their $\Delta^{17}O$ is ~0.3% heavier than terrestrial rocks (McSween & Treiman, 1998). Currently, the Martian meteorite compendium (https://www-curator.jsc.nasa.gov/antmet/mmc/ index.cfm) lists over 262 individual samples, nearly all Amazonian in age, with a total mass exceeding 198 kg (Udry et al., 2020). The majority of these samples were recovered as fortuitous finds, from 14 different countries encompassing both hot and cold deserts, with a few samples observed as falls where the fireball was observed and the meteorite was then recovered (Krämer Ruggiu et al., 2020; Treiman, 2005; Udry & Day, 2018).

Nearly all known Martian meteorites are either igneous rocks (mafic-ultramafic; ~4-30 wt.% MgO) or comprised of igneous lithologies (polymict breccia; McSween, 2002; McSween & Treiman, 1998; Udry et al., 2020). Currently, there are five distinct groupings used for Martian meteorites (Fig. 1.5) the clinopyroxene- rich shergottites and nakhlites, orthopyroxene-rich Allan Hills (ALH) 84001, the dunitic chassignites, and the polymict breccias (Udry et al., 2020). The samples represent crustal

ejecta fragments which through near-surface spallation managed to exceed the 5.03 km/s escape velocity required to enter space during one of the many different hypervelocity impact events on Mars (Bowling et al., 2020; Head et al., 2002; Melosh, 1984). Geochronological and geochemical investigations of Martian meteorites has led to the current hypothesis of there being at least 11 different ejecta sites represented in our meteorite record (Udry et al., 2020), however, the exact source crater location for any given Martian meteorite is yet to be established. In this thesis, I will be focussing solely on the Nakhlite meteorites, which are the largest group of meteorites considered to have been sourced from a single (as yet unknown) ejection crater on Mars.

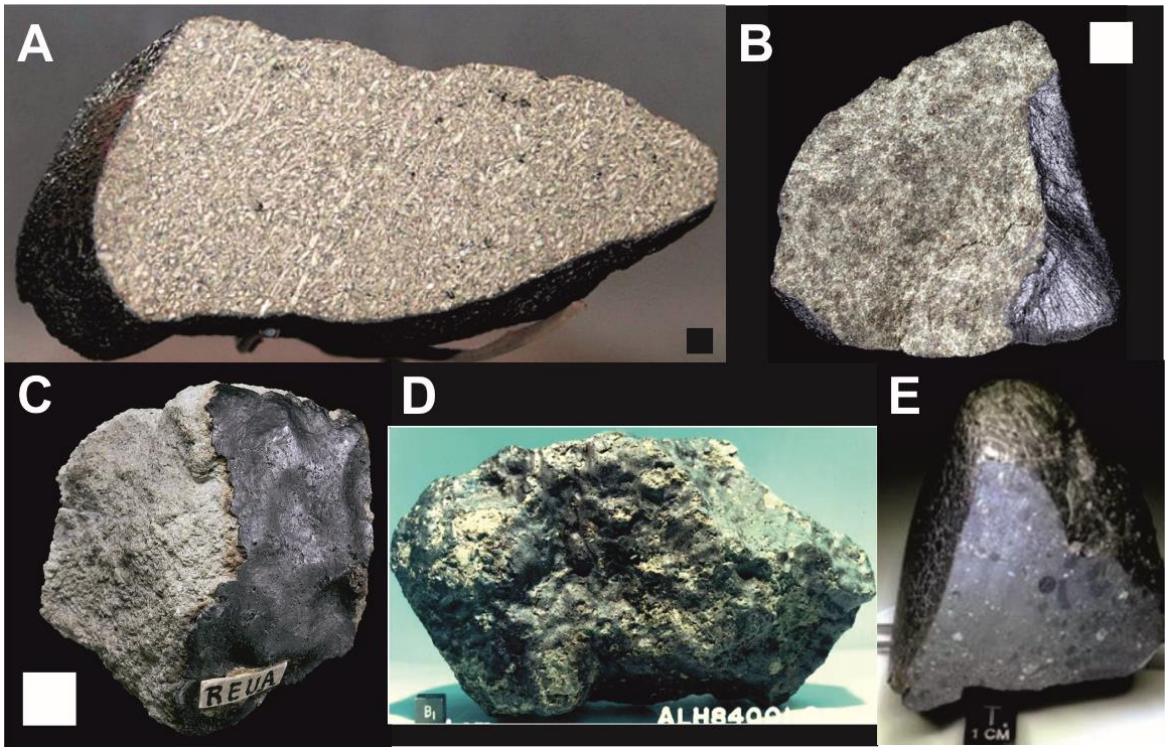

Figure 1.5. *Different types of known Martian Meteorites. A) Shergotty (shergottite; 5 kg) showing cut face with external fusion crust. Green crystals indicate clinopyroxene; B) Nakhla stone (nakhlite; total mass 10 kg from several stones) patches of fusion crust can be seen on the left-hand side. Exposed interior shows clinopyroxene and olivine crystals with orange-reddish colour is considered iddingsite alteration; C) Chassigny (chassignite; 4 kg), dunitic composition D) ALH 84001 (orthopyroxenite; 1.931 kg), patches of remaining fusion crust can be observed on the outside of the stone; E) Black Beauty (polymict breccia), multiple different clasts can be observed on the exposed cut face. Partially eroded fusion crust can be observed on the outer side of the stone. Black fusion crust is seen on all samples. Images sourced from the Natural History Museum London (Nakhla), Smithsonian (Shergotty, Black Beauty), Muséum National d'Histoire Naturelle (Chassigny), and NASA (ALH 84001). Black and white squares indicate 1 cm scale.*

1.2.1 Nakhlites

1.2.1.1 History and chosen samples

The nakhlites take their namesake, after the first recovered sample Nakhla, the only observed fall (1911 in El-Nakhla, El-Buharîya, Egypt; Fig. 1.5; Treiman, 2005). At the time of this thesis, 26 individual meteorites have been classified as nakhlites, 16 of which will be discussed within this body of work (Table 1.1). To date the nakhlites represent the second largest group of Martian meteorites (~10 % by number and ~17 % by mass; Udry et al., 2020). Aside from the continually

increasing number of identified specimens, the majority of which having been recovered within the last decade, geochronological, isotopic, geochemical and micro-structural data, indicate that the nakhlites currently represent the largest number of individual specimens sourced from a single ejection crater on Mars (Cohen et al., 2017; Magrassi et al., 2019; Nyquist et al., 2001; Treiman, 2005; Udry et al., 2020; Udry & Day, 2018).

Table 1.1. *Identified nakhlite meteorites (as of July 2021), Meteorites assessed in this thesis are indicated by their section number and source.*

Sample	Abbreviation	Mass (g)	Recovered	Location	Section(s) analysed	Source
Caleta el Cobre 022	CeC 022	474	2016	Antofagasta, Chile	CERGE	CERGE
Governador Valadares		158	1958	Minas Gerais, Brazil	BM.1975,M16,P8469; BM.1975,M16,P19783	NHM, London
Hassi Messaoud 001		75	2020	Ouargla, Algeria		
Lafayette		800	1931	Indiana, USA	USNM 1505-5	Smithsonian
Miller Range 03346	MIL 03346	715	2003	Antarctica	118	NMWG
Miller Range 090030	MIL 090030	453	2009	Antarctica	50	NMWG
Miller Range 09032	MIL 090032	532	2009	Antarctica	108	NMWG
Miller Range 090136	MIL 090136	171	2009	Antarctica	62	NMWG
Nakhla*		10, 000	1911	Al Buhayrah, Egypt	WAM 12965 USNM 426-1	MWA, Smithsonian
Northwest Africa 817	NWA 817	104	2000	Morocco	N8-1	UofG
Northwest Africa 998	NWA 998	456	2001	Northwest Africa	T1; UG-1	UofG
Northwest Africa 5790	NWA 5790	145	2009	Northwest Africa		
Northwest Africa 6148	NWA 6148	270	2009	Northwest Africa		
Northwest Africa 10153	NWA 10153	119	2014	Northwest Africa	SH65 T-2, 2	IM-UNW
Northwest Africa 10645	NWA 10645	12	2016	Northwest Africa		
Northwest Africa 10659	NWA 10659	7.2	2015	Morocco		
Northwest Africa 10720	NWA 10720	1015	2015	Mauritania		
Northwest Africa 11013	NWA 11013	20.8	2016	Northwest Africa	UG-1	UofG
Northwest Africa 12542	NWA 12542	1082	2019	Northwest Africa	F83-1	Ben Hoefnagles
Northwest Africa 13368	NWA 13368	1105	2020	Mauritania		
Northwest Africa 13669	NWA 13669	139.2	2020	Northwest Africa		
Northwest Africa 13764	NWA 13764	692	2021	Algeria		
Northwest Africa 13786	NWA 13786	27.4	2021	Northwest Africa		
Yamato 000593	Y 000593	13,710	2000	Antarctica	106-A; 127-A	NIPR
Yamato 000749	Y 000749	1283	2000	Antarctica	64-A; 72-A	NIPR
Yamato 000802	Y 000802	22	2000	Antarctica	36-A	NIPR

** = Fall*
NMWG = NASA Meteorite Working Group
MWA = Macovich Collection, The Museum of Western Australia
UofG = University of Glasgow
IM-UNW = Institute of Meteoritics, University of New Mexico

All of the nakhlites are considered to have evolved from the same parental magma source (Day et al., 2018a), despite being considered to represent separate petrogenic events (Cohen et al., 2017; Day et al., 2018a; Udry et al., 2020; Udry & Day, 2018). Geochronological dating of the nakhlites using $^{40}Ar/^{39}Ar$ identified at least four separate magmatic events spanning 93 ± 12 Ma, from 1416 ± 7 to 1322 ± 10 Ma (Cohen et al., 2017). This places the nakhlites towards the end of the early Amazonian (Fig. 1.6; Krämer Ruggiu et al. 2020; Nyquist et al. 2001; Udry and Day 2018; Udry et al. 2020). Alteration, which is frequently observed across the entire group and considered Martian in origin (Changela & Bridges, 2011), has been dated at 633 ± 23 Ma for some of the samples indicating a secondary post-emplacement mechanism (Borg & Drake, 2005). This secondary event is currently hypothesised as impact generated hydrothermal alteration (Fig. 1.6; Daly et al. 2019a). All analysed nakhlite samples have cosmogenic exposure ages that overall with analytical uncertainty (10.7 ± 0.8 Ma), indicate a single/bombardment event that ejected the nakhlites from Mars (Fig. 1.5; Cohen et al. 2017; Nyquist et al. 2001). Coincidentally, the nakhlites also share the same cosmogenic exposure

age as the Chassignites, which are also hypothesised to share a parental magma source (Day et al., 2018a; Nyquist et al., 2001).

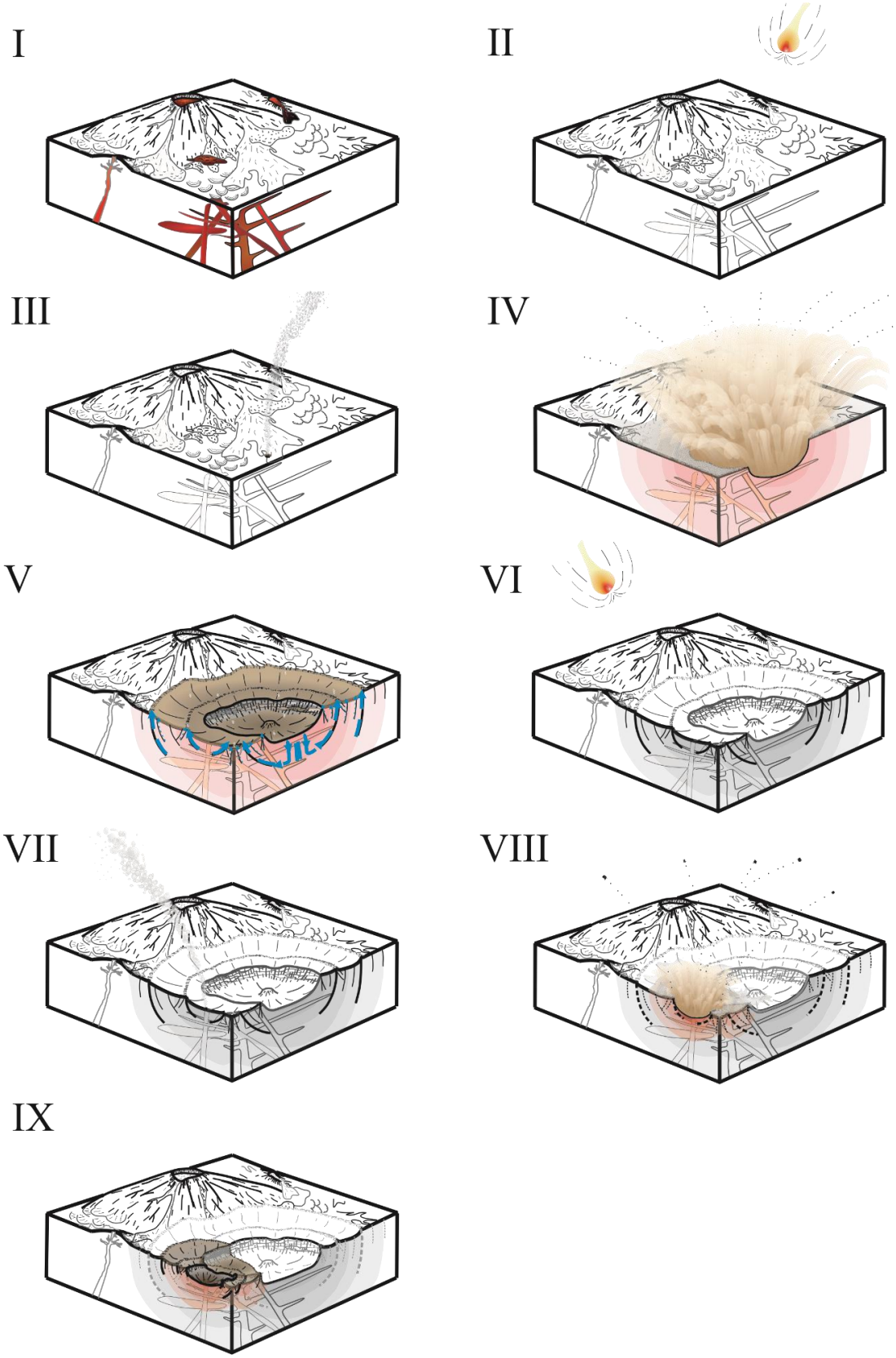

Figure 1.6. *Nakhlite formation schematic. I) emplacement as multiple lava flows and/or shallow intrusions from 1416 ± 7 Ma to 1322 ± 10 Ma (2σ); II) Incoming fireball post-emplacement; III) Meteorite impact with trail; IV) Large non-nakhlite forming impact at 670 ± 91 Ma; V) Impact hydrothermal system resulting nakhlite aqueous alteration; VI) Incoming fireball post-active hydrothermal system; VII) Meteorite impact with trail on the edge of former crater; VIII) second impact at 10.7 ± 0.8 Ma (2σ) causing nakhlite ejection; IX) nakhlite source crater on Mars modified from Daly et al. (2019a).*

1.2.1.2 Nakhlite mineral composition and known geochemistry

The nakhlites are Martian igneous rocks. They are ultramafic rocks sourced from a basaltic composition parental magma body, clinopyroxene-rich with cumulate micro-structural features, with MgO contents ranging from 7.3-32.3 wt.% (Treiman, 2005; Udry & Day, 2018). Modal mineralogy of the different samples have been shown to range in vol.% from 55–76.1 (clinopyroxene), 0-4.2 (orthopyroxene), 1.7–14.9 (olivine), 0–38 (mesostasis material), 0–33.5 (plagioclase), and 1.0–4.5 titanomagnetite, with variable amounts of post-crystallisation alteration (especially in olivine; Udry and Day 2018). Reported modal mineralogy has been shown to change up to 12% between different sections compared to 7-9 % shown from replicate analyses of the same section via different petrological techniques (Corrigan et al., 2015). In all nakhlites, euhedral augite (high Ca-clinopyroxene) is observed as the dominant phase. Olivine, forsteritic in composition, is either the second or third most abundant phase depending on the sample. The abundance of olivine is observed to vary considerably between different thin/thick sections of the same meteorite sample and can appear as either smaller crystals or larger poikilitic phenocrysts (up to ~5 mm diameter, where poikilitic refers to the inclusion of smaller crystals) within the sample (Corrigan et al., 2015; Friedman Lentz et al., 1999; Hallis & Taylor, 2011). The mesostasis material although not thermodynamically considered a phase in itself, forms the final major micro-structural/volumetric constituent within the nakhlites (Corrigan et al., 2015), comprised of low Ca-clinopyroxene, fayalite, feldspar, titanomagnetite, sulphide, apatite, and silica (Treiman, 2005). Post crystallisation alteration within the nakhlites is generally reported as either iddingsite or clays present within olivine veins, highly fractured regions or within the mesostasis (serpentine, smectite, jarosite; Bridges and Grady 2000; Bunch and Reid 1975; Gillet et al. 2002; Hallis and Taylor 2011; Irving et al. 2002; Krämer Ruggiu et al. 2020; Lee et al. 2018; Noguchi et al. 2009; Treiman 2005; Treiman and Irving 2008).

Bulk rock geochemistry shows a narrow range of SiO_2 (Fig. 1.7) with nearly all of the nakhlites plotting on a total-alkali-silica diagram as basalt (there is one basaltic andesite and one picro-basalt; Day et al. 2018a). Trace element abundances suggest at least two separate geochemical groupings (high and low trace elements) which are correlated with both mesostasis material vol.% and MgO wt.% (Udry & Day, 2018). Note that caution needs to be employed when interpreting these trace element results, as the mass of material analysed is typically small (0.5–2 g) and may not constitute representative samples given the grainsize of the nakhlites. Despite variations in trace element abundances, all of the nakhlites have similar rare earth element (REE) patterns which exhibiting light REE enrichment indicating relatively low degrees of partial melting (Day et al., 2018a; Udry & Day, 2018).

Rare earth element (REE) and trace element geochemistry of the nakhlites exhibit two distinct groupings (Fig. 1.8), with similar slopes. REE ratios indicate the nakhlites share a parental melt source. This melt source has been hypothesised to be peripheral to plume volcanism based off comparison to Terrestrial mantle trends (Day et al., 2018a). The individual meteorites exhibit a continuous fractionation pattern at a rate that cannot be resolved through fractionation of a singular

magma body agreeing with petrological and radiometric age dating of the nakhlites representing multiple magma bodies (Cohen et al., 2017; Jambon et al., 2016; Udry & Day, 2018).

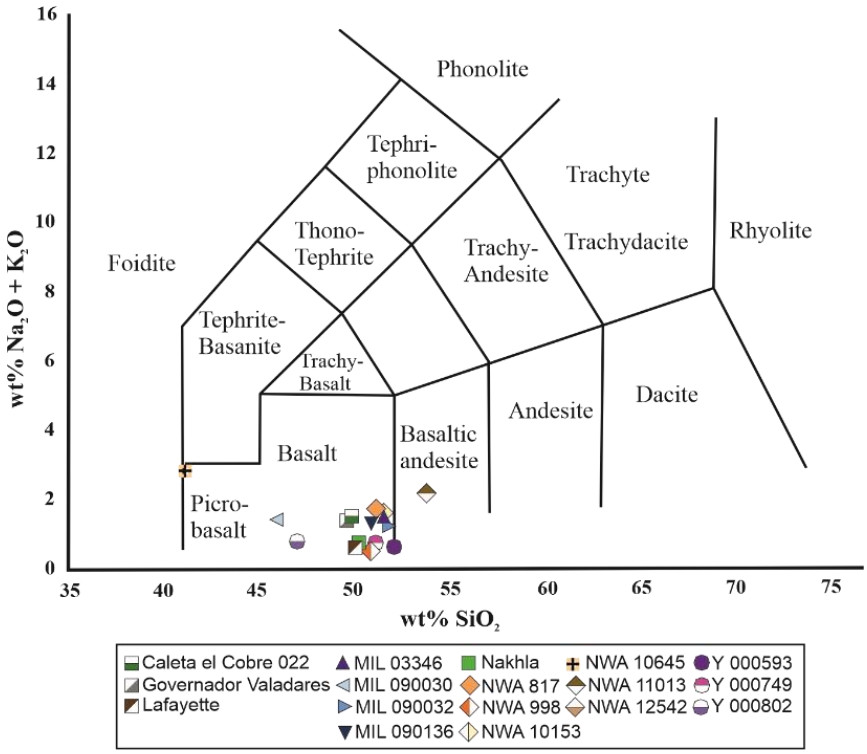

Figure 1.1.8. *Total alkali silica diagram showing the chemical composition of the nakhlites. All data from (Day et al., 2018a), except for Caleta el Cobre 022 (Krämer Ruggiu et al., 2020), Governador Valadares (Lodders, 1998), NWA 5790 (Jambon et al., 2016), Y 000802 (my data unpublished)*

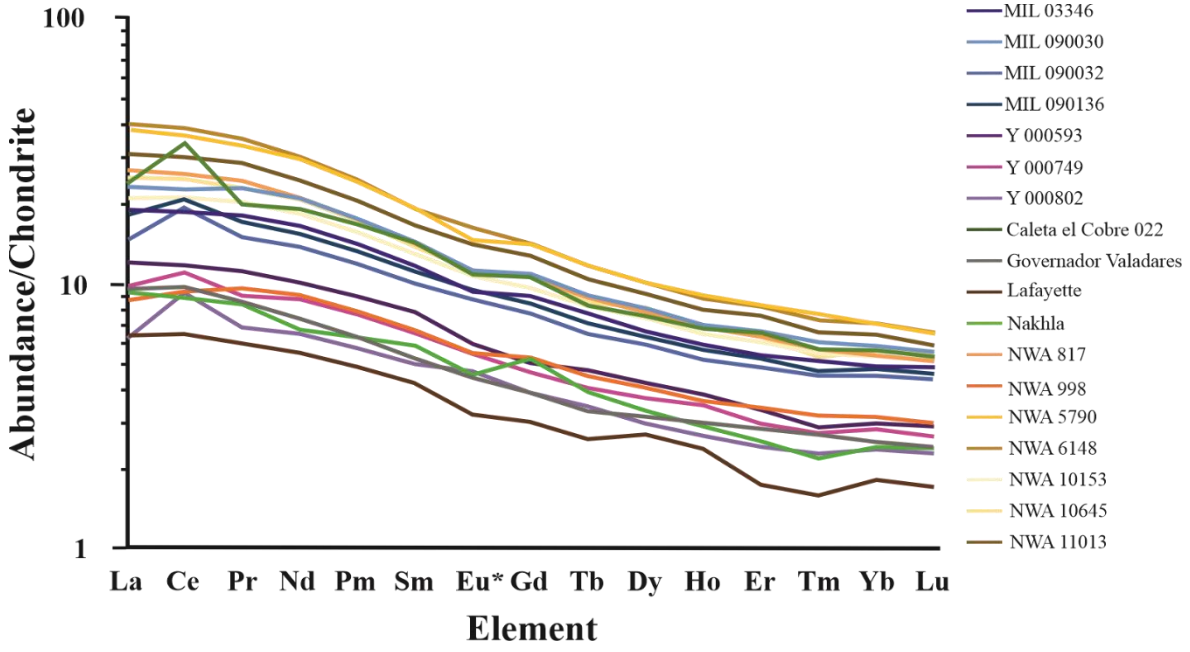

Figure 1.7. *REE elements of measured Nakhlites. All data from (Day et al., 2018a), except for Caleta el Cobre 022 (Krämer Ruggiu et al., 2020), Governador Valadares (Lodders, 1998), NWA 5790 (Jambon et al., 2016), Y 000802 (my data unpublished)*

Chemical (Mg/Fe) zoning appears within augite, creating defined cores and rims (Fig. 1.9). Zoning within the crystals indicates a shift in the magma composition over the growth period of the crystal. The transition between core and rim can either be abrupt (*e.g.*, MIL 03346, Y 000593, NWA

817) or appear as a gradation (*e.g.*, Governador Valadares, Nakhla; Friedman Lentz et al. 1999; Harvey and McSween 1992). The ratio of core:rim within augite varies across the different samples with rims generally appearing to be almost non-existent (≤5%) when in contact with other phenocrystic grains to increasing in thickness when in contact with mesostasis material (up to ~40%; Treiman 2005). Indicating a shift in magma composition occurred more towards the final crystallisation stages of the nakhlite body, most likely during emplacement. Ferroan pigeonite, a common component of the mesostasis material, is often observed at the edges of grains in contact with mesostasis material as either an additional rim in larger augites or as an overgrowth (Treiman, 2005). Chemically, the iron-rich composition of the rims is observed to decrease as it heads towards the magnesium-rich core (Friedman Lentz et al., 1999; Imae et al., 2005; Imae & Ikeda, 2007; Jambon et al., 2016; Krämer Ruggiu et al., 2020; Sautter et al., 2012; Udry et al., 2012; Udry & Day, 2018). Similar related ferroan-rich zones can also appear along augite fracture zones, particularly in regions of the sample which exhibit higher levels of alteration (Treiman, 2005). The distribution of ferroan rich regions within the nakhlite augite crystals suggest mobilisation of iron during post alteration of the nakhlites on Mars via impact-generated hydrothermal activity. Magnesium concentrations within the augite core appears relatively homogenous (Mg# = 60–64; Udry and Day 2018), however, Al_2O_3 concentrations exhibit high variability (0.6–1 wt.%). Minor element abundances also tend to decrease in concentration from the centre towards the rim of the crystal and can be wildly variable in their concentration between different cores of the same sample (Friedman Lentz et al., 1999; Imae et al., 2005; Jambon et al., 2016; Udry & Day, 2018).

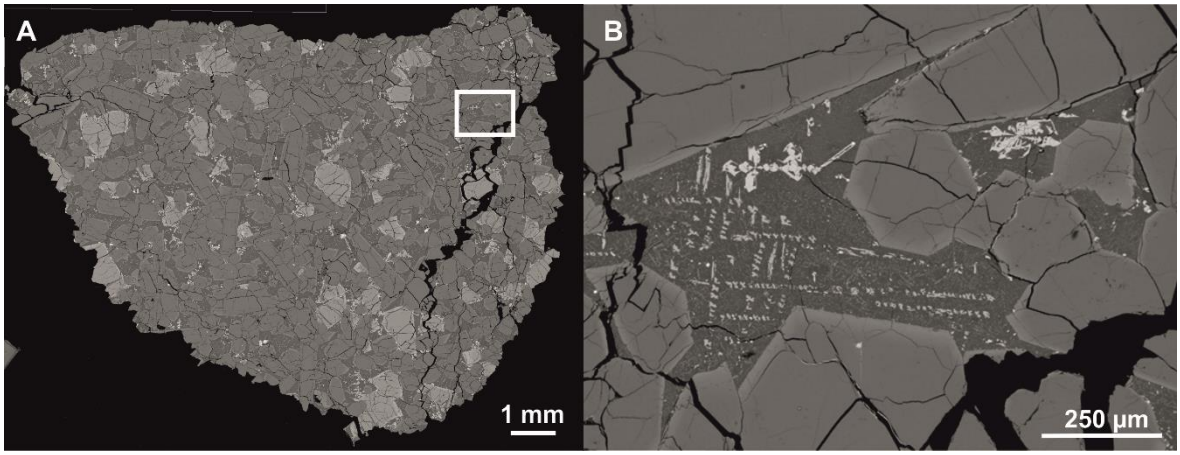

Figure 1.9. *Backscatter image (BSE) of Miller Range 090030 (this study). A) Whole section scan; B) enlargement of white box in A. Difference in greyscale indicates a variation in atomic Z number, where brighter colours indicate larger z numbers. Zoning is observed in augite grains with darker (more Mg-element rich) cores and brighter (more Fe-element) rims.*

Olivine, the second most dominant mineral within the nakhlites, also contains zoning (Berkley et al., 1980; Day et al., 2006; Friedman Lentz et al., 1999; Imae et al., 2005; Imae & Ikeda, 2007; Jambon et al., 2016; Sautter et al., 2002, 2012; Stopar et al., 2013; Treiman, 2005; Udry & Day, 2018). Zoning transitions between core and rim appear highly dependent on the Mg#, where higher Mg# indicates a sharper core:rim transition (Treiman, 2005). In general, the core composition is homogenous within the different samples but variable between the different nakhlite stones

(forsterite content ranging from 22–44; Treiman 2005; Udry and Day 2018). Calcium concentrations, both in the core and the rim, have been shown to be highly variable both within and between samples whilst iron concentrations are observed to be rich within the rims, excepting Caleta el Cobre 022, Lafayette and NWA 998 which had no identifiable zoning (Krämer Ruggiu et al., 2020; Treiman, 2005; Udry & Day, 2018). However, what is more intriguing is the mis-match in compositional patterns between the larger olivine and augite cores within the same sample (Treiman, 2005; Udry & Day, 2018). Most notably the pyroxene cores are observed to exhibit heavy REE abundance patterns which dominate over the light REE patterns compared to the olivine cores which exhibit steeper incompatible trace element patterns (Day et al., 2018a; Udry & Day, 2018). The observed relational chemical differences between the nakhlite olivine and augite cores is neither well investigated nor understood. However, in spite of the relational discrepancy between olivine and augite formation being an interesting and important consideration for the formation of the nakhlites, this particular topic will not be addressed in this thesis. I mention it here as independent formation of olivine and augite will impact the observed SPO, CPO, and microstructural deformation discussed in later chapters. For a more in depth discussion of how the nakhlite's geochemical composition relates to other known Martian samples and our current understanding of the Martian mantle I encourage the reader to look at the work of Day et al. (2018a).

The nakhlite's mesostasis material is comprised of a variety of different phases: minor glass, augite, fayalite-rich olivine, feldspar, orthopyroxene, apatite, oxides (Titanomagnetite), sulphide minerals; and their associated alteration products: iddingsite, smectite clays, iron oxy-hydrides, sulphates, and carbonates (Treiman, 2005). The combination of altered and unaltered phases within the nakhlite mesostasis material contributes to the reddish-brown colour observed in hand specimen (Bunch & Reid, 1975; Treiman, 2005). Typically fine-grained, the mesostasis material appears as pockets between the larger phenocrystic augite and olivine crystals and can appear as either 'glassy' (MIL 03346, NWA 817) or fully crystalline (NWA 998; Treiman 2005), with plagioclase (when present) appearing as splayed laths (Krämer Ruggiu et al., 2020; Treiman, 2005).

1.2.1.3 Alteration

One of the key markers that differentiate the nakhlites from all the other Martian meteorites, excepting ALH 84001, is the fact that they all (with the exception of NWA 5790) contain evidence of alteration by Martian fluids (Fig. 1.10; Bridges and Grady 2000; Bridges et al. 2001; Bunch and Reid 1975; Changela and Bridges 2011; Gillet et al. 2002; Hallis and Taylor 2011; Hicks et al. 2014; Krämer Ruggiu et al. 2020; Kuebler 2013; Lee et al. 2015a, 2015b, 2018, 2013; Noguchi et al. 2009; Stopar et al. 2013; Tomkinson et al. 2013; Treiman 2005; Treiman and Gooding 1991; Treiman and Lindstrom 1997; Treiman et al. 1993; Udry et al. 2020; Velbel 2012). This alteration event is dated within Lafayette to be ~633 ± 23 Ma (Borg & Drake, 2005), If this date is accurate, then it indicates that the alteration event significantly post-dates nakhlite emplacement (Fig. 1.6). The alteration is predominantly observed within the higher deformed regions, which are attributed to shock metamorphism (Peslier et al., 2019). Electron backscatter diffraction (EBSD) analysis of Lafayette

and MIL 03346 identified alteration veins co-located with crystals whose mechanical twinning was displaced by fractures (Daly, Lee, et al., 2019). The displacement of mechanical twinning co-located with unshocked alteration veins in observed high deformation regions in combination with the identification of hydrothermal related alteration minerals has led to the hypothesis of alteration within the samples being derived from an impact generated hydrothermal system (Daly, Lee, et al., 2019; Hicks et al., 2014). If this hypothesis is correct, then it indicates that the nakhlites were exposed to at least two separate impact events. Geochemical, isotopic, and petrographic investigations into the Martian fluids which altered the nakhlites, has revealed them to have had contact with the Martian atmosphere, be acidic, silica saturated, and brine-like in composition (Bridges & Schwenzer, 2012; Cartwright et al., 2013; Lee, Maclaren, et al., 2015).

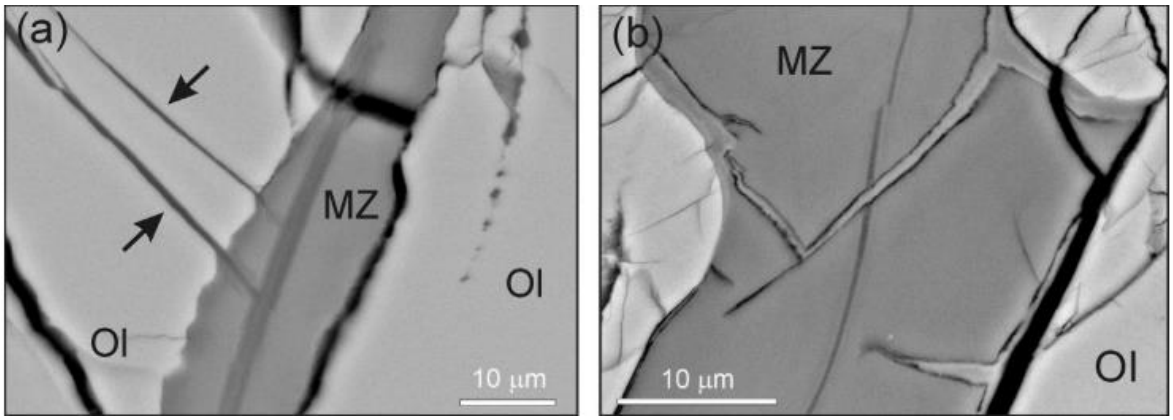

Figure 1.10. *BSE images of iddingsite veins in olivine within NWA 817, N8-1 from* (Lee et al., 2018). *Olivine (Ol), Iddingsite (MZ).*

Alteration within the nakhlites has been predominantly focussed around olivine due to its higher susceptibility to fluids (Bridges et al., 2001; Bridges & Grady, 1999; Bunch & Reid, 1975; Gillet et al., 2002; Hallis & Taylor, 2011; Hicks et al., 2014; Lee et al., 2018; Lee, Tomkinson, et al., 2015; Noguchi et al., 2009). A wide variety of alteration products have been reported within the various nakhlites the most common being iddingsite (comprised of smectite, Fe-oxyhydroxides, gypsum, halite, anhydrite, and silica) generally found within fractured olivine (Treiman, 2005; Udry et al., 2020). However, sulphide oxidation has also been investigated which also supports alteration from hydrothermal derived fluids (Bridges et al., 2001; Udry et al., 2020).

The other common location for alteration within the nakhlites is within the mesostasis material (Treiman, 2005). Typically, the mesostasis component of the sample will host the widest variety and highest levels of alteration. Highly altered olivine tends to be the crystals adjacent to mesostasis regions as are the high fracture density zones within the sample. Iddingsite, which forms along cracks within olivine, appears as larger patches within the mesostasis material alongside veinlets of other alteration assemblages indicating deposition by liquid water (Bridges et al., 2001; Treiman, 2005).

1.2.1.4 Known nakhlite SPO and CPOs

The nakhlites are unbrecciated igneous rocks, with cumulate SPO, and show low levels of shock metamorphism (*i.e.*, their initial emplacement SPO are still the dominant SPO within each of the samples; Fritz et al. 2005; Treiman 2005; Udry and Day 2018; Udry et al. 2020). The three main components which influence the nakhlites SPO are augite, olivine, and mesostasis material (Fig. 1.11) Corrigan et al. 2015; Treiman 2005; Udry and Day 2018). Augite, being the most abundant constituent (modal abundance ranging 55-71 %; Udry and Day 2018), has the largest control of the development of SPO and appears as elongate subhedral to euhedral crystals (Bunch & Reid, 1975; Udry & Day, 2018), which exhibit established simple (180° rotation about <001>) and mechanical (180° rotation about <100>) twinning and cleavage (Bunch & Reid, 1975; Treiman, 2005). Hence in this thesis I will be presenting work focussed on the quantification of augitic SPO via CPO within the nakhlites.

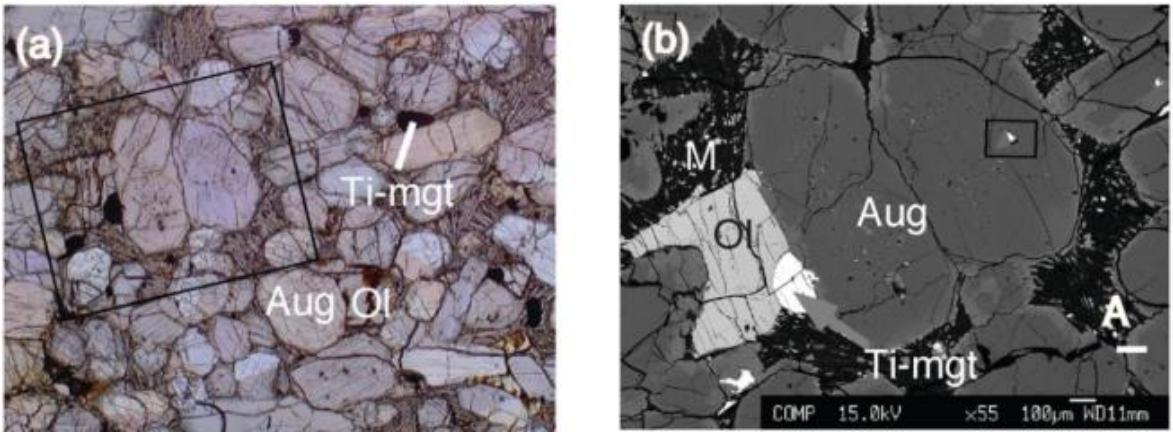

Figure 1.11. *Image of Y 000593 (61) from Imae et al. (2005). A) Representative photomicrograph showing distribution of the main micro-structural components. B) backscatter image of the square outlined in A.*

Twinning, both simple and mechanical (Fig. 1.12), is observed within augite for all nakhlites. Simple twinning along the {100} plain is commonly observed within the larger augite (Berkley et al., 1980; Treiman, 2005), whilst mechanical twinning predominantly occurs as 180° rotation about the <100> axis. Mechanical twins appear less than simple twinning within the samples and tend to be associated with regions of higher fracture densities and sheared zones (Berkley et al., 1980; Treiman, 2005), indicating a potential association with shock deformation.

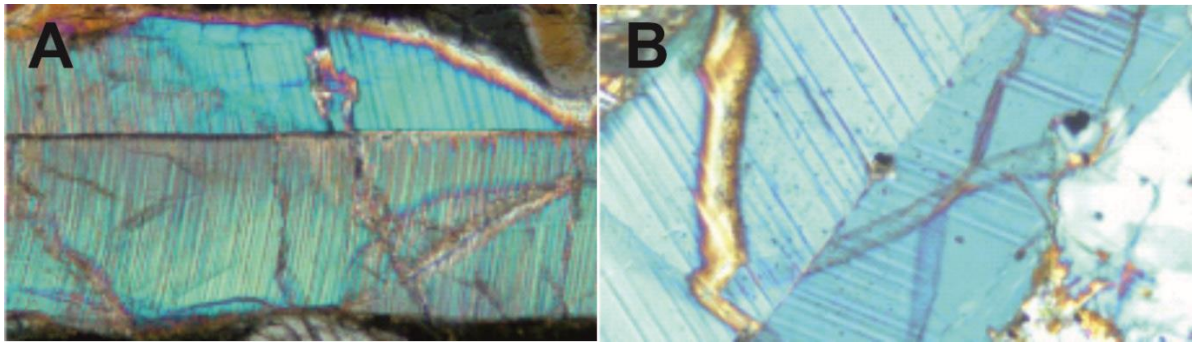

Figure 1.12. *Cross polarised light images of chevron (mechanical) twins in augite. A) MIL 03346, B) Y 000593.* (Treiman, 2005).

In the initial assessment of nakhlite micro-structures, crystallographic preferred orientation (CPO; which refers to the alignment of the crystallographic axes) using optical petrography identified augite alignment in Nakhla and Lafayette (Bunch & Reid, 1975). CPO alignment was again confirmed in both Nakhla and Lafayette and expanded to MIL 03346 and Governador Valadares in a later study using EBSD by Daly et al. (2019b). Both studies recognised lineation and foliation CPO. However, the technique of crystal size distribution (CSD) conducted by Friedman Lentz et al. (1999) and Udry and Day (2018) detected no foliation within any of the three and thirteen nakhlites assessed, respectively, indicating massive SPO for all image processed CSD assessed nakhlites. Both studies encompassed sections from the four EBSD assessed nakhlites which exhibited CPO alignment indicating foliation and lineation. An assessment of SPO and CPO using the two most recent techniques (EBSD and CSD) applied to the nakhlites which presented conflicting results (Daly, Piazolo, et al., 2019; Udry & Day, 2018) will be assessed in chapter 1 of this thesis. In chapter 2, I will expand on the identification of SPO using augite CPO assessing 16 different nakhlite specimens including several replicate sections, and those sections assessed within Daly et al. (2019b).

Olivine, which either makes up the second or third major component in the nakhlites (modal abundance 1-4.5 %; Udry and Day 2018), can be found either as larger (up to ~5 mm diameter) or smaller subhedral to euhedral crystals. The larger olivine crystals can be observed to enclose small crystals of augite, whilst the smaller crystals appear to have crystallised/recrystallised in conjunction or after the formation of augite often forming in clusters. The larger olivine crystals are not very common, often appearing in one section only to be absent in another (Corrigan et al., 2015; Treiman, 2005; Udry & Day, 2018). The lower abundance and irregularity of these larger crystals need to be considered when assessing CPO/SPO as they may contribute to a more localised effect within the given section. Alteration, which is very common within the larger olivine crystals, will also have a significant effect on the spread of alteration and shock metamorphism micro-structures across the different samples.

Plagioclase (when observed unaltered) will often form as lathes appearing either as parallel sheaves or sprays (Treiman, 2005). Majority of the other mesostasis constituents have not been reported to exhibit any identifiable SPO. The mesostasis material is generally observed to be fairly equally dispersed throughout the different sections often occurring in higher proportions around regions of higher fracture densities and alteration (Balta et al., 2017; Friedman Lentz et al., 1999; Imae & Ikeda, 2007; Tomkinson et al., 2015a; Treiman, 2005; Treiman & Irving, 2008; Udry & Day, 2018).

1.2.1.5 Known nakhlite shock deformation

The nakhlites are considered to be the least shocked of the known Martian meteorites (Fritz, Artemieva, et al., 2005; Treiman, 2005). However, they still contain observable shock deformation micro-structures. Overall, shock in the nakhlites is classified between S2 and S3, with lesser shocked specimens exhibiting 5-14 GPa shock deformation levels whilst higher shocked specimens exhibit 14-20 GPa shock deformation (Fritz, Artemieva, et al., 2005).

The current nakhlite shock level classification is based off the analysis of several stones using plagioclase (a common shock classification mineral; Fritz et al. 2005b, 2005a). Shock deformation is known to be heterogeneous. In the nakhlites this is also the case where shock deformation has been reported to appear as bands running through the samples. It is in these bands which most of the alteration by Martian fluids is also observed.

The link between alteration and shock deformation was investigated in both Lafayette and MIL 03346 by Daly et al. (2019a). In their study, they observed displaced mechanical twinning by fracturing co-located with unshocked alteration within both samples leading to the current hypothesis of the nakhlites experiencing two separate hypervelocity impact events; the first to develop brecciation regions within the samples and generate the hydrothermal system which caused the observed alteration and the second to eject the nakhlites from Mars.

1.3 Microstructure and crystallography fundamentals

1.3.1 Microstructure

Micro-structures are a 3-D phenomenon which is either assessed via either shape or crystallography. However, in most petrological studies micro-structure is assessed via the use of 2-D planes such as thin/thick sections. EBSD (the method used in this thesis) enables 3-D data to be discerned from the 2D analysis plane via detection of the crystallographic lattice orientation. Thus, using the different crystallographic lattice axes, the orientation ellipsoid of a given grain can be directly calculated when there is an observed coupling (relationship) between the shape and crystallographic axes (*e.g.,* the short <001> aka <*c*> crystallographic axis with the long shape-axis in augite). It is important to note however, that crystallography and crystal shape are not always related, particularly within scenarios where there has been micro-structural overprinting.

Quantifying grain orientations, where ‘grains’ indicates a variety of different objects *e.g.,* crystals, clasts, sediment *etc.* (Higgins, 2006) is used to understand a rocks physical history. In this thesis, as we are dealing with igneous rocks, the term ‘grains’ refers to crystals. There are a variety of different ways to identify and quantify grain orientation in this thesis we have utilised the following:

Shape preferred orientation (SPO): SPO refers to the shape orientation of the crystals generally determined from the crystal long shape-axis (Fig. 1.13). However, it can also be assessed using the crystal short shape-axis (width), and more accurately using the aspect ratio (length:width). In igneous specimens, the viscosity difference between the mesostasis and ‘grain’ (phenocryst) during a rocks development (emplacement and subsequent deformation) will have the biggest influence on the visibility and strength of observed SPO features (Higgins, 2006). On Earth, SPO is considered one of the most important parameters for understanding igneous physical development. However, the requirement of a known external reference frame or even geological context for a given sample is necessary for comprehensive interpretation of SPO data. In planetary studies, the external reference frame and geological context is almost always an unknown component thus, the assessment

and interpretation of SPO needs to be carefully considered and/or other methods considered to support SPO data.

Crystallographic preferred orientation (CPO): CPO refers to the nature and extent of preferred orientation within the crystal lattice, determined from the crystal lattice's axis orientation (Fig. 1.13; Higgins 2006). CPO can also be referred to as lattice preferred orientation (LPO) within the literature. Majority of geological studies will display CPO using pole figure lower hemisphere equal area projections, whilst crystallographic studies will utilise the upper hemisphere projection. In this instance the given data (crystallographic lattice planes, axes, or zone axes) is plotted against poles in a geologically relevant orientation. Where two or more poles are required to properly orient a given crystal. However, it should be noted that identifying geologically relevant orientations is not always possible for meteoritical studies. In this thesis, to enable comparison between multiple analysed samples the orientation reference frame of the EBSD scans has been used to define a consistent reference frame/orientation to display the data. CPO can infer both inter and intra-crystalline orientations. Inter-crystalline misorientation CPO can be used to assess SPO via selection of an appropriate crystallographic axis (*e.g.*, <001> for long shape-axis in augite, chapter 3). Intra-crystalline misorientation CPO refers to the crystallographic deformation where inverse pole figures (IPF), grain reference orientations distribution (GROD) aka mis2mean are used. Unlike standard pole figures, IPFs utilise the crystal axes as the reference frame rather than an external reference for assessing orientation, dislocation, and movement (*e.g.*, slip-systems) of the crystallographic lattice's unit cells. GROD also known as mis2mean refers to the changes in crystallographic orientation within a given crystal relative to the average orientation of said crystal. The GROD/mis2mean will tell you how deformed ("bent") a given crystal is. The GROD/mis2mean is used to calculate the grain orientation spread (GOS) and maximum orientation spread (MOS) within a grain or a given sample. GOS refers to the average deviation angle from the mean calculated angle and MOS refers to the maximum measured angle deviation from the mean orientation angle within a grain.

Lattice preferred orientation (LPO): LPO is another term used to describe CPO. As synonyms LPO/CPO are used interchangeably. However, confusion often arises in the specific use of CPO/LPO when referring to a given sample's microstructure (*i.e.*, texture and/or fabric) within the literature. This confusion comes from the different definitions applied to both texture and fabric within the fields of geoscience and materials science. For clarity and consistency, this thesis uses the term CPO, alongside the universal terms of SPO and micro-structure to describe and discuss the intra- and inter- crystal orientation relationships within the nakhlites.

Petrological micro-structures form from the growth/transformation of minerals (*e.g.*, plastic/solid-state deformation, coarsening/annealing, recrystallisation, alteration). These micro-structures can be defined by both SPO and CPO if the selected medium (*i.e.*, igneous body) is solid. The development of micro-structures in magmatic systems is highly dependent on crystal-shape and its orientation to the primary external strain field, therefore SPO is an important parameter to consider. Plastic/solid-state deformation in an igneous body will affect the crystal size and shape, whilst magmatic deformation will affect crystal position and orientation. Both types of deformation

will influence micro-structural development. Magmatic deformation is highly reliant on shear which can occur in one of two ways: 1) coaxial [pure shear (aka compaction; normal to shear plane)] where the resulting SPO and CPO will be parallel to each other (Fig. 1.14). In magmatic systems this indicates a shape-controlled micro-structure where the crystal shape is a direct reflection of the crystal lattice. However, pure shear requires a high degree of deformation to produce visible micro-structural features in a sample due to mechanistic inefficiency. 2) non-coaxial [simple shear (aka lineation; parallel to the shear plane) and hyperbolic (aka foliation; oblique angle between parallel and normal to shear plane)] where the SPO and CPO will develop at some oblique angle (indicating the shear plane) to one another. The third option within magmatic systems is where there is no relationship between SPO and CPO resulting from no/lack of deformation (*e.g.*, unobstructed environment present during crystal growth or partially dissolved crystals overprinting any prior deformation). This scenario is generally observed within plutonic rocks rather than volcanic rocks.

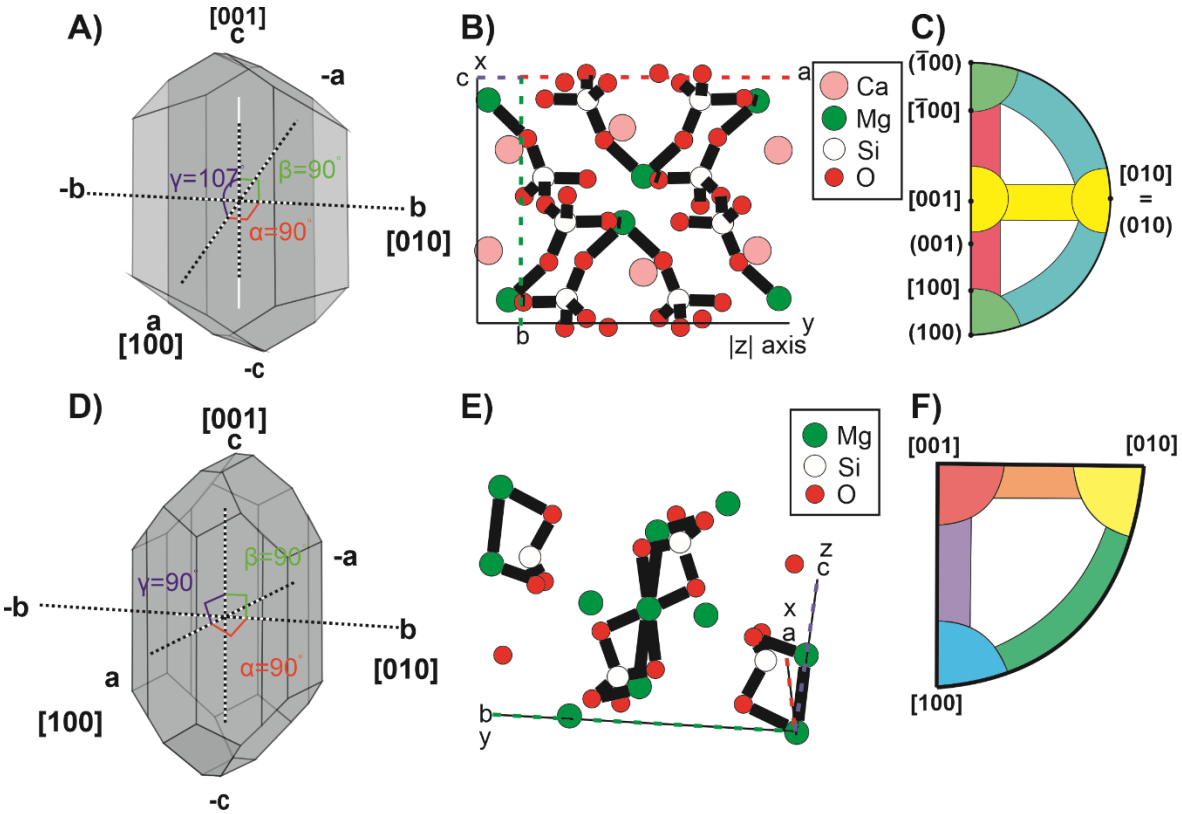

Figure 1.13. *Augite and olivine crystal, unit cell, and fundamental regions A) Augite crystal with corresponding shape-axis (white solid) and crystallographic axes. (black dotted). For augite the shorter <c> aka <001> axis is aligned with the long shape-axis. B) Augite unit cell, the smallest repeating unit within its' crystal lattice. C) Augite fundamental region corresponding to its 2/m symmetry. D) olivine crystal with corresponding shape-axis (white solid) and crystallographic axes. (black dotted). For olivine the long <b> aka <010> axis is aligned with the short shape-axis. B) Olivine (forsterite) unit cell, the smallest repeating unit within its' crystal lattice. C) Olivine fundamental region corresponding to its mmm symmetry.*

If annealing (aka coarsening, Ostwald ripening, micro-structural maturation) occurs in an undeformed igneous rock the SPO can be significantly reduced in the process through the rotation of the larger crystallising grain to fit into the remnant space of the smaller dissolved crystals. If recrystallisation is amplifying either a pure shear or simple shear scenario then a new SPO has the

potential to develop while the formerly developed CPO can either be preserved or disappear, resulting in discrepancies observed between SPO and CPO.

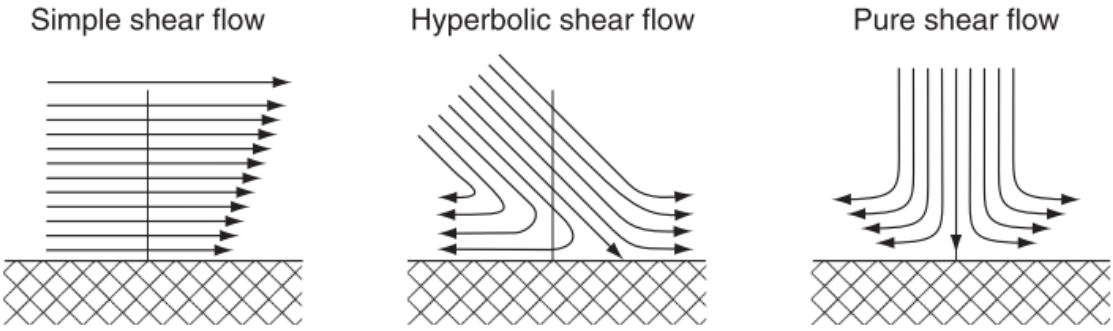

Figure 1.14. *Flow lines for the different flow types from (Higgins, 2006). Coaxial shear is indicated as pure shear (compaction; normal to shear plane); non-coaxial shear is indicated as simple shear (parallel to shear plane) and hyperbolic shear (oblique to shear plane).*

1.3.1.1 Cumulate SPO and CPO

Since the initial petrological descriptions of the nakhlites the group has been referred to as cumulates (Bunch & Reid, 1975; Treiman, 2005). A cumulate is defined as an igneous rock with a framework of touching or interlocking crystals, where the grains have been interpreted to have concentrated by gravitational settling through magmatic diversification processes (Hunter, 1996; Irvine, 1982; Fig. 1.15). Typically, the magmatic diversification is assumed to be the result of crystal-liquid fractionation and the crystal framework related to crystal mushes (Anderson, 1981; Bacon et al., 2007; Donohue & Neal, 2018; Holness, Nielsen, et al., 2017). The cumulate definition can be further refined based on accumulated magma crystals in the groundmass, where samples are referred to as adcumulates (100–93%), mesocumulates (93–85%), or orthocumulates (85–75%). The nakhlites having been described as adcumulates (Bunch & Reid, 1975; Treiman, 2005). Within adcumulates both compaction and recrystallisation contribute to the final SPO, where compaction requires an open melt and show signs of either dislocation or diffusion creep within its intra-crystalline misorientation CPO (Holness, Vukmanovic, et al., 2017; Hunter, 1996).

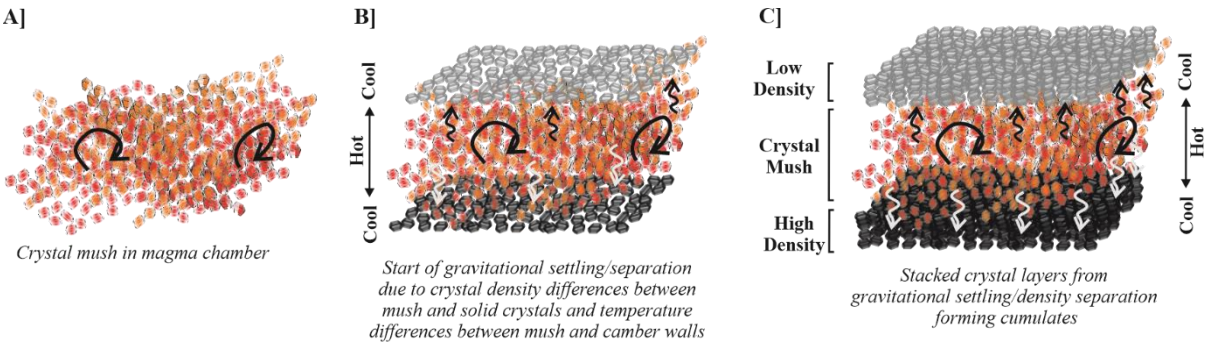

Figure 1.15. *Diagram depicting the development of cumulates. A) the initial crystal mush; B) the initiation of crystal settling layers (foliation SPO); C) Increased layering resulting in compaction forming conditions for compaction and recrystallisation CPO.*

On earth there are several cumulates that have been investigated micro-structurally *e.g.*, Rhum in Scotland (Holness et al., 2005, 2012; Holness, Vukmanovic, et al., 2017), Skaergaard in Greenland (Holness et al., 2011; Holness, Nielsen, et al., 2007; Holness, Tegner, et al., 2007;

Holness, Vukmanovic, et al., 2017; Marsh, 1998; Tegner et al., 2009), Bushveld and Vredefort in South Africa (Dyck & Holness, 2022; Holness, Vukmanovic, et al., 2017; Merkle & Wallmach, 1997; Tredoux et al., 1999; Vukmanovic et al., 2021; de Waal et al., 2006), Baima, in China (Holness, Vukmanovic, et al., 2017), and Banks Peninsula in New Zealand (Bertolett et al., 2019). Microstructures at these locations show signs of compaction, recrystallisation, and variable levels of textural maturity (Henry et al., 2021; Holness, 2007; Holness, Nielsen, et al., 2007; Holness, Vukmanovic, et al., 2017; Tegner et al., 2009). In terms identifying cumulate CPO within the nakhlites one would expect to see foliation patterns in both inter and intra-crystalline orientations related to dominant planar strain. Any evidence of lineation within the samples, as previously suggested by Daly, Piazolo, et al. (2019), could either be related to post-emplacement deformation or a non-cumulate formation for the samples.

1.3.2 Deformation

Deformation is a ubiquitous process observed in nearly all geological specimens, where the observed deformation can be derived from either anthropological or natural processes. Recrystallisation, brittle deformation, plastic deformation, and elastic deformation are the different mechanisms by which geological specimens will deform. The type/variety/absence, distribution, density, and scale of deformation recorded by one or more aforementioned mechanisms can provide vital information regarding the formation history and evolution of the source geological environment/sample.

Geological deformation tends to be categorised into either macro- or microscale deformation. However, it is commonly acknowledged that both categories are not mutually exclusive. Both categories, macro- and micro-scale, are intrinsically linked, where information on one scale can provide insight into another. It is considered good practice in micro-structural geological field studies to include and link both categories, macro- and micro-scale, to better contextualise the micro-scale analysis. This is due to the development of deformation occurring more as a continuum, where the extent and development of the deformation will be reliant on whether the deformation source is derived from a more global (*e.g.,* tectonics, weathering) or local (*e.g.,* intrusion, excavation. burial, hyper velocity impact) origins.

In this thesis I will be investigating plastic micro-structural deformation within the nakhlites through analysis of augite and olivine crystals (chapter 3). The specific type of plastic deformation assessed is referred to in the literature as either LPO or CPO, crystallographic dislocations, internal misorientations, intra-crystalline misorientations, or the more colloquial term slip-systems which assess the movement and distortion of the unit cells within a given crystal.

1.3.2.1 Basic crystallography

Crystals, which form igneous rocks, are the culmination of a regular arrangement of atoms in solid form. Minerals being crystals with a consistent and defined chemical composition. The smallest repeating unit of atoms within a crystal is referred to as the unit cell [Fig. 1.16; Kelly and

Knowles (2020)]. It is from the unit cell that the crystallographic axes lengths used for CPO analysis are derived (Britton et al., 2016; Kelly & Knowles, 2020). When multiple unit cells are joined, they form what is known as a crystal lattice (Fig. 1.17). The way that the unit cells connect to form the crystal lattice is what influences a given crystals class (*i.e.*, symmetry) which can be broken down further into seven crystal groups [*e.g.*, monoclinic and orthorhombic; Kelly and Knowles (2020)]. A given crystal's morphology and habit (*i.e.*, shape) is controlled by the nucleation, growth rate, growth direction, and arrangement of the crystal lattice in 3D.

Defects within a given crystal (*i.e.*, the departure from the regular atomic arrangement) result in the formation of point, line, and plane defects within the unit cell or crystal lattice (Kelly & Knowles, 2020). Defects within a crystal are common for naturally occurring minerals, particularly when they begin to alter. A common process which causes crystal defects is isomorphic substitution, where an atom of equivalent or smaller radius (typically transition elements or REE's) replaces a standard atom for a given mineral within a particular unit cell. The change in size and often different valency of the substituted atom creates a weak point in the crystal lattice which is more susceptible to crystallographic dislocations (Kelly & Knowles, 2020).

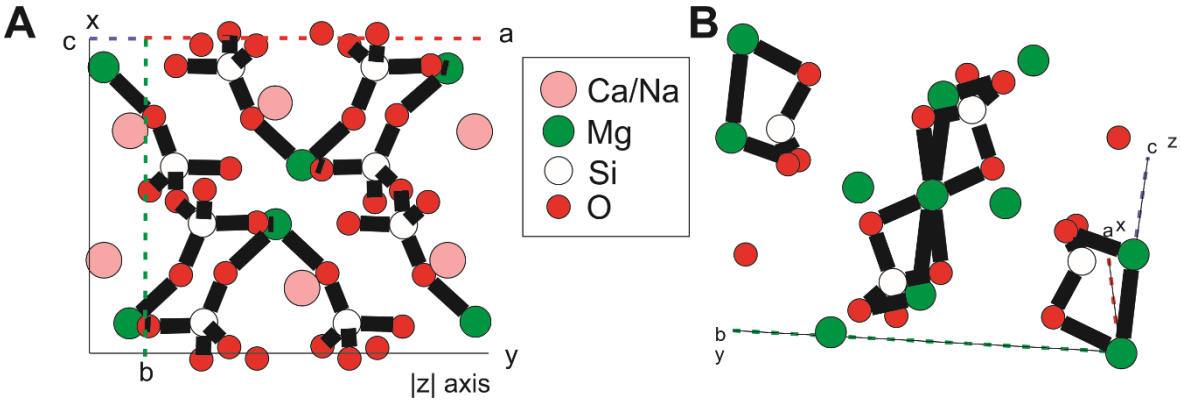

Figure 1.16. *Unit cells for A) augite and B) forsterite, which form the base unit for their respective crystal lattices.*

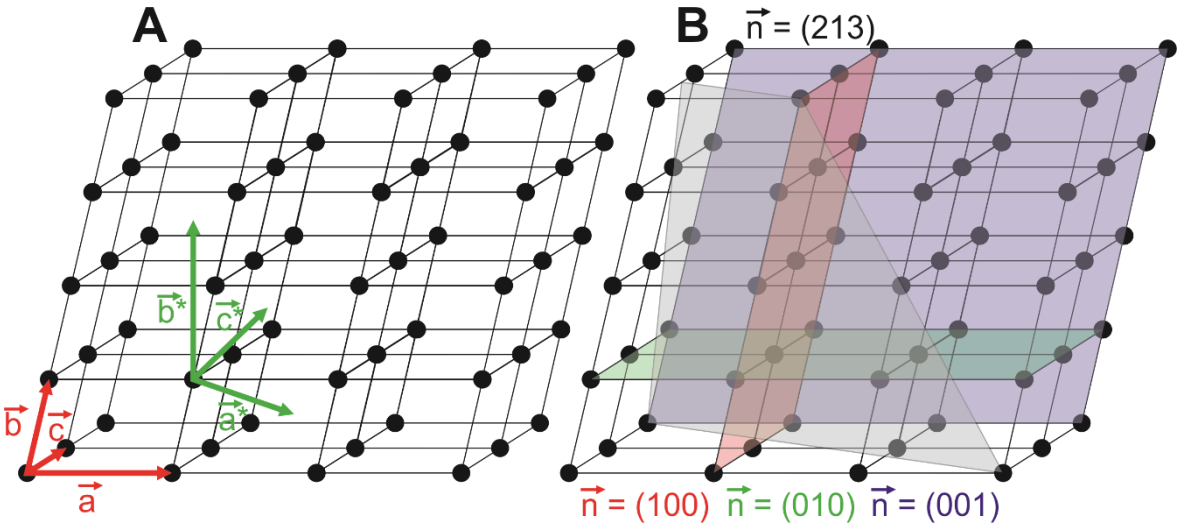

Figure 1.17. *Depiction of a generic crystal lattice. A) Crystal lattice with vector orientations (red) used to depict lattice points (black dots, <u,v,w>) and reciprocal vector orientations (green) used to depict their integers ({h,k,l} i.e., any point between points along a given plane). B) depiction of lattice planes with respect to the crystal lattice.*

The unit cell, *i.e.,* fundamental building block of a given crystal, represents the smallest repeating group of atoms within a crystal lattice (Fig. 1.16). The atoms which comprise the unit cell are what is typically used to chemically define a given mineral (Kelly & Knowles, 2020). The unit cell is often depicted by an imaginary box within a given crystallographic model or as points within a simplified crystal lattice (Fig. 1.17). The dimensions of the imaginary unit cell box refer to the crystallographic axes' lengths, the angles between the crystallographic axes (e.g., α, β, γ) relate to how the various unit cells position themselves relative to one another to form the larger crystal lattice.

Any crystal lattice will be considered in terms of its points or planes (Fig. 1.17). The points generally refer to an individual unit cell, represented by <*u, v, w*> (Britton et al., 2016). Planes, on the other hand, refer to the relationship between the various points within the lattice and are represented by {h, k, l} (Fig. 1.17). In crystallographic nomenclature crystallographic axes have a positive (*e.g.,* 100) and negative (*e.g.,* -100 or $\bar{1}00$) direction, thus different brackets are used to define whether we are talking about one or both directions (Table 1.2). A particular point or a plane within a crystal lattice can also have various relationships to one another *i.e.,* can intersect an axis at any spacing (*e.g.,* 100, 200, $\frac{1}{2}100$, etc. = u or h). When we are referring to a specific point or plane a number will be used however, to refer to multiple points or planes along a specific axis either *u, v, w* or *h, k, l* will be used (Table 1.2).

Table 1.2. *Crystallographic nomenclature*

	Points	**Planes**
Single direction	[ ]	( )
All directions	< >	{ }
nomenclature	*u, v, w*	*h, k, l*
A axis	*u* 0 0	*h* 0 0
B axis	0 *v* 0	0 *k* 0
C axis	0 0 *w*	0 0 *l*

In this thesis I will be assessing intra-crystalline misorientations within 2/m (B2/b) monoclinic (augite) and mmm (2/m) orthorhombic (olivine) both of which are low symmetry crystals. 2/m (B2/b) monoclinic refers that a crystal which has two symmetrical fundamental sectors (smallest section of symmetry) related by a 180° rotation about a mirror plane (*i.e.,* the fundamental sector needs to invert then rotate by 180° to end up in a symmetrically equivalent position). In the case of augite, the mirror/inversion plane is along the <*c*> aka <001> axis where the 180° rotation accounts for the 107° γ angle (γ = angle between the <*a*> and <*c*> axes, aka <100> and <001>) resulting in a semi-circular fundamental sector (Fig. 1.12). Mmm (2/m) orthorhombic refers to a crystal which has 3 mirror planes. For olivine α = β = γ = 90° where the mirror planes lie along each of the <*a*>, <*b*>, and <*c*> axes (*i.e.,* <100>, <010>, and <001>). An mmm (2/m) crystal consists of 8 fundamental sectors which are related by a single inversion along any of the mirror planes (Fig. 1.13).

1.3.2.2 Crystallographic slip-systems (internal misorientations)

Crystallographic slip-systems are a type of plastic deformation defined by a crystallographic plane and direction [Fig. 1.17, Table 1.2; Barber et al. (2010)]. Crystallographic dislocations within a crystal form from the activation of specific slip-systems resulting in breakages or movement within the crystal lattice where there is no volume change or brittle deformation (Kelly & Knowles, 2020). Slip-systems are activated within the crystal lattice to accommodate changes in the stress/strain field around the crystal. Slip-systems involve movement within the crystal lattice (*e.g.*, glide, creep, tilt, rotation) which can propagate to form observable features such as twin planes and low angle boundaries (Barber et al., 2010; Groves & Kelly, 1963; Kelly & Knowles, 2020). Each mineral, based on its crystal symmetry and chemical composition will have preferentially activated slip-systems. However, these preferential slip systems can change based on a variety of intrinsic and extrinsic factors *e.g.*, temperature, pressure, strain, stress magnitude, water content, crystal orientation *etc.* (Karato et al., 2008; Paul Raterron & Jaoul, 1991; Tielke et al., 2019), where current intrinsic and extrinsic parameters have been largely derived from low strain (*i.e.*, mantle rock) experiments and natural sample studies. Table 1.3 depicts the slip-systems associated with known nakhlite mineral phases. For this thesis, only the intra-crystalline misorientations (*i.e.*, the summation of multiple slip-systems within a given sample) related to olivine and monoclinic pyroxene will be discussed.

Table 1.3. *Identified slip-systems for various mineral phases within the nakhlites.*

Mineral	**Main slip systems**		**Known Burgers vectors; (*shortest)**
	Low temperature	High temperature	
Olivine (orthorhombic)	(010)[001], {110}[001]	{0k1}[100], (010)[100]	[001]*, [100]
Pyroxene (monoclinic)		(100)[001], {110}[001]	[001]*
(orthorhombic)		(100)[001],	[001]*, [010],
Plagioclase feldspar		(010)[001], {001}<110>, (001)[100], (010)[100]	[001]*, [100]

To effectively interpret the cause of slip-system activation within a given mineral, an understanding of the geological context of the host rock is important. For assessment using 2D electron backscatter diffraction (EBSD) data, knowledge of the reference frame between the analysed sample and the larger geological structure from which the stress field can be established is considered critical (Halfpenny, 2010). Recording and keeping track of the appropriate reference frame(s) is standard practice for geological EBSD investigations, particularly when investigating field data where the principal strain axis within the sample is generally unknown (Goswami et al., 2018). Not knowing the principal strain axis is also true for most extra-terrestrial specimens. However, these extra-terrestrial samples have the added complication, where there is a lack or limited knowledge of the specimen's geological 'outcrop' context, the exception being samples that have been returned to Earth by space missions (e.g., the Apollo programme). When studying meteorites, knowledge of the specific sample(s) reference frame to the geological source, specific parent body, relation to other

meteorites of the same class/group is often unknown or uncertain. Ascertaining the geological context of meteorites is an area of active research (Burbine et al., 2002; Devillepoix et al., 2020; Jenniskens et al., 2021; Suavet et al., 2010). Acknowledging this lack of a reference frame between samples is particularly important when comparing datasets across multiple meteoritical specimens, such as the presented information within this thesis assessing the nakhlites from Mars.

1.4 Techniques: background and methodology

1.4.1 Scanning electron microscope (SEM)

1.4.1.1 Overview

The scanning electron microscope (SEM) is a microscopic imaging technique which utilises a focussed beam of electrons which produce a signal through interaction with the near surface of a given sample. There are currently three basic types of SEM available: standard SEM, environmental SEM (ESEM) and low vacuum SEM (LV-SEM) where standard SEM's and LV-SEM can also be combined into variable pressure (VP)-SEM (Mohammed & Abdullah, 2018). Alongside the basic SEMs specific SEM's *e.g.,* cryo-SEM, shielded-SEM, have also been developed. For this thesis standard SEMs were used across four different laboratories. A standard SEM, (which include secondary electron (SE) and backscatter electron (BSE) detectors) is only capable of assessing the surface topography of a given sample; however, additional detectors can be added to a given SEM to enable more specialised and multi-component analysis (Joseph I. Goldstein, 2012; Joseph I. Goldstein et al., 2017; Mohammed & Abdullah, 2018; Zhou et al., 2007). The most common detector which is nowadays considered to be a standard part of an SEM is the electron dispersive X-ray spectrometer (EDS), which enables qualitative assessment and sometimes quantitative assessment of the sample's major-minor element chemistry. SEM images, which are produced in greyscale, enable the magnification of samples up to 300,000 × enabling the characterisation and analysis of nanometre-micrometre scale objects within a sample. For comparison traditional optical microscopy has a magnification range between 400-1000× (Mohammed & Abdullah, 2018).

1.4.1.2 How SEM imaging works

The electrons used to generate an SEM image are produced via an electron emission source. The emission source, referred to as the electron gun, produces a broad electron beam which can range from 100-30,000 eV (Joseph I. Goldstein, 2012; Zhou et al., 2007). The data collected within this thesis utilised four different SEM's three of which used field emission to generate electrons and the fourth SEM utilised thermal emission. The difference in voltage produced from the electron gun will inform the depth and signal strength of the data collected. Lower voltages generate lower energy electrons that do not penetrate deeply into the sample and therefore will provide data related to surficial information, whilst higher voltages generate more energetic electrons that penetrate deeper into the sample and thus provide details relating to the interior structure (typically up to 1 μm) as a result of electron sample penetration (Zhou et al., 2007). For the analysis in this thesis all images were collected using a voltage of 20,000 eV (*i.e.,* 20 keV). Beam current varied between machines

ranging from 4.1–20 nA, depending on the instrument and was varied in response to the samples to optimise data quality.

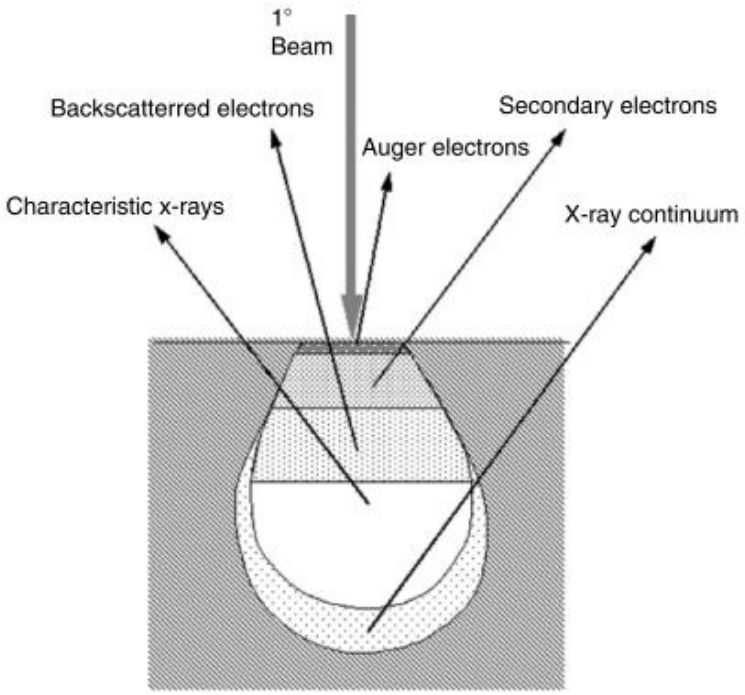

Figure 1.18. *Several types of signals generated by electron beam-specimen interaction within an SEM and their source region within the sample. Image from* (Zhou et al., 2007). *Backscattered electrons used for EBSD analysis tend to be generated within the top ~49 nm of the material.*

To produce an electron image, the electron beam is first focussed through a series of lenses (condenser and final), to generate a narrow spot size ≤10 nm (Joseph I. Goldstein, 2012; Zhou et al., 2007). The size of the focussed beam is generally reported in terms of the aperture width *i.e.,* the size of the hole which the electron beam is allowed to pass through. In this thesis we used an aperture width of 120 μm, which enables focussed 'spot' information to be obtained without amorphising specific minerals (*e.g.,* plagioclase) within the samples. Once the electron beam has passed through the aperture it is able to impinge on and interact with the sample. As the electron beam hits a spot on the sample it produces either one or two types of signals; inelastic (*e.g.,* secondary elections; SE) generally <50 eV and/or elastic [*e.g.,* back scattered electrons (BSE) which provides information about the crystallographic lattice] generally >50 eV (Zhou et al., 2007). The different types of signals generated through electron interaction with the sample are shown in Figure 1.18, where different detectors are used to collect and process the specific data. In standard SEM images it is the combination of the SE and BSE which are detected by their respective electron detectors that produce the image. Generally, a positive voltage is used to create both elastic and inelastic signals however, if a negative voltage is used only elastic signals will be collected (Zhou et al., 2007). The strength of the SE and BSE signals is dependent on the working distance between the sample as well as the tilt of the sample. Nearly all general SEM analyses are done with the sample perpendicular to the electron beam. Excepting backscatter focussed techniques *e.g.,* electron backscatter diffraction (EBSD), where the sample will be tilted 70° to maximise the collected BSE signals (Halfpenny, 2010; Prior et al., 1999), and transmission Kikuchi diffraction (TKD) where the sample is thinned to

electron transparency to allow the electron beam to pass through the sample (Sneddon et al., 2016; Trimby, 2012). In terms of the working distance between the sample and the detector, the optimum distance will depend on the set up of the instrument and the type of analysis being undertaken.

Rastering is the process that enables an electron image to be produced rather than individual data points. The process utilises scan coils located between the different condensing lenses and final lens to shift the electron beam in a linear manner across the defined magnification area (generally rectangular in shape) to produce a continually reiterating series of signals that form the working image displayed on the instrument monitor (Zhou et al., 2007). This is not to be confused with the process of region or the creation of large area map through stitching together multiple EBSD panels where the defined raster area (aka image frame) shifts across the sample either through movement of the electron gun or the sample stage. The raster (signal iteration) speed can be either speed up or down in accordance with the users' specifications.

Movement and warping of the electron beam will often require the adjustment of the detected signal and electron beam to produce a focussed image. On an SEM the brightness and contrast of the elastic and inelastic signals alongside the stigmation are adjusted at the start of any given scan/ scan area (Joseph I. Goldstein, 2012; Zhou et al., 2007). Stigmation relates to the correction of astigmatism (the warped shape of the electron beam). As the electron beam passes through the various lenses and the two apertures, defects or misalignment of the lenses and apertures can result in warping of the beam. To correct for this a stigmator, consisting of a series of coils, that surround the electron beam are used to readjust the shape (Zhou et al., 2007). For larger SEM map areas or for the analysis of tilted specimens (*e.g.,* EBSD), the focus will need to be set and adjusted at various points (generally the outer corners) of the scan region. This enables the focus to be adjusted accordingly across the map. For stitched tilted maps such as those used in this thesis, attention to the stigmation is particularly critical when focussing the stitched map area as any warping of the image will be more obvious.

1.4.2 Energy dispersive X-ray spectroscopy (EDS)

1.4.2.1 Overview

The capability of energy dispersive X-ray spectroscopy (EDS) has been used in conjunction with SEM imaging since 1968 (Mohammed & Abdullah, 2018). The technique is considered to be qualitative to semi-quantitative where the spectrometer measures resulting X-rays produced by the sample via a solid-state detector (Mohammed & Abdullah, 2018). The data produced enables the assessment of variations in a given sample's chemical composition. The data itself becomes more quantitative in nature when standards are run alongside the sample of interest to calibrate the detected X-rays.

1.4.2.2 How EDS works

When the SEM electron beam hits the sample, the electrons penetrate the top 1 µm of the material entering its coulomb field and exciting the minerals outer shell electrons (Joseph I. Goldstein

et al., 2017). Within the coulomb field the excited electrons decelerate back to their initial ground state resulting in photon emission to accommodate the loss of energy (*i.e.*, grounding of excited outer orbital electrons). The specific characteristics of photons emitted from a given material will depend on the amount of energy lost through electron deceleration and consequential photon emission (Joseph I. Goldstein et al., 2017; Mohammed & Abdullah, 2018; Zhou et al., 2007). Different materials (in this case minerals) absorb different amounts of energy in accordance with their atomic structure (*i.e.*, based on the outer shell electron configuration and specific electron excitation orbital gaps). In the case of an EDS detector, it is the intensity of the emitted X-ray photons that is collected and analysed (Joseph I. Goldstein et al., 2017; Zhou et al., 2007).

In order for the collected X-rays to be properly quantified, the EDS detector takes the X-ray photons and converts them into an electrical signal. The signal is then separated out into the various elemental characteristic components using the energy spectrum (Joseph I. Goldstein et al., 2017; Zhou et al., 2007). The amplitude of each specific X-ray peak and position along the energy spectrum can be directly correlated an elements' abundance within the sample. Thus, the combinations of various elemental peaks can be used to assess the chemical composition of the sample enabling a qualitative and semi-quantitative assessment of the major and minor element chemistry of a sample to be made.

1.4.2.3 Processing

1.4.2.3.1 AZtec

All data within this thesis was collected using the proprietary processing software AZtec from Oxford Instruments. The Aztec software is only one type of commercial software available for the collection and processing of Sem data. Aztec software is used for the collection and montaging of maps (both EDS and EBSD), the processing of EDS data, and the collection of semi-quantitative map spectra. Standard SEM images, EDS maps and EDS spectra are processed directly within the programme where as EBSD data, once montaged, is exported to be processed by specialist software such as HKL Channel 5/AZtecCrystal designed for interpreting Aztec collected data or independent software such as MTEX.

1.4.3 Electron backscatter diffraction (EBSD)

1.4.3.1 Overview

Electron backscatter diffraction (EBSD) is a scanning electron microscope (SEM) technique that uses the elastic BSE signals to provide crystallographic information (orientation, microstructure, crystal grain boundary interactions *etc.*) used in material characterisations and investigations. A BSE is technically defined as a signal that escapes the sample surface with an energy over 50 eV after one or more scattering events (Zhou et al., 2007). The manner in which BSE's are generated provide specific crystallographic information that is not necessarily observable from the surface topography of the sample. EBSD scans are collected with the sample at a 70°tilt angle to the electron beam (Fig. 1.19; Prior et al. 1999). This tilted angle alongside the distance between the detector and sample are

used to maximise the strength and quality of the BSE signal picked up by the phosphor screen of the EBSD detector. Contact between the BSE and the phosphor screen result in the formation of Kikuchi patterns (Prior et al., 1999), which are compared against a database of model Kikuchi patterns for all known crystalline materials to index the material and extract its crystallographic information, including phase and orientation.

1.4.3.2 How EBSD works

EBSD collection requires the surface analysed ideally to be damage free and uniformly flat (Halfpenny, 2010; Prior et al., 2009). This requires specific polishing of the sample and may not be as easily achieved within geological specimens, due to the different hardness of the minerals. Most samples will undergo chemical polishing after the standard mechanical polishing required for general SEM analysis (Prior et al., 2009). The chemical polishing aids in removing mechanical polishing damage to the crystal lattice creating ideally a uniform surface to the sample. The flat surface makes the collection of the elastic BSE signal easier to detect by optimising the electron entry and backscatter return angles (Halfpenny et al., 2012).

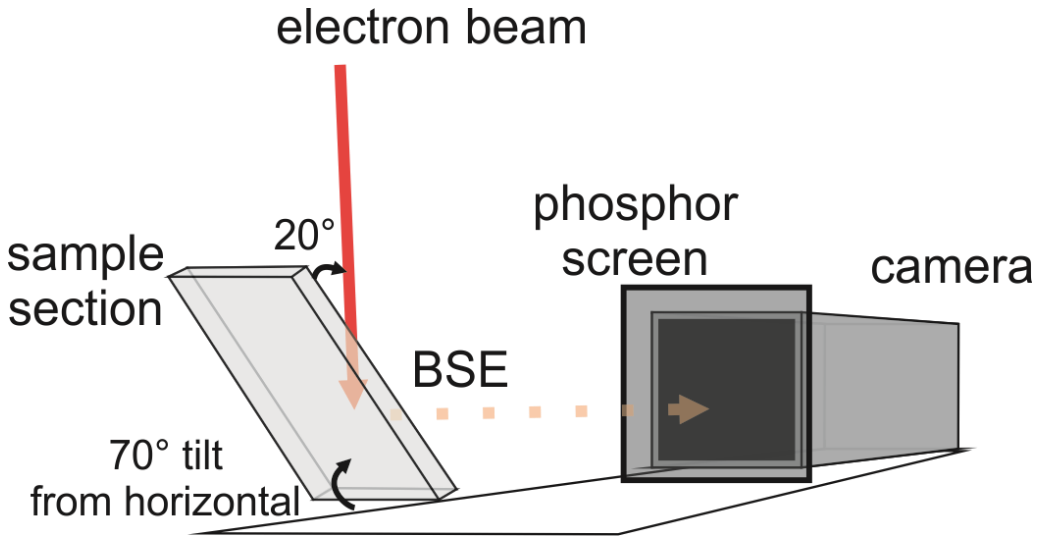

Figure 1.19. *Typical set up for electron backscatter (EBSD) experiments. The sample will be tilted 70° from horizontal (20° to the electron beam) to maximise the diffracted back scattered electrons (BSE). Camera position relative to the sample is instrument dependent and is taken into account during data processing.*

The EBSD signal is formed from the electron beam penetrating the top ~ 20-50 nm of the sample depending on the beam current/accelerating voltage during analysis (Fig. 19; Halfpenny 2010). The BSE's form from collision of electrons from the electron beam with the atomic nuclei residing in the sample's crystallographic lattice. As the width of the electron beam is normally wider than the atomic spacing within the crystallographic lattice, the collision of electron beam and sample lattice plane will result in a number of backscattered electrons with various backscatter angles (ranging 0-180°; (Prior et al., 2009; Zhou et al., 2007). The density of backscatter orientations therefore will correspond to the detected signal intensity. When assessed in 3D, the backscatter trajectory for each lattice plane forms two cones whose axis is almost normal (~180°) to the crystal lattice. This ~~180° angle forms a narrow gap between the conical structures enabling them to be approximated as planes (Higgins, 2006; Prior et al., 2009; Zhou et al., 2007). These planes are

referred to as Kikuchi bands where one side of the band will naturally be brighter than the other. The formation of the Kikuchi bands follows Bragg's law:

$$n\lambda = 2dsin\theta \quad (1.1)$$

Where *n* is the order of diffraction (integer), λ is the electron beam wavelength (related to acceleration voltage), *d* is the crystal lattice spacing, and θ is the diffraction angle. The amount of the electrons directly returned from collision correlates to the atomic number of the nuclei, where higher atomic number materials return more electrons (*i.e.*, produce greater intensity; Goldstein et al. 2017; Prior et al. 2009).

In general, between 10-50% of the incoming electrons exit the crystal lattice at the same angle. These backscattered electrons retain anywhere between 60-80% of their initial energy (Joseph I. Goldstein et al., 2017; Zhou et al., 2007). When collecting EBSD data the sample is tilted, the optimal angle being 70°, to maximise the detector's collection of returning backscattered electrons (Fig. 1.19; Halfpenny 2010; Prior et al. 2009). The EBSD detector consists of a phosphor screen in front of a CCD camera. Upon collision with the phosphor screen the backscattered electrons are converted into light, creating characteristic Kikuchi patterns (Joseph I. Goldstein et al., 2017; Zhou et al., 2007). The phosphor screen is generally placed as close to the sample as possible as this enables clearer Kikuchi patterns to be recorded through reducing their distortion. These collected patterns, through a process referred to as indexing, are compared against known Kikuchi pattern databases (EBSD libraries) to identify and extract crystal symmetry information from the material (Halfpenny, 2010; Prior et al., 2009). The detection and subsequent indexing of Kikuchi patterns can be enhanced through a process known as background subtraction, where the standard noise of the instrument is removed from the analysis (Fig. 1.20).

Kikuchi patterns [also referred to as electron backscatter patterns (EBSPs)] are the summation of all the Kikuchi bands from a given crystal lattice (Fig. 1.20; Dingley and Wright 2009). The intersection spacing, band position, band thickness, band intersections and angles within a Kikuchi pattern is what provides the crystallographic information used for EBSD analysis. For each Kikuchi pattern the bisector of each Kikuchi band plane represents the lattice direction, the width of the band corresponds to the diffraction order (*n* value ratio), the highest intensity band represents the lowest-order lattice plane diffraction (with respect to symmetry), and bright spots (points where numerous bands intersect) represent the zone axis (Dingley & Wright, 2009; Joseph I. Goldstein et al., 2017; Zhou et al., 2007). The comparison and combination of each portion of the Kikuchi pattern are what enable the crystallographic symmetrical elements of a given material to be defined.

Analysis speeds for samples will be determined by the lowest atomic material number being indexed, the area of interest and the step size used for analysis. In geological samples the lowest atomic mineral being indexed will be the rate limiting factor (Halfpenny, 2010; Prior et al., 2009). For most samples this will generally be some form of feldspar *e.g.*, plagioclase or alteration phase *e.g.*, calcite. Lower atomic numbers require longer electron beam dwell times to produce reasonable MAD values (indication of Kikuchi pattern index quality). Where the longer dwell times are a direct consequence of the lower return on diffracted electrons (Adams & Field, 2009; Prior et al., 1999).

However, the beam dwell time on the sample will also need to be less than the time/energy required to amorphise the material. Hence it is important to know what materials are being analysed as this will affect the overall analysis time.

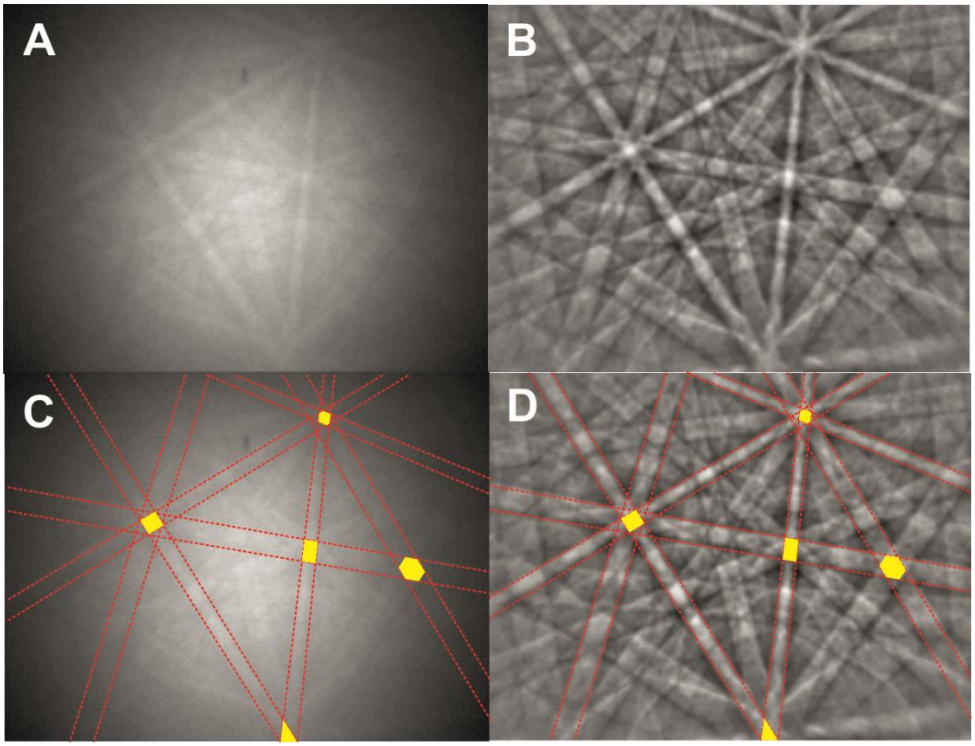

Figure 1.20. *Kikuchi diffraction patterns also known as electron backscatter patterns (EBSP) of Austenitic steel. A) original diffraction pattern; B) diffraction pattern with background subtraction; C) A with several Kikuchi band planes are outlined in red and zone axes (bright spots) highlighted in yellow; D) B with several Kikuchi band planes are outlined in red and zone axes (bright spots) highlighted in yellow. Image modified from EBSD Oxford Instruments - EBSD Pattern Collection.*

In EBSD studies it is common practice to run individual maps of selected crystals or small regions of interest. In part this has resulted from a limitation of beam stability, processing time (where indexing is the limiting step), and the size of the resulting dataset (Joseph I. Goldstein, 2012; Joseph I. Goldstein et al., 2017; Halfpenny, 2010; Prior et al., 2009). Depending on the area of interest and the type of investigation, an appropriate step size needs to be selected. The step size will determine the spatial resolution of the EBSD data thus, for any EBSD study the step size needs to be smaller than the item of interest. For general SPO and CPO studies the step size will be restricted to the smallest crystal size in the sample, whilst crystallographic dislocation studies that focus on micro-structural deformation within an individual crystal will typically require step sizes ≤ 4 μm.

Advancements in technology over the last decade, such as greater computer processing capabilities, computer memory, increased beam stability, automated stage movement *etc.* have enabled the collection of smaller step-size larger scale area maps due to the resulting increased accuracy, precision, and reproducibility. These stitched EBSD maps can be up to the size of a standard thin section and are often used for CPO studies to ensure data is collected on a statistically relevant number of crystals (Mason & Schuh, 2009; Prasannakumar & Lloyd, 2010; Qi et al., 2018). To offset the analysis time and the size of the final dataset, these studies are often run at a step size

of 10-15 µm and often only the phase of interest will be indexed. However, there is now the possibility to run EBSD using multiple phases at a high enough spatial resolution to collect CPO information (both phase orientation and slip-system deformation) at a rock representative scale. The larger scale multi-phase stitched EBSD datasets, which are presented in this thesis, enable the collection of and interpretation of contextualised statistically relevant data of whole rocks.

1.4.3.3 Processing

1.4.3.3.1 HKL Channel 5/ AZtecCrystal

HKL Channel 5 and its updated version AztecCrystal are proprietary Oxford Instruments software packages for processing EBSD data. The programmes work using an interface and in the case of HKL Channel 5 various sub programme packages. In this thesis Channel 5's Tango package was used to process the EBSD images and crystal statistics, and the Mambo package was used to produce CPO pole figure and misorientation axis inverse pole figure (IPF) plots. These plots enable CPO and crystallographic slip-systems (misorientation axis IPF) to be visualised and investigated. All data presented in this thesis has been processed in full using both HKL Channel 5 and AZtecCrystal software. Due to changes in the algorithms used between the two programmes all of the data presented we have only used the HKL Channel 5 processed data. Some of the distinct differences noted between the two programmes were the change in the manner the reference frames between the sample chamber and the section were processed and recorded alongside changes to the grain detection algorithm.

1.4.3.3.2 MTEX

MTEX is a free toolbox for MATLAB which was invented by Ralf Hielscher in 2007 and is now an opensource software developed by an interdisciplinary team of material scientists, geologists, and mathematicians. The software assists in the analysis and modelling of SPO and CPO using either EBSD or pole figure (*i.e.*, any form of orientation) data (Bachmann et al., 2010, 2011; Mainprice, Bachmann, Hielscher, Schaeben, et al., 2015). The software can be used to calculate any orientation dependent properties of a material using fundamental principles. An advantage of the software is that it is script-based, where the underlying code is focussed on basic computations which can then be developed and modified in accordance with the individual user's needs (Bachmann et al., 2011; Mainprice, Bachmann, Hielscher, & Schaeben, 2015; Mainprice, Bachmann, Hielscher, Schaeben, et al., 2015). The software enables consistent analysis of any EBSD dataset regardless of the commercial software (*e.g.,* Oxford or Brucker) used in collection. As MTEX is script-based it removes the 'black box' behind the interface of commercial software and enables types of analysis currently not available in standard commercial software packages such as Oxford Instruments Channel 5/AZtecCrystal processing software (*e.g.*, the consistent analysis of samples run using different commercial software, the ability to correct misaligned/warped data, rotate phases within maps, create plots using parameters not currently available in standard commercial software, *etc.*).

MTEX version 5.7.0 was used with MATLAB version 2020a to calculate CPO metrics from the EBSD data. The associated code used to calculate the data can be found in the appendices.

1.4.4 Application of EBSD in planetary sciences

EBSD began to be applied to geological samples in the late 1990's (Prior et al., 1999) and has been used in planetary science research since the mid 2000's. Initial work was predominantly focussed on the analysis of iron meteorites (*e.g.*, (Einsle et al., 2018; J. I. Goldstein & Michael, 2006; Nichols et al., 2018; G. Nolze et al., 2005; Gert Nolze et al., 2005), with some initial work done on the chondritic meteorite Allende, that is still being expanded and built upon (Forman et al., 2017; Ma et al., 2009, 2012; P. Trimby et al., 2018; Watt et al., 2006). The application of EBSD has since expanded in the last decade to include the identification of new mineral phases (*e.g.,* Daly et al. 2016; Ma and Rossman 2009; Ma et al. 2009, 2017; Zolensky et al. 2008), micro-structural investigations of chondritic matrix (*e.g.*, Forman et al. 2017, 2019; Watt et al. 2006), impact cratering studies (*e.g.*, Cavosie et al. 2015; Cox et al. 2019, 2020; Erickson et al. 2013; Kenny et al. 2020; Moser et al. 2011), meteorite shock deformation microstructures (e.g., Daly et al. 2019a; Darling et al. 2016, 2021; Forman et al. 2017; Kizovski et al. 2020; Ruzicka and Hugo 2018), and even CPO analyses (Daly, Piazolo, et al., 2019; Tkalcec & Brenker, 2019).

Use of EBSD within the planetary science community has only begun to expand in the last several years. Where most of the published work has been restricted to a handful of individuals/labs. A large portion of published work to date utilises EBSD in combination and often as a secondary technique to confirm, orient, or identify key areas for other specialist analysis. For those studies where EBSD is the main technique used the analysis tends to focus on specified individual crystals or small specified regions. Overall, the majority of the work has either focussed on some variation of shock deformation related microstructures, or the identification and classification of new mineral structures.

It must be noted however, that a lot of EBSD analyses applied to planetary specimens have yet to be presented in peer-reviewed publications. Currently, a significant proportion of available planetary EBSD data is only available in abstract format or in student theses. This is not just an issue for EBSD data but for many other forms of meteoritical analysis using cutting edge techniques.

1.4.4.1 Application on Martian meteorites

A large proportion of EBSD studies of Martian meteorites have been applied to the shergottites, the largest Martian meteorite group (Greshake et al., 2013; Kizovski et al., 2020; Ma et al., 2018; D. E. Moser et al., 2013; Papike et al., 2014), with fewer studies applied to the lesser abundant nakhlites and chassignites (Daly, Lee, et al., 2019; Daly, Piazolo, et al., 2019; Lee et al., 2018; Lee, Tomkinson, et al., 2015; Tkalcec & Brenker, 2019; Tomkinson et al., 2013, 2015b). The majority of these EBSD analyses focus on the mapping of selected crystals or smaller regions around specific crystals. Typically, EBSD is applied to a single section of a given meteorite with four

different meteorites being the largest variety of specimens analysed in a single study (Daly, Piazolo, et al., 2019). None of the studies assess replicate sections from the same sample.

For studies assessing the Shergottites, EBSD has been utilised to analyse, identify, and assess microstructures within zircon and its shock metamorphic polymorphs (Darling et al., 2016; Kizovski et al., 2020; McCubbin et al., 2015; D. E. Moser et al., 2013; Roszjar et al., 2017); asses orientation and confirm olivine and its alteration phases (Greshake et al., 2013; Van de Moortèle et al., 2007); confirm and identify phase structures within samples and within crystal zoning (Y. Liu et al., 2021; Ma et al., 2015, 2016, 2018, 2019; Mikouchi & Kurihara, 2008; Papike et al., 2014); and more recently determine apatite microstructures (Darling et al., 2021).

Published EBSD work on the Chassignites is limited to a single study on CPO using a section of chassignite NWA 8694 (Tkalcec & Brenker, 2019). In this study the analysis of the meteorite's CPO focussed on the M-Index of olivine, the dominant phase for the group. Where the EBSD dataset was created utilising a single small map region combined with 29 individual pattern acquisitions.

For the nakhlites (the focus of this thesis), EBSD has been used on individual olivine crystals to determine their orientation (Lee, Tomkinson, et al., 2015; Tomkinson et al., 2013); assess the microstructure of individual olivine crystals and their associated calcite veins (Tomkinson et al., 2015b); identify mesostasis material composition within NWA 817 and assess misorientation relationships within individual olivine crystals to support alteration investigations (Lee et al., 2018); assess the relationship between shock deformation and alteration within Lafayette and MIL 03346 through investigating augite microstructural relationships (Daly, Lee, et al., 2019); and characterise augite micro-structures using coupled SPO and CPO within nakhlites Governador Valadares, Lafayette, MIL 03346, and Nakhla (Daly, Piazolo, et al., 2019).

Out of all the EBSD studies published on Martian meteorites only Daly et al. (2019b, 2019a) and Papike et al. (2014) have investigated clinopyroxene, the dominant phase within both shergottites and nakhlites. Despite augite (high Ca-Clinopyroxene) being the dominant phase within the nakhlites, majority of EBSD investigations have been focussed on the lesser abundant olivine. This is in part due to olivine's apparent higher susceptibility to fluid alteration, a major investigated topic for the group.

In terms of EBSD analysis regions, Daly et al. (2019b, 2019a) are also the only studies to utilise stitched EBSD maps, where the dataset stitches connecting EBSD panels. Tkalcec and Brenker (2019) attempt to mimic this type of EBSD dataset through analysing multiple individual EBSD panels taken across a section, and then subsequently collating the individual data into one larger dataset. For SPO, CPO, and other micro-structural analyses, this approach can ensure crystal fracturing does not bias the final dataset; however, it lends itself toward biased crystal selection and representation. Their methodology also severely limits the types of micro-structural analysis and interpretations that can be applied and derived to/from the dataset.

1.5 Overview of thesis chapters

1.5.1 Chapter 1: Investigating the igneous petrogenesis of Martian volcanic rocks revealed by augite quantitative analysis of the Yamato nakhlites.

In this chapter two modern methods of quantitative micro-structural analysis: crystal size distribution (CSD) and electron backscatter diffraction (EBSD) are applied to the three Yamato nakhlites Y 000593, Y 000749, and Y 000802. The study investigates the disparities, strengths, and weaknesses of the two techniques in response to the conflicting SPO results of Udry and Day (2018) and Daly et al. (2019b) which reported no SPO and SPO, respectively, for the nakhlites Governador Valadares, Lafayette, MIL 03346, and Nakhla.

The Yamato nakhlites on initial inspection were initially proposed as 'launch paired' samples (Imae et al., 2003). However, $^{39}Ar/^{40}Ar$ dating of Y 000593 and Y 000749 by Cohen et al. (2017) presented distinct crystallisation ages that conflicts with the 'paired' stone hypothesis. The presented study assesses all three Yamato nakhlites to see whether any differences between the individual stones can be discerned. Five sections: Y 000593 (106-A), Y 000593 (127-A), Y 000749 (64-A), Y 000749 (72-A) and Y 000802 (36-A), were analysed in total. Two of these sections, Y 000593 (106-A) and Y 000749 (72-A), having been previously analysed using CSD in Udry and Day (2018). The assessment of two replicate sections (four in total) sourced from each of the larger Yamato nakhlite meteorites (Y 000593 and Y 000749) enabled variation within the same meteorite stone to be assessed and thus provide a baseline for comparison between the three individual stones.

The study concluded that all Yamato nakhlites formed in a similar manner, comparable magma chamber residence times with emplacement dominated by gravitational settling, and that for SPO studies, multiple sections of the same sample should ideally be assessed. Both CSD and EBSD techniques utilised datasets ranging from 287–508 crystals (n_{MTEX}) sized datasets for all sections, which has been hypothesised to be representative of whole rock features. However, variation was still prevalent between the two sets of replicate sections. In terms of comparing results between CSD and EBSD techniques the major difference was the manner in which the 2D analysed crystals were corrected for 3D orientation. CSD utilising shape and EBSD utilising crystallographic axes. Utilising only shape-based criteria, both CSD and EBSD techniques showed random SPO within the Yamato nakhlites. However, the use of crystallographic axes as a proxy for SPO in EBSD analyses enabled low intensity girdle CPO to be discerned in all samples.

1.5.2 Chapter 2: Constraints on the emplacement of Martian nakhlite igneous rocks and their source volcano from micro-petrofabric analysis.

This study expands on the initial study of Daly et al. (2019b), who used EBSD to quantify SPO and CPO within four nakhlite meteorites. In this study 16 individual nakhlite meteorites are

analysed using EBSD. EBSD and EDS derived data were also used as input parameters to calculate potential crude unit thicknesses for each meteorite's emplacement igneous unit on Mars

The nakhlite CPO was assessed using the dominant mineral augite. Data is presented on augite SPO and CPO; where quantitative metrics J-Index, M-Index, and Eigenvalues are used in conjunction to investigate CPO. Low intensity <001> foliation fabrics ranging in strength from weak to medium are identified in all samples, with a large proportion of the samples also exhibiting a low-intensity weak-lineation CPO within the <100> axis. All samples show S-LS type eigen CPO with low to medium strength J-Index values. M-Index values show random CPO. SPO shows alignment for two of the meteorites, two competing alignments perpendicular to one another in five of the meteorites and random orientation in nine of the analysed meteorites. The culmination of the analysed CPO and SPO within the nakhlites suggest formation where crystal settling processes overprint initial emplacement CPO

Rough calculated unit thicknesses are presented for three endmember scenarios: Thermal diffusion – which represents the maximum thickness, crystal/gravitational settling – the intermediate thickness, and crystal convection – the minimum potential magma body thickness. Due to the associated error in the calculations, unit thickness distributions are reported in terms of magnitude. For thermal diffusion all samples exhibit calculated magma body thicknesses that are in the tens of meters range. For crystal/gravitational settling three different orders of magnitude are observed for calculated unit thicknesses: less than one metre, metre, and tens of metres. These can be separated outwith error into two distinct groupings (group 1 <10 m thicknesses and group 2 >10 m thicknesses). Crystal/gravitational settling is the emplacement mechanism that best correlates with observed SPO and CPO data. Crystal convection calculations resulted in unit thicknesses that were less than the average crystal size within the nakhlites. The study concludes that crystal/gravitational settling is the dominant mechanism for nakhlite emplacement where magma body thickness >1 m would also exhibit lesser components of crystal convection.

Modelling and CPO results of the nakhlites show that all analysed meteorites within the group formed under similar mechanistic conditions yet appear inherently random when modelled thicknesses are compared against age, geochemistry, and reported SPO and CPO. Dominant crystal/gravitational settling with minor components of lineation and crystal convection is observed at low intensities in all analysed samples. The observation of two distinct orders of magnitude within the nakhlites when compared against published crystallisation ages shows that there was variable discharge over time, differences in the topography where each nakhlite was emplaced, or variable viscosity magmas. Disparity between observed CPO and SPO could be a biproduct of the sections' orientation or indicate that there was a switch in emplacement mechanism resulting in the overprinting of initial emplacement SPO. More importantly the assessment of a larger dataset highlights the danger of interpreting trends from limited sample selection.

1.5.3 Chapter 3: Can the magmatic conditions of the Martian nakhlites be discerned via investigation of clinopyroxene and olivine intra-crystalline misorientations?

In this study plastic deformation in the form of intra-crystallographic misorientations were assessed for sixteen different nakhlite meteorites. Overriding intra-crystalline misorientation patterns for whole section, high deformation regions, and low deformation regions were collected for both augite (high Ca-clinopyroxene) and forsteritic olivine in all samples. The combined assessment of both augite and olivine intra-crystalline misorientation patterns were then used to group the nakhlites based on the dominant observed misorientation patterns and their associated preferential activation parameters to assess the influence of shock deformation and emplacement deformation within the nakhlites.

Olivine intra-crystalline misorientations (and their underlying slip-systems) have been well documented within the literature, where misorientation axis inverse pole figures (mIPF) patterns were shown to link to specific crystallographic slip-systems (Ruzicka & Hugo, 2018) that preferentially activated under different environmental parameters (Bernard et al., 2019; Karato et al., 2008; Katayama et al., 2004). In this study we present equivalent intra-crystallographic misorientation compiled results for clinopyroxene.

This study identified nine different mIPF pattern combinations within the sixteen analysed meteorites. These mIPF patterns indicate low temperature/high pressure to high temperature/low pressure environments, where most analysed samples showed lower temperature/moderate pressure patterns. The study assesses the analytical criteria for appropriate EBSD analysis, the applicability of using dominant intra-crystalline misorientation patterns to interpret representative plastic deformation within a given meteorite, and tests experimental clinopyroxene data against naturally deformed rock specimens.

1.6 Summary of thesis aims and objectives

To answer this thesis's overarching science question of "what can the nakhlite meteorites tell us about their source volcano on Mars?" I have tackled three secondary questions using the crystallographic technique of electron backscatter diffraction (EBSD): 1) Can EBSD be used to distinguish and identify different igneous units within the nakhlite Martian meteorites; 2) What does the micro-structural information reveal about the individual nakhlites emplacement on Mars; and 3) What crystallographic relationship patterns can be revealed from assessing a significant proportion of the currently identified nakhlite group.

To answer the afore-mentioned questions, I have further broken down my aims into the following objectives: 1) conduct a large sample study of the nakhlite meteorites to encompass the growing diversity within the group. In this thesis 16 individual stones are investigated, the largest amount in a single study to date, enabling a wider view to be taken and potential patterns to be assessed. 2) Determine parameters for the identification of representative features within the nakhlites. This will push the current *status quo* within the planetary community of presenting

planetary scale conclusions from the analysis of an unrepresentative number of crystals/small regions within a sample. Finally, 3) Investigate the micro-structures within the nakhlites in a quantitative manner. Micro-structural investigations enable the physical processes behind a rock's formation and subsequent history. Majority of the previously published literature concerning the nakhlites has been highly focussed on the small regions of alteration as well as the sample's geochemistry. By investigating the physical processes, I will be providing complementary information to the already extensive geochemical and isotopic understanding of the nakhlite formation. Achieving my set objectives and answering these questions can provide critical insight into understanding Amazonian volcanism on Mars and provide further constraints towards locating the nakhlite's Martian source and ejection crater.

2 Investigating the igneous petrogenesis of Martian volcanic rocks using augite quantitative analysis of the Yamato nakhlites

S. Griffin[1], A. Udry[2], L. Daly[1,3,4], L. V. Forman[5,6], M. R. Lee[1], B. E. Cohen[6]

[1]School of Geographical and Earth Sciences, University of Glasgow, UK. [2] Department of Geoscience, University of Nevada Las Vegas, Las Vegas, NV 89154, USA. [3]Australian Centre for Microscopy and Microanalysis, The University of Sydney, Australia. [4]Department of Materials, University of Oxford, UK. [5]Space Science and Technology Centre, School of Earth and Planetary Sciences, Curtin University, Australia. [6]Department of Earth and Planetary Sciences, Western Australia Museum, Australia. [7]School of Geosciences, University of Edinburgh, UK.

Key Points:

- Yamato nakhlites exhibit low intensity LS-type CPO indicative of gravity settling driven formation.
- Augite within the Yamato nakhlites experienced long magma residence times with uninterrupted growth.
- Combining IP- QTA (CSD) and EBSD analyses enables more robust interrogation of observed SPO data.

In Press: *Meteoritics and Planetary Science*
DOI:10.1111/maps.13934

S.G. and A.U. designed the research project
S.G. undertook EBSD analyses and A.U. undertook CSD and SDP analyses
S.G. wrote the paper based of discussions with A.U., L.D., and L.V.F
S.G., A.U., L.D., L.V.F, M.R.L., and B.E.C. contributed to editing the paper.

2.1 Abstract

To better understand volcanism on planetary bodies other than Earth, quantification of physical igneous processes is needed. Here, the petrogenesis of the achondritic Martian Yamato (Y) nakhlites (Y 000593, Y 000749, and Y 000802) is reinvestigated via quantitative analysis of augite (high-Ca clinopyroxene) phenocrysts: crystal size distribution (CSD), spatial distribution patterns (SDP), and electron backscatter diffraction (EBSD). Results from CSD and EBSD quantitative datasets show augite to have continuous uninterrupted growth resulting in calculated minimum magma chamber residence times of either 88–117 ± 6 years or 9–12 years. All samples exhibit low-intensity S-LS-type crystallographic preferred orientation (CPO). Directional strain is observed across all samples with intra-crystalline misorientation patterns indicative of (100)[001]:(001)[100] (Y 000593 and Y 000802) and {110}<001> or {110}$^{1}/_{2}$<110> (Y 000749) slip-systems. SDP results indicate phenocryst-bearing crystal-clustered rock signatures. Combined findings from this work support the Yamato nakhlites forming on Mars as individual low viscosity lava flows or sills. This study shows that through combining these different quantitative techniques over multiple samples, one can more effectively compare and interpret resulting data to gain a more robust, geologically contextualised petrogenetic understanding of the rock suite being studied. The techniques used in this study should equally be applicable to igneous achondrites from other parent bodies.

2.2 Plain language summary

The petrogenesis of the three Yamato nakhlites was revisited by applying two modern quantitative techniques: crystal size distribution (CSD) with spatial distribution patterns (SDP)] and electron backscatter diffraction (EBSD) to the dominant mineral augite (high Ca-clinopyroxene). Results showed that augite crystals experienced either 88–117 ± 6 years or 9–12 years (depending on the chosen growth rate) of uninterrupted growth within the magma chamber before emplacement. Identified crystal orientations (SPO and CPO) suggest all three Yamato nakhlites were emplaced in separate crystal setting environments (*e.g.*, a sill or lava lake), where gravity was the dominant source of strain.

2.3 Introduction

Igneous processes play an important role in the formation and development of planetary bodies such as the Earth, its Moon, and Mars, with the latter having features that are heavily influenced by volcanic activity (Carr & Head, 2010; Greeley & Spudis, 1981; Grott et al., 2013; Taylor, 2013). Almost all Martian meteorites are igneous rocks (Blamey et al., 2015; McSween & Treiman, 1998; Udry et al., 2020). These samples therefore provide valuable insights into magmatic processes and conditions including planetary differentiation (McSween, 1994; Shearer et al., 2015), volcanic events (Cohen et al., 2017), magmatic evolution (Borg & Drake, 2005; Day et al., 2018a; Udry & Day, 2018), and igneous process mechanisms (Longhi 1991; Rahib et al. 2019; Santos et al. 2015; Udry and Day 2018).

The Yamato (Y) meteorites (Y 000593, Y 000749, and Y 000802) belong to the nakhlites, which are the second largest group of Martian achondrites (Udry et al., 2020). Found on the same blue ice field in Antarctica (*e.g,*. Imae et al. 2003, 2005; Misawa et al. 2003), isotopic and geochemical data indicate a common parental melt but unidentified source location on Mars (Cohen et al., 2017; Day et al., 2018a; Korochantseva et al., 2011; Nyquist et al., 2001; Okazaki et al., 2003; Treiman, 2005). Initial analysis classified the Yamato nakhlites as fall-paired, and interpreted the samples as fragments belonging to a single large nakhlite cumulate pile (Imae et al., 2003). However, high resolution $^{40}Ar/^{39}Ar$ dating of Y 000593 and Y 000749 by Cohen et al. (2017) concluded that they sample at least two different igneous units soured from a shared parental magma system. The significant increase over the last decade in both number and variability (mineralogical, micro-structural, and chemical) of recovered nakhlites supports the conclusion of Cohen et al. (2017) that the nakhlites represent multiple igneous bodies rather than the initially hypothesised large cumulate pile (Day et al., 2018a; Krämer Ruggiu et al., 2020; Tomkinson et al., 2015b; Udry et al., 2020; Udry & Day, 2018).,

The Yamato nakhlites are excellent samples to use for understanding emplacement through micro-structural analysis as they contain some of the lowest measured relative shock levels across all currently identified Martian meteorites [5–14 GPa (Fritz, Artemieva, et al., 2005)]. To summarise their properties, the Yamato nakhlites are unbrecciated mafic igneous rocks of basaltic composition with shape preferred orientation (SPO) indicating clinopyroxene accumulation (Imae et al., 2005). Euhedral augite (high-Ca clinopyroxene, 69–77 vol.%) is identified as the dominant phase with phenocryst crystal sizes averaging ~1 mm × 0.5 mm. Also observed are olivine (11–15 vol.%), titanomagnetite (1–4 vol.%), and a mesostasis (9–16 vol%) comprised of lath-shaped plagioclase with minor augite, pigeonite, olivine, titanomagnetite, K-feldspar, pyrrhotite, apatite, tridymite, and iddingsite (Corrigan et al., 2015; Imae et al., 2003, 2005; Udry & Day, 2018).

A rock's micro-structure is defined by the relationships (spatial, orientation *etc.*) between and within its constituent components (in this instance crystals). Studies of these relationships provide key insights into physical and material properties, petrogenesis, magmatic evolution, emplacement history (Barsdell, 1988; Corrigan et al., 2015; Daly, Piazolo, et al., 2019; Donohue & Neal, 2018), and post emplacement deformation (Daly, Lee, et al., 2019; Helmstaedt et al., 1972). Here, two quantitative techniques are used: 1) image processed crystal size distribution (CSD) and related spatial distribution patterns (SDP), and 2) crystallographic analysis using electron backscatter diffraction (EBSD). For ease of comparison between the two presented datasets; the image processed dataset (used for CSD and SDP analysis) will henceforth be referred to as CSD and the EBSD dataset as EBSD. To aid the reader, a list of acronyms and definitions used in this paper can be found in Table 2.1.

Table 2.1. *Acronyms used in this paper and their definitions*

Acronym	Definition
A aka "A-Type"	Component of the BA-Index referring to girdle CPO in the crystallographic [100] aka [*a*] axis
B aka "B-Type"	Component of the BA-Index referring to lineation CPO in the crystallographic [010] aka [*b*] axis
BA-Index	the A and B crystallographic axes index; Shows the relationship between the perpendicular <*a*> and <*b*> crystallographic axes where 1 = indicates complete $P_{(010)}$ CPO (B-type) and 0 = complete $G_{(100)}$ CPO (A-type).
CSD	Crystal size distribution
CPO	Crystallographic preferred orientation
EBSD	Electron backscatter diffraction
EDS	Energy dispersive X-ray spectroscopy
GOS	Grain orientation spread; measurement of the angle deviation within crystals across a given dataset
IPF	Inverse pole figure
J-Index	A type of CPO index which uses the second moment of an ODF, where the ODF is the distribution of discrete crystal orientation data in Euler angle space
L aka "L-type"	Component of the LS-Index, referring to lineation or point CPO within the crystallographic [010] aka [*b*] axis
LS-Index	the B and C crystallographic axes index; Shows the relationship between the perpendicular <*b*> and <*c*> crystallographic axes where 1 = indicates complete $P_{(010)}$ CPO (L-type) and 0 = complete $G_{(001)}$ CPO (S-type).
MAD	Mean angular deviation; an assessment of Kikuchi pattern quality
M-Index	Misorientation index (a type of CPO index)
MOS	Maximum orientation spread; maximum angle deviation angle from the mean crystal orientation
M.U.D.	Multiples of uniform distribution, an expression of ODF
Nikon LV100POL	Model of reflective light polarised microscope
ODF	Orientation distribution function
OPPG	One point per grain
PGR	Point (a.k.a. lineation), girdle (a.k.a. foliation), random ternary endmembers of Eigenvalue analysis (a type of CPO index)
S or "S-type"	Component of the LS-Index, referring to "schistose" or girdle CPO within the crystallographic [001] aka [*c*] axis
SEM	Scanning electron microscope
SDP	Spatial distribution pattern
SPO	Shape preferred orientation

The technique of CSD is limited by the resolution of the source images. CSD theory was originally developed to understand crystallisation within chemical engineering but has since been applied to understand crystallisation processes in igneous rocks (Marsh, 1988). The EBSD technique originates from materials science, where it was developed as a characterisation technique (Schwartz et al., 2000). The technique is commonly used via a scanning electron microscope (SEM) which enables the analysis of samples at higher magnifications than traditional optical microscopy (Higgins, 2006; Zhou et al., 2007). This higher magnification is particularly useful when assessing samples of igneous origin, especially fine-grained samples and/or when there is often a limited amount of material available to study (such as meteorites).

Recent CSD and SDP analyses of eleven nakhlites by Udry and Day (2018), including Y 000593 and Y 000749, showed that they consistently exhibit random SPO, *i.e.*, they lacked any form of lineation (axis alignment along a singular plane indicating at least two directions of strain), and/or

foliation, (axis alignment within a singular plane indicating a single direction of strain; Paterson et al., 1998a). The random SPO indicates formation from a larger body with no source of significant external strain. However, recent EBSD investigations of four nakhlites by Daly, Piazolo, et al. (2019) identified weak-moderate foliation, with some of the meteorites also exhibiting lineation CPO and SPO. The results from Daly, Piazolo, et al. (2019) imply diverse formational histories for the nakhlites, where the lineation results indicate an origin that is not solely driven by crystal settling (Holness, 2007; Holness, Nielsen, et al., 2007; Hunter, 1996). In this paper, CSD and EBSD analyses have been applied to further physically constrain the petrogenesis of the individual Yamato nakhlite stones, to better understand their igneous emplacement prior to their impact ejection from Mars.

2.4 Materials and methods

Augite was analysed in five polished thick sections representing all three Yamato nakhlites: Y 000593 (106-A and 127-A), Y 000749 (64-A and 72-A), and Y 000802 (36-A). Augite phenocrysts were chosen for two reasons: 1) their high (~60–80 vol.%) modal abundance in the nakhlites (Imae et al. 2003; Treiman 2005; Udry and Day 2018), and 2) their crystal shape enables the short crystallographic <001> *i.e.*, <c> axis (*i.e.*, CPO) to be used as a proxy for the long shape-axis (SPO) to assess preferred orientation (Daly, Piazolo, et al., 2019; Morimoto et al., 1988). Our analysis includes previous CSD and SDP results from Udry and Day (2018) for sections Y 000593 (106-A) and Y 000749 (72-A) that are supplemented by new EBSD analysis described here. All samples analysed in this study were provided by the Japanese National Institute of Polar Research (NIPR) as premade thick sections and as such were not cut with respect to any SPO nor an external common reference point. Meteorite samples typically lack external reference points. For this study, an arbitrary principal orientation was defined based on the EBSD maps (Fig. 2.1) to enable consistency in comparing and presenting data between the different sections where: Y = top-bottom direction of the thick section, X = left-right direction of the thick section, and Z = direction perpendicular to the plane of the thick section. Additionally, for ease of comparison between CSD and EBSD data sets, all EBSD measurements are reported in mm or mm^2 rather than the more typical units of µm and $µm^2$.

2.4.1 Electron microscopy

In preparation for EBSD analysis, each of the five thick sections underwent a fine mechanical polish using 1 µm then 0.3 µm aluminium spheres suspended in glycol for 5 minutes before being chemically polished for 4 hours using 0.1 µm colloidal silica suspended in a NaOH solution. These polishing steps were followed by the application of a ~10 nm thick conductive carbon coat using a sputter coater.

All samples were studied by SEM. Backscatter and forescatter electron images, and energy dispersive X-ray spectroscopy (EDS) and EBSD data were obtained at the ISAAC imaging centre, University of Glasgow. The SEM used was a Zeiss Sigma Field Emission Gun Variable Pressure Scanning Electron Microscope (FEG-VP-SEM) operating Oxford Instruments AZtec analysis

software v3.3. Conditions were tilt 70°, high vacuum (3.5 x 10^{-4} Pa) accelerating voltage 20 keV, aperture 120 µm, beam current 4.1 nA (full analysis settings for each studied section are available in Supplementary Appendix 1). EDS analyses were collected simultaneously with the EBSD data using an Oxford Instruments X-Max 80 mm^2 silicon drift detector energy dispersive X-ray spectrometer and NordlysMax^2 EBSD detector.

Step sizes for each individual EBSD measurement (ranging 3–5 µm) were chosen to maximise the surface area covered by the maps, ensure data collection over reasonable time frames (<2 days), while still being smaller than each section's augite crystals. For data processing the phase augite (crystallographic axes a = 10.97 < b = 10 < c = 05.96 Å) was selected. Kikuchi diffraction patterns were assessed to provide reasonable mean angular deviation (MAD) values (0.51–0.72) that were in range of acceptable indexing values for geological specimens (Prior et al., 2009). EBSD data were noise-reduced using Oxford Instruments HKL Channel 5 software as per standard procedure; a single wildspike correction followed by an iterative 8, 7, then 6 point nearest neighbour zero solution reduction to remove erroneous data points (mis-indexed and non-indexed points) and facilitate crystal definition without generating significant artefacts within the data set (Bestmann & Prior, 2003; Daly, Lee, et al., 2019; Forman et al., 2016, 2019; Watt et al., 2006). EDS scans encompassing the entire thick section were acquired for Y 000593 (127-A), Y 000749 (64-A), and Y 000802 (36-A) to incorporate regions outside the EBSD maps to assist CSD and SDP analyses. These larger scans were acquired on the Zeiss SEM at a 0° tilt angle, under high vacuum (3.5 x 10^{-4} Pa) with a field of view of 0.6 × 0.8 mm per frame, working distance 8.5 mm, 20 keV, and a 4.1 nA beam current.

2.4.2 Shape preferred orientation (SPO) and crystallographic preferred orientation (CPO) analyses

2.4.2.1 Electron backscatter diffraction (EBSD)

Individual augite crystals were identified via HKL Channel 5's automated "grain detect" algorithm. Crystal boundaries were determined based on a >10° internal crystallographic misorientation threshold of each neighbouring pixel, accounting for visually identified twin boundaries [180° rotation around augite's (100), (001), (204), or (104) planes]. Crystals <10 pixels in size were removed from the complete dataset as they would constitute too few datapoints to robustly sample the mineral and define its crystal size based on the scan resolution, the step size, and the crystal fracturing within each section (Forman et al., 2019; Watt et al., 2006). To enable consistent comparison between EBSD and CSD datasets crystals <0.3 mm (the resolution limit of the CSD dataset) were ignored for CPO and SPO analysis. Prior to inter-crystalline CPO and SPO analysis a one point per grain (OPPG) data reduction was applied to each sample, where the OPPG subset was visually checked for artefacts against Euler and inverse pole figure (IPF) results and an additional manual reduction applied. This manual reduction removed any excess crystallites associated with fractured crystals, whose boundaries exceeded the >10° internal misorientation threshold.

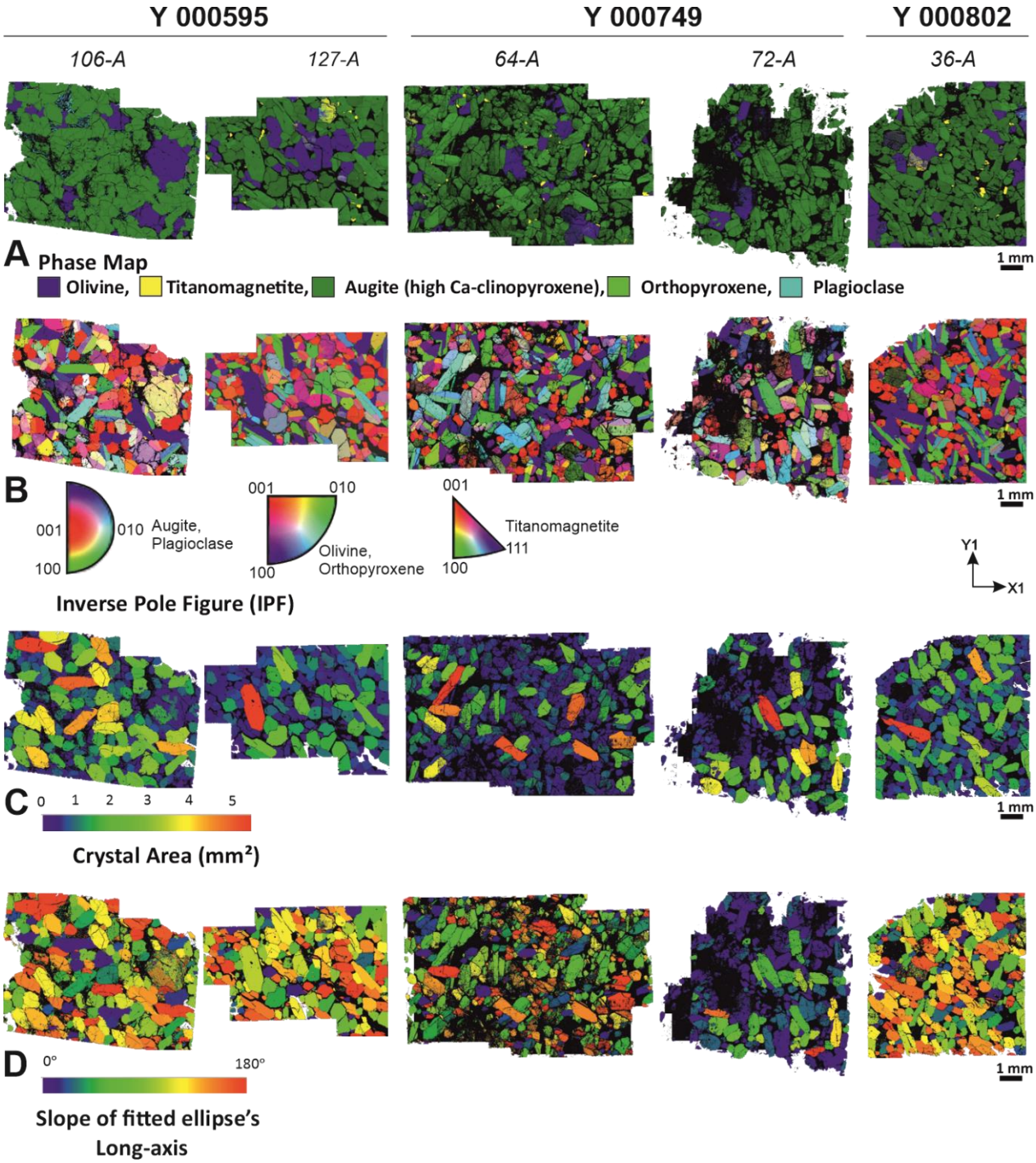

Figure 2.1. *EBSD results from the Yamato nakhlites. A) Phase map showing augite (px, green) as the dominant phase within all samples. Other phases indicated are olivine (blue), orthopyroxene (lime green), plagioclase (aqua), and magnetite (yellow). Px abundance in volume % is as follows: 54% Y 000593 (106-A), 53% Y 000593 (127-A), 45% Y 000749 (64-A), 32% Y 000749 (72-A), 61% Y 000802 (36-A). For the full breakdown of modal mineralogy please refer to supplementary materials; B) Inverse Pole Figure (IPF) oriented in the Z direction (axes perpendicular relative to the map plane); C) Crystal area referring to the thick section 2D SPO; D) Slope relating calculated fitted ellipse long-axis relative to the map plane. Fitted ellipse major axis represents the true SPO crystal long axis corrected for crystallographic orientation using the <c> crystallographic axis (coupled to crystal long shape-axis).*

EBSD SPO was derived using the slope angle calculated from the best-fit ellipse algorithm in Oxford Instruments' HKL Channel 5 Tango module. This algorithm was used to calculate crystal area, length of the long shape-axis, and slope of the ellipse relative to the thick section surface.

EBSD inter-crystalline CPO was determined using a reduced OPPG sunsets (n (OPPG), Table 2.4) and plotted on lower hemisphere equal area projections (pole figures) using HKL Channel 5's Mambo software module. Pole figures were plotted using the following settings: cluster 3°, half

width 15°, with the maximum multiples of uniform density (MUD.; *i.e.*, relative density of data points) value ranging 0–5 (exceeds individual scan MUD values) to enable comparison between samples.

The strength and intensity of CPO in each sample was quantified using three combined CPO calculations: M-index, J-index, and Eigenvalue analysis (Bunge, 1982; Skemer et al., 2005; Vollmer, 1990); via the MATLAB toolbox 'MTEX' (Bachmann et al., 2011). Data used for these calculations were sourced from the raw exported EBSD data. CTF files underwent noise reduction (equivalent to HKL Channel 5's Wildspike), crystal boundaries established at 10° misorientation between pixels, and all crystals <0.3 mm were removed (n_{MTEX}, Table 2.4). CPO was assessed using the code of Daly, Piazolo, et al. (2019), with amendments according to Mainprice et al. (2015). Here the CPO strength values and parameters are defined based on available pyroxene data sourced from compositionally similar Terrestrial igneous rocks (*i.e.*, plutonic intrusive or extrusive basaltic igneous specimens).

M-index CPO results will sit between 0 (random CPO) and 1 (single crystal CPO; Skemer et al. 2005). The calculation attributes equal weighting to all crystallographic axes and assesses the amount of rotation required for two neighbouring crystals to be aligned (Skemer et al., 2005). Stable M-Index values require <2% convergence. where the exact number of crystals is dependent upon the CPO intensity of the specimen. For the nakhlites, ~ 300 crystals are required.

J-index utilises the crystal's Euler angles, where CPO values theoretically increase from 0 (random CPO) to infinity (single crystal CPO; Bunge 1982). For this study CPO strengths are classified using the same ranges as Daly, Piazolo, et al. (2019), *i.e.*, where low CPO = 1.40–1.80, low-medium CPO = 1.80–2.40, medium CPO = 2.40–5.00, medium-strong CPO = 5.00–12.00 and strong CPO = >12. Statistically relevant datasets for J-Index results are also directly linked to the intensity of the CPO, where the number of crystals required (~300) increases with decreasing intensity (Ismaïl & Mainprice, 1998).

Eigenvalue measurements assess the shape, intensity, and strength of CPO. These results are typically reported for each crystallographic axis as a fraction of random (R), point maxima (lineation; P), and girdle (foliation; G) where the combined PGR value for each axis is equal to 1 (Vollmer, 1990). Due to the nature of geological materials, pure 100% end members are uncommon and therefore strong CPO is considered to have representative Eigenvalues of ~50% (Boneh & Skemer, 2014; Daly, Piazolo, et al., 2019). Eigenvalue analysis here uses the same parameters reported in Daly et al. (2019a), which infers random CPO as R >90%, weak CPO (P and G 10–30%), moderate CPO (P and G 30–50%), and strong CPO (P and G >50%). Additional CPO shape information can be calculated from relating augites two sets of perpendicular crystallographic axes: [010] and [001] using the LS-Index, and [100] and [010] using the BA-Index. LS and BA indices were calculated using the following equations:

$$LS = \frac{1}{2}\left[2 - \left(\frac{P_{010}}{G_{010}+P_{010}}\right) - \left(\frac{G_{001}}{G_{001}+P_{001}}\right)\right] \quad (2.1)$$

$$BA = \frac{1}{2}\left[2 - \left(\frac{P_{010}}{G_{010}+P_{010}}\right) - \left(\frac{G_{100}}{G_{100}+P_{100}}\right)\right] \quad (2.2)$$

Where P_x and G_x refer to the Eigenvalue P and G results of a given crystallographic axis (x). Calculated index values = 1 (L or B-type) indicate lineation dominant CPO and values = 0 (S or A-type) indicate foliation type CPO for the respective index.

The level of internal crystal deformation for each sample was investigated using average grain orientation spread (GOS), the mean deviation angle from the crystal's average orientation, and the maximum orientation spread (MOS), the highest angle difference across the sample, using HKL Channel 5's grain detect algorithm. Intra-crystalline misorientation patterns, which allude to the activated slip-systems within a crystal's internal grain boundaries, were processed from the EBSD dataset prior to OPPG reduction. Crystal and sample reference plots were created using HKL Channel 5's Mambo software module using the following settings: cluster 3°, half width 15°, with the MUD values ranging 0–5 to enable comparability between different EBSD scans.

2.4.2.2 Crystal size distribution (CSD) and spatial distribution pattern (SDP) analysis

New augite population CSD and SDP analyses for sections Y 000593 (127-A), Y 000749 (64-A), and Y 000802 (36-A) were conducted following the same collection and data processing procedure as outlined in Udry and Day (2018), including the same user (Udry). All final images (Fig. 2.2), which form the foundation of the resultant CSD dataset, were hand drawn using *Adobe*© *Illustrator*© and were processed and corrected using *ImageJ*, CSD*slice* and CSD*corrections* software packages (Higgins, 2006; D. J. Morgan & Jerram, 2006; Schneider et al., 2012). Construction of Figure 2.2 images was aided by visual identification of crystal boundaries using several tools: (i) X-ray elemental maps from the University of Nevada Las Vegas (UNLV) *JEOL* JXA-8900 electron microprobe (operated at 15 kV acceleration voltage, 60 nA beam current, pixel dwell time of 9 s, step size 2 µm); (ii) reflected light microscopy using a *Nikon* LV100POL microscope at UNLV; (iii) EBSD IPF, phase, and Euler maps and EDS (combination of Al, Fe, Mg, P, and S) elemental maps collected using the FEG-VP-SEM at the University of Glasgow.

Modal abundances of different crystalline phases and melt percent using pixel counting from the X-ray elemental maps were calculated from the CSD dataset (Table 2.2; for a full breakdown the reader is referred to supplementary materials).

Crystallisation kinetic and mechanical processes (cooling rate, crystal growth rate, fractionation, accumulation, and crystal coarsening) were assessed using the following steady-state crystal population equation applied to the CSD dataset:

$$n = n^{0^{(L/G\tau)}} \tag{2.3}$$

where n is the crystal population density, n^0 is the final crystal nucleation density (*i.e.,* the slope intercept derived from plotting the negative natural log of measured crystal population density versus crystal size; Fig. 2.3), L is the crystal size, G is the calculated growth rate, and τ is the residence time (Cashman and Marsh 1988; Marsh 1988, 1998).

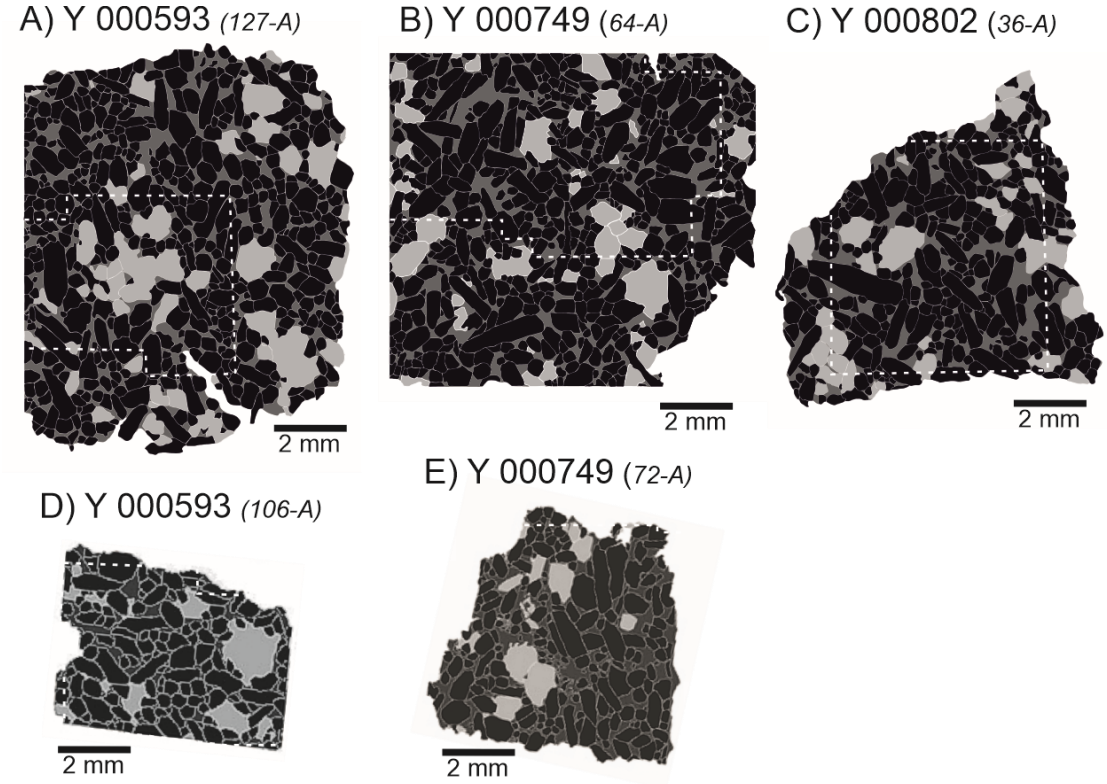

Figure 2.2. *Manually outlined crystals identified for CSD analysis (CSD dataset) where augite (high-Ca pyroxene; px) is black, olivine (ol) is light grey, mesostasis phases (mes) are dark grey. Abundance of phases is in vol.%: A) Y 000593 (127-A; px: 67%, ol: 16%, mes:17%). B) Y 000749 (64-A; px: 70%, ol: 11%, mes: 19%). C) Y 000802 (36-A; px: 66%, ol: 16%, mes: 18%)* D) *Y 000593 (106-A; px:72.1%, ol: 14.9%, mes: 12.9%) and E) Y 000749 (72-A; px: 68.8%, ol: 10.8%, mes: 20.3%). All images are at the same scale. Images D and E and associated CSD results are originally published in Udry & Day (2018). For the full mineralogical breakdown, please refer to supplementary materials. White dashed lines indicate EBSD analysis regions shown in Fig. 2.1*

SDP analysis uses CSD data to assess crystal population ordering, crystal frameworks, and rock formation processes (*e.g.*, compaction, crystal orientation, and flow settling). SDP plots percentage melt against *R*, the ratio of predicted vs observed crystal centre distance for a 2D dataset, defined as:

$$R = \sqrt[2]{\rho \Sigma r / N} \tag{2.4}$$

where ρ is the observed crystal population density, r is the distance between the centre of a crystal and the centre of its nearest neighbouring crystal taken from the corrected intercept of the short:intermediate:long axes, and N is the total number of crystals measured (Jerram, 2003; Jerram et al., 1996).Note for these analyses melt percentage refers to anything that is not augite, (*i.e.*, includes olivine, finer grained mesostasis material (crystals <0.3 mm), and void space within the sample)

Results

2.5.1 Augite morphology

Augite abundances were identified using datasets from both CSD (Table 2.3) and EBSD (post-OPPG data reduction; Table 2.4). Higher numbers of crystals per polished section were detected within the EBSD dataset than the CSD dataset despite EBSD analysing smaller areas of each sample (Figs. 2.1 and 2.2). This higher number of detected crystals is in part due to the fractured

nature of the analysed augite. Thus, the reduced OPPG EBSD dataset is referred to when reporting results, as it accounts for crystal fracturing within the samples.

Table 2.2. *Yamato nakhlite SDP analysis (CSD dataset).*

	Y 000593		**Y 000749**		**Y 000802**
	*106-A**	*127-A*	*64-A*	*72-A**	*36-A*
R	1.43	1.44	1.39	1.36	1.41
% Melt	31.2	33.4	29.7	37.3	33.4
% Crystallinity (all phases)	68.8	66.6	70.3	62.7	66.7

*Data from Udry and Day (2018).
Both % melt and crystals have been corrected for SDP analysis from the CSD dataset
R = the ordering of crystals based on distance and quantity of neighbouring crystals from a given crystals centre (R < 1.65 clustered and R> 1.65 ordered)

Augite crystals within all three Yamato nakhlites are euhedral crystals with zoned edges. Measured averaged crystal sizes reported below indicate the samples to be fine-grained according to igneous terminology rather than coarse-grained as previously reported (Winter, 2013) rather than course-grained as previously reported (Treiman, 2005).

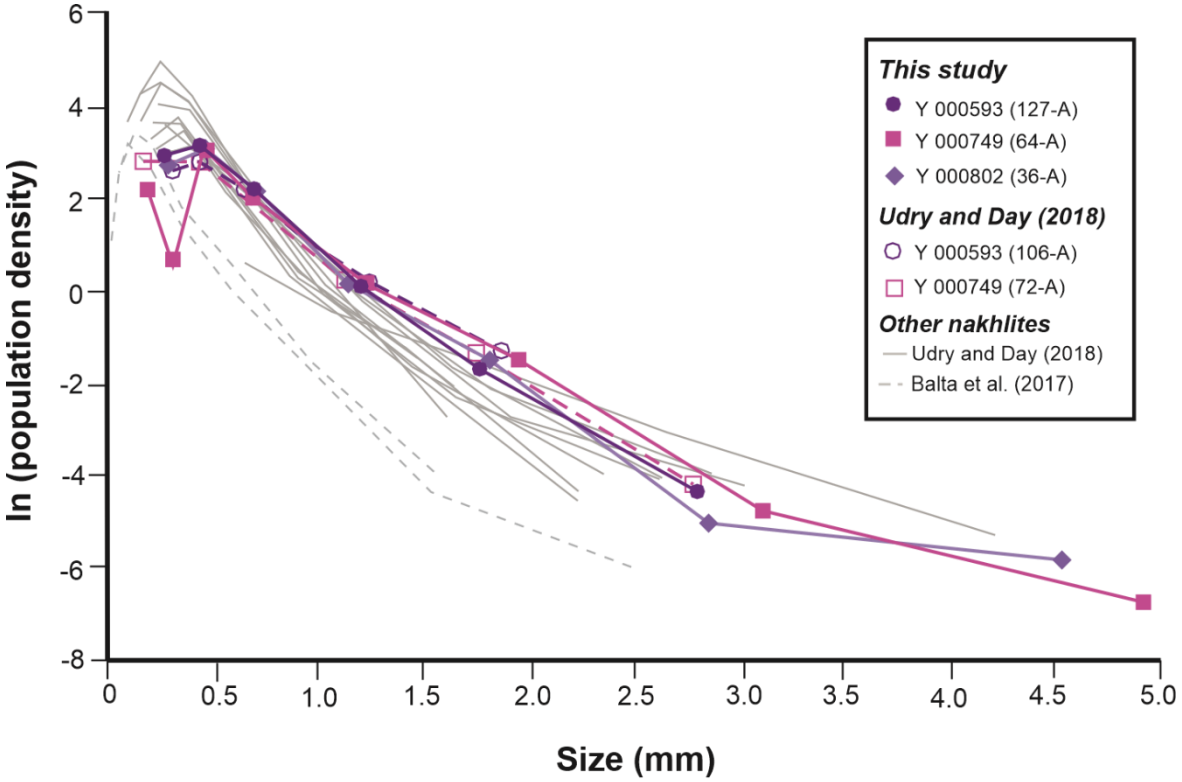

Figure 2.3. *Crystal Size Distribution (CSD) profiles for augite based on the CSD dataset. The three Yamato thick sections: Y 000593, 127-A (solid dark purple circle); Y 000749, 64-A (solid pink square), and Y 000802, 36-A (solid light purple diamond). CSD profiles for sections Y 000593 (106-A) and Y 000749 (72-A) having been previously reported alongside other nakhlites (solid grey lines) by Udry and Day (2018) and Balta et al. (2017). CSD results from the present study are consistent with the distribution reported by Udry and Day (2018).*

Augite CSD results using the long shape-axis produce an average length of 0.45 mm for Y 000593 (127-A), 0.51 mm for Y 000749 (64-A), and 0.46 mm for Y 000802 (38-A). These measurements all lie within 1σ of each other (Table 2.3) and are within error of the measurements from Udry and Day (2018) [0.47 mm and 0.45 mm, Y 000593 (106-A) and Y 000749 (72-A),

respectively]. The best fit ratio corresponding to the short:intermediate:long shape-axis ratio of the pyroxene population ranges from 1.00:1.15:1.60 for Y 000593 (127-A), to 1.00:1.20:1.70 for Y 000802 (36-A), to 1.00:1.30:2.00 for Y 000749 (64-A; Table 2.3). These axis length ratios (Table 2.3) sit within range of previous reported CSD results 1.00:1.25:1.90 for Y 000593 (106-A) and 1.00:1.30:1.80 for Y 000749 (72-A; Udry & Day, 2018). All five augite CSD profiles exhibit a negative linear correlation (Fig. 2.3), with a downturn (*i.e.*, a slight positive slope) for crystal sizes ≤0.3 mm. An anomalous decrease in the abundance of measured 0.55 mm sized crystals is observed in Y 000749 (64-A). Excluding crystal sizes below 0.3 mm, the slopes vary from -3.03 mm^{-1} in Y 000749 (64-A) to -3.43 mm^{-1} in Y 000802 (36-A) and -3.61 mm^{-1} inn Y 000593 (127-A; Table 2.3; Fig. 2.4). Similar results were reported by Udry & Day (2018): -2.72 mm^{-1} in Y 000593 (106-A) and -2.84mm^{-1} in Y 000749 (72-A).

Table 2.3. *Augite crystal statistics from CSD (crystals ≥0.3 mm shape diameter).*

	Y 000593 *106-A**	*127-A*	**Y 000749** *64-A*	*72-A**	**Y 000802** *36-A*
Area (mm)	22	69	86	34	10
n	118	419	446	193	227
R^2	0.84	0.9	0.87	0.84	0.88
Shape aspect ratio**	1.00:1.25:1.90	1.00:1.15:1.60	1.00:1.30:2.00	1.00:1.30:1.80	1.00:1.20:1.70
R	1.44	1.43	1.39	1.35	1.41
Augite length (mm)					
Av. length	0.47	0.45	0.51	0.45	0.46
SD (1σ)	0.27	0.27	0.29	0.33	0.31
Max length	1.46	1.78	2.66	2.34	2.87
Min length	0.09	0.04	0.11	0.08	0.12
Slope (mm^{-1})					
All crystals	–2.85	–3.45	–2.9	–3.03	–3.43
SD (1σ)	0.25	0.14	0.12	0.19	0.21
Crystals ≥0.3 mm	–2.72	–3.61	–3.03	–2.84	–3.43
Slope Intercept					
All crystals	3.89	4.43	4.04	3.86	4.39
SD (1σ)	0.23	0.20	0.11	0.16	0.17
Crystals ≥0.3 mm	3.77	4.61	4.18	3.70	4.39
Px (%)	72.1	67.2	70.4	68.8	66.8
Alignment Factor	0.10	0.17	0.12	0.12	0.17
Residence T (years)					
T^a (all crystals)	111	92	109	105	92
T^a Crystals ≥0.3 mm	117	88 ± 4	105 ± 4	112	88 ± 6
T^b (crystals ≥0.3 mm)	12	9	10	11	9

*Data from Udry and Day (2018)
N = number of crystals
R^2 = coefficient of determination
** = average augite shape aspect ratio (short:intermediate:long)
R = R value (ratio between predicted and measured crystal centre)
SD = standard deviation
T = residence time
[a]based clinopyroxene growth rates of 10^{-10} mm/s from Leu, (2010)
[b]based on silicate growth rates of 10^{-9} mm/s from Cashman and Marsh, (1988) and Jerram et al. (2003)

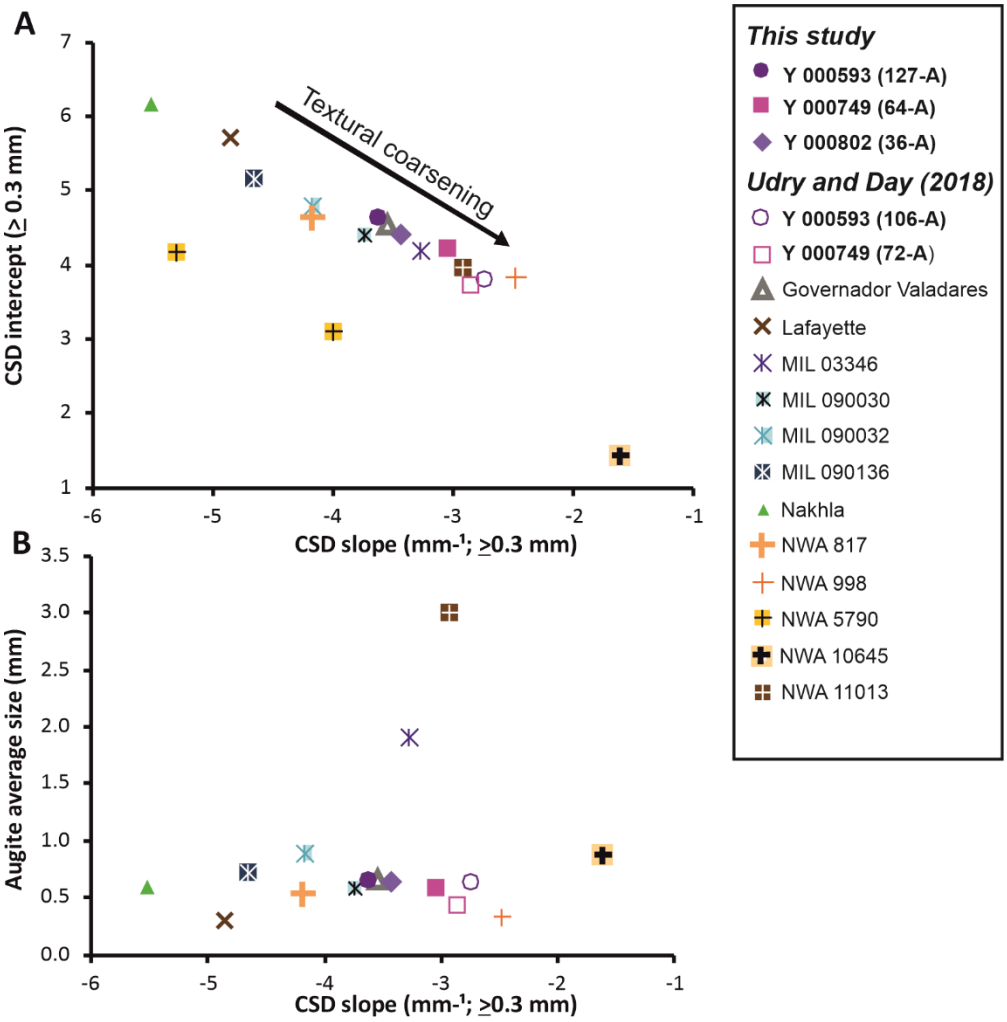

Figure 2.4. *CSD data of Yamato augite (CSD dataset of crystals ≥ 0.3 mm). A) CSD slope (mm^{-1}) versus intercept (summarised Table 2.3)). B) CSD slope versus augite average size (mm; summarised Table 2.3). Samples from the present study exhibit a lower slope in comparison to previously analysed thick sections of the same meteorites but lie within the overall nakhlite trend (Udry & Day, 2018)*

EBSD determined data identifies 1.8–11.6% elongate crystals oriented in the map plane (Table 2.4). A subset was created to assess crystal shape more accurately (Table 2.4: Elongate grains oriented in the map plane), using crystals with the <001> crystallographic axis oriented parallel to the map plane (± 5°), highlighting the importance of slope angle corrections when assessing crystal habit and SPO data. GOS values across the samples show low levels of intragrain deformation ranging 0.48–1.24° (Table 2.4). HKL Channel 5 best-fit ellipse algorithm calculates aspect ratios that cluster around 1–3 with higher ratio's trending towards larger crystals (Fig. 2.5). Calculated crystal areas show Y 000593 (106-A) and Y 000749 (64-A) to have the largest range (0.1–0.5 mm^2; Fig. 2.6), and Section Y 000593 (127-A) to have the smallest range (0.1–0.3 mm^2, Fig. 2.6). Phenocryst long shape-axis values derived from the crystallographic <*c*> axis range between 0.3–0.6 mm (Fig. 2.6), averaging 0.35–0.44 mm in length (Table 2.4).

Table 2.4. *Augite crystal statistics from EBSD (crystals ≥ 0.3 mm shape diameter).*

		Y 000593 *106-A*	*127-A*	**Y 000749** *64-A*	*72-A*	**Y 000802** *36-A*
Augite indexed (%)		53.7	52.6	44.7	31.9	61.3
n (all data)		1035	395	7450	2478	670
n (OPPG)		93	109	197	111	138
Shape long-axis length (mm)						
Av.		0.44	0.35	0.44	0.42	0.43
SD		0.13	0.14	0.12	0.88	0.14
MOS (°)		4.36–6.26	2.64–6.78	4.44–8.54	1.42–6.26	2.84–35.95
Av.		5.42	4.61	6.15	3.64	13.36
SD		0.84	2.00	1.13	1.52	11.61
GOS (°)		0.42–3.17	0.37–1.07	0.52–2.13	0.19–0.98	0.45–3.12
Av.		1.13	0.58	0.90	0.48	1.24
SD		1.36	0.33	0.53	0.25	1.16
Aspect ratio						
A–axis						
Av.		–	–	1.63	3.51	1.65
n_A		0	0	4	2	5
SD		–	–	0.45	0.08	0.68
B–axis						
Av.		–	–	1.4	–	–
n_B		0	0	1	0	0
SD		–	–	–	–	–
C–axis						
Av.		1.86	1.24	2.11	2.36	2.11
n_C		4	2	6	7	11
SD		0.79	0.20	0.95	0.72	2.21
All axes						
Av.		1.86	1.24	1.91	2.62	2.02
n_T		4	2	10	9	16
SD		0.79	0.20	0.80	0.81	1.91
Elongate crystals oriented in map plane (%)		4.3	1.8	5.1	8.1	11.6
CPO						
N_{MTEX}		287	299	508	303	383
M–Index		0.03	0.03	0.04	0.04	0.02
J–Index		3.55 ± 0.71	4.76 ± 0.23	2.92 ± 0.14	3.79 ± 0.18	2.72 ± 0.14
Eigenvalue						
Point (P)	[100]	0.04	0.06	0.14	0.13	0.12
	[010]	0.13	0.14	0.07	0.08	0.08
	[001]	0.17	0.10	0.10	0.18	0.15
Girdle (G)	[100]	0.19	0.11	0.04	0.02	0.15
	[010]	0.09	0.08	0.16	0.24	0.05
	[001]	0.27	0.41	0.44	0.38	0.19
Random (R)	[100]	0.78	0.78	0.89	0.84	0.73
	[010]	0.78	0.79	0.71	0.68	0.87
	[001]	0.56	0.49	0.45	0.44	0.65
LS index		0.40	0.28	0.37	0.54	0.41
BA index		0.29	0.36	0.58	0.81	0.41
$MUD_{max–min}$		0.23–5.92	0.26–2.91	0.46–2.22	0.22–4.78	0.59–2.26

n = number of crystals
OPPG = one point per grain
GOS = grain orientation spread
MOS = maximum orientation spread
Av. = average
SD = standard deviation
n_A = number of crystals in subset A with <a> axis (± 5°) to the plane of the sample
n_B = number of crystals in subset B with <b> axis (± 5°) to the plane of the sample
n_C = number of crystals in subset C with <c> axis (± 5°) to the plane of the sample
n_T = total number of crystals with any axis parallel (± 5°) to the plane of the sample
CPO = crystal preferred orientation
LS index = assessment of lineation (L=1) and foliation (S=0) CPO between <010> and <001> eigenvalue results from equation 2.1
BA index = assessment crystallographic preference between <010> (B=1) and <100> (A=0) from equation 2.2
MUD = multiples of uniform density

2.5.2 Augite preferred orientation

Inverse pole figure (IPF) and Euler angles measured by EBSD provide crystal orientation (Fig. 2.1B, Table 2.4). A subset of crystals with at least one crystallographic axis oriented parallel to the map plane (± 5°) was subsequently created to assess crystal shape more accurately (Table 2.4: Elongate grains oriented in section). For the oriented subset aspect ratios averaged 1.24 ± 0.2–2.62 ± 0.81 (Table 2.4). Considering crystals where the <*c*> axis (*i.e.*, long shape-axis) is oriented parallel to the map plane, a larger discrepancy is observed in the aspect ratio (Table 2.4; Aspect ratio C-axis) compared to the aspect ratio of all axes (Fig. 2.5, Table 2.4; Aspect ratio all axes). The percentage of crystals with their <*c*> axis oriented in the section is low for all samples and ranges from 1.8 to 11.6 (Table 2.4; Elongate grains oriented in the section), where the smallest range occurs in Y 000593 (127-A) and the largest in Y 000802.

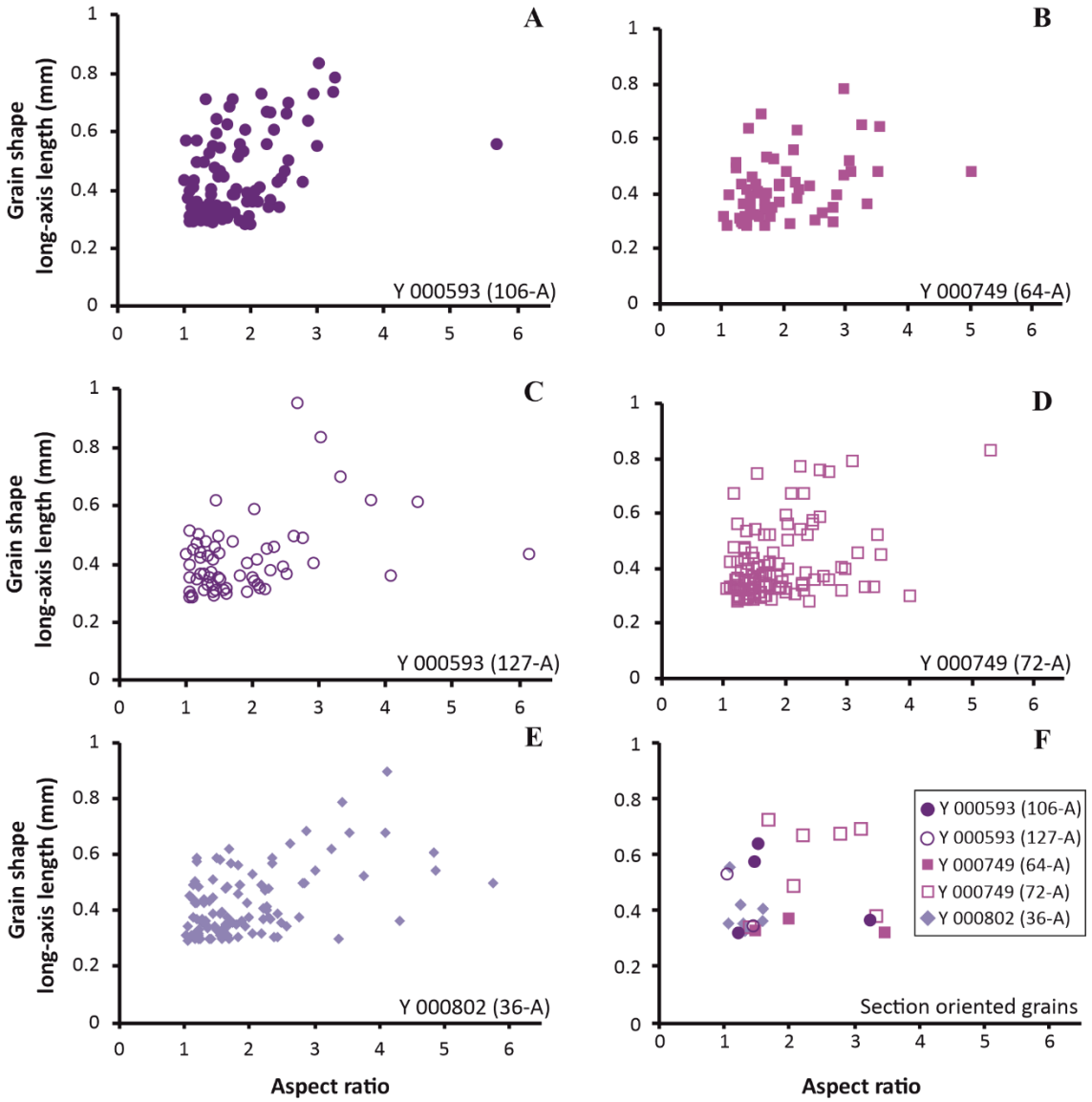

Figure 2.5. *Crystal long-shape axis length vs. aspect ratio of Yamato nakhlites for crystals ≥0.3 mm from EBSD dataset (summarised Table 2.4). A) Y 000593 (106-A); B) Y 000749 (64-A) C) Y 000593 (127-A); D) Y 000749 (72-A); E) Y 000802 (36-A); F) Crystal shape long axis diameter of all crystals with <c> axis parallel (±5°) to the plane of the analysed section.*

2.5.2.1 Augite SPO

EBSD data confirms coupling between the long shape-axis and the crystallographic <001> axis in augite for all samples (Fig. 2.1B, 2.7A, B). Therefore, the CPO of the crystallographic [001] axis can be utilised as a proxy for the long shape-axis to assess orientation corrected SPO within the samples. For SPO analysis only crystals ≥0.3 mm within the EBSD reduced OPPG subset were considered (Fig 2.7A). Aligned SPO was observed along 45–225° and 135–315° in sections Y 000749 (64-A) and Y 000802 (36-A), respectively. Two conflicting SPO orientations; one major SPO plus one or more minor SPO (*i.e.*, weaker/secondary SPO) is observed within sections Y 000593 (106-A) and Y 000593 (127-A; Fig. 2.7A). Section Y 000749 (72-A) exhibits two potential competing SPOs at ~90° to each other around 90–270° and 15–195°, with the 90–270° SPO appearing slightly more dominant. IPF data (Fig. 2.1B) visually confirm the presence of two major crystal alignments within both Y 000593 sections and Y 000749 (64-A)'s map plane.

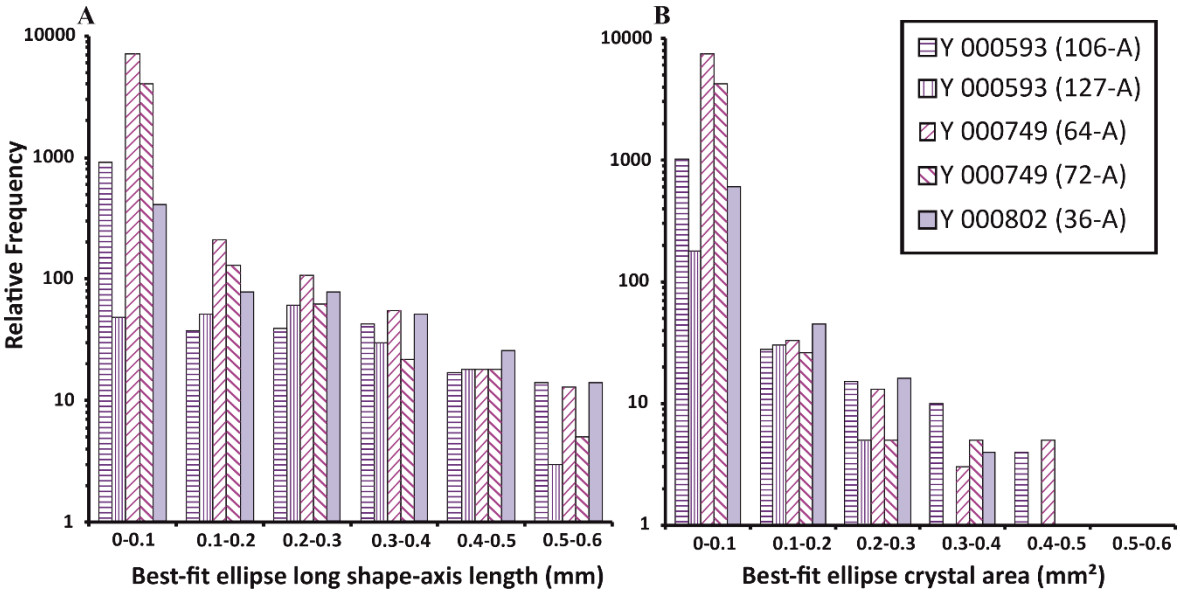

Figure 2.6. *EBSD derived augite size. A) crystal size determined from the <c> axis length, which corresponds to the crystal's long shape-axis corrected for crystal orientation (summarised for crystals ≥0.3 mm in Table 2.4), B) crystal area as calculated using HKL Channel 5's best-fit ellipse algorithm. Relative frequency of both parameters is plotted on a log scale.*

2.5.2.2 Augite CPO

Inter-crystalline CPO using the reduced OPPG EBSD dataset [Table 2.4: n(OPPG) is plotted in Figure 2.7B]. However, CPO index calculations were assessed using the MTEX derived dataset (n_{MTEX}; Table 2.4) which calculated a higher number of crystals within the EBSD datasets. For the CPO index calculations only Y 000593 (106-A) was calculated from <300 crystals and as such is associated with a slightly higher analytical uncertainty (Table 2.4: n_{MTEX}). M-index indicates random CPO for all samples (Table 2.4). Y 000749 exhibiting the highest index value (0.04), followed by Y 000593 (0.03), with Y 000802 exhibiting the lowest (0.02). J-Index values correspond to medium strength CPO, typically observed in plutonic rocks. The highest J-Index value of 4.76 ± 0.23 is in Y 000593 (106-A) and lowest value of 2.72 ± 0.14 in Y 000802 (36-A; Table 2.4). The averaged J-index values for Y 000593 and Y 000749 sit outside analytical uncertainty, where Y 000593 exhibits

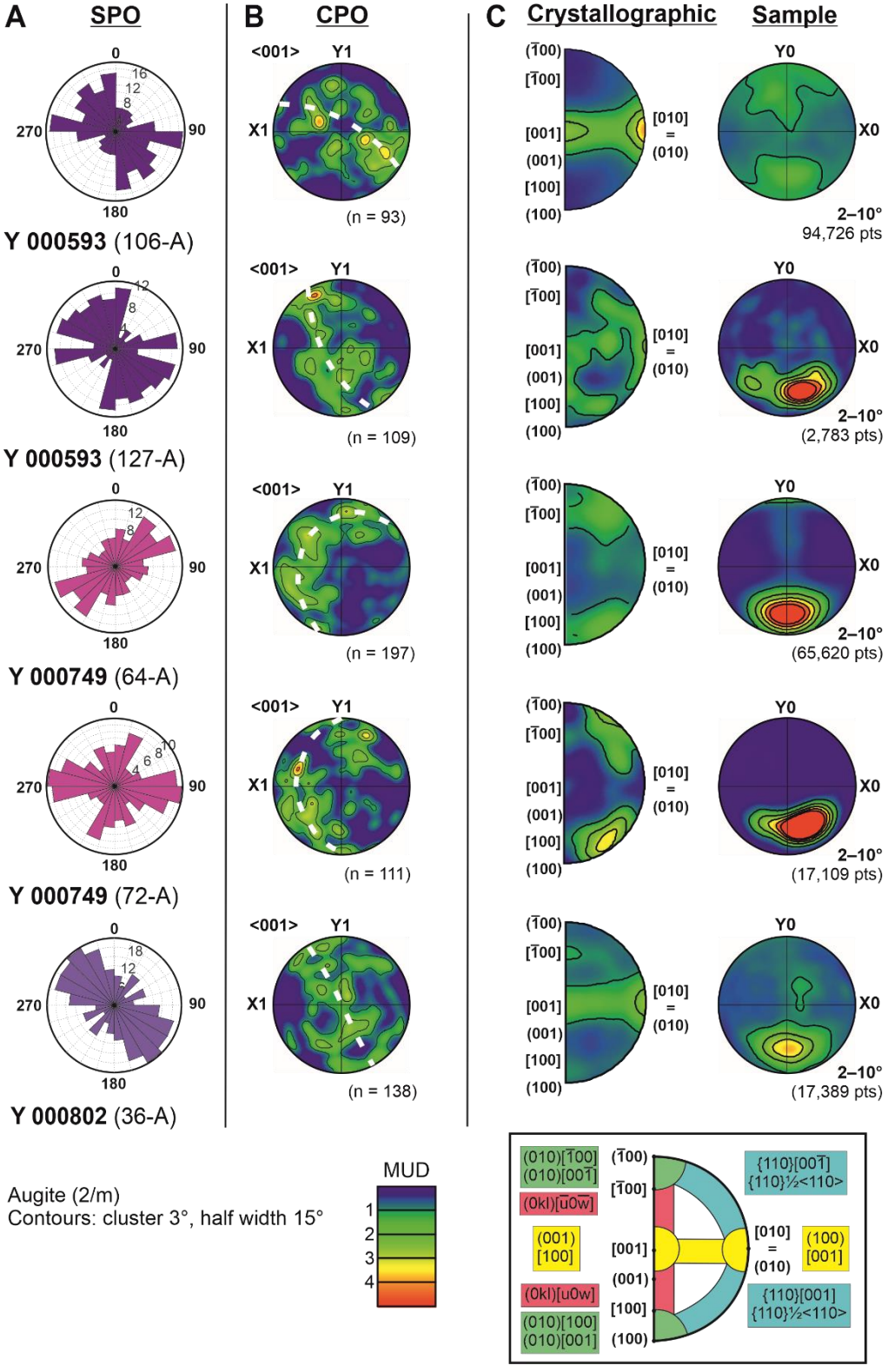

Figure 2.7. *EBSD Augite inter-crystalline and intra-crystalline orientations A) Shape preferred orientation (SPO) from one point per grain (OPPG) data, where SPO is determined from the 2D long shape-axis of fitted ellipse slope angle of grains ≥0.3 mm. B) Equal area, lower hemisphere stereographic projection (pole figure) for <100> axis of OPPG crystals ≥0.3 mm, where n refers to n(OPPG) (EBSD dataset; Table 2.4). All samples exhibit a <c> axis girdle (i.e., foliation) crystal preferred orientation (CPO) indicated by the white dashed lines. Quantitative results from further MTEX CPO analysis are in Table 2.4. C) Intra-crystalline misorientation 2–10° in both crystal (semi-circle) and sample (circle) reference frames. Shifts between the type of misorientation is observed in the crystal reference plots (left) indicating different external stress/strain conditions for each stone. Point maxima shown in the sample reference plots (right) reveal directional strain indicating a non-cumulate formation mechanism. For additional CPO plots the reader is referred to Appendix 1 of the supplementary materials).*

an overall stronger averaged medium alignment (4.10 ± 0.21) than Y 000749 (3.19 ± 0.16; Table 2.4).

Eigenvalue analysis of CPO (summarised in Table 2.4 and plotted in Fig. 2.8) identifies the presence of a low intensity weak-moderate [001] girdle CPO in all sections (G_{001} = 0.19–0.44; Fig. 2.8, Table 2.4). A significant discrepancy between the CPO strengths is observed within the two Y 000593 samples (G_{001} = 0.27 and 0.41; Figs. 2.7B and 2.8) indicating both a weak and moderate strength CPO for the meteorite. Weak strength point CPO (P_{100} Y 000749 and Y 000802 and P_{010} Y 000593) which are overshadowed by the more dominant G_{001} CPO are also observed (Figs. 2.7B and 2.8; Table 2.4). LS-Index results indicate foliation (Pure G_{100}) 'S-type' CPO to a combined lineation (P_{010})- foliation (G_{001}) 'LS-type' CPO (0.28–0.54) for all samples (Table 2.4). BA-Index results indicate lineation (P_{010}) 'B-type' CPO for Y 00593 [0.29 (106-A) and 0.36 (127-A)], foliation (G_{100}) 'A-type' CPO for Y 000749 [0.58 (64-A) and 0.81 (72-A)], and combined lineation (P_{010})- foliation (G_{100}) 'BA-type' CPO for Y 000802 (0.41; Table 2.4)

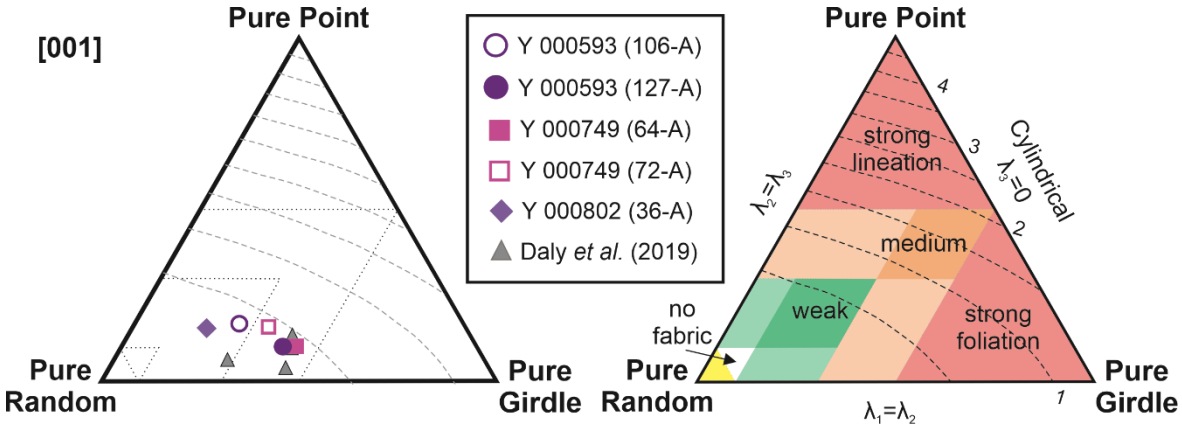

Figure 2.8. *Ternary plot of augite [c] axes in Yamato nakhlites determined using EBSD Eigenvalues; pure random (R), pure point (P), and pure girdle (G) maxima (EBSD dataset Table 2.4). Differences in CPO strength and type between the two Y 000593 samples may be an artefact of separation within the meteorite from where each thick section was cut, or an example of the meteorite's heterogeneity.*

Intra-crystalline misorientation patterns (Fig. 2.7C) can be used to indirectly assess slip-systems. Sample referenced misorientation patterns indicate directional strain across all the Yamato nakhlites. The observed misorientation patterns in the crystal reference frame relate to the following dominant slip-systems expressed as either (001)[100]:(100)[001] in Y 000593 (both sections) and Y 000802 and {110}<001> or {110}$^{1}/_{2}$<110> in both Y 000749 sections.

2.5.3 Augite spatial distribution

New SDP analyses of the Yamato nakhlites sections Y 000593 (127-A), Y 000749 (64-A), and Y 000802 (36-A) (CSD dataset). *R*-values, which reflect the degree of crystal ordering, range from 1.39–1.44, while melt percent values range from 29.7–33.4% (Table 2.2). These new SDP results fall within the touching crystal framework region (Fig. 2.9). SDP results for samples Y 000593 (106-A) and Y 000749 (72-A) are reported in Udry & Day (2018).

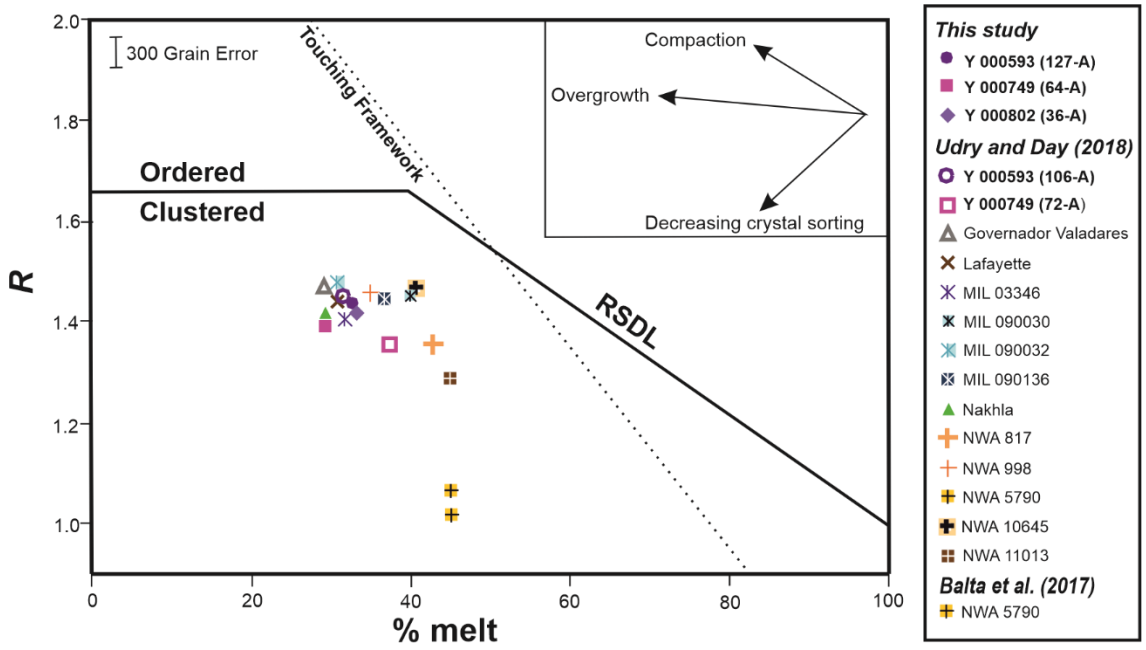

Figure 2.9. *Spatial distribution pattern (SDP) analysis of augite within the Yamato nakhlites (CSD dataset, Table 2.2), where the % melt is plotted against the R-Value (the ratio between the predicted and measured crystal centre from the 2D CSD dataset). Results from the present study are consistent with those reported by (Balta et al., 2017; Udry & Day, 2018). RSDL – random sphere distribution line.*

2.5.4 Augite residence and crystallisation

Magma chamber residence times were calculated for Y 000593 (127-A), Y 000749 (64-A), and Y 000802 (36-A) using phenocryst populations ≥0.3 mm from the CSD dataset. Results for sections Y 000593 (106-A) and Y 000749 (72-A) are reported in Udry & Day (2018). Calculations using the clinopyroxene specific growth rate of Leu (2010) yielded residence times of 88 ± 4 for Y 000593 (127-A), 88 ± 6 years for Y 000802 (36-A) and 105 ± 4 years for Y 0000749 (64-A; Table 2.3). While calculations using the growth rates of Cashman & Marsh (1988) and Jerram (2003) resulted in residence times of 9 years for Y 000593 (127-A) and Y 000802 and 10 years for Y 000749 (64-A; Table 2.3).

The CSD slope and intercept reflect a given sample's crystallisation/cooling rate. Slopes generated from sections Y 000593 (127-A), Y 000749 (64-A), and Y 000802 (36-A; this study) range from -2.9 mm^{-1} ± 0.12 to -3.45 mm^{-1} ± 0.14, with their associated CSD slope intercepts ranging from 4.04 ± 0.11 to 4.43 ± 0.2 (Table 2.3). Note, Y 000749 (64-A) exhibits an anomalous decrease at 0.5 mm crystal size, which is not seen in the section Y 000749 (72-A) analysed by Udry & Day (2018).

2.6 Discussion

2.6.1 Strengths of CSD and EBSD techniques

CSD and EBSD, are powerful quantitative techniques (Cashman & Marsh, 1988; Marsh, 1988; Prior et al., 1999, 2009; Zieg & Marsh, 2002), each of which can answer different micro-structural questions. However, for most studies on achondrite meteorites only CSD or EBSD is used. The application of multiple quantitative techniques enables a more robust investigation and understanding as the collected data is scrutinised from more than one point of view. This enhanced

perspective in turn provides greater reliability and dimension to the derived interpretations as illustrated by the Yamato nakhlite petrogenesis presented here.

Both EBSD and CSD analysis derive their data from a 2D surface plane where the results are interpreted using multiple lines of evidence. In the case of EBSD, the data is derived from the crystal lattice diffraction patterns (Kikuchi patterns). Once processed these patterns are typically assessed via a series of images (*e.g.*, Fig. 2.1) where the spatial resolution of is the data is determined by the analysis step size (Halfpenny, 2010; Prior et al., 2009). EDS maps are often acquired in parallel to check for pattern mis-indexing. For larger stitched-area EBSD maps (*e.g.*, Fig 2.1), machine and beam drift can impact the detected crystal sizes and panel overlap, and if not treated properly can introduce artifacts (Halfpenny, 2010). CSD datasets on the other hand are manually produced. The manual creation of the map means that the derived data are operator specific. For the present study, multiple different petrographic images (including those produced from EBSD and EDS analysis) were consulted in conjunction with optical assessment to produce the CSD dataset (Fig. 2.2). A single operator (AU) conducted analyses for all CSD images to reduce operator bias between datasets, however, as with any manual analysis, an element of user bias will still be present.

Typically, 2D polished sections that are used for microstructural analysis are prepared perpendicular to the structure of interest, or at least to a known external reference. However, sections made from samples which lack their emplacement context (*e.g.*, meteorites), require crystal orientation to be corrected prior to any interpretation. EBSD excels in detecting crystal orientation (Prior et al., 2009). The technique leverages the position of each crystallographic axes to access the third dimension of a crystal relative to the 2D analysis plane, as reported as via IPF or Euler data. This IPF/Euler EBSD data can assist in the correction of CSD datasets which traditionally apply assumed crystal habits to reorient user-inputted crystal aspect ratios using the software CSD*corrections* (Higgins, 2000).

Crystal shape is intrinsically linked to the crystallographic axis, where the shortest crystallographic axis typically relates to the long shape-axis. Identification of the corresponding axes (*e.g.*, <001> for augite) enables EBSD to identify and constrain preferred orientations that are not obviously aligned in the section. In the case of the Yamato nakhlites, the EBSD identified preferred orientation is of a low intensity and weak-moderate strength, where the section is not ideally oriented with respect to the SPO. These factors mean that SPO is difficult to identify in the 2D plane without leveraging CPO. Thus, even though CSD can be used to identify SPO in samples, EBSD would be the recommended technique for SPO identification in achondrite samples.

Assessment of crystal growth and magma residence times requires an accurate determination of a crystal's shape (aspect ratio, width, and length), and CSD is the recommended technique. CSD is highly user-dependent and relying on the experience of the user can be considered an advantage or disadvantage when it comes to determining grain boundaries. Using CSD, crystal boundaries are identified from multiple lines of evidence, whereas EBSD uses computational algorithms based off diffraction patterns and user-inputted misorientations. Thus, EBSD reported crystal sizes will often be smaller than those measured using CSD due to the loss of diffraction pattern quality along the

edges of crystals, and the misidentification of fractured crystallites as individual crystals (hence the use of a reduced OPPG dataset used here). These constraints would ultimately result in crystal growth rates and magma chamber residence times being less accurate.

Both EBSD and CSD are modern quantitative techniques. This study, which revisits the petrogenesis of the Yamato nakhlites, shows how each technique can aid and enhance data collection and interpretation from the other. Although both techniques have their strengths and weaknesses, when their data are combined and assessed together, the physical processes recorded within the Yamato can be more accurately quantified.

2.6.2 Petrogenesis of the Yamato nakhlites

The Yamato nakhlites are mafic augite-rich rocks (Imae et al., 2005; Misawa et al., 2003; Udry & Day, 2018). Initial discussions of their petrogenesis considered the three individual Yamato nakhlite stones as fall-paired fragments sourced from a larger nakhlite-source cumulate pile on Mars (Imae et al., 2005; Misawa et al., 2003) However, the identification of new nakhlites since the Yamato nakhlites were recovered in 2000, together with higher resolution dating by Cohen et al. (2017), has shown that the nakhlites represent multiple igneous bodies sourced from a more diverse environment than initially hypothesised (Day et al., 2018a; Jambon et al., 2016; Krämer Ruggiu et al., 2020; Treiman & Irving, 2008; Udry et al., 2020; Udry & Day, 2018). The CSD and EBSD data for all three Yamato nakhlites that are presented below are discussed and compared against previously reported petrological results [*e.g.*, Corrigan et al. (2015), Imae et al. (2005), and Udry and Day (2018)]. The discussion below is in four parts: (i) SDP of the crystals within the Yamato nakhlites are discussed to assess the formation processes; (ii) the crystal growth rates of augite via CSD are assessed to interpret magma chamber residence and the impact on emplacement micro-structures; (iii) the identified SPO and CPO are discussed; (iv) all of the results are compiled to build a picture of the petrogenesis of the Yamato nakhlites.

2.6.2.1 Constraining augite formation processes from spatial distribution patterns

The SDP results from CSD analysis are in agreement with previous investigations of nakhlite CSD (Imae et al., 2005; Udry & Day, 2018). They are also consistent with SDP observations from other achondrite meteorites such as lunar basalts (Donohue & Neal, 2015). Four of the five datasets exhibit crystal ordering within a similar clustered region (Fig. 2.9), indicating an igneous source where the augite mostly grew in the magma chamber prior to emplacement (Fig. 2.9). Crystal frameworks, or clustered crystals, are structures typically associated with cumulates (Jerram, 2003; Jerram et al., 1996; Tegner et al., 2009). However, on Earth cumulate-type descriptions can be associated with other igneous-type bodies, but rarely with surficial flows as they produce ordered phenocryst SPO (Hunter, 1996; Jerram et al., 1996; Rudge et al., 2008).

Differences in SDP results are observed between the two Y 000749 sections (Fig. 2.9). Even within the same igneous body standard igneous processes, *e.g.*, mechanical compaction, have been observed to result in variations in crystal ordering (Jerram et al., 1996, 2018). In the case of Y

000749, the disparity arises from contrasting calculated melt fractions resulting in a slightly lower ordering of the Y 000749 (64-A)'s crystals (Table 2.2). This lower calculated melt fraction indicates heterogeneity in Y 000749, where the difference in melt fraction sits within the variation parameters typically observed between sections made from the same nakhlite stone (Corrigan et al., 2015). The here reported average crystal size, crystal distribution, and crystal aspect ratios for all Yamato nakhlites indicate a similar formation process and mechanism for all three stones, albeit with some subtle differences accounting for sample heterogeneity (Figs. 2.3 and 2.6, Table 2.3).

2.6.2.2 Augite growth and magma chamber residence time

Residence times calculated for augite are dependent on the CSD measured slope and intercept generated from crystal population density versus crystal size (Fig 2.3; Table 2.3). The Yamato nakhlite magma chamber residence times calculated using the silicate growth rates of Cashman & Marsh (1988) and Jerram (2003) suggest similar residence times to Udry & Day (2018) that sit within a three year period (9–12 years, Table 2.3). Growth calculations using the clinopyroxene specific growth rate of Leu (2010) imply longer residence times for all samples spanning a 29 year period. Y 000593 (127-A) and Y 000802 (36-A) have the shortest residence times (88 ± 4 and 88 ± 6 years, respectively), that sit outside the analytical uncertainty of Y 000749 (64-A; 105 ± 4 years; Table 2.3) and previously reported ages [117 years Y 000593 (106-A) and 112 years Y 000749 (72-A); Udry & Day (2018)].

Note that these calculations assume that the augite crystals were growing continuously without interruptions, and so represent minimum magma chamber residence times. Y 000593 exhibits the largest residence time range, encompassing the calculated ages of the other two stones (Table 2.3). The two clinopyroxene ages reported for Y 000593 sit outside analytical uncertainty, indicating heterogeneity within the stone. This heterogeneity could indicate convection within the nakhlite magmatic chamber, slight crystal settling during emplacement, potential recrystallisation within part of the Y 000593 meteorite, or even that the meteorite contains a boundary between volcanic units or an inclusion.

In thicker flows, sills and dykes the rate of heat dissipation will often vary as a function of the external temperature and mechanical pressures (Goode, 1976; Iezzi & Ventura, 2002; Settle, 1979). Parts of the igneous body that retain heat longer due to insulating properties would enable coarser phenocrysts to grow and a crystalline (rather than glassy) mesostasis material to develop, thus increasing the calculated residence age (Hunter, 1996). This type of mechanism would agree with calculated growth rates from Cashman & Marsh (1988) and Jerram (2003), and with the Yamato nakhlites forming as a single unit. This mechanism would even explain the 7 year Leu (2010) Y 000749 (64-A and 72-A) calculated residence time difference if the igneous body was plutonic, but not the Y 000593 (106-A and 127-A) 29 year Leu (2010) calculated difference, or the crystallisation age discrepancy reported by Cohen et al. (2017) between the different stones. As it is a 13.7 kg rock (Misawa et al., 2003) the difference in crystal residence times between different samples of Y 000593 would require a fairly localised mechanism, *e.g.*, chilled margin of a sill, dyke, base of a lava flow,

slower heat dissipation from localised clusters or mushes, or shock melting (Holness et al., 2017; Jerram, 2003; Jerram et al., 1996; Smith, 2002; Zieg & Marsh, 2002). Results from the intra-crystalline misorientation patterns (Fig. 2.7C), suggest crystal annealing/partial recrystallisation within Y 000593 (127-A) as the most likely explanation for heterogeneity in the residence time.

Previous investigations of several different nakhlites, including the Yamato nakhlites, have found evidence for dissolution in olivine phenocrysts ≥4 mm (Krämer Ruggiu et al., 2020; Treiman, 2005). Chemical and size discrepancies within nakhlite olivine's indicate at least two growth events or non-continuous growth of the mineral. Although olivine data is not being discussed in this paper, the possibility of augite dissolution needs to be considered as the process would impact on calculated residence times and interpretations of CSD data. Crystals with long shape-axis lengths ≥4 mm were detected by CSD but not EBSD. The discrepancy in identified long shape-axis ≥4 mm crystals is most likely related to grain boundary determination in the EBSD dataset. Petrological investigation of the larger augite crystals revealed However, an anomalous dip in the frequency of 0.4 mm sized crystals was observed in Y 000749 (64-A; Fig. 2.3, CSD dataset). When assessed against the EBSD dataset no anomaly is observed in the corresponding crystal-shape length data (Fig. 2.6A). A dip is observed though, in the EBSD crystal area frequency of crystal area sizes in the range of 0.3–0.4 mm^2 for Y 000749 (64-A; Fig. 2.6B). Assessment of Y 000749 (64-A)'s CSD frequency anomaly against its companion EBSD dataset in conjunction with no anomaly being observed in Y 000749 (72-A) indicate the frequency anomaly to be related to introduced sampling bias in the section, most likely related to cutting artefacts. Lack of evidence for dissolution of augite in conjunction with measured crystal size distributions (both datasets) and previously determined chemical compositions (Imae et al., 2005; Treiman, 2005; Udry & Day, 2018) indicate homogenous uninterrupted growth from a single evolved unmixed magma source for augite in all samples.

Intra-crystalline misorientation patterns from the EBSD dataset agree with Y 000593 and Y 000749 forming as different units. The patterns indicate external stress/strain conditions that could not be resolved from fragments of the same parent rock: high temperature low pressure conditions for Y 000749 (Ingrin et al., 1991; Kollé & Blacic, 1983) and moderate temperature/moderate pressure for both Y 000593 and Y 000802 (Avé Lallemant, 1978; Kollé & Blacic, 1982, 1983). Signatures within Y 000593 (127-A) indicate creep deformation within the augite that could be related to a partial recrystallisation or an annealing event within the section that is not observed in Y 000593 (106-A; Fig. 2.7C). This could quite easily be related to a localised event such as heating from hypervelocity impact or from a neighbouring intrusion, which would result in a lower localised calculated residence age for the section.

2.6.2.3 Quantifying igneous micro-structures from preferred orientation

Augite crystals within the Yamato nakhlites are euhedral with a defined long shape-axis. Crystals that form habits with a defined long shape-axis typically become aligned in response to increased internal strain (Bhattacharyya, 1966). However, variable SPO is common throughout all studied igneous bodies (Chin et al., 2020; Piazolo et al., 2002; Shelley, 1988) where the development

of SPO can be disrupted by minor phases or even smaller crystals within the igneous body (Piazolo et al., 2002). In the case of highly crystalline melts (*e.g.*, cumulates), lack of melt may also hinder SPO development (Hunter, 1996). Representative SPO analysis requires a statistically relevant number of crystals to be assessed. However, statistically relevant datasets are not always attainable for meteorite studies due to limited sample availability coupled with generally lower intensity crystal orientations. Crystal fracturing, often related to shock deformation, is a common feature within meteorites that can bias SPO results if not properly accounted for (Leroux, 2001).

SPO is a 3D feature but has traditionally been identified using 2D analysis. The reference frame of the section relative to the inherent SPO is vital component which impacts on the visibility of SPO. A good example is the consistent visible [001] girdle CPO (Fig. 2.7B) but variable SPO (Fig. 2.7A) results for the Yamato nakhlites. For meteorites and some types of terrestrial plutonic samples, lack of an initial knowledge relating the analysis surface to any SPO present requires additional analyses such as CPO to be undertaken. CPO assesses each crystal orientation with respect to rotation of the crystallographic axis. This is particularly useful when comparing preferred orientation across multiple samples, as the crystallographic axis is used as a consistent reference frame removing bias from the lack of geological context between each stone and/or section as well as any bias between the analysed surface and the inherent SPO.

SPO and CPO within fine-grained mafic rocks, such as the Yamato nakhlites can be difficult to identify even in Terrestrial samples. The use of techniques such as EBSD CPO enables quantified identification of weaker and lower intensity SPO. Despite Figure 2.7B showing an identifiable girdle CPO across all Yamato nakhlite sections, neither the strength of the CPO nor its intensity can be quantified from the presented pole figure. Each of the three metrics used to quantify the identified CPO (M-index, J-Index, and Eigenvalue Analysis) impart subtly different information that when assessed in combination can provide a better characterisation of CPO.

EBSD-calculated quantitative CPO metrics confirms the presence of a comparable low-intensity weak-moderate strength [001] axis girdle CPO (*i.e.*, foliation – alignment of the [001] axis within a singular plane) for all three Yamato nakhlite stones (Fig. 2.7B; Table 4). Girdle CPO is consistent with crystal settling SPO commonly observed in sills, lava lakes, and larger volume lava flows (Daly, Piazolo, et al., 2019; Iezzi & Ventura, 2002; Piazolo et al., 2002). The development of girdle CPO is also common for cumulate-like rocks (Hunter, 1996). However, the identified girdle CPO is coupled with a low-intensity weak point CPO (*i.e.*, lineation – alignment in a given direction) within either the [100] or [010] axis indicating two or more strain fields acting on the sample evidencing a lesser component of flow in all samples (Table 2.4; Bertolett et al., 2019; Daly, Piazolo, et al., 2019; Prior et al., 1999). This presence of the weaker lineation CPO is supported by the sample referenced intra-crystalline misorientation patterns (Fig. 2.7C), which show directional strain within all of the sections that is evidence for non-cumulate formation.

The observed shift between [100] and [010] point CPO indicates different strain forces being recorded within Y 000593 compared to Y 000749 and Y 000802 (Table 2.4). Different external strain conditions between Y 000593 and Y 000749 are also observed in the intra-crystalline misorientation

patterns (crystal reference Fig. 2.7C) however, in this instance Y 000802 indicates patterns consistent with Y 000593. Thus, the combined inter-crystalline and intra-crystalline CPO agree with Cohen et al. (2017) for the Yamato nakhlites to be considered as separate nakhlite units rather than parts of the same unit. However, depending on the original thickness of the emplaced layer the stones could still potentially be considered as being fall-paired.

Comparison of SPO and CPO results for the replicate Yamato nakhlite sections highlight that although the identification of 2D SPO within a sample is important for assessing micro-structures, common reference frames are required for accurate SPO interpretations. Due to the random cut of each section and lack of external geological context, it is recommended that the identification of micro-structures for achondritic meteorites, such as the Yamato nakhlites, should be made considering both 2D SPO and CPO analysis.

2.6.3 Emplacement of the Yamato nakhlites

Variation in CPO and SPO strength within the same igneous body is fairly common within terrestrial sills, dykes, or large surficial lava flows (Iezzi & Ventura, 2002). In these types of contexts flow micro-structures are observed to be stronger along the margins of the igneous body compared to the centre. Sub-flows occurring in the opposite direction to the dominant flow direction are also common features within igneous bodies. These opposing flow SPO and CPO can in turn influence the strength and order of any detected micro-structures (Iezzi & Ventura, 2002; Ildefonse et al., 1992; Shelley, 1985). Geological samples (particularly from low viscosity magmas) typically have significant heterogeneity. Considerable changes in SPO and CPO within a relatively short distance, *i.e.*, within a single sample, are not uncommon. In terms of Martian meteorites, visible SPO and CPO heterogeneity has only been reported for shergottites Zagami (Becker, 2011) and Allan Hills (ALH) 77005 (Ikeda, 1994). Although both examples above are sourced from different regions on Mars than the nakhlites, they indicate that variability is also characteristic of Martian magmas.

When all the micro-structural information is compiled and considered for both CSD and EBSD analyses, the following quantitative description of the Yamato nakhlites' petrogenesis can be derived. Relative to other nakhlite samples, augite crystals in the Yamato nakhlites grew slowly in a magma chamber, with minimum residence times of either 9–12 years or 88–117 ± 6 years (Fig. 2.4; Udry & Day 2018). The magma (with augite phenocrysts) was then brought towards/close to the planet's surface, where the phenocrysts continued to grow as indicated by their augite rims. External stress/strain conditions during the Yamato nakhlites' emplacement on Mars resulted in low-intensity SPO and dominant girdle CPO (foliation) along the <001> axis with a minor point (lineation) component along the [100] axis for Y 000749 and Y 000802, and [010] axis in Y 000593 (Table 2.4). Assessment of inter-crystalline CPO using the three quantitative metrics, reveal subtle differences between the different meteorite stones. These CPO results when assessed individually, often show as a continuum between the samples. However, when assessed in combination the relationship between the stones appears to be more random. Assessment of the intra-crystalline misorientation CPO patterns of augite across all stones show evidence of directional strain implying a component

of flow during emplacement (Fig. 2.7C), where intra-crystalline misorientation CPO patterns show Y 000749 to have undergone higher temperature stress/strain conditions than Y 000593 and Y 000802.

In summary, the data presented suggest the following series of geological events during the Yamato nakhlite's emplacement: (i) augite phenocrysts grew in the nakhlite magma chamber for either 9–12 or 88–117 years, which are longer magma chamber residence times than other analysed nakhlites (Udry and Day 2018); (ii) magma was transported from the magma chamber and either erupted at the surface only to pool as a low viscosity lava or was injected into the crust as a shallow sill. During emplacement cooling the Yamato nakhlites crystallised in a clustered touching framework; (iii) During cooling of the magma body all stones formed micro-structures relative to a dominant planar external strain direction (most likely gravity) with minor directional strain (indicating a component of flow), *e.g.*, from gravitational settling within a non-cumulate stagnant magma body, as indicated by the observed [001] girdle CPO, LS and BA index values, and the directional sample referenced intra-crystalline misorientation patterns. The combination of information from CPO, SPO, CSD, SDP, and crystal residence times indicates that the Yamato nakhlites formed as separate bodies within a similar magmatic regime. Most likely as a series of shallow sills or different lobes at the edge of a stagnant lava pond or lake.

2.7 Conclusions

CSD (including CSD and SDP analyses) and EBSD are quantitative analytical techniques, which excel in different aspects of micro-structural measurement and answer different fundamental questions pertaining to the petrogenesis and evolution of a given sample. Comparison of these techniques shows that CSD is best used to assess crystal growth and magmatic residence times, whereas EBSD is most effective for quantifying features such as those produced by magmatic flow or crystal settling.

Application of CSD and EBSD techniques to the Yamato nakhlites has enabled their petrogenesis to be further quantified and therefore better constrained. CSD calculated magmatic residence times indicate that augite crystals in Yamato nakhlites spent between either 9–12 or 88–117 ± 6 years in the magma chamber. CSD analyses indicate that phenocrysts within these samples grew over a longer period than the overall nakhlite group. The magma and crystals were brought to (or near) the surface, where SDP analyses indicate that the Yamato nakhlites formed within a clustered touching framework. Finally, using EBSD the presence of variable strength [001] axis girdle CPO is identified with a weak point CPO in one of the other crystallographic axes in each sample. Intra-crystalline misorientation patterns indicate non-cumulate formation strains in all samples with differing external parameters for Y 000749 in comparison to Y 000593 and Y 000802 indicating formation as separate units. The reported CPO has been observed in low viscosity terrestrial basaltic lavas, and sills, where crystal settling due to gravity is the dominant source of strain during emplacement. This study shows that quantitatively assessing SPO and CPO using multiple techniques in conjunction with each other can be used as a springboard for future analyses,

particularly for achondrite meteorites from known planetary bodies (*e.g.*, other Martian and lunar samples). Such work can provide more contextualised and comparable interpretations and results.

2.7.1 Acknowledgments, specimens, and data

We thank the Antarctic Meteorite Research Centre, National Institute of Polar Research, Japan for providing the samples used in this study via loans to M. R. Lee (No 0714). We thank Peter Chung and the ISAAC imaging facility, University of Glasgow for assistance with EBSD analysis, Minghua Ren at UNLV for assistance with EMP analyses, and the UK STFC for funding through grant ST/H002960/1. We also thank the helpful comments of Associate Editor Akira Yamaguchi, B. Tkalcec, B. Balta, C. Corrigan, another anonymous reviewer, as well as David Prior and Iain Neill which have greatly enhanced our manuscript.

3 Constraints on the emplacement of Martian nakhlite igneous rocks and their source volcano from advanced micro-structure analysis.

S. Griffin[1], L. Daly[1,2,3,4], T. Keller[1], S. Piazolo[5], M. R. Lee[1], L.V. Forman[2,6], R.J. Baumgartner[7,8], P.W. Trimby[9], G. K. Benedix[2,6,10], A. J. Irving[11], and B. Hoefnagels.

[1]School of Geographical and Earth Sciences, University of Glasgow, UK. [2]Space Science and Technology Centre, School of Earth and Planetary Sciences, Curtin University, Australia. [3]Australian Centre for Microscopy and Microanalysis, The University of Sydney, Australia. [4]Department of Materials, University of Oxford, UK. [5]School of Earth and Environment, University of Leeds, UK. [6]Department of Earth and Planetary Sciences, Western Australia Museum, Australia. [7]School of Biological, Earth and Environmental Sciences, The University of New South Wales, Kensington, NSW, Australia. [8]CSIRO Mineral Resources, Australian Resources Research Centre, Kensington, WA, Australia. [9]Oxford Instruments Nano analysis, High Wycombe, UK. [10]Planetary Institute, USA. [11]Department of Earth and Space Sciences, University of Washington, Seattle, WA, USA.

Key Points:

- S-type CPO with some weak L-type CPO are identified in the nakhlites.
- CPO indicate nakhlite formation in environments characteristic of crystal/gravitational settling
- CPO and emplacement modelling suggest random variation in discharge through time with overarching consistent emplacement.

Published: *Journal of Geophysical Research: Planets*
DOI: 10.1029/2021JE007080

S.G. and L.D. designed the research project
S.G., L.D., L.V.F, P.W.T, and R.J.B undertook EBSD analyses
S.G., processed all EBSD data
S.G. with the assistance of T.K. undertook the modelling
S.G. wrote the paper based of discussions with L.D., L.V.F, S.P., and M.R.L.
S.G., L.D., M.R.L., R.J.B, S.P., L.V.F, A.J.I., and G.K. contributed to editing the paper.
B.H. provided sample NWA 12542

3.1 Abstract

The Martian nakhlite meteorites, which represent multiple events that belong to a single magma source region represent a key opportunity to study the evolution of Martian volcanic petrogenesis. Here 16 of the 26 identified nakhlite meteorite specimens are studied using coupled electron backscatter diffraction (EBSD) mapping emplacement endmember calculations. EBSD was used to determine the 3D shape preferred orientation (SPO) of contained augite (high Ca-clinopyroxene) phenocrysts by considering crystallographic preferred orientation (CPO). Parameters derived from EBSD, and energy dispersive X-ray spectroscopy (EDS) spectra were used to calculate maximum and minimum magma body crystallization thicknesses via three endmember emplacement scenarios: thermal diffusion, crystal settling, and crystal convection. Results from CPO analyses indicate low intensity weak-moderate CPO. In all samples, a consistent foliation within the <001> axis of augite is observed typically coupled with a weaker low intensity lineation CPO in one of the other crystallographic axes. These CPO results agree best with crystal settling being the dominant emplacement mechanism for the nakhlites. Modelled crystal settling results identify two distinguishable groups outside of the model's resolution indicating the presence of secondary emplacement mechanisms. Comparison of the two identified groups against CPO, geochemical, and age parameters indicate random variability between individual meteorites. Therefore, coupled CPO and emplacement modelling results identify an overarching characteristic of a dominant crystal settling mechanism for the nakhlite source volcano despite exhibiting random variation with each discharge through time.

3.2 Plain language summary

A group of Martian meteorites, known as the nakhlites was investigated to better understand volcanism on Mars by using the specialised microscope technique of electron backscatter diffraction (EBSD) and basic modelling of known igneous processes. The presented data suggests that the magma that was discharged from the nakhlite source volcano varied randomly through time but solidified into rocks via the consistent mechanism of crystal settling. These findings show Martian volcanism is dynamic, where individual eruptions are variable, yet retain overarching volcanic source characteristics that can be identified from large studies of multiple samples.

3.3 Introduction

Mars is a planet whose landscape has been created to a large degree by igneous processes (Carr & Head, 2010; Greeley & Spudis, 1981; Grott et al., 2013; Taylor, 2013) and modified by hypervelocity impacts (Carr & Head, 2010; Zuber, 2001). From remote sensing studies of the volcanic provinces present on Mars, it is clear that volcanism on the planet has been long lived spanning several billions of years (Lapen et al., 2017; Lapen et al., 2010; Werner, 2009). Despite orbital monitoring since 1964, observation of active Martian volcanism has not yet occurred. Despite the wealth of knowledge gained from remotely analysing Martian volcanoes, there is a limit to our

understanding of the magmatic processes on Mars that can be gained from remote sensing alone (*e.g.*, constraints on interior volcanic processes, magma chamber evolution, quantitative assessment of magma composition, determination of physical parameters such as emplacement micro-structures and compositional variability) that can only be achieved through the analysis of physical specimens.

The Martian meteorites are the only Martian materials currently available for laboratory-based examination (McSween & Treiman, 1998; Udry et al., 2020). These samples encompass a range of different Martian rocks (*e.g.*, the various types of shergottites, nakhlites, chassignites, an orthopyroxenite, and polymict breccias) that are interpreted to have been ejected from at least 11 different sites on Mars, most likely in the southern highlands (Udry et al., 2020). However, despite being able to group these samples chemically, isotopically, and using micro-structures including shape preferred orientation (SPO), the location of any ejection sites on Mars, their source volcano(es), and their emplacement style (*e.g.*, flow/intrusion, sub-aerial/hypabyssal) remain unknown. Knowing how these meteorites were emplaced (flows versus intrusions) can provide information relating to locating their launch crater on Mars. Identifying patterns in emplacement mechanisms can provide information about whether through volcanic activity, the Martian crust (as sampled by these meteorites) has the potential to act as heat source capable of generating and sustaining liquid water on timescales relevant to create habitable regions for the development and sustenance of life (Kurokawa et al., 2014; McSween et al., 2001).

The nakhlites are currently the largest group of Martian meteorites derived from a singular parental magma source, interpreted to be a single volcano on Mars (Udry et al., 2020). At the time of this publication, there are 27 catalogued specimens (several of which are considered to be paired) representing at least four distinct magmatic events spanning 93 Ma (1,416 ± 7 to 1,322 ± 10 Ma; Cohen et al., 2017). Classed as basalts, the nakhlites are the only group of igneous rocks, with the exception of Allan Hills (ALH) 84001, to exhibit evidence of Martian fluid/rock interaction (Lee et al., 2018; Treiman, 2005). However, it is unknown whether the nakhlites are sampling a volcanic source which had a regular eruption record or a history consisting of longer dormant phases with condensed bursts of magmatic activity, and whether the meteorites originated solely as surficial flows, only intrusions, or as a combination of both.

Despite geochemical and isotopic data being excellent at identifying magmatic sources, distinguishing between individual lava flows derived from a single volcano or volcanic province can be difficult to discern in cases where there is little chemical or mineralogical variation between units. The exception is where additional information is obtained through micro-structural analysis, geochronological data, or geological context (Fenton et al., 2004). Micro-structural and SPO properties of an igneous rock record the physical processes of a magmatic event from source to emplacement (Jerram et al., 2018). Thus, micro-structural and SPO analysis of multiple magmatic units sourced from a single magmatic source can provide important information regarding evolution and historical processes.

Recent electron backscatter diffraction (EBSD) crystal preferred orientation (CPO) measurements on Governador Valadares, Lafayette, Miller Range (MIL) 03346, and Nakhla by Daly,

Piazolo, et al. (2019) showed evidence for gravitational (*i.e.*, crystal) settling in all four samples. Weak flow CPO was also identified in Governador Valadares and Nakhla, indicating potential complex petrogenesis within the nakhlite launch crater. Daly, Piazolo, et al., (2019) hypothesised at least three distinct magmatic systems encompassing two regimes (subaerial hyperbolic flow and crystal settling) are represented within the nakhlites. Here we use EBSD data to substantially expand on this work, assessing CPO formed during emplacement and generating input parameters to calculate magmatic body end-member emplacement mechanisms via calculated unit thicknesses for 16 known nakhlite meteorite stones. The acquired data were then used to investigate what variation and/or trends can be discerned to better understand the hypothesised diversity of magmatic systems within the nakhlites proposed by Daly, Piazolo, et al., (2019) are applicable across an expanded nakhlite suite or to just a few individual samples.

3.4 Materials and methods

3.4.1 Electron backscatter diffraction (EBSD)

EBSD analysis used a combination of premade and newly made polished nakhlite thick sections (21 sections encompassing 16 individual stones; Table 3.1). The samples were chosen to capture the growing diversity of the nakhlite suite considering the recovery location, known crystallisation age, and model mineralogy. All sections were cut with random orientations that is, without respect to any known/inferred shape preferred orientation (SPO) and/or CPO. To ensure comparability and consistency between the different datasets, EBSD map principal orientations are reported as follows: X = left–right map direction, Y = top–bottom map direction, and Z = direction perpendicular to the map plane. Data used in our analyses include previously presented EBSD datasets which can be found in Daly, Lee, et al., (2019), Daly, Piazolo, et al. (2019), and Lee et al., (2018).

Prior to EBSD analysis, all sections were mechanically and chemically polished. Mechanical polishing was achieved using 1 µm and then 0.3 µm aluminium spheres suspended in glycol for 5 minutes each. Subsequent chemical polishing was achieved using 0.1 µm colloidal silica suspended in a NaOH solution for 4 hours. Following polishing, a ~10 nm thick conductive carbon coat using a sputter coater.

Coupled EBSD and energy dispersive X-ray spectroscopy (EDS) analysis was run on four different instruments: a Zeiss Sigma Field Emission Gun Variable Pressure Scanning Electron Microscope (FEG-VP-SEM) operating Oxford Instruments AZtec analysis software v3.3 (ISAAC imaging centre, University of Glasgow); a Carl Zeiss EVO SEM using a HKL NordlysNano high Sensitivity EBSD detector [Geochemical Analysis Unit (GAU), Macquarie University], a Hitachi SU70 FEG-SEM equipped with a Symmetry CMOS detector and indexed using Aztec analysis software v3.4 (Oxford Instruments Nanoanalysis HQ, High Wycombe), and a Tescan MIRA3 VP-FEG-SEM with the NordlysNano EBSD detector and Aztec EDS/EBSD acquisition system (John de Laeter Centre, Curtin University). All analyses were run at 20 KeV, 4-8 nA beam current, 20 keV, 70° tilt, aperture of 120 µm, under high vacuum (~3.5 x 10^{-4} Pa) apart from Lafayette (USNM 1505-

1) and MIL 03346 (118), which were run at low vacuum (~49 Pa). Selected step sizes for each sample were chosen to maximise the area covered by the EBSD maps and ensure data collection over available timeframes. The detailed analysis settings for each analysed section, including step sizes (ranging from 2 to 15 µm), can be found in Table 3.1.

Table 3.1. *Nakhlite EBSD analysis settings*

	Caleta el Cobre 022	**Governador Valadares**		**Lafayette**	**MIL 03346**	**MIL 090030**	**MIL 090032**	**MIL 090**
	CEREGE	BM.1975, M16, P8469	BM.1975, M16, P19783	USNM 1505-5	118	50	108	62
Area (mm²)	112.83	15.48	21.03	73.56	106.4	79.64	14.69	43.1
Pixel Count	16430075	1719852	93456	1659474	6653595	8848637	1631700	36060
Hit Rate (%)	100	55.53	90.98	1659474	59.1	100	69.62	28.6
Section analysed	Partial	Whole	Partial	Partial	Partial	Partial	Partial	Partia
Step size (µm)	3	3	15	4	4	3	3	3
Tilt (°)	70	70	70	70	70	70	70	70
Accelerating voltage (keV)	20	20	20	20	20	20	20	20
Aperture (µm)	120	120	120	120	120	120	120	120
Beam Exposure (ms/ EBSP)	24	28	30-40	30-40	30-40	21	26	24
Beam Current (nA)	21	4.1	8	4.1	4.1	21	4.1	4.1
Total (all phases)								
MAD	0.74	0.6	0.48	0.59	0.59	0.76	0.61	0.68
Mean BS	42.32	62.35	92.01	62.87	59.1	34.01	64.80	75.0
Mean BC	58.11	81.53	119.04	78.31	72.65	61.32	68.88	55.3
Augite								
MAD	0.76	0.56	0.48	0.65	0.59	0.8	0.65	0.68
Mean BS	43.64	69.44	91.9	56.31	58.53	32.91	62.33	74.8
Mean BC	57.42	90.5	118.90	66.54	71.14	58.1	65.15	54.9
Forsterite								
MAD	0.67	0.47	0.43	0.52	0.65	0.73	0.58	0.74
Mean BS	44.88	87.37	111.57	68.64	54.61	33.9	62.89	84.7
Mean BC	65.21	122.53	142.80	88.4	64.31	58.56	64.84	74.0
Bin criteria	4 x 4	4 x 4	4 x 4	4 x 4	4 x 4	1 x 1	4 x 4	4 x 4
EDS collected	Yes	Yes	Yes	Yes	Yes	Yes	Yes	Yes
Additional EDS map	Yes	No	No	No	No	Yes	Yes	Yes
Collected	CU	UofG	MU	UofG	UofG	CU	UofG	UofG

EDS = electron dispersive spectroscopy
EBSP = electron backscatter patterns a.k.a. Kikuchi diffraction patterns
MAD = Mean angular deviation
BS = Band slope
BC = Back contrast
CU = Curtin University
MU = Macquarie University
UofG = University of Glasgow
OIN = Oxford Instruments Nano-analysis, High Wycombe

Table 3.1. *Continued*

	Nakhla		NWA 817	NWA 998		NWA 10153	NWA 11013
	WAM 12965	USNM 426-1	N8-1	T1	UG-1	SH65 T-2, 2	UG-1
Area (mm²)	13.3	209.57	7.6	9.86	36.14	37.01	37.01
Pixel Count	59450	23285660	47493378	1578314	1784876	12537585	5921530
Hit Rate (%)	75.29	50.05	42.37	56.4	55.57	59.15	46.36
Section analysed	Partial	Partial	Partial	Whole	Partial	Partial	Partial
Step size (µm)	15	3	0.4	2.5	4.5	3	2.5
Tilt (°)	70	70	70	70	70	70	70
Accelerating voltage (keV)	20	20	15	20	20	20	20
Aperture (µm)	120	120	120	120	120	120	120
Beam Exposure (ms/ EBSP)	30-40	28		24	26	25	32
Beam Current (nA)	8	21	12	4.1	4.1	18	4.1
Total (all phases)							
MAD	0.78	0.82	0.56	0.69	0.7	0.82	0.69
Mean BS	93.82	33.96	104.81	50.68	0.08	39.19	52.65
Mean BC	118.87	53.94	96.77	57.46	0.38	47.71	62.47
Augite							
MAD	0.78	0.82	0.56	0.71	0.71	0.84	0.69
Mean BS	93.39	33.76	104.81	50.67	48.54	40.27	51.67
Mean BC	118.05	53.17	96.77	57.12	55.68	47.86	60.58
Forsterite							
MAD	0.76	0.83	0.57	0.62	0.6	0.78	0.6
Mean BS	0.12	34.4	106.54	56.6	56.8	40.04	61.95
Mean BC	0.49	53.4	98.05	71.25	73.69	49.18	81.24
Bin criteria	4 x 4	4 x 4	4 x 4	4 x 4	4 x 4	4 x 4	4 x 4
EDS collected	Yes	Yes	Yes	Yes	Yes	Yes	Yes
Additional EDS map	No	No	No	No	No	No	No
Collected	MU	CU	OIN	UofG	UofG	CU	UofG

All data were processed using Oxford Instruments HKL Channel 5 software. Noise reduction was done using a wildspike correction followed by a consecutive 8–6 point nearest neighbour zero solution reduction to facilitate crystal definition without generating significant artefacts within the data set and to remove erroneous, mis-indexed and non-indexed, data points (Bestmann & Prior, 2003; Forman et al., 2016). From the cleaned dataset grain orientation spread (GOS) and maximum orientation spread from the mean grain orientation (MOS) values were ascertained. Note that the cleaning of the dataset impacts the reported values by lowering the spread of orientations (Ruzicka & Hugo, 2018). The noise-reduced data were then further processed through the one point per grain (OPPG, *i.e.*, one point per crystal) reduction scheme, where excess points resulting from fractured crystals were manually removed from the dataset prior to CPO and SPO analysis. Crystals containing <10 pixels and measuring <20 µm^2 were also removed from the dataset as they contained too few datapoints to robustly sample the crystal's phase, based on the scan resolution, step size, and shock levels within the sample (Forman et al., 2019; Watt et al., 2006). Crystal grain boundaries (defined as >10° internal crystallographic misorientation from the nearest-neighbour pixel) within the datasets were determined using HKL Channel 5's automated "grain detect" algorithm. These crystal boundaries were further processed to exclude twin boundaries (180° rotation) identified to occur

along augite's <100>, <001>, <204>, or <104> axes. Thus, HKL Channel 5 derived crystal lists can be used to interpret and quantify CPO within the different scans. GOS and MOS were also calculated using HKL Channel 5 taking into account identified twin boundaries, fractured crystals, and stitched map boundaries. To assess CPO three different quantitative metrics J-Index, M-Index, and Eigenvalues (PGR) were compared together. All three metrics assess the orientation distribution function (ODF) of the crystals in a slightly different manner: J-Index uses the Euler angles (Bunge, 1982), M-index assesses the crystal axes with equal weighting (Skemer et al., 2005), and eigenvalues assess the ODF of each crystallographic axis individually between three endmembers (Vollmer, 1990). For calculating the quantitative metrics and providing crystal statistics for thickness calculations raw files in *.ctf* (common transfer file) format were imported into MTEX. In MTEX the data underwent denoising (equivalent to HKL Channel 5's wildspike), before establishing 10° misorientation as the crystal boundary and identifying twin crystals. The detected crystals were then separated into two groups; crystals <200 µm were classed as mesostasis crystals, and crystals ≥200 µm were classed as phenocryst crystals

Table 3.1. *Continued*

	NWA 12542	**Y 000593**		**Y 000749**		**Y 000802**
	F83-1	106-A	127-A	64-A	72-A	36-A
Area (mm²)	113.65	36.09	23.78	64.56	48.92	35.86
Pixel Count	12627810	4010028	2183888	5928192	5546892	1434422
Hit Rate (%)	76.81	66.71	69.04	48.88	31.68	73.16
Section analysed	Partial	Whole	Partial	Partial	Whole	Partial
Step size (µm)	3	3	3.5	3.5	3	5
Tilt (°)	70	70	70	70	70	70
Accelerating voltage (keV)	20	20	20	20	20	20
Aperture (µm)	120	120	120	120	120	120
Beam Exposure (ms/ EBSP)	25	29	26	26	30	24
Beam Current (nA)	4.1	4.1	4.1	4.1	4.1	4.1
Total (all phases)						
MAD	0.57	0.67	0.55	0.73	0.66	0.66
Mean BS	68.86	51.54	87.91	50.35	68.97	53.4
Mean BC	82.56	62.34	98.45	51.79	78.05	65.8
Augite						
MAD	0.56	0.65	0.54	0.75	0.66	0.69
Mean BS	70.93	54.4	88.99	48.7	68.17	50.43
Mean BC	84.12	67.97	99.3	48.26	76.64	59.57
Forsterite						
MAD	0.49	0.7	0.46	0.64	0.69	0.57
Mean BS	73.62	52.06	104.4	54.87	72.89	58.69
Mean BC	91.23	60.85	122.3	61.92	85.03	77.04
Bin criteria	4 x 4	4 x 4	4 x 4	4 x 4	4 x 4	4 x 4
EDS collected	Yes	Yes	Yes	Yes	Yes	Yes
Additional EDS map	Yes	No	Yes	Yes	No	Yes
Collected	UofG	UofG	UofG	UofG	UofG	UofG

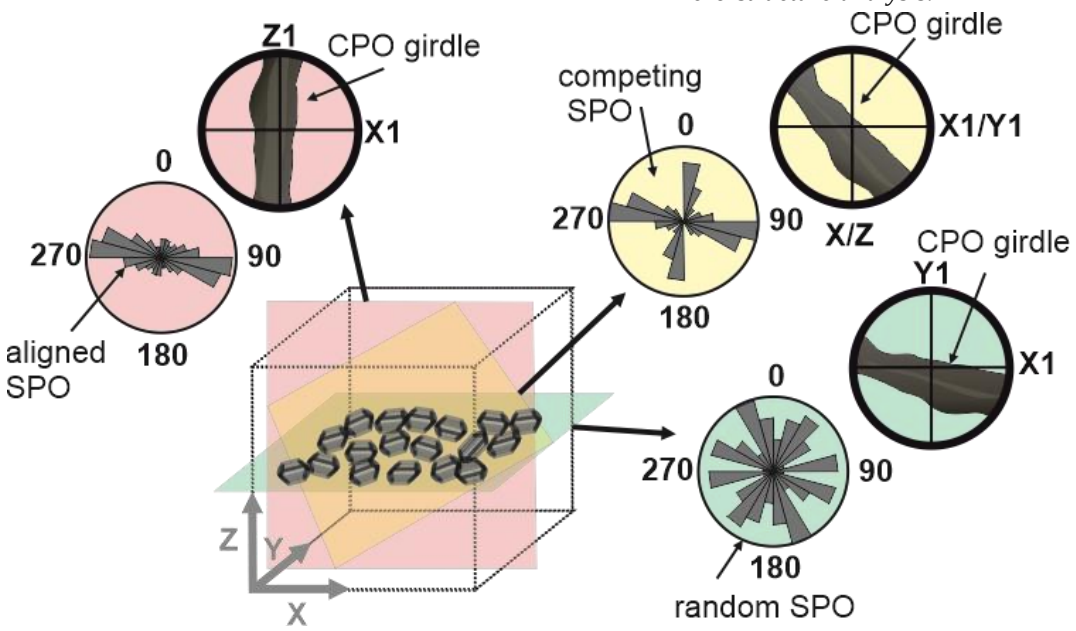

Figure 3.1. *Example SPO (rose diagram) and CPO (pole figure) plots of a sample exhibiting crystal settling (crystals aligned parallel to the green plane) relative to the section analysis surface orientation [perpendicular (pink, ZX), oblique, (yellow, X1||X, Y1||Z) and parallel (green, XY)]. SPO plots show the long axes of crystals which represent the trace of the crystal directions. CPO plots depicted as pole figures show the dominant crystal axes orientation corresponding to the trace of the crystal directions relative to the analysis plane (coloured).*

3.4.2 Shape preferred orientation (SPO)

SPO represents the orientation relationships of the crystals within a given sample. The study of Daly, Piazolo, et al. (2019) showed that a coupling exists in augite between the long shape-axis and the <001> also referred to as the <c> crystallographic axis within the nakhlites Governador Valadares, Lafayette, MIL 03346, Nakhla. Correlation between the long shape-axis and <001> was also assessed and confirmed for all analysed samples in this study. Thus, for SPO analysis, the slope of the crystallographic <001> axis of the OPPG subset is used here as a proxy for the long shape-axis within the sections to assess the 3D corrected SPO. The oriented crystals from the reduced OPPG datasets provides consistency across the multiple specimens analysed, removes bias against the lack of geological context or unknown sample orientation (*e.g.*, Fig. 3.1), as well as bias from crystal fracturing within each of the sections. The trace of the crystallographic axis was calculated using the slope angle of Oxford Instruments' HKL Channel 5 Tango module best-fit ellipse algorithm, which was also used to calculate crystal area and length of the long shape-axis.

3.4.3 Crystallographic preferred orientation (CPO)

CPO refers to the preferred orientation of the crystallographic lattice axis for a selected phase within a sample. CPO was visually assessed from the reduced OPPG dataset (accounting for fractured crystals) where one pixel/crystallographic orientation is used to define a crystal. Lower hemisphere equal area projections contoured using a maximum multiple uniform density (MUD; representing the density of data points) of 5 with 5° clustering and a half width of 15° were used to plot <100>, <010>, and [001] crystallographic axes.

CPO intensity and/or presence was quantified from the phenocryst group of crystals (≥200 µm) using an adapted MATLAB MTEX code from Daly, Piazolo, et al. (2019), adapted from Vollmer (1990) with corrections from Mainprice et al. (2015), generating J-index, M-index, and Eigenvalue values (Bunge, 1982; Skemer et al., 2005; Vollmer, 1990). Assessment of CPO metrics has shown that comparable datasets are required for an accurate assessment where the minimum number of crystals required to produce stable metrics (~2% variation) will result from the symmetry and intensity of the CPO (Mainprice, Bachmann, Hielscher, & Schaeben, 2015; Skemer et al., 2005). For the nakhlites the minimum number of crystals to produce stable metrics was determined to be ~300. Where possible, each metric was calculated utilising the largest 300 crystals or the entire phenocryst population (if less than 300 crystals present) to enable more accurate comparison between the different sized datasets.

The strength and intensity for each CPO metric was determined using the same comparative terrestrial equivalent parameters as stated in Daly, Piazolo, et al. (2019). Briefly, J-index values and their associated CPO were assessed as: low = 1.40–1.80, low–medium = 1.80–3.00, medium 2.40–5.00, medium–strong = 4.00–12.00 and strong <12; M-index: 0 = random orientation and 1 = single crystal (note that although M-Index calculations work well for many different minerals, clinopyroxene has been recognised to produce weak M-Index CPO irrespective of the overall classified CPO strength of the rock); and Eigenvalue end-members: random (R) = >90%, weak point (P) and girdle (G) = 10–30%, moderate P and G = 30–50 %, and strong P and G = >50%. , Eigenvalues typically notated as λ_1, λ_2, and λ_3, assesses the CPO symmetry and axis orientation as a fraction between three end-members (P, G, R) where the combined PGR value for each crystallographic axis equals 1 (Mainprice, Bachmann, Hielscher, & Schaeben, 2015; Vollmer, 1990). Common eigen index parameters, BA and LS which assess the shape relationship of the Eigenvalue CPO between perpendicular axes were calculated using the following equations:

$$BA = \frac{1}{2}\left[2 - \left(\frac{P_{010}}{G_{010}+P_{010}}\right) - \left(\frac{G_{100}}{G_{100}+P_{100}}\right)\right] \quad (3.1)$$

$$LS = \frac{1}{2}\left[2 - \left(\frac{P_{010}}{G_{010}+P_{010}}\right) - \left(\frac{G_{001}}{G_{001}+P_{001}}\right)\right] \quad (3.2)$$

These index parameters result in a number ranging 0-1. The BA-index (eq. 3.1) assesses shape between a pure <100> girdle Eigenvalue (“A”-type foliation = 0) and a pure <010> axis point Eigenvalue (“b”-type lineation = 1). The LS-index (eq. 3.2) assess the shape between a pure <001> girdle Eigenvalue (“S”-type foliation = 0) and a pure <010> point Eigenvalue (“L”-type lineation = 1).

3.4.1 Calculating magma body thicknesses used to indicate feasibility of dominant end-member emplacement mechanism

Approximate magma body thicknesses (D) for each dataset, used to indicate feasibility of three dominant end-member emplacement mechanisms for the nakhlites, were calculated using MATLAB with MTEX toolbox (Bachmann et al., 2011). These three equations of thermal diffusion (3.3), crystal settling (3.4), and crystal convection (3.5) were selected as they represent processes

that result in the maximum possible thickness, intermediary thickness, and minimum thickness, respectively, of a given magmatic unit:

$$D_{diff} = \sqrt{\kappa T} \quad (3.3)$$

$$D_{sett} = (1-\theta)^4 \frac{\Delta\rho}{\mu} g a^2 T \quad (3.4)$$

$$D_{conv} = \frac{\mu}{T\theta\Delta\rho g}. \quad (3.5)$$

In equation (3.3) κ is the thermal diffusivity of basalt (7.5 x 10^{-7} m/s; Durham et al., 1987). In equations (3.3), (3.4), and (3.5), T is the residence time taken from (Krämer Ruggiu et al., 2020; Udry & Day, 2018). In equation (3.4) and (3.5), θ is the crystal volume fraction [from EBSD data derived from dividing the total phenocrysts area (all phases) by the total EBSD map area], $\Delta\rho$ is the density difference between the melt and solid lava (calculated from CIPW normative EDS spectra), g is the Martian gravity, a is the crystal diameter (from MTEX calculated phenocryst grouped crystal), and μ is the viscosity (calculated from CIPW normative EDS spectra).

To calculate CIPW normative spectra, spectra encompassing the EDS map areas were collected. The collected spectra was then processed following standard CIPW normative procedures (Bickel, 1979; Pruseth, 2009). The CIPW normative results were then used to calculate different model input parameters such as density and viscosity. Liquid magma temperatures used for density and viscosity estimates were calculated using the linear equation of McBirney (1993), which bases temperature from silica content within the sample. These estimated temperatures ranged between 1043 and 1121°C (For CIPW results, full code, and input parameters see supplementary materials).

3.5 Results

3.5.1 Modal mineralogy and augite morphology

The EBSD scans of the nakhlites show a wide range of relative proportions of phenocrysts (*c*, *i.e.*, crystals ≥0.2 mm), mesostasis material (*ms*; *i.e.*, crystals <0.2 mm), and glass-non indexed phases (*ni*; representing the combination of fractures, glass, non-indexed phases, and crystals smaller than the analysis step size to yield EBSD patterns; Fig. 3.2, 3.3). Overall, deviations (σ) of ± 0.15 (*c*), 0.11 (*ms*), and 0.13 (*ni*) vol.%, respectfully are observed. Governador Valadares exhibits the highest volume percent of phenocrysts (averaging 40 vol.%), Caleta el Cobre 022 contains the highest volume percent of mesostasis material (60 vol.%), and Y 000749 contains the highest volume percent of glass/non-indexed phases (averaging 61 vol. %), respectively. All samples show augite as the dominant phase [62 vol.% (Y 000802) to 32 vol.% (NWA 817)], followed by olivine [12 vol.% (averaged Y 000593) to 0.3 vol.% (NWA 11013)] and lesser percentages of plagioclase [9 vol.% (Caleta el Cobre 022) to 0 vol.% (MIL 03346, MIL 090030, MIL 090032, MIL 090136, NWA 817, Y 000749, Y 000802)], titanomagnetite [1.7 vol.% (NWA 12542) to 0.1 vol.% (MIL 090136,)], and alteration products [0.9 vol.% (NWA 817) and 0.1 vol.% (Governador Valadares, Nakhla, NWA 10153)] (Fig. 3.3). The modal mineralogy determined agrees with previously reported values, sitting within the known 40% variability range for a given nakhlite (Corrigan et al., 2015). Replicate sections sourced from the same meteorite, result in crystallinity: mesostasis material: void

space/glass/non-indexed ratio variations are well below the variation (σ ±0.15) observed across the whole dataset, with exception of the two Y 000593 scans (σ ± 0.3; Fig. 3.3).

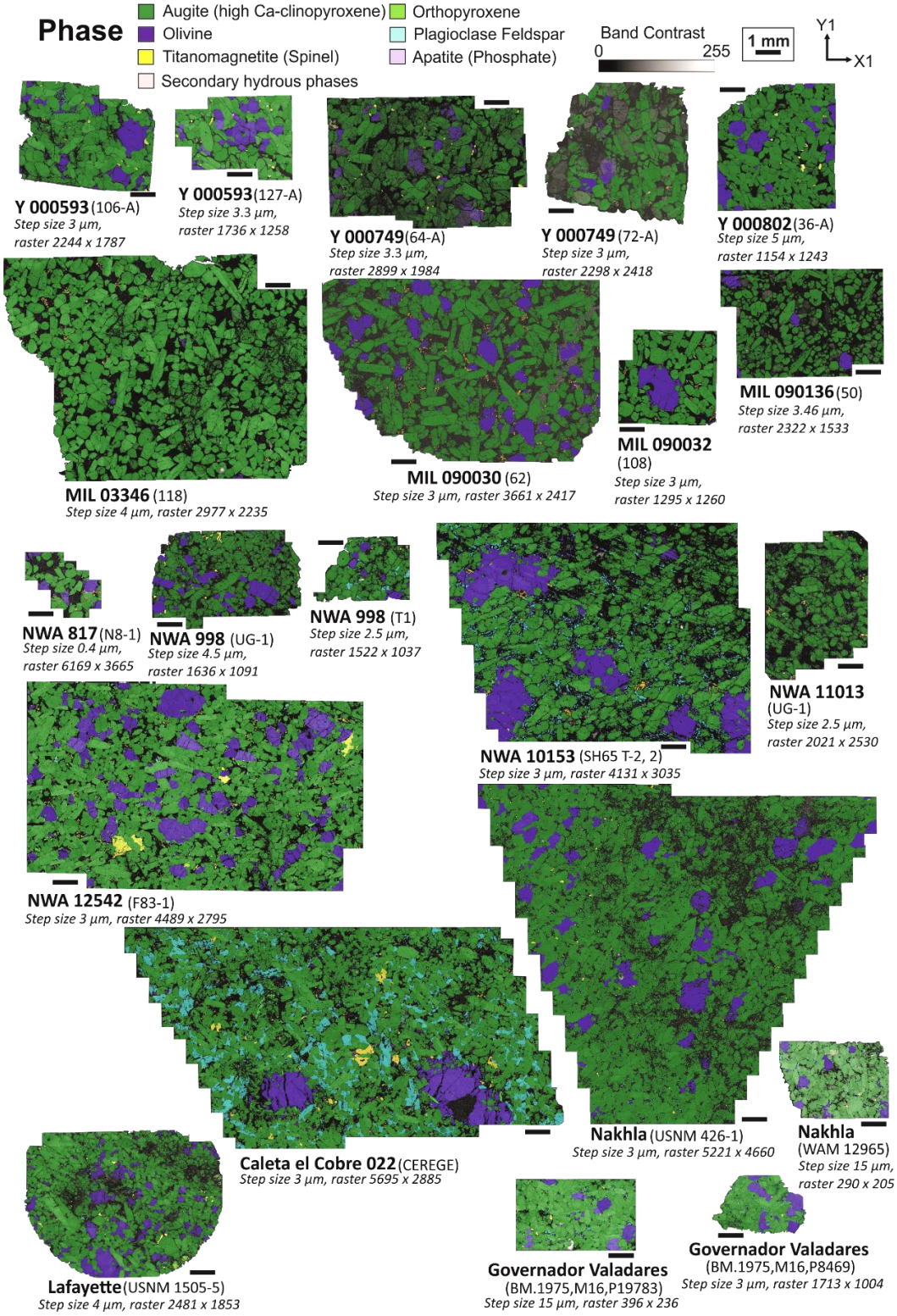

Figure 3.2. *EBSD phase maps showing the characteristic mineralogy of the nakhlite meteorites, consisting of augite (high Ca-clinopyroxene; dark green) and lesser olivine (indexed as forsterite; dark blue) together with minor orthopyroxene (indexed as enstatite; light green), iron-titanium oxide (indexed as titanomagnetite; yellow), and plagioclase feldspar (indexed as albite; light blue). Note the unusually high proportion of plagioclase mesostasis material in the Caleta el Cobre 022 meteorite compared to the other nakhlites studied here.*

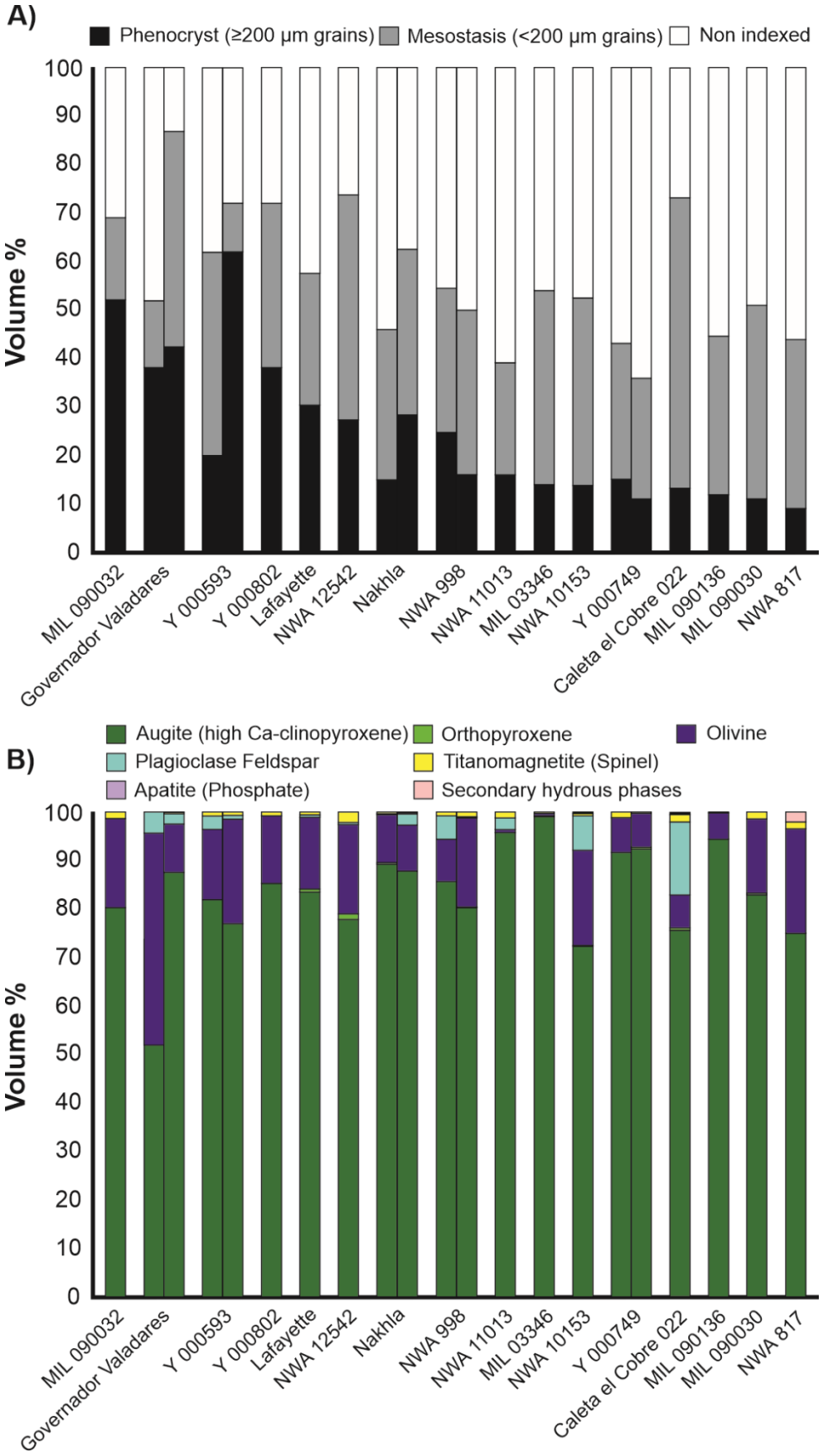

Figure 3.3 *Modal mineralogy of the nakhlites from EBSD data. A) Volume percent of phenocrysts (≥200 µm crystals), mesostasis material (<200 µm crystals), and non-indexed material (e.g., glass, voids, fractures, amorphous material). B) Volume percent of indexed phases in EBSD data i.e., this is for both phenocryst and mesostasis phases.*

3.5.2 Augite phenocryst shape preferred orientation (SPO)

The subhedral to euhedral augite crystals exhibit coupling between the short <001> crystallographic axis and the long shape-axis (Fig 3.4). This enables the <001> to be used as a proxy tracer for the long shape-axis in the nakhlites. The nakhlites show a range of SPO from moderate (one dominant direction of alignment with a smaller less dominant direction *e.g.,* NWA 12542) to random (no alignment *e.g.,* NWA 11013; Fig. 3.4). Moreover, the data show an average crystal orientation spread (GOS) of 1.2° ± 0.8°, reflecting the high proportion of low angle deviations, despite datasets exhibiting higher GOS ranges *e.g.,* 0.1–14.2° (Caleta el Cobre 022) to 0.1–3.5° (MIL 090136; Fig. 3.5, Table 3.2). MOS values indicate deviation ranges from 0.41–9.78 (MIL 090136) to 0.56–57.39 [Governador Valadares (BM1975, M16,P8469)] with values averaging 4.5° ± 3.3° across all datasets (Fig. 3.5, Table 3.2). Within the 21 individual datasets a low percentage of augite crystals were observed to have any of the three crystallographic axes aligned parallel (±5°) to the cut surface of the thick sections (Fig. 3.6, Table 3.2). Parallel <001>-axis aligned crystal values range from 3.3% in NWA 998 (T1) to 16.6% in MIL 090032 with an overall deviation of 2.9%. The reduced OPPG dataset detected crystals with <001> axis oriented ±5° parallel to the acquisition surface range from 0% in NWA 998 (T1) to 21% in Lafayette. These oriented crystals deviated 5.7% across the 21 individual scans. Assessing <001> oriented crystals across the complete dataset an overall deviation of ± 1% is observed ranging from 0.8% in Y 000593 (127-A) to 4% in NWA 10153. The proportion of aligned elongate crystals (*i.e.,* has at least one crystallographic axis oriented parallel (±5°) to the analysis plane) ranges from 2.5% to 10.0% [Y 000593 (127-A) and Lafayette, respectively; Fig. 3.6, Table 3.2].

3.5.3 Crystallographic preferred orientation (CPO)

CPO is variable across the set of analysed nakhlite specimens. All meteorites show low intensity, weak to moderate girdle CPO within the <001> axis, which becomes more defined against the multiples of uniform density (MUD) contouring with increased crystal count (Fig 3.4). The lowest MUD range appears within section Y 000749 (64-A; 0.46–0.22). The largest MUD range is observed within NWA 817 (0.00–4.68). However, the position of the gridle in sample MIL 090030 makes the feature hard to discern (Fig. 4, for the complete set of pole figures see supplementary materials). To calculate quantitative metrics, the number of crystals were also detected within MTEX. Augite crystals identified using MTEX's grain detection algorithm reported as n_{MTEX} range from 43 crystals (NWA 817) to 2,492 crystals [Nakhla (USNM 426-1; Table 3.2]. Twelve of these datasets contain <300 crystals resulting in higher errors for all CPO calculations. Out of the twelve smaller datasets only the NWA 817 results contain <100 crystals (Table 3.2). Thus, despite including the data for NWA 817 in this study the results are not discussed and interpreted owing to the large associated error (*e.g.,* Fig. 3.7).

Quantitative metrics of CPO calculated using MTEX show low M-Index values, ranging from 0.01 ± 0.0002-0.0003 (Caleta el Cobre 022, Lafayette, and MIL 090030) to 0.04 ± 0.0007-0.004 [Y 000749 (72-A) and Governador Valadares (both sections)], with a significant proportion of

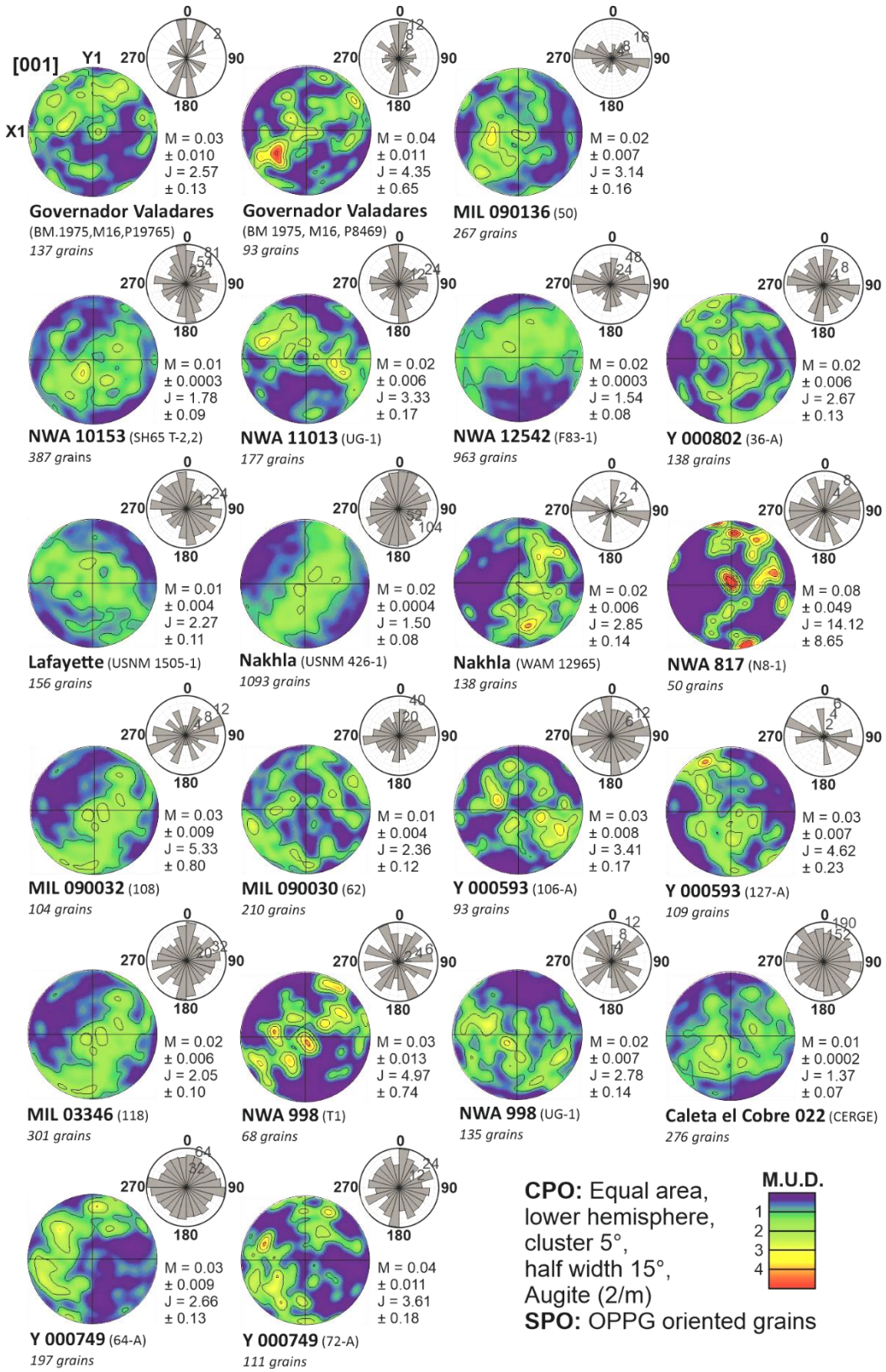

Figure 3.4. *Representation of augite phenocrysts (≥200 µm) crystal preferred orientation (CPO) in the [001] axis shown on a pole figure and shape preferred orientation (SPO) shown on a rose diagram oriented in the plane of analysis. CPO girdle features are observed within all samples. SPO plots show near random orientation in nine sections [e.g., Y 000749 (64-A and 72-A) and NWA 998 (T1)], and two main orientations also in nine sections [e.g., Nakhla (WAM 12965) and NWA 998 (UG-1)]. Only three sections show aligned SPO with one dominant orientation [samples Governador Valadares (BM1975,M16,P19765, and BM1975,M16,P8469) and MIL 090136]. All crystallographic data depicts the reduced OPPG dataset (Table 3.2) to remove bias from fractured crystals (Fig. 3.1, 3.2).*

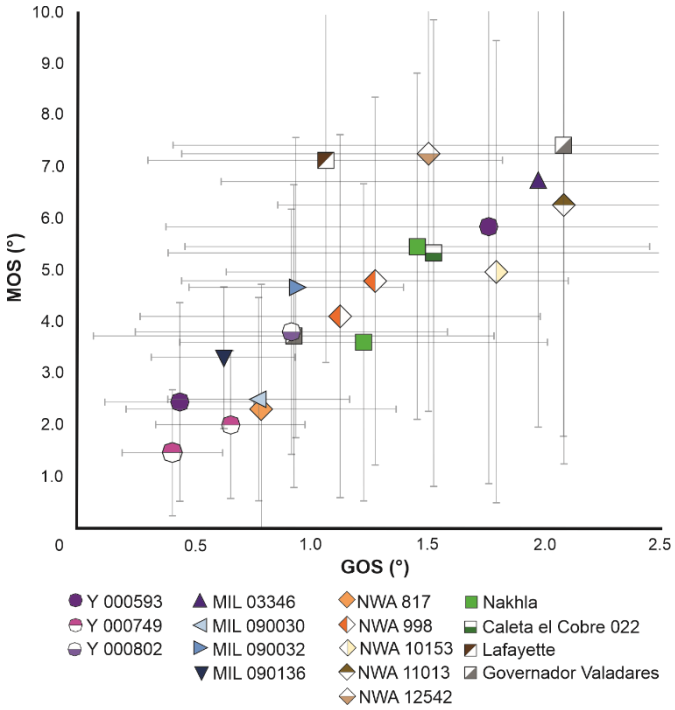

Figure 3.5. *Average grain (i.e., crystal) orientation spread (GOS) versus maximum orientation spread from the mean orientation value (MOS) of augite phenocrysts (≥200 µm) within all the analysed nakhlites.*

the data showing M-Index values around 0.02 (Fig 3.7; Table 3.2). J-Index values are observed to range from 1.37 ± 0.07 (Caleta el Cobre 022) to 4.97 ± 0.74 [NWA 998 (T1); Table 3.2] giving an average J-Index value of 2.96 ± 1.12; this value places the nakhlites in the medium CPO strength range (Fig. 3.7). Resulting PGR values from Eigenvalue analysis support low intensity CPO which range in CPO strength. Calculated CPO intensity in the analysed nakhlites ranged from 0.25 (Caleta el Cobre 022, MIL 090030) to 0.75 (Nakhla, WAM 12695, Y 000749, 72-A) indicating weak intensity for all samples. Identified girdle strengths for the <001> axis range from weak [G = 0.19 (Y 000802, 36-A)] to medium [G = 0.48 (Nakhla, USNM 426-1); Fig. 3.8, Table 3.2], where fifteen of the twenty-one sections exhibited medium strength <001> girdle CPO. Low intensity (≤0.4) weak <100> point CPO are also present in a large portion of the samples ranging in strength from 0.10 to 0.18 (Fig. 3.8). Samples Caleta el Cobre 022, Lafayette, NWA 998 (UG-1 only), and Y 000593 (both sections) exhibited random <100> point CPO (Fig. 3.8). MIL 090032, and NWA 998 (T1 only) exhibit weak point CPO in both <100> (0.15 and 0.26, respectively) and <010> axes (0.10, Fig. 3.8). Both replicate sections of Y 000593 exhibited low intensity (~0.3) weak point CPO (0.13) (Fig. 3.8, Table 3.2). Lafayette and Y 000749 (section 72-A only) exhibit random <100> CPO (R = 0.90) and Caleta el Cobre 022 and NWA 10153 scans exhibit random <010> CPO (R = 0.92 and 0.96, respectively; Fig. 3.8, Table 3.2). Assessing the shape of the observed PGR values, BA-Index calculated values range from 0.27 [Y 000593 (127-A)] to 0.79 [Y 000749 (72-A)], where all samples exhibit BA-type to B-type CPO, except for Y 000593 which has A-type CPO (Fig. 3.9; Table 3.2). Assessing the shape of the observed PGR values, BA-Index calculated values range from 0.27 [Y 000593 (127-A)] to 0.79 [Y 000749 (72-A)], where all samples exhibit BA-type to B-type CPO, apart from Y 000593 which has A-type CPO (Fig. 3.9; Table 3.2). LS-Index

calculated values range from 0.16 [Nakhla (USNM 426-1)] to 0.54 [Y 000749 (72-A)], indicating S type to LS type CPO for all analysed samples (Fig. 3.9, Table 3.2).

Table 3.2. *Nakhlite augite crystal statistics*

	Caleta el Cobre 022	**Governador Valadares**		**Lafayette**	**MIL 03346**	**MIL 090030**
	CERGE	*BM.1975, M16, P8469*	*BM.1975, M16, P19783*	*USNM 1505-5*	*118*	*108*
Augite indexed (%)	46.7	40.9	79.5	52.1	58.5	55.8
N (all data)	48844	1215	355	4572	5675	620
N (OPPG; >200 µm)	276	93	137	156	301	104
N (MTEX; >200 µm)	1789	134	326	899	984	126
Diameter (µm)						
Av.	86.23	37.837	204.2	57.6	59.09	65.88
SD	95.78	70.57	124.31	81.30	97.21	112.99
Aspect ratio						
A-axis						
Av.	1.83	2.65	2.12	1.87	2.05	2.09
N_A	1788	10	10	244	331	75
SD	0.64	2.26	0.92	0.7	0.92	1.03
B-axis						
Av.	1.83	2.17	2.09	1.92	2.13	1.94
N_B	146	58	3	37	10	9
SD	0.63	0.94	0.30	0.91	0.61	0.87
C-axis						
Av.	1.86	2.30	2.26	1.86	1.90	1.63
N_C	1954	22	10	178	165	19
SD	0.72	1.88	1.03	0.66	0.71	0.54
All axes						
Av.	1.84	2.34	1.97	1.87	2.00	2.01
N_T	3888	90	23	459	506	103
SD	0.69	1.71	0.77	0.69	0.86	0.97
Elongate crystals (%)	7.96	7.41	6.48	10.04	8.92	16.61
GOS (°)	0.14–45.29	0.56–57.39	0.41–20.46	1.93–31.00	0.45–46.51	0.55–16.11
Av.	5.33	7.41	3.72	7.12	6.71	4.66
SD	4.51	6.16	2.93	3.94	4.74	2.9
MOS (°)	0.09–14.19	0.22–11.02	0.24–6.31	0.35–6.01	0.25–10.19	0.27–4.07
Av.	1.53	2.09	0.93	1.07	1.98	0.94
SD	1.14	1.68	0.86	0.77	1.36	0.46
CPO						
M-Index	0.01 ± 0.0002	0.04 ± 0.011	0.03 ± 0.010	0.01 ± 0.004	0.02 ± 0.006	0.03 ± 0.009
J-Index	1.37 ± 0.07	4.35 ± 0.65	2.57 ± 0.13	2.27 ± 0.11	2.05 ± 0.10	5.33 ± 0.80
Eigenvalue						
Point (P) <100>	0.08	0.10	0.15	0.05	0.17	0.16
<010>	0.05	0.09	0.08	0.08	0.05	0.10
<001>	0.05	0.14	0.13	0.07	0.03	0.15
Girdle (G) <100>	0.07	0.07	0.07	0.05	0.04	0.05
<010>	0.04	0.26	0.17	0.12	0.56	0.08
<001>	0.27	0.37	0.42	0.29	0.45	0.21
Random (R) <100>	0.86	0.83	0.79	0.90	0.79	0.80
<010>	0.92	0.66	0.75	0.81	0.90	0.81
<001>	0.68	0.49	0.45	0.64	0.52	0.64
LS index	0.31	0.51	0.46	0.40	0.30	0.43
BA index	0.50	0.66	0.69	0.56	0.67	0.60
$MUD_{max-min}$	0.06–2.54	0.00–3.96	0.00–2.64	0.06–2.29	0.04–2.97	0.00–3.85

N = number of crystals
OPPG = one point per grain
Av. = average
SD = standard deviation
MOS = maximum orientation spread from the calculated mean orientation value
NA = number of crystals in subset A
NB = number of crystals in subset B
NC = number of crystals in subset C
NT = total number of crystals with any axis parallel to the plane of the sample
CPO = crystal preferred orientation
MUD = multiples of uniform density
GOS = grain orientation spread

(See supplementary materials for spreadsheet format)

Table 3.2. *Continued*

	MIL 090032	**MIL 090136**	**Nakhla**		**NWA 817**	**NWA 998**		**NWA 10153**
	108	*50*	*USNM 426-1*	*WAM 12965*	*N8-1*	*T1*	*UG-1*	*SH65 T-2, 2*
Augite indexed (%)	55.8	43.2	44.6	66	31.7	48.3	44.5	42.8
N (all data)	620	1567	23824	304	4282	998	1888	19759
N (OPPG; >200 µm)	104	267	1093	138	50	68	135	385
N (MTEX; >200 µm)	126	355	2492	234	43	110	356	849
Diameter (µm)								
Av.	65.88	69.31	34.44	148.34	6.6	38.31	59.08	24.27
SD	112.99	99.69	58.62	90.55	26.61	66.44	78.58	45.87
Aspect ratio								
A-axis								
Av.	2.09	1.75	1.8	1.66	1.99	1.7	1.79	1.76
N_A	75	102	1177	23	72	49	84	687
SD	1.03	0.59	0.57	0.43	0.68	0.48	0.55	0.57
B-axis								
Av.	1.94	1.66	1.76	1.14	2.07	1.74	2.25	1.74
N_B	9	8	166	1	4	8	7	69
SD	0.87	0.57	0.55	n.d.	1.01	0.45	0.87	0.46
C-axis								
Av.	1.63	1.80	1.78	1.51	2.25	1.81	1.79	1.80
N_C	19	25	638	5	64	36	54	797
SD	0.54	0.54	0.55	0.28	1.02	0.67	0.55	0.76
All axes								
Av.	2.01	1.76	1.78	1.63	2.11	1.75	1.81	1.78
N_T	103	135	1981	29	140	93	145	1553
SD	0.97	0.58	0.55	0.41	0.86	0.55	0.57	0.67
Elongate crystals (%)	16.61	8.62	8.32	9.54	3.27	9.32	7.68	7.86
GOS (°)	0.55–16.11	0.41–9.78	0.13–32.6	0.61–19.00	0.10–25.35	0.30–19.73	0.00–29.47	0.06–46.65
Av.	4.66	3.31	3.60	5.45	2.31	4.1	4.79	4.96
SD	2.9	1.37	3.06	3.34	2.41	3.51	3.56	4.47
MOS (°)	0.27–4.07	0.13–3.53	0.07–9.16	0.28–5.86	0.05–5.29	0.24–8.38	0.00–6.78	0.01–10.41
Av.	0.94	0.63	1.23	1.46	0.79	1.13	1.28	1.80
SD	0.46	0.31	0.79	1.00	0.58	0.86	0.83	1.16
CPO								
M-Index	0.03 ± 0.009	0.02 ± 0.007	0.02 ± 0.0004	0.02 ± 0.006	0.08 ± 0.049	0.03 ± 0.013	0.02 ± 0.007	0.01 ± 0.0003
J-Index	5.33 ± 0.80	3.14 ± 0.16	1.5 ± 0.08	2.85 ± 0.14	14.42 ± 8.65	4.97 ± 0.74	2.78 ± 0.14	1.78 ± 0.09
Eigenvalue								
Point (P)								
<100>	0.16	0.13	0.13	0.12	0.26	0.09	0.04	0.15
<010>	0.10	0.06	0.08	0.08	0.11	0.10	0.09	0.03
<001>	0.15	0.08	0.01	0.04	0.24	0.10	0.01	0.06
Girdle (G)								
<100>	0.05	0.16	0.04	0.14	0.24	0.08	0.10	0.08
<010>	0.08	0.10	0.03	0.06	0.34	0.11	0.18	0.01
<001>	0.21	0.33	0.48	0.47	0.29	0.37	0.38	0.32
Random (R)								
<100>	0.80	0.71	0.83	0.7.9	0.50	0.83	0.86	0.77
<010>	0.81	0.84	0.90	0.87	0.55	0.79	0.73	0.96
<001>	0.64	0.59	0.51	0.49	0.47	0.53	0.62	0.63
LS index	0.43	0.42	0.16	0.25	0.60	0.37	0.35	0.23
BA index	0.60	0.55	0.53	0.44	0.64	0.53	0.50	0.48
$MUD_{max-min}$	0.00–3.85	0.08–3.01	0.14–2.19	0.00–3.87	0.00–4.68	0.00–4.42	0.00–3.23	0.08–2.52

Table 3.2. *Continued*

	NWA 11013	**NWA 12542**	**Y 000593**		**Y 000749**		**Y 000802**
	UG-1	*F83-1*	*106-A*	*127-A*	*64-A*	*72-A*	*36-A*
Augite indexed (%)	44.4	59.1	54.6	53.2	44.7	29.2	62.4
N (all data)	8922	9964	1035	395	7450	2478	670
N (OPPG; >200 µm)	177	963	93	109	197	111	138
N (MTEX; >200 µm)	273	1081	241	219	447	281	341
Diameter (µm)							
Av.	23.37	46.32	71.04	227.86	33.76	32.46	132.19
SD	38.17	79.95	132.94	144.54	59.36	113.90	154.33
Aspect ratio							
A-axis							
Av.	1.81	2.05	2.36	1.85	1.968	1.88	2.02
N_A	214	400	13	5	287	66	42
SD	0.6	0.93	1.30	0.92	0.65	0.72	0.88
B-axis							
Av.	1.85	1.88	1.90	5.33	2.09	1.84	2.01
N_B	10	27	21	2	60	52	14
SD	0.57	0.67	0.70	1.19	0.65	0.52	1.04
C-axis							
Av.	1.95	2.10	2.04	1.59	1.96	2.35	1.98
N_C	338	138	27	3	84	25	22
SD	0.81	0.97	0.88	0.63	0.68	1.09	1.27
All axes							
Av.	1.91	2.05	2.07	2.47	1.97	1.95	1.98
N_T	562	565	66	10	556	149	78
SD	0.74	0.93	0.94	1.70	0.66	0.76	1.11
Elongate crystals (%)	6.30	5.67	6.38	2.53	7.46	6.01	11.64
GOS (°)	0.55–16.11	0.45–37.69	0.43–45.96	0.46–35.95	0.25–10.75	0.40–31.24	0.23–9.61
Av.	4.66	6.26	7.25	5.83	2.44	2.00	1.46
SD	2.9	4.48	4.99	4.96	1.92	1.43	1.22
MOS (°)	0.27–4.07	0.12–9.10	0.20–10.37	0.29–8.78	0.13–3.94	0.23–6.97	0.11–2.50
Av.	0.946.31	2.09	1.51	1.77	0.44	0.66	0.41
SD	0.4617.76	1.23	1.06	1.39	0.32	0.32	0.22
CPO							
M-Index	0.02 ± 0.006	0.02 ± 0.0003	0.03 ± 0.008	0.03 ± 0.007	0.03 ± 0.009	0.04 ± 0.011	0.02 ± 0.006
J-Index	3.33 ± 0.17	1.54 ± 0.08	3.41 ± 0.17	4.62 ± 0.23	2.66 ± 0.13	3.61 ± 0.18	2.67 ± 0.13
Eigenvalue							
Point (P)							
<100>	0.18	0.12	0.04	0.06	0.13	0.13	0.12
<010>	0.04	0.06	0.01	0.14	0.07	0.08	0.08
<001>	0.07	0.06	0.17	0.10	0.10	0.16	0.15
Girdle (G)							
<100>	0.09	0.07	0.18	0.11	0.03	0.02	0.15
<010>	0.15	0.05	0.09	0.08	0.15	0.20	0.05
<001>	0.37	0.40	0.27	0.41	0.42	0.37	0.19
Random (R)							
<100>	0.74	0.81	0.78	0.83	0.90	0.87	0.73
<010>	0.81	0.90	0.78	0.78	0.72	0.72	0.87
<001>	0.56	0.54	0.56	0.49	0.46	0.50	0.65
LS index	0.48	0.28	0.38	0.29	0.44	0.54	0.41
BA index	0.73	0.54	0.27	0.37	0.74	0.79	0.42
$MUD_{max-min}$	0.02–4.00	0.03–2.37	0.23–5.92	0.26–2.91	0.46–2.22	0.22–4.78	0.59–2.26

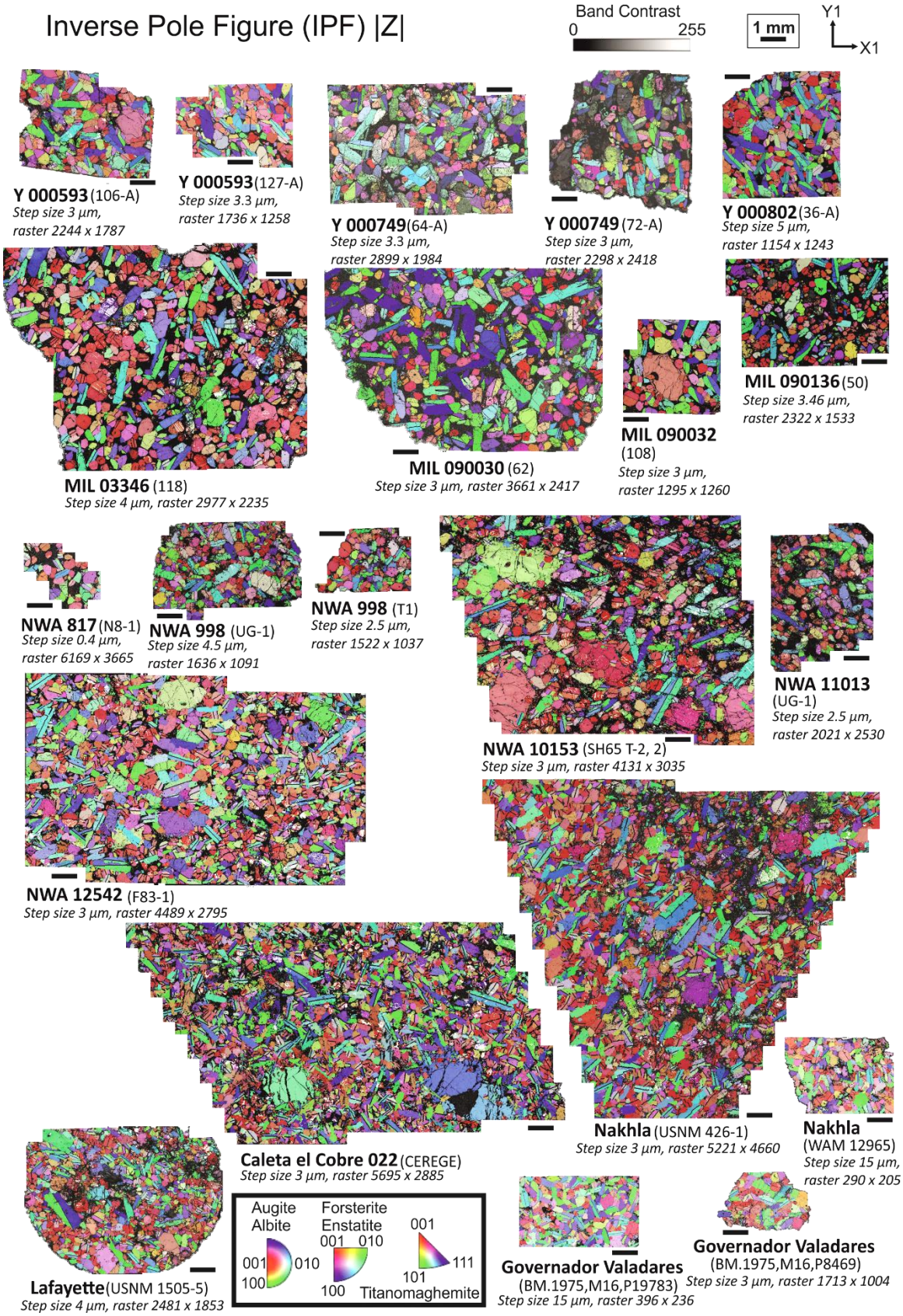

Figure 3.6. *Inverse pole figure (IPF) |z| maps of the nakhlites. The samples show simple twinning (black) and mechanical twinning (white), predominantly within crystals of augite (high Ca-clinopyroxene). There appears to be a slight alignment of augite along its [001] axis, despite crystal orientation appearing for the most part random in nature when considering all the different phases.*

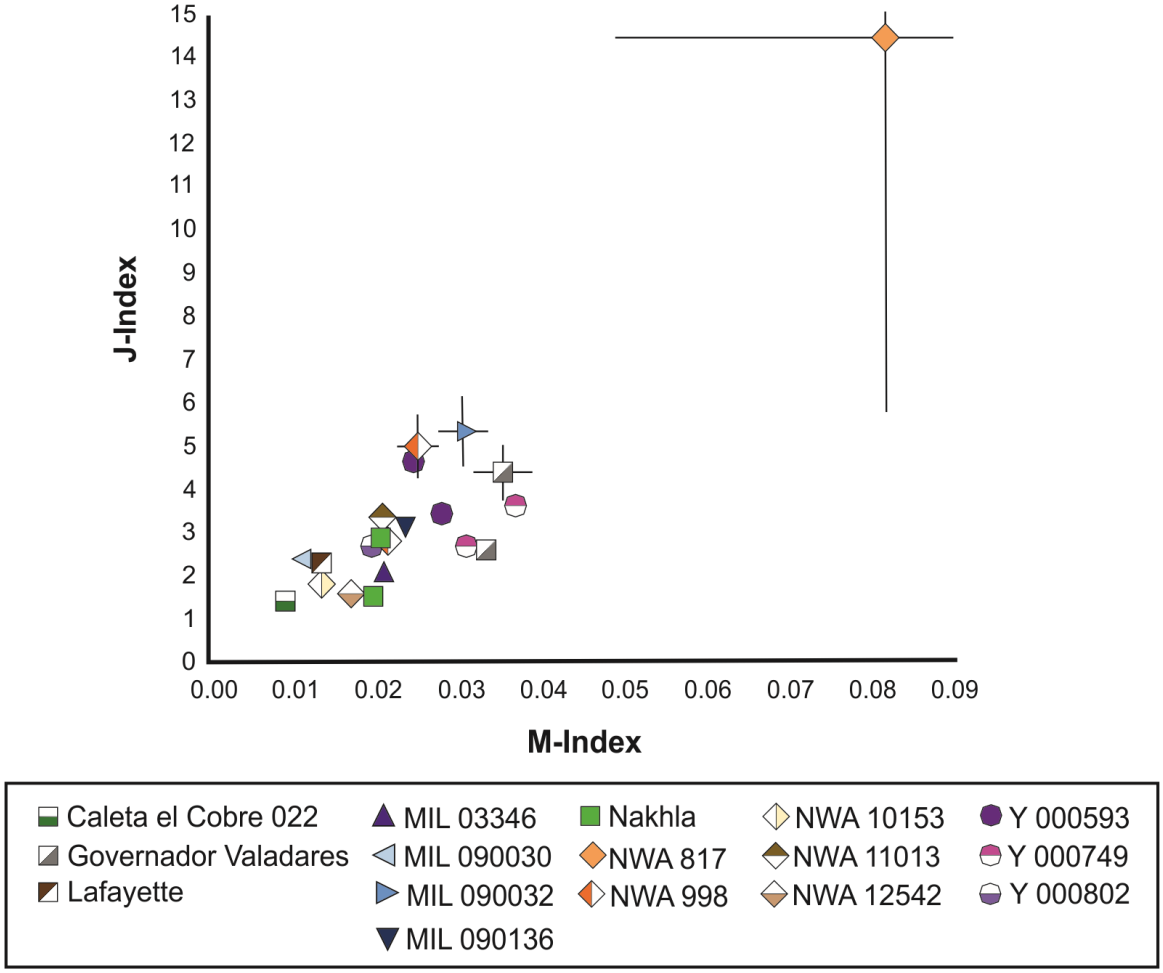

Figure 3.7 *M-Index and J-Index values for the nakhlites. Caleta el Cobre 022 exhibits the lowest J-Index and M-Index values, while the highest observed J-Index and M-Index values, for NWA 817, are interpreted to be a function of the smaller dataset size (n_{MTEX} = 43 crystals).*

3.5.4 Calculated magma body thicknesses used to assess feasibility of dominant emplacement mechanism

Calculated thicknesses for the individual nakhlites reported here are preliminary and are intended to serve as general indicators to direct future modelling work. Results are intended to determine the most viable emplacement mechanism for the nakhlites, rather than exact unit thicknesses. Due to the resolution of the current calculations reported results are only able to be discussed in terms of magnitude scale (*i.e.*, centimetre, metre, vs, tens of metres).

For a thermal diffusion emplacement mechanism (equation 3.3), calculated magma body thicknesses (within error) were found to sit within the tens of metres scale (Table 3.3). For a crystal settling emplacement mechanism (equation 3.4), magma body thicknesses were observed to span several different orders of magnitude that outside or error can be placed into two distinguishable groups <10 m (11 sections) and >10 m (10 sections; Table 3.3). Lastly, the calculations for the crystal convection emplacement mechanism (equation 3.5), provided unrealistic thickness values in the range of tens to hundreds of nanometres (Table 3.3). The thicknesses as calculated via equations 3.3-3.5 are very different to each other, the reasons for these differences are further evaluated in section 3.4.2. No correlations could be discerned when comparing calculated magma body thicknesses

against modelling input parameters (*e.g.*, Fig. 3.10), observed CPO metrics (*e.g.*, Fig. 3.11), or available published geochemistry or age parameters.

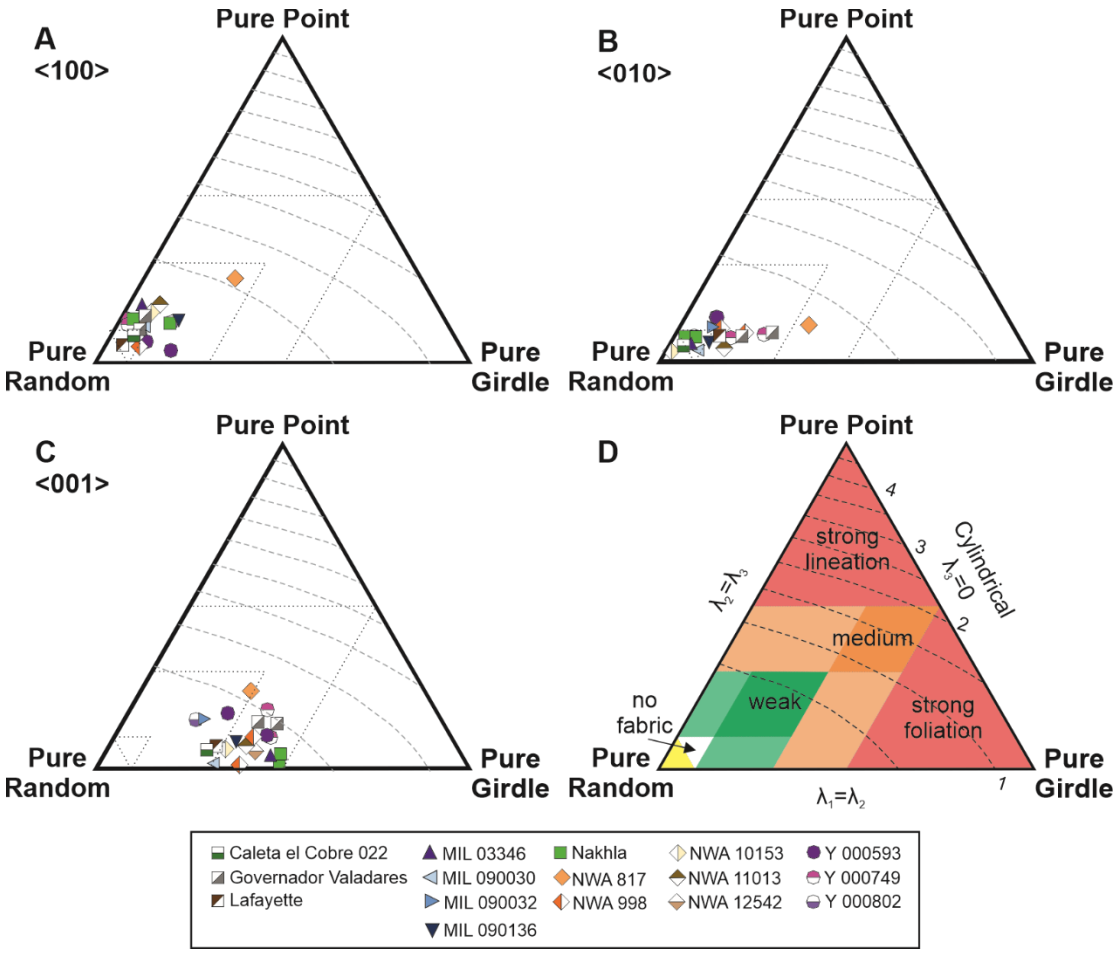

Figure 3.8. *Eigenvalue (PGR) ternary plots of the nakhlites. A) <100> axis showing low intensity weak point (i.e., lineation) to no CPO. B) <010> axis shows low intensity random to weak point CPO. C) <001> axis showing low intensity weak to moderate girdle strengths of contained crystals (corresponding to the long shape-axis), with some samples also exhibiting weak point CPO. D) Eigenvalue PGR key. Dashed lines indicate CPO intensity, where lower intensity indicates higher levels of symmetry within the CPO. Dotted lines indicate CPO strength relative to the three endmembers.* λ_1, λ_2, *and* λ_3 *refer to the specific Eigenvalues that combine to form PGR end-members.*

3.6 Discussion

3.6.1 Nakhlite CPO observations

Orientation relationship observations, here defined as the geometric relationships between the sample's constituent crystals, provide insights into important petrological processes such as crystallisation growth rates, magma mixing, emplacement mechanisms *etc.*. Specifically, EBSD provides third dimension orientation information for crystals analysed within the 2D sample analysis plane (thin or thick petrologic section) through the relationships between crystallographic and shape axes. This information is important for the study of meteorites derived from large achondritic bodies, such as the Martian nakhlites, where gravitational forces undoubtedly influenced crystallisation but the original orientation of the meteorites is unknown (Daly, Piazolo, et al., 2019).

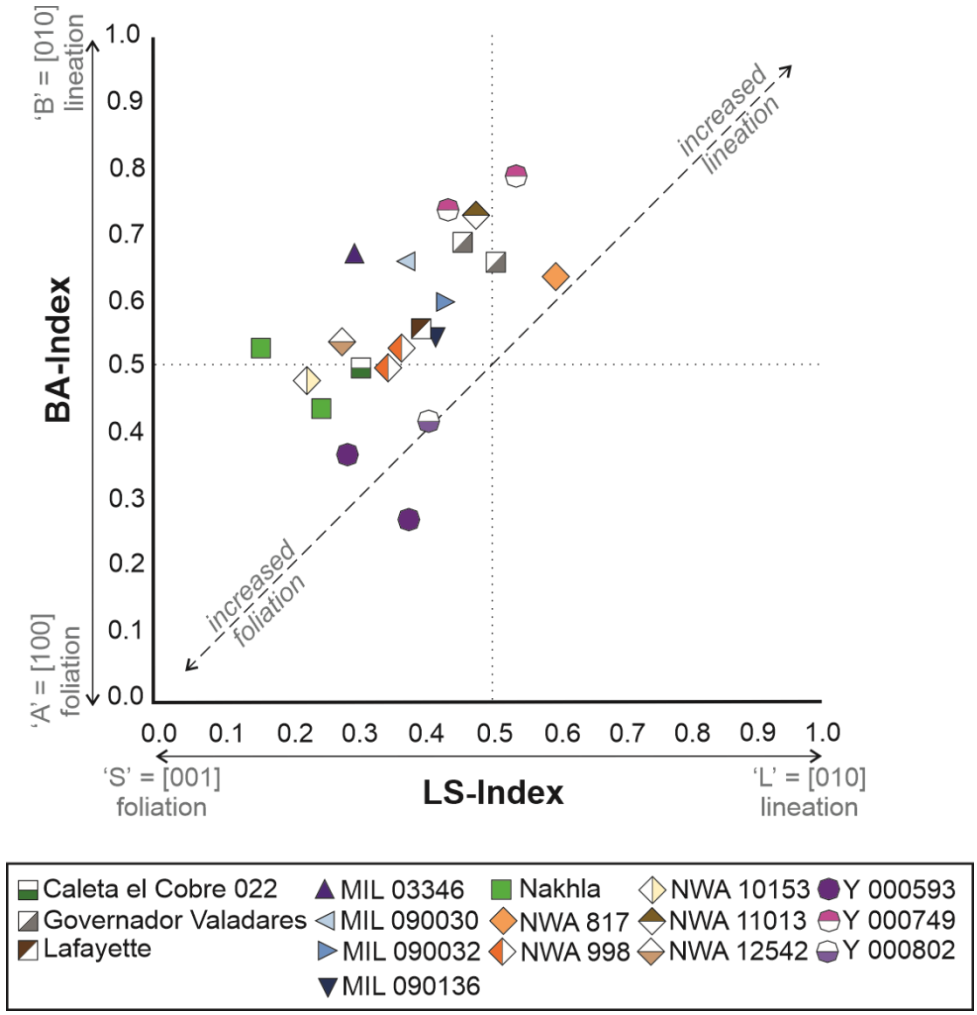

Figure 3.9. *BA-Index versus LS-Index for the nakhlites. BA-Index assesses the shape relationship where 0 indicates a dominant girdle <100> foliation signature (A) and 1 indicates a dominant point <010> lineation signature (B; eq. 3.1). LS-Index assesses the shape relationship where 0 indicates a dominant girdle <001> foliation signature (S) and 1 indicates a dominant point <010> lineation signature (L; eq. 3.2). The nakhlites exhibit S type-LS type CPO with B type-BA-type CPO, exempting Y 000593 which exhibits S and BA-A type CPO.*

Previous EBSD studies of a limited set of Martian nakhlite meteorites provide a baseline for understanding crystallisation processes in their origin on basis of detected SPO and CPO of earliest crystallised – and gravitationally settled – mineral phases, particularly augite (Daly, Piazolo, et al., 2019). Data presented in this study were acquired on a much larger set of nakhlites (16 specimens (Fig. 3.4), confirm these observations, *i.e.*, augite in each of the analysed materials shows a coupling of the <001> axis – long shape-axis.

In general, clinopyroxenes (*i.e.*, augite investigated in this study) will typically exhibit weaker CPO strengths than other associated minerals (*e.g.*, olivine and orthopyroxene) particularly in intrusive samples (Hidas et al., 2019; Van Der Werf et al., 2017). For augite, the combination of its euhedral shape with its monoclinic symmetry will impact observed CPO strengths. Thus, when using quantitative metrics to assess CPO strength, the overall relationship between a given crystal's shape and symmetry needs to be considered to properly contextualise the results.

Table 3.3. *Calculated magma body thicknesses*

		Unit thickness scale		
Nakhlite	**Section**	**Thermal Diffusion**	**Crystal Settling**	**Crystal Convection**
Caleta el Cobre 022	CERGE	10s m	10s m	n.v.
Governador Valadares	BM.1975,M16, P8469	10s m	10s m	n.v.
	BM.1975,M16, P19783	10s m	10s m	n.v.
Lafayette	USNM 1505-5	10s m	10s m	n.v.
MIL 03346	118	10s m	10s m	n.v.
MIL 090030	62	10s m	10s m	n.v.
MIL 090032	108	10s m	10s m	n.v.
MIL 090136	50	10s m	10s m	n.v.
Nakhla	USNM 426-1	10s m	m	n.v.
	WAM 12965	10s m	≤1 m	n.v.
NWA 817	N8-1	10s m	10s m	n.v.
NWA 998	T1	10s m	m	n.v.
	UG-1	10s m	m	n.v.
NWA 10153	SH65 T-2,2	10s m	m	n.v.
NWA 11013	UG-1	10s m	m	n.v.
NWA 12542	F83-1	10s m	10s m	n.v.
Y 000593	106-A	10s m	≤1 m	n.v.
	127-A	10s m	≤1 m	n.v.
Y 000749	64-A	10s m	≤1 m	n.v.
	72-A	10s m	m	n.v.
Y 000802	36-A	10s m	≤1 m	n.v.

n.v. = not valid

(See supplementary materials for spreadsheet format)

3.6.1.1 CPO strength from the M-Index

The M-Index values, which span a range of 0.03 (Figs. 3.7 and 3.11A), indicate no CPO within any of the analysed nakhlites. Note, however, that M-Index is commonly applied in the study of olivine and other orthorhombic minerals but not clinopyroxene mainly because consideration of the latter alone can provide either erroneously low CPO strength estimates or even nonsensical values even in rocks with moderate CPO strengths (*e.g.,* Hidas et al., 2019). The M-Index determines CPO strength through assessing the degree of rotation required for two crystals to become crystallographically aligned. To achieve this, the M-Index utilises a subset of the overall ODF spherical harmonic (Mainprice et al. ,2015; Skemer et al., 2005). Among all the nakhlites studied here, a significant proportion of the augite crystals exhibit simple twins (180° rotations; Fig. 3.6). Note, however, that a current limitation of the used MTEX code is the inability to remove twinning orientation discrepancy within crystals of lower order symmetry such as monoclinic augite. In other words, simple twins impact the M-Index calculations by underestimating true CPO strengths. The values that are observed do sit in a similar range to reported ultramafic rocks on Earth (Hidas et al., 2019; Van Der Werf et al., 2017), although clinopyroxene is not the dominant phase in these studies.

For the analysed sections, the CPO strength from M-Index calculations is at odds with the estimates from the CPO plots but does agree with the observed SPO (Fig. 3.4).

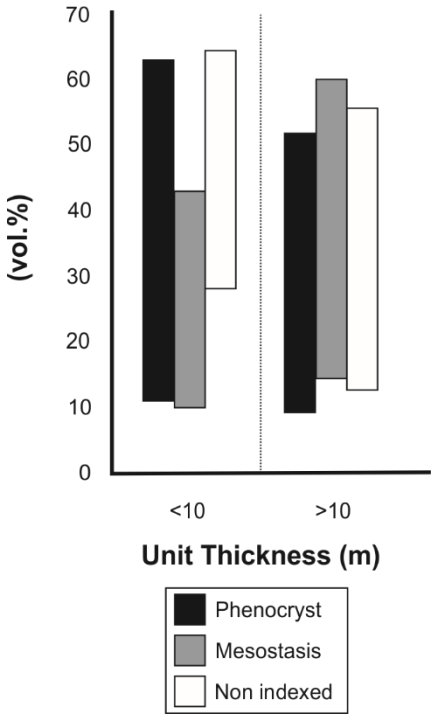

Figure 3.10. *Identified groups based on calculated unit thickness ($D_{sett,}$ eq. 3.4) assuming crystal settling as the dominant mechanism influencing crystal orientation versus modal variability within analysed nakhlites. Phenocryst (≥200 µm), mesostasis (<200 µm). and non-indexed (glass, non-indexed phases), and fractures/holes.*

3.6.1.2 CPO strength from the J-Index

The J-Index values indicate different CPO strengths across the across the nakhlite suite, ranging from borderline no CPO to weak CPO in Caleta el Cobre 022, to medium strength CPO in Governador Valadares, MIL 090136, NWA 998, NWA 11013, Y 000593, Y 000749, and Y000802 (Figs. 3.7 and 3.11A, Table 3.2). These results are consistent with data from intrusive fine-grained clinopyroxenites and coarser grained websterites on Earth (Frets et al., 2012; Henry et al., 2017). The results also indicate CPO diversity within the nakhlites emplacement environment. However, variation in CPO within a singular magmatic body (flow and/or intrusion) is common within igneous rocks, particularly those that formed in convecting flow regimes (Lofgren, 1983; Marsh, 2013; Perugini et al., 2003).

3.6.1.3 CPO shape and strength from Eigenvalue analysis

PGR analysis shows a consistent yet variable intensity <001> girdle CPO *i.e.*, <*c*> foliation as the dominant CPO across all 21 analysed nakhlite sections (Figs. 3.4, 3.8 and 3.11D). Girdle CPO is defined here as the alignment of one or two crystal axes along a singular plane, also known as magmatic foliation (Paterson et al., 1998). In addition to the more dominant <001> girdle CPO, almost all sections (exempting Caleta el Cobre 022 and Lafayette) exhibit very weak to weak intensity point CPO within either <100> or <010> *i.e.*, <a> and <b> axes, respectively (Figs. 3.4, 3.8, 3.9 and 3.11). Point CPO is defined as the consistent alignment of a given crystallographic axis

along a singular direction also known as magmatic lineation (Paterson et al., 1998). Finally, some sections show PGR values within the <100> and <010> axes which indicate a combination of weak point with weaker <100> girdle CPO (Figs. 3.8, 3.9 and 3.11C).

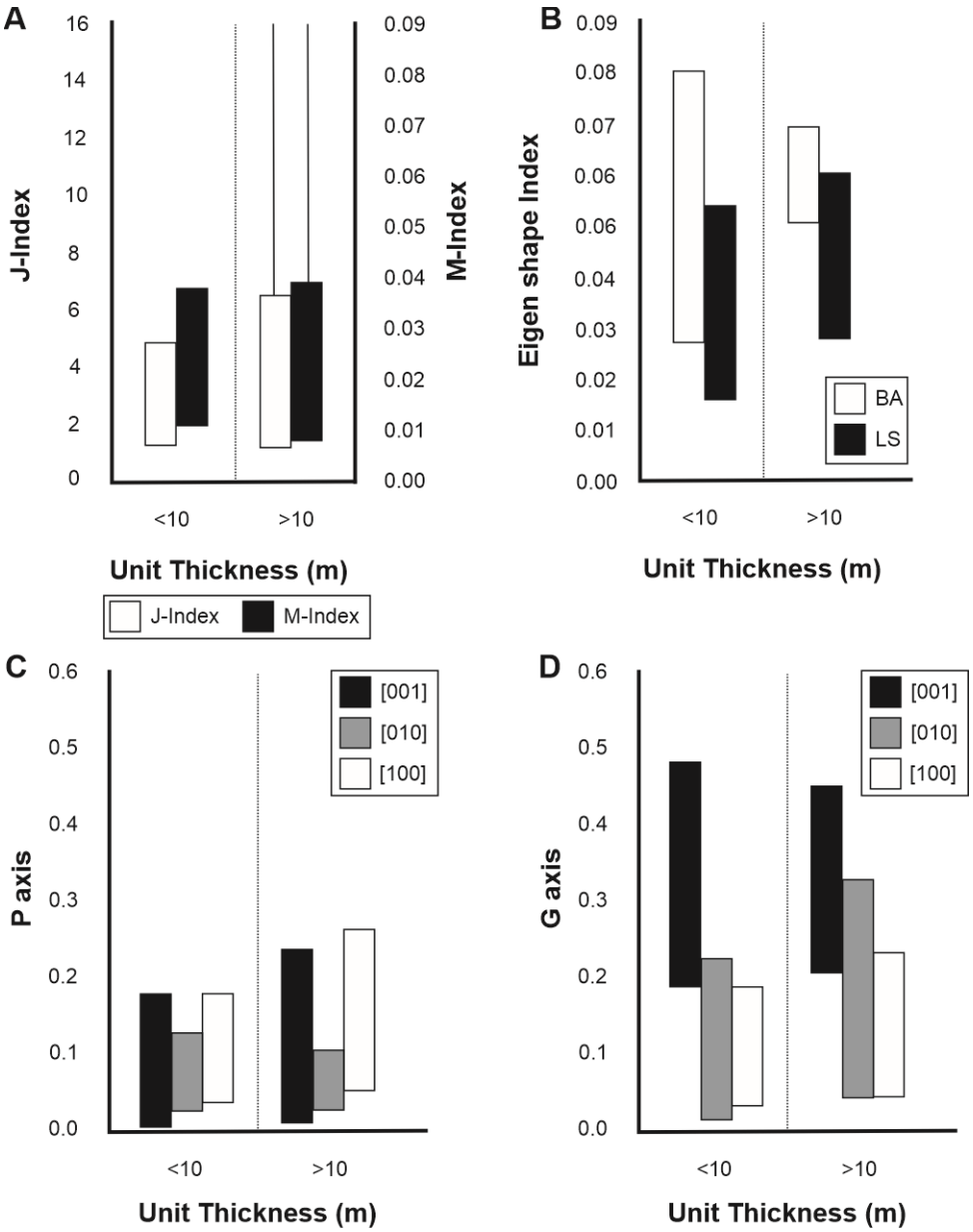

Figure 3.11. *Calculated CPO indices compared against calculated crystal settling magma body thicknesses (Eq. 3.4). A) J-Index (here defined as low = 1.4–1.8, low-medium 1.8–3.0, medium = 2.4–5.0, medium-strong = 4.0–12.0, and strong >12.0) and M-Index (0 = random 1 = a single crystal); B) Eigenvalue shape indices which range from 0–1 (0 = A or S and 1 = B or L). The BA-Index range for calculated magma bodies is observed to be more restricted for those > 10 m; C) Lineation strengths (0.1–0.3 = weak, 0.3–0.5 = moderate, and >0.5= strong) between the different crystallographic axes; and D) foliation strengths for the different crystallographic axes (0.1–0.3 = weak, 0.3–0.5 = moderate, and >0.5= strong). Between the lineation and foliation strengths foliation within the <001> axis is observed to range from weak to moderate, while all other axes show weak to no CPO.*

3.6.1.4 Intra-sample variability

To assess variability in individual analyses for each meteorite two sections from each of five different meteorites were analysed (Governador Valadares, Nakhla, NWA 998, Y 000593, and Y

000749). Previous work assessing modal mineralogy variation between replicate nakhlite sections (*i.e.,* sections sourced from the same meteorite) showed up to 40% variation in the nakhlites (Corrigan et al., 2015). Significant changes in modal composition will impact the expression of SPO and CPO, particularly within igneous rocks. Higher levels of mesostasis material will, in general, enable easier mobility of phenocryst crystals, whilst highly crystalline solids will have less movement (Nicolas, 1992; Piazolo et al., 2002). The calculated standard deviation between replicate sections' quantitative CPO metrics were highest for J-Index (0.75 ± 0.13), followed by PGR (0.022 ± 0.002), then M-Index (0.02 ± 0.08; Table 3.2). The M-Index and J-Index standard deviations, sit within the same CPO strength groupings (weak, moderate *etc.*) but are often outside of the metrics associated calculation error. The PGR values sit qualitatively within the same regions (Fig 3.8), however, quantitatively they do not overlap (Table 3.2). Both M-Index and J-Index calculations are highly dependent on the ODF. A sample's ODF represents the variability in crystal orientation relative to the analysis plane. Crystal orientation used in ODF is calculated using the Euler density, which is derived from the crystal's symmetry. Calculation of an accurate ODF is highly dependent on the associated halfwidth (selected as 15° for all samples in this study), which if not properly considered can distort the Euler space and bias the results (Gerth & Schwarzer, 1993; Kalidindi et al., 2009). Variable sized datasets and failure to properly accommodate fractured crystals can further influence CPO calculations. However, the third CPO metric, Eigenvalue analysis (PGR), does not rely on ODF. What the PGR metric does instead is utilise the direct Euler angle of the crystal with respect to the crystal's Miller reference frame (which for augite is <100>, <010>, <001>). The orientation deviation of each crystal relative to the overall sample is then normalised. This normalised orientation is then assessed as a fractional component (*i.e.,* using one Miller reference frame) between three endmembers (P, G, and R). This is distinctly different to the two end-member scale used for both M-Index and J-Index, which both consider a crystal in its entirety.

Across the replicate sections the major variable that could have affected the resulting CPO values is the discrepancy in the number of detected crystals. Assessment of the compositional breakdown between phenocryst, mesostasis material, and non-indexed space within the samples (Fig. 3.2) showed the largest deviations between all three components in Y 000593 [±21 (*c*), ±16 (*ms*), ±5 (*ni*)] and the smallest deviation within in Y 000749 [±2 (*c*), ±1.5 (*ms*), ±3.5 (*ni*)]. In terms of the vol.% augite within the samples, deviation within the replicate samples is observed to range from ±0.7 (Y 000593) to ±19.3 (Governador Valadares). Placing the replicate section CPO metric deviations within the context of augite's variable abundance within each section helps to explain the observed differences in metric results outside of analytical uncertainty. It also reinforces the importance of crystal distribution heterogeneity to the development and variation of observable CPO within a given sample. More importantly, in lieu of assessment of CPO from datasets containing representative numbers of crystals, analysis of multiple replicate section can provide an increased understanding on how the CPO metric is influenced by the inherent heterogeneity of the sample. The impact on CPO calculation variability in the number of augite crystals was minimised through setting the identified 300 minimum crystal requirement as the upper limit for all datasets (affecting 12

datasets). The gold standard for number of crystals required for CPO studies is intensity dependent, where samples exhibiting lower intensity CPO, such as the nakhlites, require larger datasets than samples exhibiting higher CPO (Ismaïl & Mainprice, 1998; Skemer et al., 2005). The requirement for larger crystal datasets to assess CPO can be impractical and potentially problematic for many planetary studies, where often the material available to study is limited and the amount of sample per section is generally a fraction of the size typically found in a traditional petrological section. If the ideal range were to be applied to the presented nakhlite datasets, only 12 of the 21 datasets using n_{MTEX} (4 datasets using n_{OPPG}; Table 3.2) would produce viable CPO values (*i.e.*, with 2% error margins). Thus, CPO metrics should only be used as crude indicators, particularly in the study of scarce meteorites.

3.6.1.5 CPO related to calculated dominant emplacement end-member mechanisms

The bulk volume of an igneous body can have significant impact on the external strain field's CPO expression within an igneous sample (Marsh, 2013). Specifically, a specimen that forms in a large flow/intrusion within which crystals are convecting (producing localised strain fields with at least two major strain directions within a larger strain field) would be expected to exhibit a stronger CPO. The strength of this CPO would also vary more throughout the igneous body than would be found for a sample formed from either crystal settling (one dominant strain field *a.k.a.* gravity) or thermal diffusion [no strain field; Callot & Guichet (2003), Marsh (2013), and Nicolas, (1992)]. However, the convection end-member model calculation of equation 3.5, which was intended to provide the absolute minimum potential manga body thickness, resulted in unit thicknesses that are significantly below the measured average crystal size (Tables 3.2 and 3.3). Thus, results from equation 5 do not support a pure crystal convection mechanism as the dominant emplacement mechanism for the nakhlites. However, calculated magma body unit thicknesses for the other two mechanisms require crystal convection to also be present as a secondary mechanism. Particularly, for the crystal settling calculated >10 m unit thicknesses in order to satisfy fundamental physics. If, however, crystal convection was the overriding emplacement mechanism for the nakhlites, then the residence times used in our calculations would have to represent a single round of convection rather than representing the entire crystallisation process in order to produce viable results. Out of the three emplacement end-members modelled for the nakhlites, crystal settling agrees best with the observed CPO (Figs. 3.4 and 3.8) and moreover, produces the largest range of magma bogy thicknesses distinguishable as two separate groups (>10 and < 10 m, Figs. 3.10 and 3.11, Table 3.3). The identification for two distinct groups outside of error indicate that if crystal settling is the overriding dominant emplacement for the nakhlites, then different proportions for both crystal convection and thermal diffusion are contributing to the observed CPO as secondary mechanisms. This contribution will result in different unit thicknesses than presented here in this paper.

3.6.1.6 Magmatic emplacement style of the nakhlites from CPO

The observed moderate low intensity <001> foliation (Fig. 3.4, 3.8, 3.9, and 3.11, Table 3.2) indicates a dominant shear or flattening flow regime, which is commonly observed within cumulate-type igneous rocks (Hunter, 1996; Iezzi & Ventura, 2002; Merle, 1998). Only Caleta el Cobre 022, Lafayette, MIL 090032, Y 000593 (section 127-A only), and Y 000802 exhibit weak <001> foliation (Fig. 3.4, Table 3.2). This weak foliation indicates a lower influence of pure shear (σ, *i.e.*, where $\sigma_1>\sigma_2=\sigma_3$). Out of the identified nakhlites with weaker strength foliations, Caleta el Cobre 022 is the only sample to exhibit no other form of CPO (foliation or lineation) within its <100> and <010> axes, which is consistent with its low J-Index value. Even Lafayette, the section with the next lowest foliation strength, exhibits a weak <010> girdle CPO that is weaker than the <001> axis girdle CPO (Fig. 3.4, Table 3.2). The lower pure shear component and lack of other CPO present within both samples indicate emplacement in a relatively stagnant magmatic body compared with the other nakhlites. All other nakhlites exhibit some form of <100> [MIL 03346, MIL 090030, MIL 090136, Nakhla (USNM 426-1), NWA 10153], <100> + <010> [MIL 090032, NWA 998 (T1)], or <010> (Y 000593) lineation in combination with a more dominant <001> foliation (Table 3.2). The general preference within the nakhlites towards the development of a weaker secondary CPO within the <100> axis rather than the <010> axis is inconsistent with most common CPO observed within clinopyroxene-rich igneous rocks on Earth despite plastic deformation within the crystal favouring dislocation along the <001> and <100> axes (Bascou, Tommansi, et al., 2002; Godard & van Roermund, 1995). Even though Y 000593 has a weak lineation, the alignment of <010> over the <100> could indicate different external strain conditions during emplacement compared to the other nakhlites (Bascou, Tommansi, et al., 2002). For all but two of the studied nakhlites, the combination of stronger foliation with a weaker lineation suggests a common emplacement mechanism/environment, regardless of whether or not each sample represents an individual flow/intrusion (Corrigan et al., 2015; Daly, Piazolo, et al., 2019; Udry & Day, 2018).

Dominant pure shear (flattening) with a lower component of simple shear (rotational) is commonly associated with gravitationally driven crystal settling, which is the dominant emplacement mechanism in stagnant magma body regimes. Environments where such CPO can develop include intrusions, lava pools and ponds (Iezzi & Ventura, 2002; Merle, 1998), low viscosity slow moving basaltic lavas, or as has been previously suggested for the nakhlites thick lava flows (Friedman Lentz et al., 2011; Treiman, 2005). However, variation (heterogeneity) in CPO strength and the formation of weaker lineation CPO is a common occurrence within magmatic bodies where pockets of CPO can be highly localised, particularly for bodies associated with a higher discharge volume. In general, greater CPO strengths which tend towards lineation are often observed along the edges of the magmatic body, gravitational settling CPO towards the lower portions (but not the direct base), and random CPO towards the central regions (Nicolas, 1992; Shelley, 1985). Previous CPO analyses of several nakhlites resolved CPO that are consistent with both subaerial flow and stagnant lava lake emplacement environments (Daly, Piazolo, et al., 2019). Results in the present study from a much larger set of nakhlites are consistent with variable emplacement mechanisms and environments.

Importantly, they indicate that formation in pure crystal settling environments (*e.g.*, stagnant lava lakes/ponds) may have been less common formation in dynamic flow regimes, be it intrusive or subaerial. In the case of an intrusive emplacement environment, such as a sill or a dyke, stronger CPO with a higher simple shear component is common along the margins but not the central portions of the magma body (Gibb & Henderson, 1992; Komar, 1972; Piazolo et al., 2002; Shelley, 1985). In such a scenario, the low intensity moderate <001> foliations observed among augite crystals could suggest crystal settling via dynamic sorting (Bagnold effect), where each of the nakhlites represents a different axial region from a series of interconnecting dykes or inclined sills (Corrigan et al., 2015; Marsh, 1996) which span at least four separate magmatic events (Cohen et al., 2017). The identification of secondary multiple axis lineations plus the random SPO in most of the analysed samples suggest that the observed <001> foliations have overprinted the initial primary flow CPO within each of the putative nakhlite igneous bodies. During emplacement, such a switch from flow to gravitational crystal settling would account for random SPO, agree with the SPO interpretations of Udry and Day (2018) whilst also maintaining regions of stronger CPO and SPO particularly along the margins of the intrusion (for comparison see Berkley et al., 1980).

3.6.2 Implications for the nakhlite source volcano

Igneous rocks, whether formed on Earth or elsewhere in the Solar System, usually show significant mineralogical heterogeneities down to the scale of a few tens of micrometres (Hammer et al., 2010; Jankovics et al., 2012; Kouchi et al., 1986; Lofgren, 1983; Marsh, 2013; Perugini et al., 2003). This characteristic hampers the extrapolation across scales, particularly for meteoritic materials like the nakhlites, of which only millimetre to centimetre-sized fragments is available for in-depth micro-structural analysis. To date, however, significant micro-structural variation within an individual Martian meteorite specimen (325 samples as of January 2022) has only been reported for the shergottite Zagami (Becker, 2011). Different conditions on Mars *e.g.*, lower gravity, would undoubtedly affect the SPO and CPO expression of Martian magmatic rocks when compared to those formed on Earth. For example, a relatively stronger strain field is required to produce lineation CPO within equal-sized magmatic rocks on Mars compared to Earth, mainly because of the lower gravity on Mars and its subsequent effects on parameters like viscosity, strain, apparent density, and general flow dynamics (Niu & Pang, 2020; Vetere et al., 2019). However, despite the differences between Earth and Mars creating variation in the parameters required to form particular SPO and CPO, the SPO and CPO's significance in terms of the general environment of formation are directly comparable. For igneous rocks, increased M-Index and J-Index metric values signal a flow-dominated environment, accounting for increased lineation/simple shear; in PGR analysis, the same is indicated by higher P values. Crystal alignment, which influences CPO development, has been shown to have a number of controls outside of the external strain field (simple shear). The alignment of crystals within an igneous body will be influenced by factors such as the elongate nature of the individual crystals, density and viscosity of the melt, the mineralogical composition and distribution, as well as the surface: volume ratio of the igneous body (Piazolo et al., 2002). CPO heterogeneity

between different igneous specimens may be even more pronounced in cases that they formed in multiple events of emplacement (Fenton et al., 2004). Despite the lack of (geological emplacement) context for the nakhlites, the size of each meteorite constrains the maximum relative distance between the replicate sections to centimetre-scale, and the vicinity of the individual meteorites relative to one another to within the area of the currently unknown ejection crater, whose diameter is estimated to be on the scale of kilometres (Artemieva & Ivanov, 2004; Kereszturi & Chatzitheodoridis, 2016).

Coupled modelling and CPO analysis results demonstrate that the nakhlite specimens analysed formed via gravity settling dominated crystallisation with variable minor components of flow. These results are in agreement with, and expand upon the findings in Daly, Piazolo, et al. (2019). Whereas these results are in striking contrast to the findings in Udry and Day (2018), who reported random SPO for the thirteen nakhlite specimens they studied. The conflicting results in Udry and Day (2018) may be due to their use of more traditional SPO measurements corrected for slope via measured crystal shape dimensions (rather than proxied SPO via CPO used here). Another option for the reported discrepancy could be from the nakhlites forming under a dynamic sorting regime (Corrigan et al., 2015). An intrusive dyke and sill field could produce the observed random SPO with an aligned CPO via a dynamic sorting regime (Horsman et al., 2005), as reported in Figure 3.4. In all studied specimens, the percentage of crystallographically aligned phenocrysts within the analysis plane is low (2.53-10.04%; Table 3.2). This results in the observable SPO, even when accounting for the phenocryst's slope relative to the analysis plane, to appear random in almost all analysed nakhlite sections (Fig. 3.4). If each section's CPO was not considered, then the presented data from this study would agree with the interpretations of Udry and Day (2018).

Lastly, it is important to evaluate whether the calculated magma body end-member thicknesses for each specimen can aid in localisation of the nakhlites' origin in the Martian crust. We the authors reiterate that the exact values presented for the end-member mechanisms are not the actual nakhlites unit thicknesses rather they are indicators of end-member viability. Out of the three tested end-member mechanisms pure crystal settling agrees best with the observed nakhlite CPO. From this calculation two distinct groups (within the model's current resolution) are identified (3.2). These two groups imply that the nakhlites did not form from a pure crystal settling regime, *i.e.*, have contributing secondary mechanisms (thermal diffusion and/or crystal convection), or formed in the exact same manner. The proportion between the dominant and secondary mechanisms during emplacement is an area for future work. However, based off physical principals, the current calculated unit thicknesses for the calculated >10 m nakhlites require crystal convection to also be present.

Comparison of the two crystal settling groups against CPO and SPO data, published geochemical data [*e.g.*, Day et al. (2018) and Krämer Ruggiu et al. (2020)], or age [*e.g.*, (Cartwright et al., 2013; Cohen et al., 2017; Krämer Ruggiu et al., 2020; Mikouchi et al., 2016; Park et al., 2009, 2016)] show no identifiable trends or correlations. This observation infers the overall nakhlite dataset to be inherently random in terms of both CPO variation, proportion of emplacement mechanisms,

and potential magmatic body thicknesses through time (Figs. 3.10, 3.11). This heterogeneity of the larger dataset could be very easily overlooked when only assessing a subset of the samples. On Earth, individual magmatic events from the same volcano or even multiple lobed flows from a singular event have been observed to shift and evolve in an inconsistent manner (*e.g.*, unit thickness, chemical composition, viscosity, CPO, and SPO), particularly when analysing relatively short periods of a volcano/magma bodies lifespan (Gamble et al., 1999). This intrinsic variability is why field-mapping and high-resolution age dating are critical tools used to understand the evolution of volcanic systems over shorter time periods. Even though the nakhlites are shown to have a formation window of at least 93 ± 12 Ma (Cohen et al., 2017) magmatic sources on Mars have been shown to span several billion years (Lapen et al., 2017). In terms of the positioning of the nakhlites, the distal relationship between the samples is limited to their ejection crater on Mars (Cohen et al., 2017; Day et al., 2018a; Nyquist et al., 2001; Udry & Day, 2018). Comparison of identified calculated emplacement mechanism groups to published age data showed no observable trends over time which could indicate variable discharge or region of emplacement from the nakhlite magmatic source, or be the result of other factors such as magma viscosity, topography, restriction/spread of the flows/intrusions *etc.* (Baumgartner et al., 2017). The resolution of the magma body thicknesses presented here do not yet enable localisation parameters to be fully discerned at a reasonable resolution. However, they do provide a starting point for building more complex models to start investigating other influential parameters such as, mixing of the here calculated end-member emplacement mechanisms calculated here, intrusion versus flow, depth of burial, cooling rate, distance travelled from source *etc.*, which in lieu of field-mapping should assist in narrowing the localised criteria for the nakhlites.

3.7 Conclusions

The nakhlite have a low intensity weak-medium <001> foliation CPO with all bar two samples exhibiting a weak form of lineation CPO along either one or both remaining crystallographic axes. The dominant foliation CPO agrees best with an emplacement mechanism based on crystal settling (*e.g.*, lava ponds, lava lakes, intrusive sills, and dykes. Disparity between observed SPO and CPO across the nakhlites could either be the result of the sections' orientation or an overprinting of initial CPO by the now more dominant <001> foliation. Modelled end-member results for a crystal settling mechanism identifies two distinct groups (outside of error) based on calculated unit thickness within the nakhlites. The identification of two distinct groups within the nakhlites indicates the presence of secondary emplacement mechanisms contributing to the nakhlites' development. Comparison of the two identified modelled crystal settling groups to presented CPO, SPO, as well as published age and geochemistry data show no correlations or trends. These results highlight the inherent randomness of the large dataset, and therefore the source volcanoes discharge through time. However, the nakhlites all exhibit a common dominant emplacement mechanism and CPO, which indicate an overarching first-order characteristic belonging to their source volcano. Overall, this study highlights the importance of assessing larger datasets for investigations into first-order

processes, particularly for samples (such as meteorites) where due to the lack of external context, the assessment of limited data can lead to the over-interpretation of local variations.

3.7.1 Acknowledgments, specimens, and data

The authors are grateful to the following curational facilities for providing the samples used in this stud: NHM London (Governador Valadares), Japanese Antarctic Meteorite Research Centre (NIPR; Y 000593, Y 000749, Y 000802), Macovich Collection, The Museum of Western Australia(Nakhla WAM 12965), Centre Européen de Recherche et d'Enseignemet de Géosciences de l'Environment (CEREGE; Caleta el Cobre 022), the Institute of Meteoritics University of New Mexico (NWA 10153, NWA 12542), Smithsonian National museum of Natural History (Lafayette, Nakhla USNM 426-1), and ANSMET (MIL 03346, MIL 090030, MIL 090032, and MIL 090136). US Antarctic meteorite samples are recovered by the Antarctic Search for Meteorites (ANSMET) program, which has been funded by the NSF and NASA, and characterised and curated by the department of Mineral Sciences, of the Smithsonian Institution and Astromaterials Acquisition and Curation Office at NASA Johnson Space Centre. The authors thank the editor Laurent Montési, our reviewers Alex Ruzicka and Jon Friedrich as well as David Prior and Iain Neill for their helpful comments which significantly enhanced our manuscript. This work was funded by the Science and Technology Facilities Council through grants ST/N000846/1 and ST/H002960/1 to M.R.L). All data are available at Griffin et al. (2021).

4 Can the magmatic conditions of the Martian nakhlites be discerned via investigation of clinopyroxene and olivine intra-crystalline misorientations?

S. Griffin[1], L. Daly[1,2,3,4], S. Piazolo[5], L.V. Forman[2], B. E. Cohen[6], M. R. Lee[1], P.W. Trimby[7], R.J. Baumgartner[8,9], G. K. Benedix[2,10,11], and Ben Hoefnagels.

[1]School of Geographical and Earth Sciences, University of Glasgow, UK. [2]Space Science and Technology Centre, School of Earth and Planetary Sciences, Curtin University, Australia. [3]Australian Centre for Microscopy and Microanalysis, The University of Sydney, Australia. [4]Department of Materials, University of Oxford, UK. [5]School of Earth and Environment, University of Leeds, UK. [6]School of Geosciences, University of Edinburgh, UK. [7]Oxford Instruments Nano analysis, High Wycombe, UK. [8]School of Biological, Earth and Environmental Sciences, The University of New South Wales, Kensington, NSW, Australia. [9]CSIRO Mineral Resources, Australian Resources Research Centre, Kensington, WA, Australia. [10]Department of Earth and Planetary Sciences, Western Australia Museum, Australia. [11]Planetary Institute, USA.

Key Points:

- EBSD reveals shock-derived deformation to mask non-shocked deformation even in identified low deformation regions in the nakhlites.
- Intra-crystalline misorientation patterns indicate nine distinct derived deformation signatures for 16 nakhlites.
- Intra-crystalline misorientation patterns are identified within low deformation regions interpreted as emplacement deformation.

Published: *Journal of Geophysical Research: Planets*
DOI: 10.1029/2021JE007082

S.G. and L.D. designed the research project
S.G., L.D., L.V.F, P.W.T, and R.J.B undertook EBSD analyses
S.G., processed all EBSD data
S.G. wrote the paper based of discussions with L.D., L.V.F, S.P., B.E.C., and M.R.L.
S.G., L.D., M.R.L., B.E.C., R.J.B, S.P., L.V.F, and G.K. contributed to editing the paper.
B.H. provided sample NWA 12542

4.1 Abstract

Deformation is a near ubiquitous process that is observed within nearly all naturally forming rocks. Electron backscatter diffraction (EBSD) is a technique that enables slip-systems (a form of plastic deformation) to be inferred from intra-crystalline misorientations at a comparable scale to representative CPO analysis (≥300 crystals). Extensive laboratory and studies on naturally occurring samples have identified preferential mantle condition extrinsic parameters for specific slip-system signatures within. Intra-crystalline misorientation patterns for olivine and augite (high Ca-clinopyroxene) for 16 different Martian nakhlite meteorites (21 sections) were analysed and assessed against these known parameters. Investigation of high and low deformation regions revealed a shift in the intra-crystalline misorientation patterns for 10 of the 21 sections. Interpreted as both shock (high deformation) and emplacement (low deformation) signatures. The observed variations in deformation patterns for the two main regimes of deformation indicate heterogeneous sampling of the nakhlite source crater. Our findings indicate that shock deformation is prevalent throughout the nakhlites, and that great care needs to be taken when interpreting intra-crystalline misorientations of crystals within apparent lower deformation regions.

4.2 Plain language summary

Clinopyroxene and olivine are important minerals for studying igneous processes on Mars and Earth (from the surface to the upper mantle). Here, clinopyroxene and olivine intra-crystalline misorientation patterns - deformational movement within a crystal - were investigated in a group of meteorites from Mars using the specialist microscopic technique of electron backscatter diffraction (EBSD). The nakhlites are mafic rocks representing the largest collection of rocks from a singular – but as yet unknown – location on Mars. Combined intra-crystalline misorientation patterns for both olivine and clinopyroxene reveal nine different shock deformation signatures for the nakhlites indicating that they were sourced from multiple locations within the ejection crater. Non-shock related deformation can also be observed but tends to be masked by the dominance of shock deformation features even in low deformation regions.

4.3 Introduction

Deformation within rocks is driven by a wide variety of geological processes *e.g.*, compaction (mountain building, subduction, burial), extension (rifting), shear (flow, faulting), and dramatic changes in both temperature (contact metamorphism, melting/recrystallisation, hypervelocity impacts, and hydrothermal activity) and pressure (hypervelocity impacts, rapid burial). Extrinsic parameters present over a rocks geological history will impact the way each crystal within the sample will grow and deform. Mineral deformation within rocks can occur via several mechanisms including elastic, brittle, and ductile deformation. Where ductile deformation includes dislocation creep, diffusion creep, and dissolution-precipitation creep. Micro-structures and defects (*e.g.*, dislocations) present within a mineral's crystal lattice record important information pertaining

to its crystal plastic deformation (Ashby, 1970, 1983; Fleck et al., 1994; Poirier, 1975, 1985, 1995; Poirier & Nicolas, 1975; Sciences, 1978; Stocker & Ashby, 1973).

Plastic deformation is defined as a stress and/or strain derived permanent change lacking brittle failure or volume change within a material. Plastic deformation in rocks is typically accommodated at the nano-meter scale by crystallographic slip or rotation. Crystallographic slip-systems are directional movement of either slip or rotation which occurs around specific crystallographic axes within either the crystal lattice, sub-boundaries, or inequant crystals (Law, 1990). In geological specimens, plastic deformation has been shown to develop through either crystallisation processes e.g., mantle/flow rheology, growth twins, (Cordier, 2002; Fei et al., 2012; Frets et al., 2012; Henry et al., 2017; Yao et al., 2019; Zhang et al., 2006) and/or subsequent modification processes *e.g.*, metamorphic shear, mineralogical dehydration/degassing, compaction, or shock (Friedrich et al., 2017; Godard & van Roermund, 1995; van Roermund & Boland, 1981; Ruzicka & Hugo, 2018; Tasaka et al., 2008; Yao et al., 2019). The accumulation of these deformation microstructures, are reported for a given phase as crystallographic preferred orientations (CPO) also known as lattice preferred orientation (LPO; Bernard et al., 2019; Hunter, 1996; Mainprice, Bachmann, Hielscher, & Schaeben, 2015). When combined across a representative area of a rock, these micro-structures produce a macroscale pattern of plastic deformation.

Previous studies of crystallographic dislocation systems, have shown an activation dependence of slip around specific crystallographic axes, when a crystal is exposed to a differential stress under varying extrinsic conditions *e.g.*, stress, strain, temperature, pressure, and water content (*e.g.*, Raterron and Jaoul, 1991; Katayama et al., 2004; Karato et al., 2008; Raterron et al., 2011; Bernard et al., 2019; Liu et al., 2019). Subsequently, through extensive laboratory experiments and studies of naturally occurring samples, the ability to broadly ascertain the environment (pressure, temperature, stress, strain, and water content) parameters a rock has started to develop. These activation parameters therefore have the potential to provide insight into a given sample's geological history (Barber et al., 2010). However, despite the wealth of information that is stored within crystallographic dislocations and the ever-increasing body of literature, there is a lot about these systems that yet to be fully utilised and understood.

Intrinsic controls (*e.g.*, chemistry) alongside extrinsic controls (*e.g.*, temperature, pressure, stress magnitude and strain rate) have long been recognised as important factors for the activation of crystallographic slip-systems in minerals (Ashby, 1983; Barber et al., 2010; Bernard et al., 2019; Groves & Kelly, 1963; Jaoul & Raterron, 1994; Müller et al., 2008; Poirier, 1982; Woodward, 2005). However, recent studies of olivine have shown that there are additional factors that can also influence the activation of a given slip-system (Barber et al., 2010; Bernard et al., 2019). These factors include the mechanism of deformation, water content, deformation geometry, presence of melt, and previous deformation history (Boneh & Skemer, 2014; Hansen et al., 2014; H. Jung et al., 2006; Haemyeong Jung et al., 2009; Katayama & Karato, 2006; Précigout & Hirth, 2014; Qi et al., 2018; Sundberg & Cooper, 2008). These other identified factors have the capacity to shift the previously identified activation boundaries of specific slip-systems, related to the minerals chemistry, and the local

temperature, pressure, and time frame over which deformation occurs. This is why slip-systems observed in some naturally occurring samples show slip-system signatures at lower extrinsic values compared to those determined from laboratory experiments (Bernard et al., 2019).

Here the activation of crystallographic slip-systems within olivine and augite (high Ca-clinopyroxene; Fig. 4.1 and 4.2), representatives of the orthorhombic and monoclinic crystal systems, respectively, are inferred from analysis of intra-crystalline misorientations. Olivine has been extensively studied, both experimentally and in naturally occurring samples of mantle rocks (Bernard et al., 2019; Kaboli et al., 2017; Li et al., 2020; Mainprice et al., 2005; Mei & Kohlstedt, 2000; Poirier, 1975; Soustelle & Manthilake, 2017). Thus, the activation criteria for olivine's crystallographic slip-systems over a variety of parameters are fairly well constrained (Bernard et al., 2019; Karato et al., 2008; Katayama & Karato, 2006).

Augite, on the other hand, is only starting to be studied in the same level of detail (Tedonkenfack et al., 2021; Van Der Werf et al., 2017). Previous work exploring slip-systems in clinopyroxene has predominantly focused on diopside (monoclinic with a similar crystal lattice structure to augite), but mostly in laboratory settings (Bascou, Tommasi, et al., 2002; Bystricky & Mackwell, 2001; Ingrin et al., 1991; Jaoul & Raterron, 1994; Mauler et al., 2000; Skrotzki, 1994); where many of these crystallographic slip-systems have yet to be observed within naturally occurring rocks(Keppler, 2018; Skrotzki, 1994; Tedonkenfack et al., 2021; Van Der Werf et al., 2017). Current knowledge of clinopyroxene crystallographic slip-system activation [often based off numerical simulations *e.g.*, Ulrich & Mainprice (2005)], show strong dependence on crystal orientation relative to the principal stress axes. Observations of clinopyroxene indicate that a dominant slip-system signature pairing dominant (100)[001] with minor (001)[100] (Fig. 4.2) will form under most Earth relevant extrinsic conditions (Kollé & Blacic, 1982; P. Raterron et al., 1994).

The majority of Martian meteorites are mafic-ultramafic igneous rocks (Udry et al., 2020 and references therein). To date the Martian meteorites, consist of the clinopyroxene rich shergottites and nakhlites, orthopyroxenite ALH 84001, the dunitic chassignites, and a non-igneous group of polymict breccias. The nakhlites, which are the focus of this study, are currently considered the largest group of Martian rocks sourced from a singular location on Mars, due to their consistent 10.7 ± 0.8 Ma ejection age and tight crystallisation ages (Cohen et al., 2017; Udry et al., 2020). Nearly all of the meteorites within the group contain evidence of aqueous alteration on Mars in the form of iddingsite (Bunch & Reid, 1975; Hallis & Taylor, 2011; Krämer Ruggiu et al., 2020; Lee, Tomkinson, et al., 2015; Noguchi et al., 2009; Treiman, 2005; Udry et al., 2020), and have been shown to sample several temporally distinct igneous events that are geochemically related by a shared magma source region (Cohen et al., 2017; Day et al., 2018a; Treiman, 2005; Udry et al., 2020).

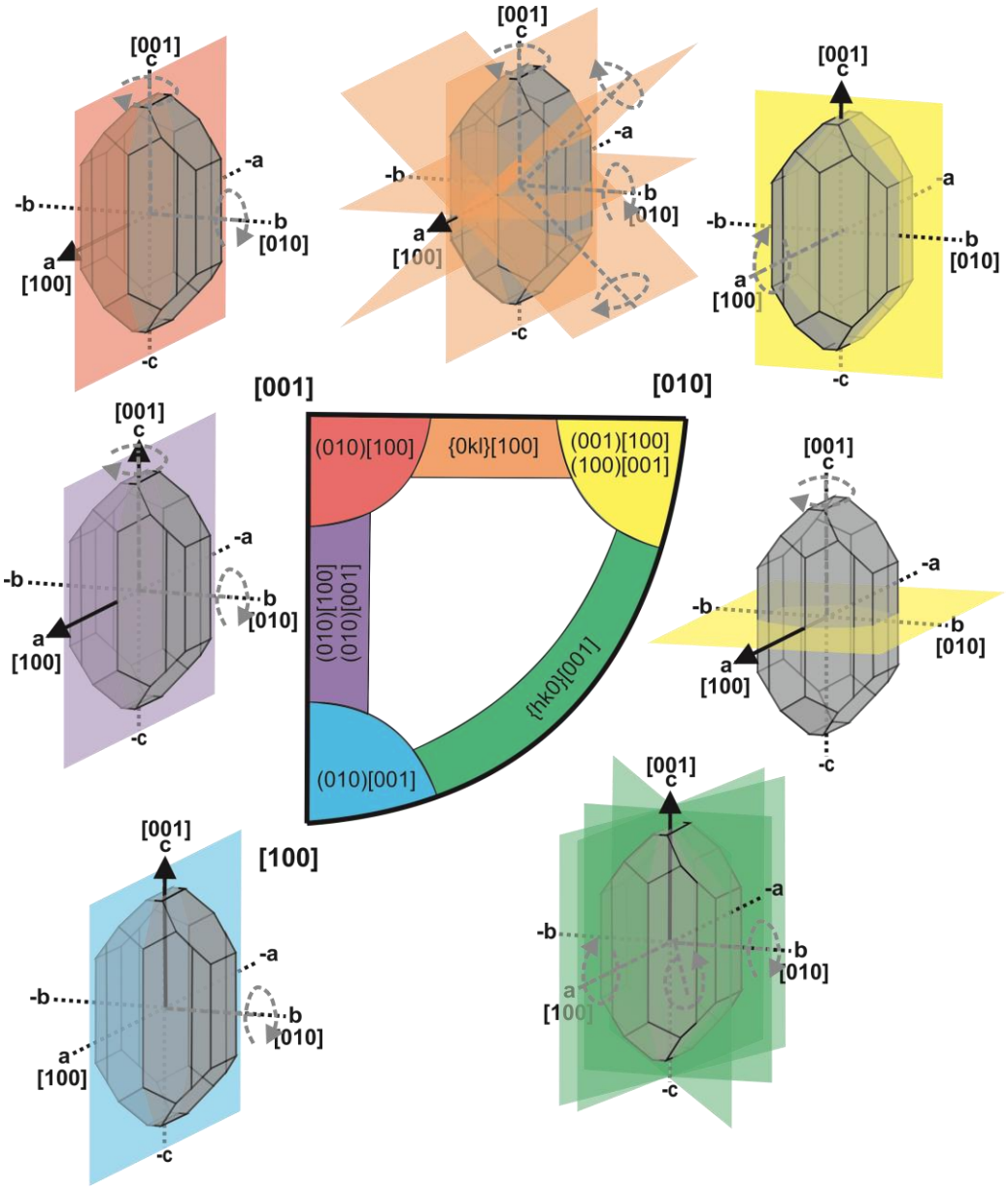

Figure 4.1. *Olivine (forsterite; mmm; unit cell lengths a = 0.466, b = 1, c = 0.587) crystallographic slip-system signature key (notated as the slip plane and slip direction) expressed as the orthorhombic crystallographic fundamental sector [lowest form of crystal symmetry; modified from Ruzicka and Hugo (2018)]. The corners of the key refer to olivine's specific crystallographic axis (<a> = [100], <b> = [010], and <c> = [001]). The surrounding diagrams visualise the different slip planes where the straight black arrows indicate the direction of slip for both twist and tilt boundaries. For a tilt boundary [movement perpendicular (axis parallel) to the plane] the black arrows also indicate the tilt axis whereas the plane rotation axis for a twist (i.e., rotating) boundary [movement within (axis perpendicular) to the plane] is indicated by the grey dashed arrows.*

The nakhlites are basalts with crystal-sizes ranging from 0.29–1 mm, crystal clustering frameworks (Udry & Day, 2018), and low intensity low-moderate strength girdle CPO (Griffin et al., 2021). Their mafic composition is dominated by augite [55–71 modal%; (Udry & Day, 2018)[with low-moderate abundances of olivine (1.7–14.9 modal%). The remaining 0–42 modal% of the nakhlites is mesostasis consisting of varying proportions of clinopyroxene, orthopyroxene, olivine, plagioclase, titanomagnetite, iron sulphides, and glass (Corrigan et al., 2015; Udry & Day, 2018). Important for this study, the nakhlites contain relative low levels of shock [*i.e.*, high strain, maximum bulk shock pressures 5–20 GPa (Fritz, Artemieva, et al., 2005)] that is variable across the different specimens.

Shock features within the group, reported to occur as bands within the samples, appear as reduced refractive index in plagioclase and deformation features (planar fractures, mechanical twinning, and undulose extinction) in olivine and pyroxene (Daly, Lee, et al., 2019; Fritz, Artemieva, et al., 2005). This deformational banding potentially indicates regions within the sample that could represent low strain (*i.e.*, mantle) deformation.

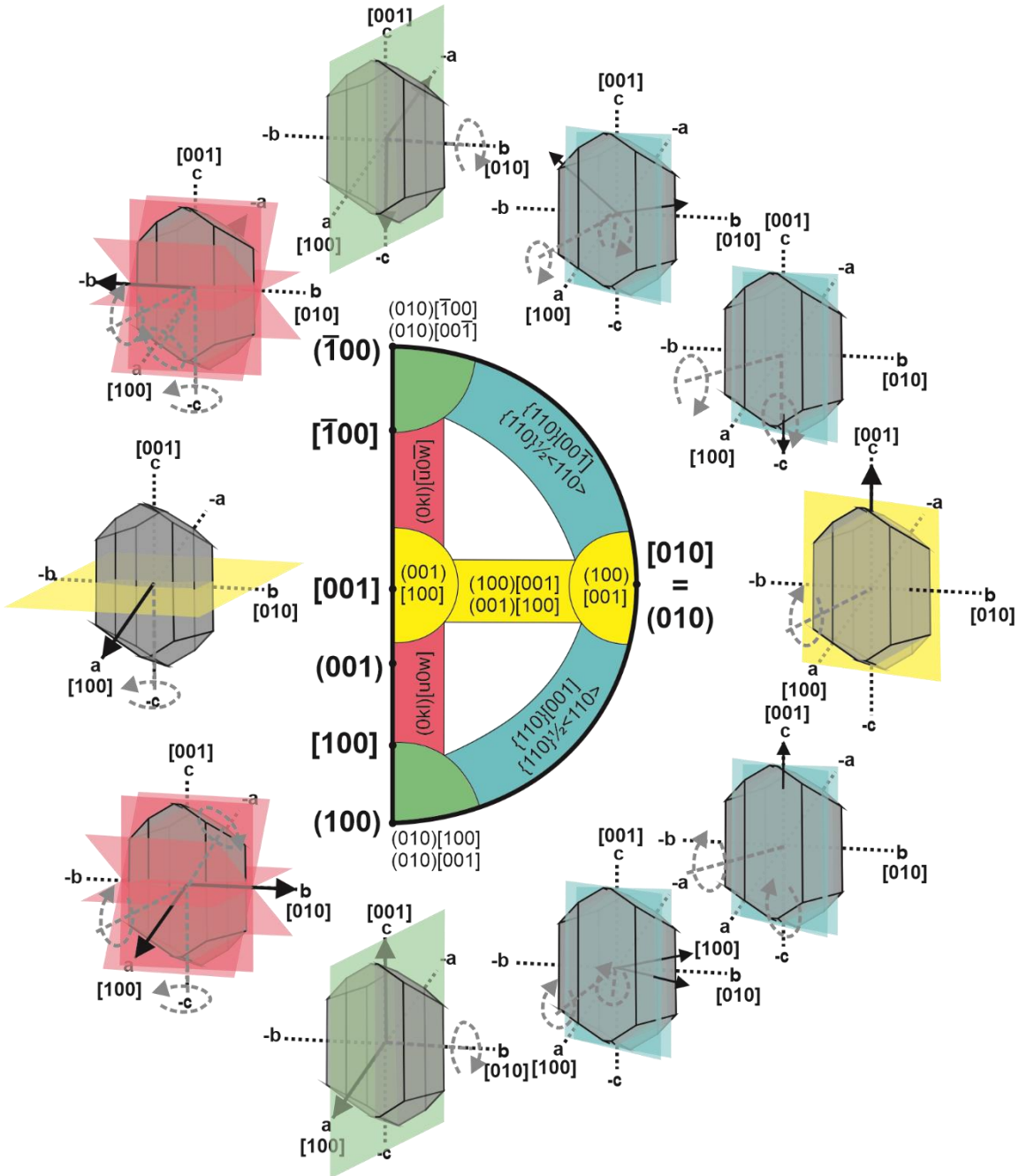

Figure 4.2. *Augite (high Ca-clinopyroxene; 2/m; unit cell lengths a = 1.097, b = 1, c = 0.596) crystallographic slip-system signature key (notated as the slip plane and direction) expressed as the monoclinic crystallographic fundamental sector (lowest form of crystallographic symmetry). The outer bracketed labels of the key refer to augite's specific crystallographic axis (<a> = [100], <b> = [010], and <c> = [001]). The surrounding diagrams visualise the different slip planes where the straight black arrows indicate the direction of slip for both twist and tilt boundaries. For a tilt boundary [movement perpendicular (axis parallel) to the plane] the black arrows also indicate the tilt axis whereas the plane rotation axis for a twist (i.e., rotating) boundary [movement within (axis perpendicular) to the plane] is indicated by the grey dashed arrows.*

Majority of the work on augite and olivine deformation has been focused on understanding mantle (*i.e.*, low strain rate, low stress, high temperature) conditions. The nakhlites are ejected from the Martian near surface by hypervelocity impact (Melosh, 1984). During impact ejection, the nakhlites were shock metamorphosed, which induces high strain rate deformation. This shock deformation although reported to be low in comparison to other Martian meteorites (Fritz, Artemieva, et al., 2005), despite recent EBSD investigations suggesting the nakhlites were exposed to two hypervelocity impact events (Daly, Lee, et al., 2019). These hypervelocity impact events will have influenced and may have overprinted the magmatic deformation signatures within the nakhlites. However, the deformational banding observed suggests that the nakhlites could in fact exhibit deformation signatures related to both emplacement and ejection. This study asks: can crystallographic deformation parameters be used to further the understanding of rocky (planetary) bodies other than Earth, including the Moon, asteroids, and Mars? To tackle this question, olivine and clinopyroxene intra-crystalline misorientation patterns formed from crystal plastic deformation (slip-systems) in the nakhlites are investigated.

4.4 Materials and methods

Twenty-one EBSD datasets were collected for this study, covering sixteen individual nakhlite meteorites: Caleta el Cobre 022, Governador Valadares, Lafayette, Miller range (MIL) 03346, MIL 090030, MIL 090032, MIL 090136, Nakhla, Northwest Africa (NWA) 817, NWA 998, NWA 10153, NWA 11013, NWA 12542, Yamato (Y) 000593, Y 000749, Y 000802 (Table 4.1). The presented EBSD data includes all known 'paired stones' for the Miller Range (MIL) and Yamato (Y) nakhlites. Two sections of five meteorites: Governador Valadares, Nakhla, Northwest Africa (NWA) 998, Y 000593, and Y 000749 were also analysed to assess the influence of experimental parameters as well as result consistency across different sections.

Prior to EBSD analysis each thick section was coated with a ~10 nm thick conductive carbon coat using a sputter coater. Prior to coating each section underwent both mechanical (iterative 1 µm followed by 0.3 µm aluminium spheres suspended in glycol for 5 minutes each) and chemical (4 hours using 0.1 µm colloidal silica suspended in a NaOH solution).

EBSD analyses were run using four different instruments in four different labs: ISAAC imaging centre, University of Glasgow (Zeiss Sigma Field Emission Gun Variable Pressure Scanning Electron Microscope (FEG-VP-SEM) with Oxford Instruments NordlysMax^2 EBSD detector, operating Oxford Instruments AZtec analysis software v3.3); Geochemical Analysis Unit (GAU), Macquarie University (Carl Zeiss IVO SEM using a HKL NordlysNano high Sensitivity EBSD detector); Oxford Instruments Nanoanalysis HQ, High Wycombe (Hitachi SU70 FEGSEM equipped with a Symmetry CMOS detector and indexed using AZtec analysis software v3.4); and the John de Laeter Centre, Curtin University (Tescan MIRA3 VP-FESEM with the NordlysNano EBSD detector and AZtec EDS/EBSD acquisition system). All analyses were run at 20 keV, 4–8 nA beam current, at a 70° tilt, under high vacuum (~3.4 x 10^8 Pa) apart from MIL 03346 (118) and Lafayette (USNM 1505-1), which were run at low vacuum (~49 Pa). Selected step sizes (ranging 0.4–15 µm) for each

sample were chosen to maximise the area covered by the EBSD maps and ensure data collection over available timeframes whilst ensuring the MAD values, indicators of index quality, were <1 (all phases ranging 0.48–0.82; Table 4.1).

Table 4.1. *Nakhlite EBSD analysis settings*

	Caleta el Cobre 022	**Governador Valadares**		**Lafayette**	**MIL 03346**	**MIL 090030**	**MIL 090032**
	CEREGE	BM.1975, M16, P8469	BM.1975, M16, P19783	USNM 1505-5	118	50	108
Area (mm²)	112.83	15.48	21.03	73.56	106.4	79.64	14.69
Pixel Count	16430075	1719852	93456	1659474	6653595	8848637	1631700
Hit Rate (%)	100	55.53	90.98	1659474	59.1	100	69.62
Section analysed	Partial	Whole	Partial	Partial	Partial	Partial	Partial
Step size (µm)	3	3	15	4	4	3	3
Tilt (°)	70	70	70	70	70	70	70
Accelerating voltage (keV)	20	20	20	20	20	20	20
Aperture (µm)	120	120	120	120	120	120	120
Beam Exposure (ms/ EBSP)	24	28	30-40	30-40	30-40	21	26
Beam Current (nA)	21	4.1	8	4.1	4.1	21	4.1
Total (all phases)							
MAD	0.74	0.6	0.48	0.59	0.59	0.76	0.61
Mean BS	42.32	62.35	92.01	62.87	59.1	34.01	64.80
Mean BC	58.11	81.53	119.04	78.31	72.65	61.32	68.88
Augite							
MAD	0.76	0.56	0.48	0.65	0.59	0.8	0.65
Mean BS	43.64	69.44	91.9	56.31	58.53	32.91	62.33
Mean BC	57.42	90.5	118.90	66.54	71.14	58.1	65.15
Forsterite							
MAD	0.67	0.47	0.43	0.52	0.65	0.73	0.58
Mean BS	44.88	87.37	111.57	68.64	54.61	33.9	62.89
Mean BC	65.21	122.53	142.80	88.4	64.31	58.56	64.84
Bin criteria	4 x 4	4 x 4	4 x 4	4 x 4	4 x 4	1 x 1	4 x 4
EDS collected	Yes	Yes	Yes	Yes	Yes	Yes	Yes
Additional EDS map	Yes	No	No	No	No	Yes	Yes
Collected	CU	UofG	MU	UofG	UofG	CU	UofG

EDS = electron dispersive spectroscopy
EBSP = electron backscatter patterns a.k.a. Kikuchi diffraction patterns
MAD = Mean angular deviation
BS = Band slope
BC = Back contrast
CU = Curtin University
MU = Macquarie University
UofG = University of Glasgow
OIN = Oxford Instruments Nano-analysis, High Wycombe

All EBSD datasets were processed using Oxford Instruments HKL Channel 5 software. Crystallographic axes for the forsterite and augite phases were defined as b = 1 > c = 0.587 > a = 0.466 (forsterite) and a = 1.097 > b = 1 > c = 0.596 (augite). To remove erroneous data (i.e., mis-indexed, and non-indexed data points) without generating significant artefacts within the datasets (Bestmann and Prior, 2003; Watt et al., 2006; Forman et al., 2016; Daly et al., 2019a; Forman et al., 2019) the data was first noise reduced using a wildspike correction followed by a consecutive 8–6 point nearest neighbour zero solution reductions. Crystal boundaries were defined as >10° internal

crystallographic misorientation from the nearest-neighbour pixel. Mechanical twins were identified as 180° rotation around augite (100), (204), or (104) axes and 60° rotation around forsterite (011), (012), and (100) axes. Simple twin boundaries were also identified in augite as 180° rotation around augite (001).

Table 4.1. *Continued*

	MIL 090136	**Nakhla**		**NWA 817**	**NWA 998**		**NWA 10153**	**NWA 11013**
	62	WAM 12965	USNM 426-1	N8-1	T1	UG-1	SH65 T-2, 2	UG-1
Area (mm²)	43.17	13.3	209.57	7.6	9.86	36.14	37.01	37.01
Pixel Count	3606066	59450	23285660	47493378	1578314	1784876	12537585	5921530
Hit Rate (%)	28.66	75.29	50.05	42.37	56.4	55.57	59.15	46.36
Section analysed	Partial	Partial	Partial	Partial	Whole	Partial	Partial	Partial
Step size (µm)	3	15	3	0.4	2.5	4.5	3	2.5
Tilt (°)	70	70	70	70	70	70	70	70
Accelerating voltage (keV)	20	20	20	15	20	20	20	20
Aperture (µm)	120	120	120	120	120	120	120	120
Beam Exposure (ms/ EBSP)	24	30-40	28		24	26	25	32
Beam Current (nA)	4.1	8	21	12	4.1	4.1	18	4.1
Total (all phases)								
MAD	0.68	0.78	0.82	0.56	0.69	0.7	0.82	0.69
Mean BS	75.01	93.82	33.96	104.81	50.68	0.08	39.19	52.65
Mean BC	55.39	118.87	53.94	96.77	57.46	0.38	47.71	62.47
Augite								
MAD	0.68	0.78	0.82	0.56	0.71	0.71	0.84	0.69
Mean BS	74.89	93.39	33.76	104.81	50.67	48.54	40.27	51.67
Mean BC	54.96	118.05	53.17	96.77	57.12	55.68	47.86	60.58
Forsterite								
MAD	0.74	0.76	0.83	0.57	0.62	0.6	0.78	0.6
Mean BS	84.76	0.12	34.4	106.54	56.6	56.8	40.04	61.95
Mean BC	74.02	0.49	53.4	98.05	71.25	73.69	49.18	81.24
Bin criteria	4 x 4	4 x 4	4 x 4	4 x 4	4 x 4	4 x 4	4 x 4	4 x 4
EDS collected	Yes	Yes	Yes	Yes	Yes	Yes	Yes	Yes
Additional EDS map	Yes	No	No	No	No	No	No	No
Collected	UofG	MU	CU	OIN	UofG	UofG	CU	UofG

Meteorites, such as the nakhlites presented here, lack any consistent external reference frame. EBSD is a reference-frame based technique thus, assigning a pseudo-external reference frame enables consistent comparison in the analysis across all the datasets. EBSD map principal orientations were arbitrarily defined as Y = top–bottom direction of the map, X = left–right direction of the map, and Z = direction perpendicular to the plane of the map. Grain (*i.e.*, crystal) reference orientation distribution (GROD) angle maps and local misorientation maps were used to identify regions of high deformation and low deformation within each of the nakhlites. Once the identified regions were checked against inverse pole figure (IPF), Euler, and phase maps specific subsets were created. All intra-crystalline misorientation diagrams for both crystal reference frame (mIPF) and sample reference frame (mCPO; see supplementary material) plots (high deformation (H), low deformation (L), and whole section (H+L) datasets) were checked for map stitching artifacts before plotting. All plots were contoured using the settings of a maximum multiple uniform density (MUD,

representing the density of data points) of 5 with 3° clustering and a half width of 15°. Presented are the 2–10° mIPF plots for additional plots see the supplementary materials. Indicative slip-systems present within each dataset were identified from the MUD distribution patterns within the mIPF plots.

Table 4.1. *Continued*

	NWA 12542	**Y 000593**		**Y 000749**		**Y 000802**
	F83-1	106-A	127-A	64-A	72-A	36-A
Area (mm²)	113.65	36.09	23.78	64.56	48.92	35.86
Pixel Count	12627810	4010028	2183888	5928192	5546892	1434422
Hit Rate (%)	76.81	66.71	69.04	48.88	31.68	73.16
Section analysed	Partial	Whole	Partial	Partial	Whole	Partial
Step size (µm)	3	3	3.5	3.5	3	5
Tilt (°)	70	70	70	70	70	70
Accelerating voltage (keV)	20	20	20	20	20	20
Aperture (µm)	120	120	120	120	120	120
Beam Exposure (ms/ EBSP)	25	29	26	26	30	24
Beam Current (nA)	4.1	4.1	4.1	4.1	4.1	4.1
Total (all phases)						
MAD	0.57	0.67	0.55	0.73	0.66	0.66
Mean BS	68.86	51.54	87.91	50.35	68.97	53.4
Mean BC	82.56	62.34	98.45	51.79	78.05	65.8
Augite						
MAD	0.56	0.65	0.54	0.75	0.66	0.69
Mean BS	70.93	54.4	88.99	48.7	68.17	50.43
Mean BC	84.12	67.97	99.3	48.26	76.64	59.57
Forsterite						
MAD	0.49	0.7	0.46	0.64	0.69	0.57
Mean BS	73.62	52.06	104.4	54.87	72.89	58.69
Mean BC	91.23	60.85	122.3	61.92	85.03	77.04
Bin criteria	4 x 4	4 x 4	4 x 4	4 x 4	4 x 4	4 x 4
EDS collected	Yes	Yes	Yes	Yes	Yes	Yes
Additional EDS map	Yes	No	Yes	Yes	No	Yes
Collected	UofG	UofG	UofG	UofG	UofG	UofG

4.5 Results

4.5.1 Nakhlite modal mineralogy

Augite is observed as the dominant phase 29.2 vol% [Y 000749 (72-A)] to 66.0 vol.% [Nakhla (WAM 12965)] in all collected datasets with variable proportions of olivine 0.3 vol.% (MIL 03346 and NWA 11013) to 14.9 vol.% [Y 000593 (127-A); Fig. 4.3]. The mineralogy is observed to be heterogeneously dispersed with pockets of increased mesostasis abundance 10 vol.% [Y 000593 (127-A)] to 60 vol.% (Caleta el Cobre 022) relative to phenocrysts 9 vol.% NWA (817) to 62 vol.% [Y 000593 (127-A); Fig. 4.3].

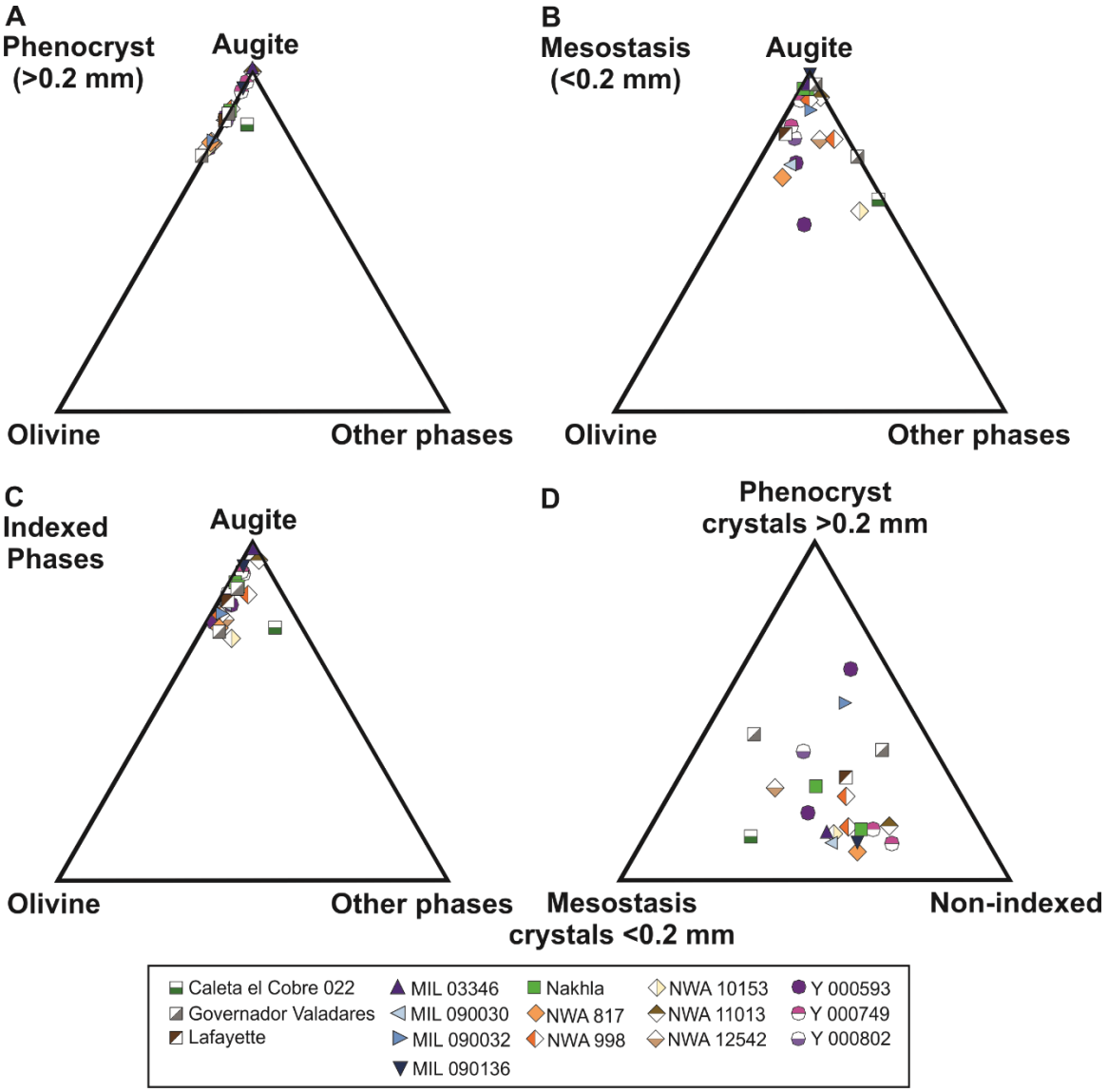

Figure 4.3. *Compositional breakdown of EBSD datasets for analysed nakhlite samples. A) compositional breakdown of indexed phenocrysts (>0.2 mm crystals). A higher proportion of other phases is observed within Caleta el Cobre 022 reflecting the increased abundance of plagioclase within the sample. B) Compositional breakdown of indexed mesostasis (<0.2 mm crystals) C) Compositional breakdown of all indexed phases (phenocrysts and mesostasis). D) Distribution between phenocrysts crystals (>0.2 mm), mesostasis crystals (<0.2 mm), and non-indexed portions (representing the combination of voids, glass, and amorphous phases) of the EBSD maps. For a full breakdown of indexed phases, the reader is referred to the supplementary Table A4.1 and Figure A4.1.*

4.5.2 Identification of nakhlite high and low deformation regions

Assessment of combined augite and olivine major mIPF patterns for all twenty-one analysed nakhlite sections reveal nine distinct groupings (Fig. 4.4). These nine groups are the culmination of both high and low strain deformation within the samples. However, GROD angle maps of the sections show defined regions of high and low deformation (*e.g.*, Fig. 4.5). GROD maps are used to assess bending (*i.e.*, plastic deformation) within a given crystal. Here the average orientation of a crystal is chosen as a fixed reference point and the amount of deviation in orientation is depicted from blue [0 (*i.e.*, same orientation)] through to red [10° deviation (*i.e.*, the determined cut-off for a crystal boundary)]. Thus, within the GROD angle map blue crystals indicate no bending within the crystal [interpreted as low strain (L)] and regions of yellowish-green through to red depict bent

regions within the crystal [interpreted as high strain (H)]. In figure 4.5, and other analysed sections (see supplementary materials), high strain regions are observed to form as bands. These bands are typically located in mesostasis-rich and glass-rich regions, where the associated phenocrysts often exhibit increased density of fractures, and irregular linear features that do not produce diffraction patterns higher, as well as mechanical twins (white bands).

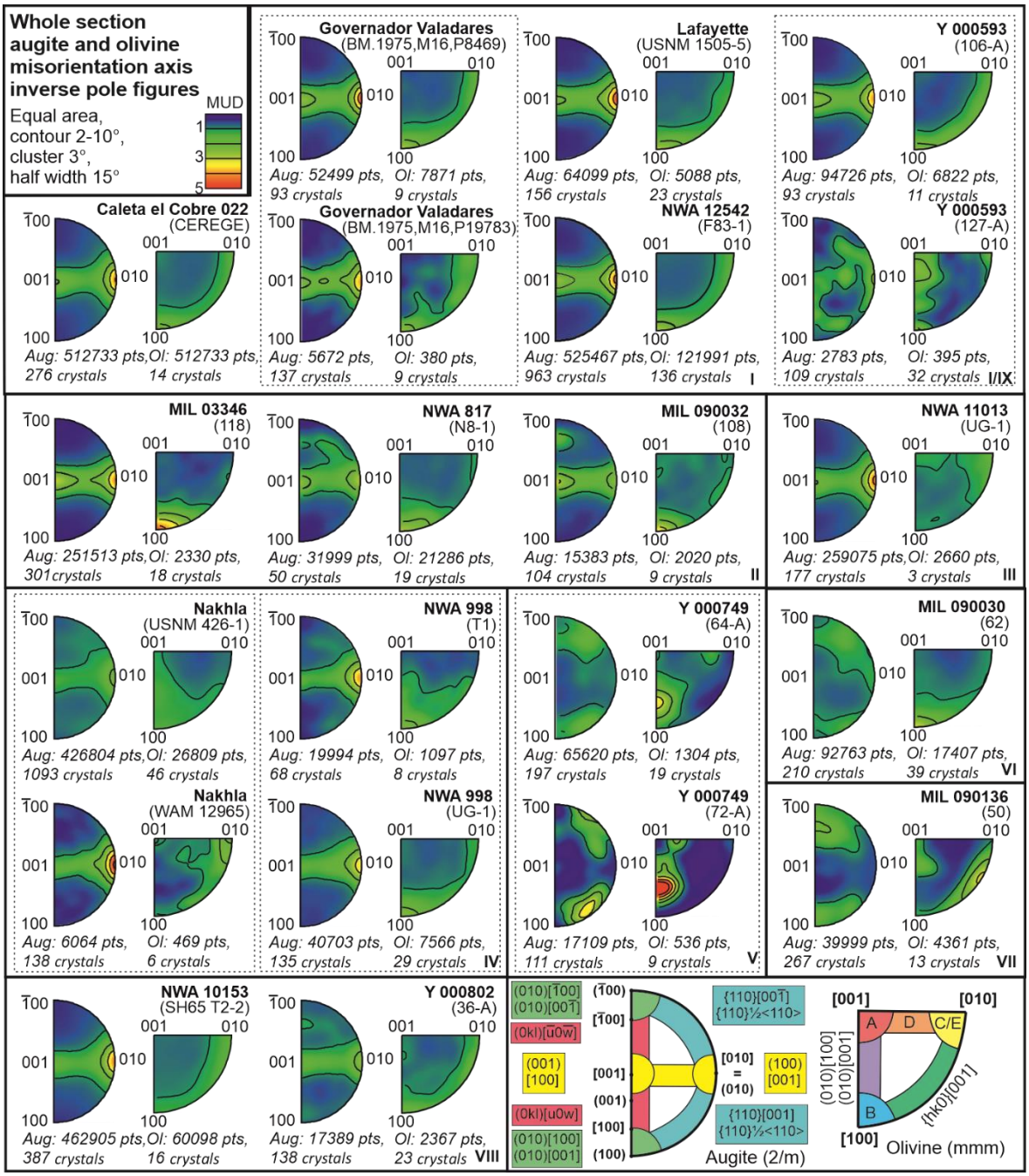

Figure 4.4. *Misorientation axis inverse pole figure plots (mIPF) for nakhlite whole section data. Augite (half-circles) and olivine (quarter circles) represented as their fundamental sectors (lowest form of crystal symmetry) where the misorientation is referenced against the crystal co-ordinate system. We identify 8 (potentially 9) different major slip system combinations for the nakhlites based on their respective keys (bottom right box) where each colour indicates a different type of dominant slip-system. Olivine key: A = (010)[100], B = (010)[001], C = (100)[001], D = {0kl}[100], E = (001)[100].*

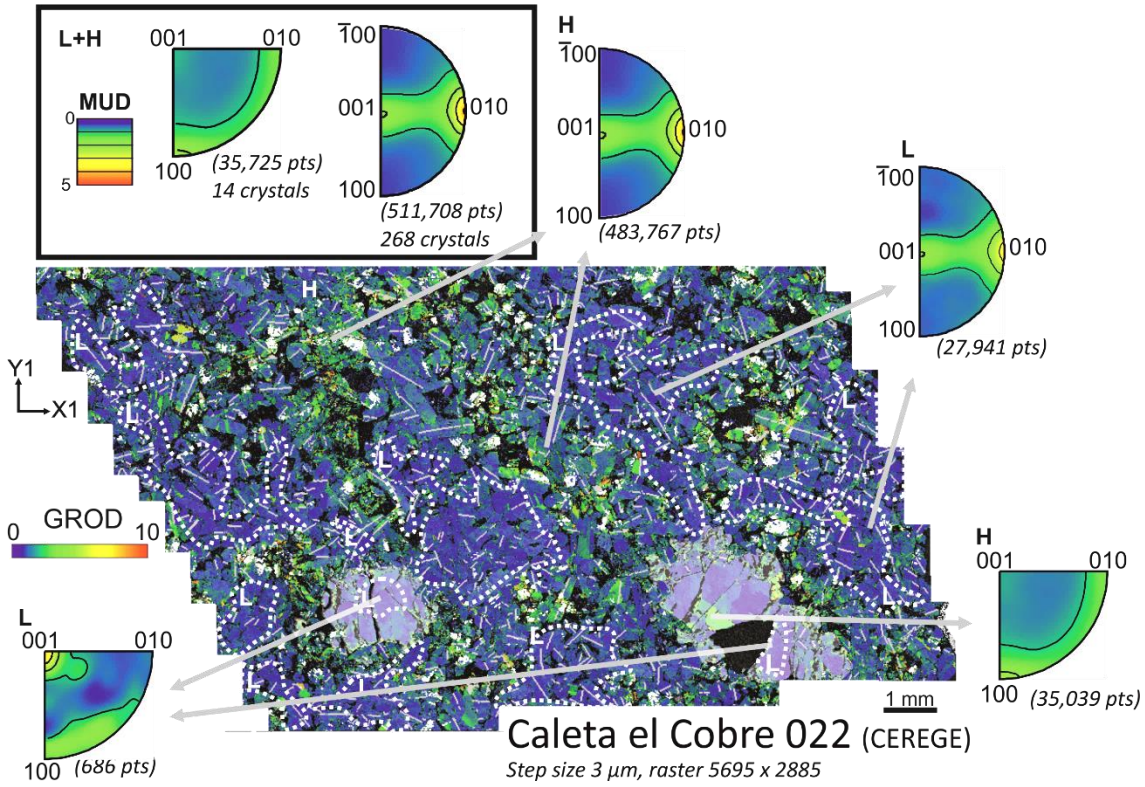

Figure 4.5. *Grain relative orientation (GROD) angle map (0–10°) Caleta el Cobre 022 (group I) with augite and olivine misorientation axis inverse pole figures (mIPF)s for low deformation regions (L), high deformation regions (H), and whole section representative slip-system signatures (L+H). Combined slip-system signature is dominated by high deformation signature. Between L and H mIPF, a shift is observed in olivine signature while augite signatures remain constant. The GROD map depicts the changes in crystallographic orientation within a given crystal between 0–10° relative to the average crystallographic orientation of the crystal. Higher internal misorientations 3–10° angles are observed as green-red regions in each section. These bands of higher internal misorientation align with regions of increased mesostasis abundance. Augite and olivine mechanical twins [white lines; <100> axis in augite (180° rotation) and olivine (60° rotation)], and regions of higher fracture density. Augite simple twins (light grey lines, 180° rotation about <001> axis) an indicator of shock deformation appear throughout both the high and lower misorientation regions. Olivine within the sample is indicated by the white transparent layer. For additional maps the reader is referred to the supplementary materials*

Out of the twenty-one analysed sections, both NWA 10153 and NWA 11013 (Fig. 4.7) exhibit significantly less areas of low deformation (<2° GROD angles). In these sections the distribution of the higher deformation regions is observed to be more ubiquitous throughout the map area (Fig. 4.7). Section Y 000593 (127-A) on the other hand, shows minimal internal deformation relative to the other analysed sections, including its replicate section Y 000593 (106-A). Majority of the analysed crystals within the section exhibit GROD angles <1°, where the highest GROD angle observed is observed at <5° and restricted to smaller fractured crystals.

Within the analysed nakhlites, augite exhibits two types of twins: simple twins (grey lines depicting 180° rotation about the <001> axis in augite) and mechanical twins (white lines representing the rotation of 180° and 60°around the <100> axis in augite and olivine, respectively). The simple twins are observed throughout the various analysed sections appearing in both low and high deformation regions. The mechanical twins, however, only appear in high deformation regions (*e.g.*, Fig 4.5). The mechanical twins appear with noticeable chevron patterns within augite crystals with higher GROD angle values or crystals on the boundary of regions of increased angle

misorientation, particularly within samples Caleta el Cobre 022 (Fig. 4.5), Governador Valadares (BM.1975,M16,P8469), Lafayette, MIL 03346, MIL 090032, NWA 817, NWA 10153, NWA 11013, NWA 12542, and Y 000593 (106-A). The mechanical twins are observed to span either the width of the crystal or where simple twinning is also present (occurring along the <001> axis in augite) the mechanical twins form from the edge of the crystal into the simple twin boundary (light grey lines). Simple twins observed in augite appear throughout the sections appearing in both high and low deformation designated regions (Fig. 4.5).

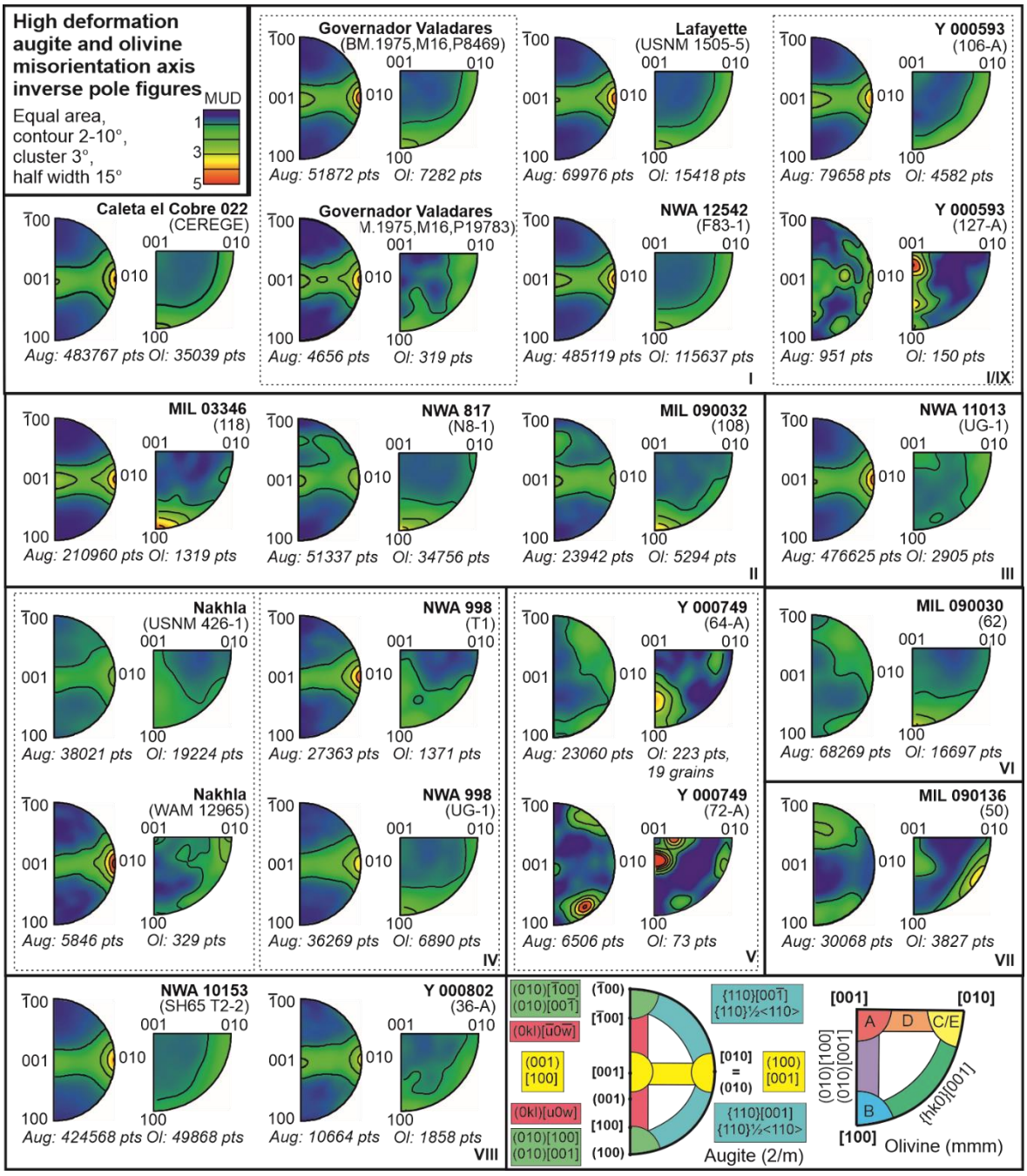

Figure 4.6. *High strain deformation mIPF plots for augite and olivine. Nine different major slip system combinations are identified for the nakhlites that match whole section mIPF patterns. Slip-system patterns are based on the respective keys (bottom right box) where each colour indicates a different type of dominant slip-system. Olivine key: A = (010)[100], B = (010)[001], C = (100)[001], D = {0kl}[100], E = (001)[100].*

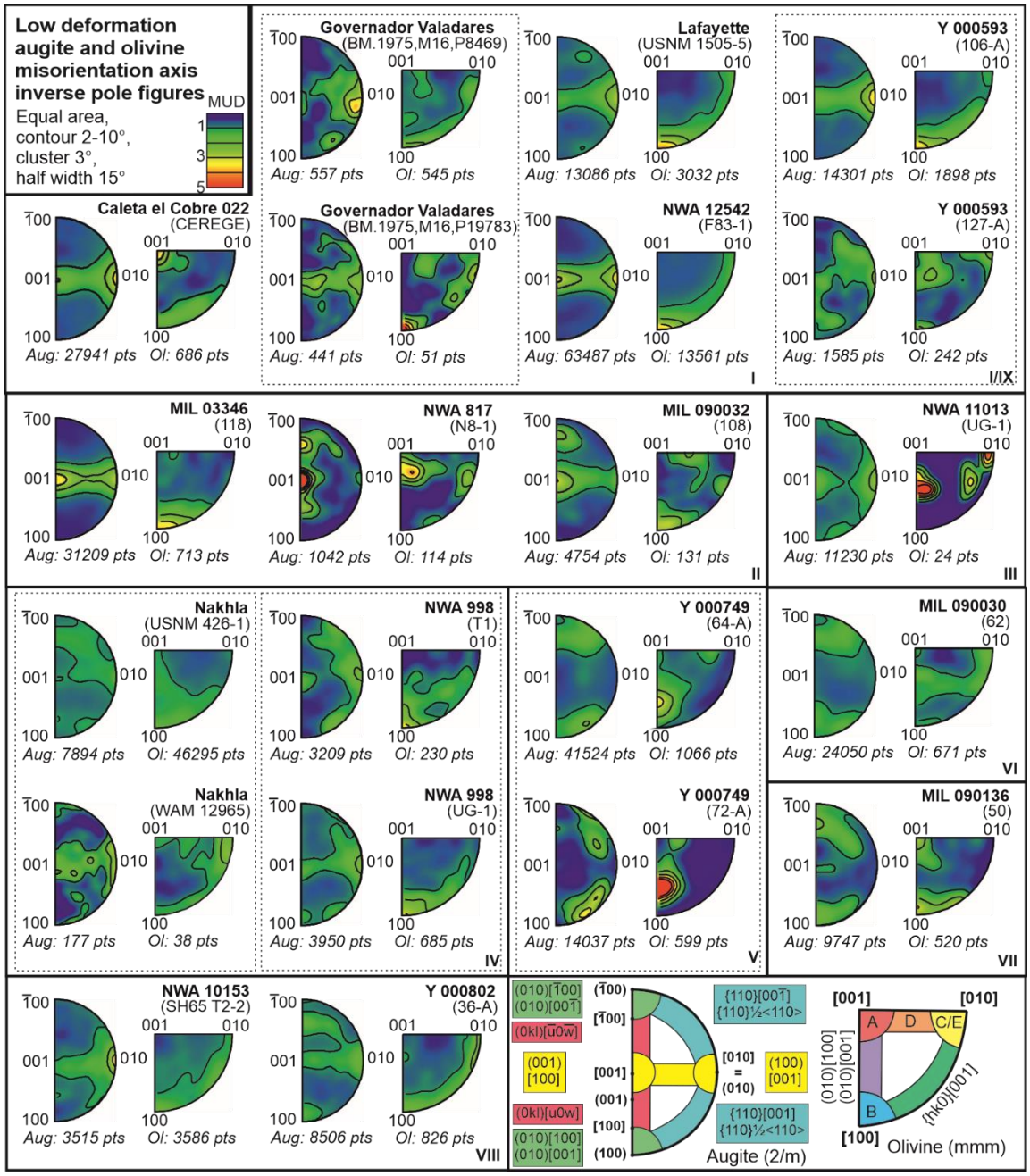

Figure 4.7. *Low strain deformation mIPF plots for augite and olivine. Variation from high strain deformation slip-system patterns is observed for 9 of the 21 analysed sections. Two different low strain mIPF slip-system patterns are observed within group II, while no significant shift in pattern is observed for group V. Slip-system patterns are based on the respective keys (bottom right box) where each colour indicates a different type of dominant slip-system. Olivine key: A = (010)[100], B = (010)[001], C = (100)[001], D = {0kl}[100], E = (001)[100].*

Investigation of augite and olivine mIPF patterns for the depicted H and L regions within each analysed section (*e.g.*, Figs. 4.5), reveal shifts in the observed patterns (Figs. 4.6 and 4.7, Table 4.2). Overall, the dominant mIPF patterns identified in the H regions match those of the overall section mIPF patterns (Figs 4.4 and 4.6, Table 4.2) depicting nine different groups. However, changes in the pattern intensity and secondary mIPF patterns are observed (*e.g.*, Fig. 4.5). Within olivine (forsterite) mIPF plots (010)[001] combined with {hk0}(001) is observed as the most common mIPF pattern for nakhlite olivine [Group I (5 meteorites): Caleta el Cobre 022, Governador Valadares, Lafayette, NWA 12542, and Y 000593 (Fig. 4.4)]. Note that due to the low modal abundance of olivine within the samples overall (0.3–14.9 vol.%; Fig. 4.3) the number of crystals contributing to the observed mIPF patterns are far below those recommended for statistically relevant and whole-rock representative results (5–84 crystals, *i.e.*, <300 crystals; Watt

et al., 2006). Thus, the mIPF olivine plots presented below are included as a check for observed augite mIPF patters but should not be considered representative on their own. Overall, five unique olivine mIPF patterns [{hk0}, (010)[001], (010)[100]+(010)[001], (001)[100]/(100)[001], (010)[001]+{hk0}] are observed across the analysed samples where the overriding mIPF pattern becomes clearly defined from the minor mIPF patterns with increased crystal count (Fig. 4.6).

Table 4.2. *Nakhlite augite and olivine slip-system patterns for high and low deformation regions.*

	Nakhlite	section	high deformation region slip-system		Low deformation region slip-system*
I	Caleta el Cobre 022* Governador Valadares Lafayette NWA 12542 Y 000593	*CEREGE* *BM1975,M16,P8469* *BM1975, M16,P19783* *USNM 1505-5* *F83-1* *106-A*	Forsterite (010)[001]+{hk0}[001] Augite (100)[001]>(001)[100]	I	Forsterite (010)[100]+{hk0}[001] Augite (100)[001]>(001)[100]
II	MIL 03346* MIL 090032 NWA 817*'	*118* *108* N8-1	Forsterite (010)[001] Augite (100)[001]+(001)[100]	II	Forsterite* (010)[001] Augite (100)[001]<(001)[100]
				II'	Forsterite*' (010)[100]+{hk0}[001] Augite (001)[100]+(0kl)<u0w>
III	NWA 11013*	*UG-1*	Forsterite (100)[001] Augite (100)[001]>>(001)[100]	III	Forsterite (010)[u0w]+(100)[001]+(001)[100] Augite (100)[001]>(001)[100]+ {110}[001]+{110}1/2<110>
IV	Nakhla* NWA 998	*USNM 426-1* *WAM 12965* T1 UG-1	Forsterite (010)[001]+{hk0}[001] Augite (100)[001]>>(001)[100]	IV	Forsterite (010)[001]+{hk0}[001] Augite {110}[001]+ {110}$^{1}/_{2}$<110>+(100)[001]
V	Y 000749	*64-A* *72-A*	Forsterite (010)[100]+(010)[001] Augite {110}[001]+{110}$^{1}/_{2}$<110>	V	
VI	MIL 090030*	*62*	Forsterite (010)[001] Augite {110}[001]+{110}$^{1}/_{2}$<110>	VI	Forsterite (010)[u0w]+{hk0}[001] Augite {110}[001]+{110}$^{1}/_{2}$<110>
VII	MIL 090136*	*50*	Forsterite {hk0}[001] Augite {010}<100>+{010}<001>	VII	Forsterite (010)[001]+(010)[u0w] Augite {010}<100>+{010}<001>
VIII	NWA 10153 Y 000802*	SH65 T-2, 2 *36-A*	Forsterite (001)[100] Augite (100)[001]>>(001)[100]	VIII	Forsterite (100)[001]+{hk0}[001] Augite (100)[001]+(001)[100]+(0kl)<u0w>
IX	Y 000593*	*127-A*	Forsterite (010)[001]+(001)[100]+{0kl}[u0w] Augite (100)[001]+(0kl)[u0w]	IX	Forsterite (010)[001]+(001)[100]+{0kl}[u0w] Augite (100)[001]+(0kl)[u0w]

N.B. Whole section slip system data exhibits the same slip-system patterns as those reported for the high deformation regions above.
** and *' indicate samples for which either augite, olivine or both augite and olivine slip-system patterns have changed between regions.*

For augite, 4 out of the 21 EBSD can be considered statistically relevant (>300 phenocryst crystals; (Griffin et al., 2021). Four datasets contained <100 crystals [Governador Valadares (BM1975,M16,P8469), MIL 090032 (62), NWA 817 (N8-1), NWA 998 (T1), and Y 000593 (106-

A); Figs. 4.3–4.5]. For augite four distinct mIPF patterns are identified with the two most commonly observed mIPF patterns involving the paring of (100)[001] and (001)[100] dislocations expressed at varying proportions (groups I–III, VIII; Fig. 4.6). Within Figure 4.6, groups I and II exhibit a higher proportion of (001)[100] dislocations compared to groups III and VIII (*e.g.*, Fig. 4.5). Augite {110}[001] + {110}½<110> mIPF patterns are also observed in groups V and VI, (010)[100]+(010)[001] in group VII, and a combination of multiple mIPF patterns, including components of (100)[001], (001)[100], {0kl}<u0w>, {110}[001] + {110}½<110>, within Y 000593 (section 127-A; Fig. 4.6).

When assessing the identified L regions mIPF dominant mIPF patterns were observed to shift but only for certain analysed sections [*i.e.*, sections relating to nakhlites Caleta el Cobre 022 (Fig. 4.5), NWA 817, NWA 11013, Nakhla, MIL 090030, MIL 090136, Y 000802, and Y 000593 (both sections)].Out of the nine identified high deformation region groups, excepting group V, at least one analysed section exhibited different low deformation region mIPF patterns (Table 4.2, Figs. 4.6 and 4.7). For the sections that showed different mIPF patterns between the H and L regions, pattern shifts were often only observed to occur in either olivine or augite, where olivine is the more likely mineral to exhibit a shift (Fig, 4.7, Table 4.2). However, additional shifts in mIPF patterns and intensity can also be observed as additional mIPF patterns within the L regions even when the major mIPF pattern remains the same (Fig. 4.7). All L region mIPF patterns appear unique to the individual meteorite. More importantly, different low deformation mIPF patterns are observed to occur within group II (Table 4.2, Fig. 4.7), where meteorites MIL 03346 and NWA 817 exhibit the same H region mIPF pattern but distinct L region mIPF patterns (Figs. 4.6 and 4.7, Table 4.2). This indicates that the cause of the H region patterns is most likely independent of the L region mIPF patterns

To assess consistency in the presented analysis, replicate sections were run for five of the sixteen analysed nakhlites. In these replicate sections, the same major augite and olivine mIPF patterns (both H and L region) are expressed for the meteorites Governador Valadares, NWA 998, and Y 000749. However, discrepancies in olivine mIPF patterns are observed between the two Nakhla sections {USNM 426-1 exhibiting (010)[001] H region patterns and WAM 12965 exhibiting (001)[100]/(100)[001] H region patterns} as well as differences in both augite and olivine mIPF patterns between the two Y 000593 sections {106-A exhibiting dominant (100)[001] with minor (001)[100] for augite and (010)[001] with {hk0}[001] for olivine and section 127-A exhibiting multiple dislocations in augite and (010)[100]+(010)[001] for olivine}. Furthermore, low amounts of intra-crystalline misorientation are observed within the GROD angle map. 120° triple junctions (typical annealing micro-structures) are also observed within Y 000593 (127-A)'s clustered olivine which were not identified within Y 000593 (106-A). The observed variability of mIPF patterns within Nakhla and Y 000593 meteorites have direct implications for methodological parameters *e.g.*, step-size and number of assessed crystals, sample heterogeneity, *etc.* which will be further evaluated in the discussion.

4.6 Discussion

4.6.1 Electron backscatter diffraction mapping (EBSD) appropriate step-size for intra-crystalline misorientation pattern determination

Compiling large stitched maps using EBSD is becoming a more common tool for observing CPO within samples. The ability to analyse whole thin/thick sections however, is still a time-consuming and data intensive process - and is not without associated error (*e.g.*, mis-indexing, improper-indexing, beam drift *etc.*) even with recent technological advancements (Winiarski et al., 2021). The ability to cover larger areas is often counteracted by using larger step sizes, where the limiting factor for step size is controlled by the size of the crystal (to ensure >10 pixels/EBSD measurements are acquired per crystallite to adequately define its orientations), sacrificing higher spatial resolution (≤4 μm step size) required for intra-crystalline micro-structural analysis (Ruggles & Fullwood, 2013). Whilst micro-structurally focused EBSD studies that utilise a smaller step size ≤4 μm will often observe either multiple single crystals from specific regions of a section or a selection of small areas where the total crystal count is below statistically stable results (Skemer et al., 2005; Vollmer, 1990). Within the nakhlite datasets, five sections with a step size >4 μm (ranging from 4.5–15 μm) were run (Table 4.1), where three of these sections had a replicate section which was run at a step size <4 μm (Table 4.1). Replicate sections for two samples were also run at higher spatial resolution (*i.e.*, step size <4 μm). Comparison of results from these different step sized replicate sections, show clearer dominant mIPF patterns are able to be discerned from ≤4 μm particularly with smaller area maps. However, data presented here suggests that confirmation of similar mIPF patterns across multiple sections could be achieved using larger step sizes >4 μm on the condition that at least one of the sections is run at ≤4 μm.

4.6.1.1 Analytical limitations and essential criteria for slip-system determination in EBSD datasets

Comparing results between replicate datasets, little difference is observed in the GROD angle distribution patterns between each section. However, the lower spatial resolution in some of the datasets makes it more difficult to accurately assess the variability in GROD angle across a given crystal *i.e.*, larger GROD angles are observed where most of the crystal is at a single value. The lower spatial resolution of specific datasets also makes it difficult to ascertain the presence and interaction between a given crystal and any mechanical twinning present (Fig. 4.5). Comparing mIPF plots for the replicate sections, the number of crystals analysed is observed to have a greater impact on the determination, refinement, and identification of the samples dominant mIPF pattern over the specific step size of the analysis (Figs. 4.4, 4.6, and 4.7), with the caveat that the chosen step size is appropriate for the identification of intra-crystalline misorientations *i.e.*, ≤4 μm. Note that this observation is only relevant when assessing the overriding major dislocation slip-system expressed within a section. To investigate micro-structural changes between different regions throughout the sample, inspect secondary mIPF patterns, or investigate how sub-crystal boundary interactions in

combination with crystal orientation contribute to the overall observed deformation then step sizes ≤4 μm are required.

4.6.1.2 Can EBSD derived intra-crystalline misorientations be whole rock representative?

Analysis of the replicate sections revealed consistent augite and olivine mIPF patterns for whole section, high deformation and low deformation datasets within Governador Valadares, NWA 998, and Y 000749 (Figs. 4.6 and 4.7, Table 4.2). However, the same correlation is not observed within the replicate Nakhla or Y 000593 sections (Figs. 4.6 and 4.7, Table 4.2). For the two Nakhla replicate sections there is consistency in the mIPF patterns of augite for all three datasets (whole section high deformation, and low deformation) and a discrepancy in expression of mIPF patterns in olivine where the of mIPF patterns expressed are consistent but the dominant expressed mIPF pattern is different for whole section and high deformation datasets. The difference in expressed olivine mIPF patterns could be a function of the crystal differential (40 crystals, 26,340 datapoints) between the two datasets, the modal distribution of crystals between the sections, the larger (15 μm) step size of section WAM 12965 compared to USNM 426-1 (3 μm; Table 4.1), or the heterogeneous influence and distribution of shock between the two sections in relation to olivine's location. More consistent MUD patterns are observed for augite within section USNM 426-1 (MUD = 0.53–1.37) compared to section WAM 12965 (MUD = 0.35–2.48) despite only USNM 426-1 containing CPO statistically relevant crystal numbers. A similar fluctuation in MUD values is also observed between the two replicate Governador Valadares sections. In this instance, consistent mIPF patterns are observed for all three datasets. In this instance each of the EBSD datasets sample equivalent areas olivine (9 crystals each) and augite crystals (93 vs. 137 crystals; Fig. 4.4, Table 4.2). The only difference being a similar analysis step size discrepancy between the two Governador Valadares replicate sections as Nakhla (Table 4.1). This difference indicates the importance of comparable sized datasets for meaningful comparison between replicate sections. For both NWA 998 replicate sections which have a 0.5 μm step size differential and Y 000749 replicate sections which have the same analysis step size, no fluctuations are observed in the dominant augite and olivine mIPF patterns. Across the nakhlite datasets at <4 μm step size were observed to have cleaner MUD distribution patterns and narrower MUD ranges [*e.g.*, Governador Valadares MUD = 0.35–4.55 vs 0.25–3.56 (mIPF) and MUD = 0.55–2.72 vs. 0.35–2.68 (olivine mIPF) for sections BM.1975,M16,P8469 and BM.1975,M16,P19783, respectively; Fig. 4.4, 4.6 and 4.7, Table 4.1]. Where decreased crystal count and larger step sizes contribute to increased MUD distributions within the mIPF plots [*e.g.*, Nakhla MUD = 0.63–2.30 vs 0.27–5.26 (augite mIPF) and 0.53–1.37 vs. 0.34–2.48 (olivine mIPF) for sections USNM 426-1 and WAM 12965, respectively; Figs. 4.4, 4.6, and 4.7; Table 4.2]. Suggesting that differences observed within Nakhla's replicate section olivine mIPF patterns is most likely to be the result of both analysis step size and analysis area.

Out of all the replicate sections, only Y 000593 exhibited completely different augite mIPF slip-system patterns between sections; (100)[001]:(001)[100] for section 106-A and multiple mIPF

patterns for section 127-A. Olivine mIPF patterns are also non-congruent (010)[001] with {hk0}[001] for section 106-A and (010)[100]+(010)[001] for section 127-A. In low strain mantle systems these mIPF patterns would indicate low temperature moderate strain conditions for section 106-A and high temperature low strain condition for section 127-A (Figs 4.4, 4.6. and 4.7). Multiple slip-systems as suggested by Y 000593 (127-A) augite mIPF patterns have been associated with partial melting and recrystallisation conditions (Fig. 4.7; Ave Lallemant, 1978). which would be consistent with observed olivine annealing micro-structures [120° triple junctions in clustered olivine within Y 000593 (127-A); Fig 4.12] and lower dispersed deformation (GROD angle values). For section 106-A clear banding of high deformation can be observed within the GROD angle map, where mIPF patterns even within the low deformation regions still express high deformation region signatures (Table 4.2). Deformation, particularly that associated with shock metamorphism, is known to be heterogeneous (Stöffler et al., 2018). Variability in temperature and pressure resulting from hypervelocity impacts can create pockets within a sample that may have experienced higher temperature and/or pressure conditions. Furthermore, recrystallisation has been shown to overprint a given crystal's deformation history to its new recrystallised conditions (Muto et al., 2011; Wenk & Tomé, 1999; Yao et al., 2019). Annealing on the other hand has been shown to significantly reduce, overprint, and sometimes completely override a given crystal's former deformation history to the current conditions acting on the sample during the annealing process (Farla et al., 2011; H. Jung et al., 2006). Investigations of shock deformation within the Yamato nakhlites has shown some of the lowest bulk shock pressures (5–14 GPa for Y 000593) within the already low shocked nakhlites (Fritz, Artemieva, et al., 2005). However, the presence of annealing within the sample could have contributed to the lower inferred shock pressure values. Thus, the differences in mIPF patterns observed between the two Y 000593 sections could therefore indicate either an extreme change in emplacement environment, which would have had to occur within the cm scale of the meteorite stone (Imae et al., 2005), shock banding within the meteorite, or could indicate that the two sections represent two distinct neighbouring geological units present within the same meteorite stone.

4.6.1.3 EBSD derived slip-systems for extrinsic parameter determination

Studies on assessing intra-crystalline misorientation at a statistically relevant scale are still in their infancy. This is predominantly due to the specific cost, time, and equipment constraints (*e.g.*, beam stability, indexing time, computer processing ability, post processing time *etc.*) required to run ≤4 μm step size EBSD experiments. Comparison between collected EBSD datasets show that to use crystallographic slip-systems inferred from intra-crystalline misorientations to assess extrinsic parameters within a given sample, higher spatial resolution (step sizes ≤4 μm) EBSD is required to ensure reasonable and rational results (Figs. 4.4, 4.6, and 4.7). Rocks in general are not homogeneous, while rocks that have experienced shock metamorphism (which in the case of MIL 03346, Lafayette, and most likely the entire nakhlite suite occurred on at least two occasions; Daly et al., 2019) exhibit even higher levels of microstructural and mineralogical heterogeneity (*e.g.*, Figs. 4.5–4.13), through increased fracturing, partial melting, and partial recrystallisation (Stöffler et al., 2018). Experimental

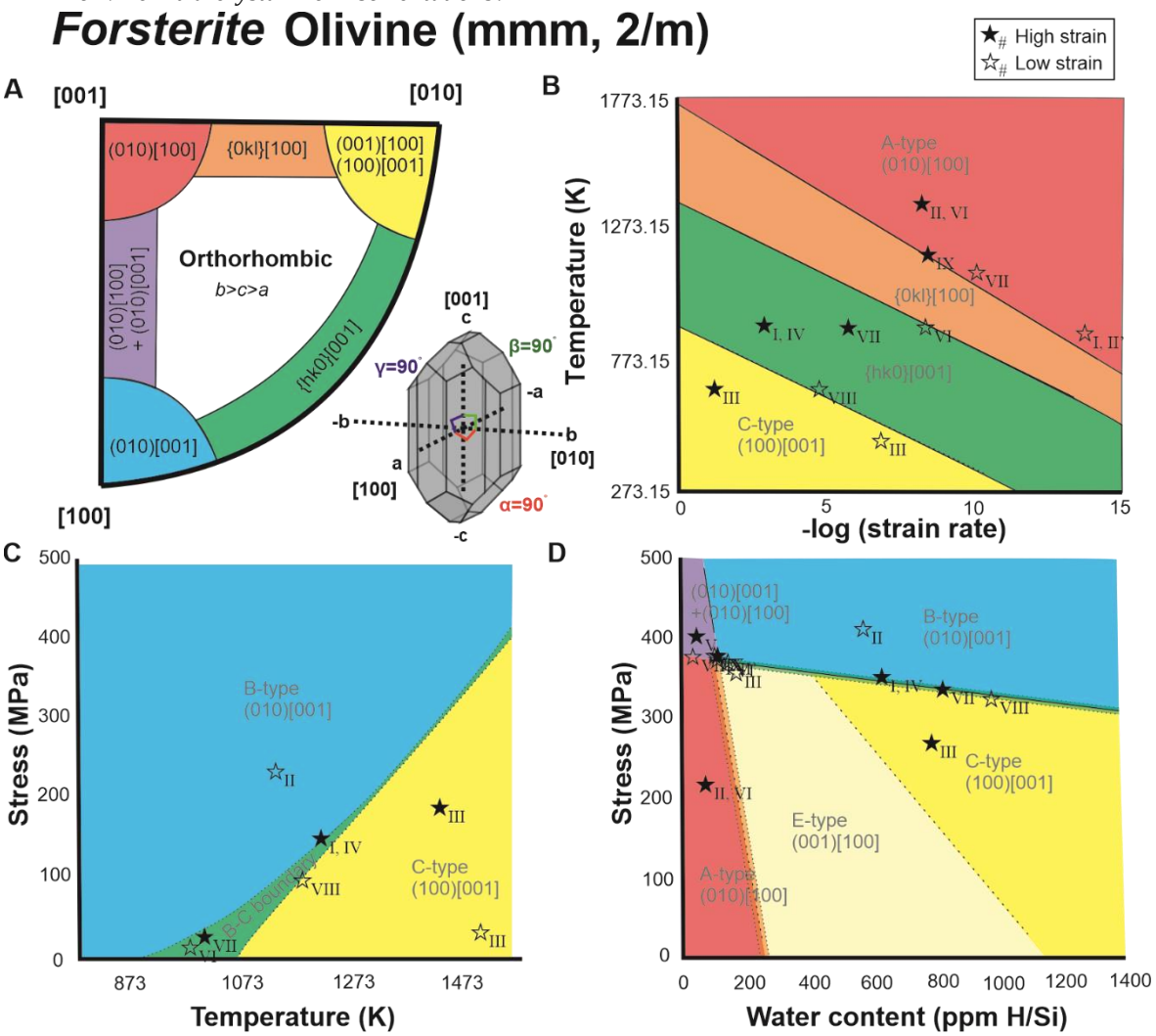

Figure 4.7. *Known olivine (forsterite) slip-system deformation regions key (unit cells b>c>a). Colours indicate different slip-system regions. A) orthorhombic fundamental region slip-system key modified from (Ruzicka & Hugo, 2018) with a sketch of an olivine crystal illustrating its orthorhombic symmetry. B) Temperature vs. strain rate modified from (Katayama et al., 2004). C) Stress vs. Temperature modified from (Karato et al., 2008). D) Stress vs water content modified from (Karato et al., 2008). Note extrinsic parameters are based off low strain data. Note the placement of the identified nakhlite groupings (stars; Table 4.2) is only an indication of the related region and not absolute values.*

data has shown that a crystal's orientation relative to external deformation parameters is one of many important factors for the selection and activation of particular slip-systems (Bascou, Tommasi, et al., 2002; Bernard et al., 2019; Kollé & Blacic, 1982; Müller et al., 2008). Therefore, a relationship between CPO formation and slip-system activation would be expected even if it is not direct (Bascou, Tommansi, et al., 2002; Karato et al., 2008; Katayama et al., 2005; Müller et al., 2008; Nagaya et al., 2014). The presence of CPO within a sample for post emplacement deformation, such as shock metamorphism, should therefore help contribute to the development of a dominant slip-system being activated within a given sample through increasing the number of crystals oriented in a similar geometry with respect to the external strain field (Müller et al., 2008; Satsukawa & Michibayashi, 2009). Rocks, such as the nakhlites and other types of meteorites, which lack majority of the geological context used for terrestrial crystallographic deformation studies, such as sample orientation, require these larger datasets to begin to enable valid interpretations to be made from the data. We would even go so far as to insist that for samples such as meteorites slip-systems from

multiple phases should be considered (where possible) to help counteract the lack of geological context and often the smaller amount of available sample for analysis before crystallographic slip-systems are used to infer extrinsic deformation parameters for a sample as opposed to a singular crystal.

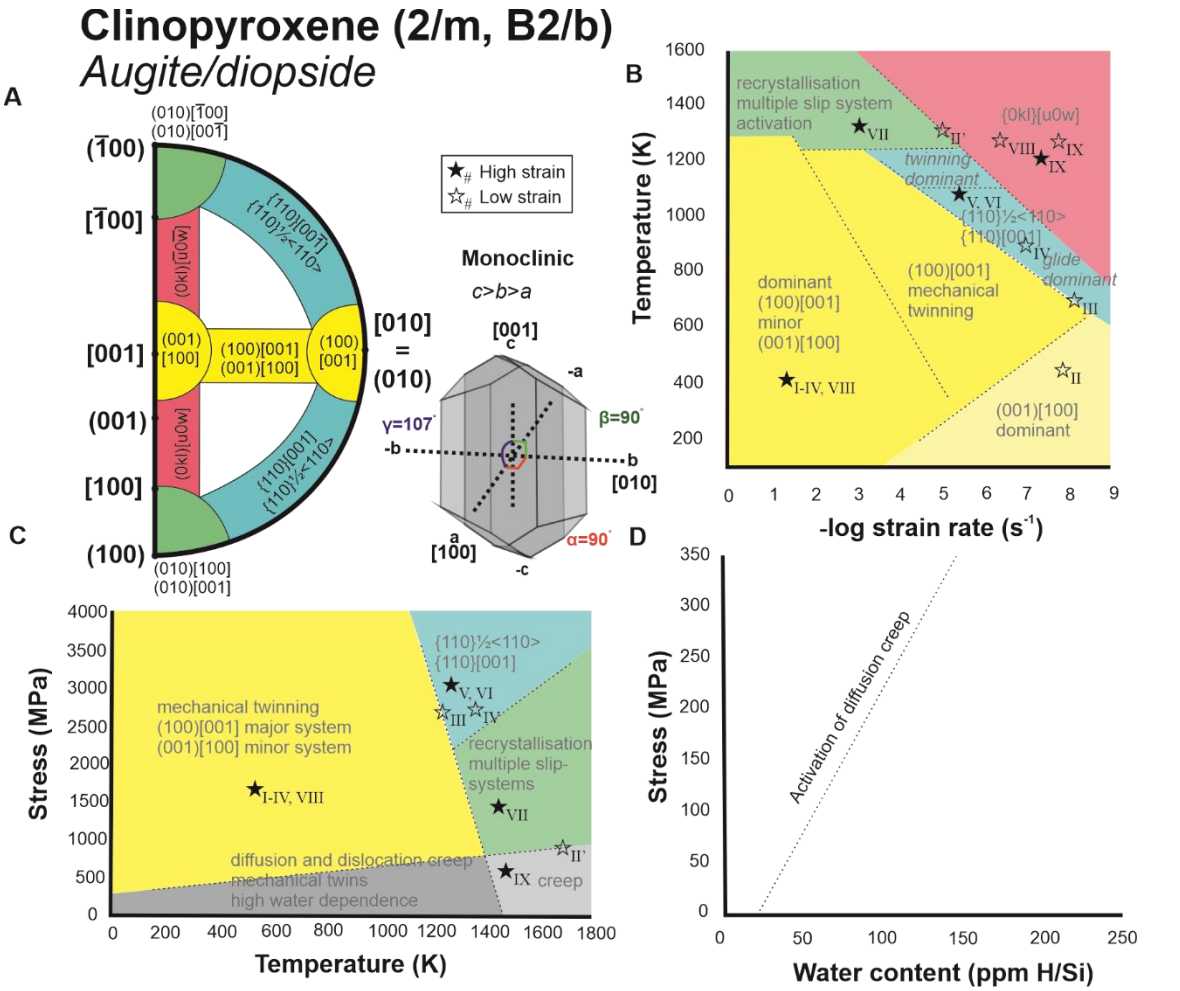

***Figure 4.8**. Proposed deformation conditions for clinopyroxene (augite/diopside) slip-systems key (unit cell c>b>a) based on experimental data. Colours indicate different slip-system regions. A) monoclinic fundamental region slip-system key for unit cell c>b>a with a sketch of an augite crystal illustrating its monoclinic symmetry. B) Temperature vs. strain rate (Avé Lallemant, 1978; Kollé & Blacic, 1982; Raleigh, 1967). C) Stress vs. Temperature (Avé Lallemant, 1978; Bystricky & Mackwell, 2001; Jaoul & Raterron, 1994; Kollé & Blacic, 1982; Müller et al., 2008; Zhang et al., 2006; Zhang & Green, 2007). D) Stress vs water content (Hier-Majumder et al., 2005). Due to the paucity of experimental data involving augite deformation in the presence of water, currently we can only state that there is a trend of lower extrinsic parameters required to induce the activation of specific slip-system signatures in augite with increased water content. Note extrinsic parameters are derived from low strain data. Note the placement of the identified nakhlite groupings (stars; Table 4.2) is only an indication of the related region and not absolute values.*

4.6.2 The correlation between slip-system signature and deformation conditions

In order to compare observed slip-systems in both olivine and augite (Figs. 4.14 and 4.15, Table 4.2) to deformation parameters, existing olivine diagrams (Fig. 4.16) have been modified and equivalent diagrams created for clinopyroxene (Fig. 4.17) using data from the literature. Note that the current extrinsic parameters presented in Figures 4.16 and 4.17 are based on low strain (*i.e.*, mantle induced) observations and experiments not naturally occurring specimens exposed to high

strain rates such as the nakhlites. Studies assessing mantle olivine have shown that extrinsic parameters for slip-systems can be much lower in value for natural occurring samples compared to laboratory studies (Bernard et al., 2019) and references therein. It is therefore possible that the exact extrinsic parameters (axis values) stated for mantle augite and olivine in Figures 4.16 and 4.17 will be subject to change and may not be directly comparable to the presented data However, the positioning of each slip-system signature relative to one other will remain constant enabling the use of both Figure 4.16 and 4.17 in a more qualitative manner.

Comparison of slip-system signatures in laboratory studies for both clinopyroxene and olivine has shown that although there are preferred slip-systems activated along crystallographic planes under specific certain conditions within a given mineral (Avé Lallemant, 1978; Bystricky & Mackwell, 2001; Gueguen & Nicolas, 1980; Ingrin et al., 1991; Jaoul & Raterron, 1994; Kollé & Blacic, 1982; Zhang et al., 2006), a given slip plane is not necessarily tied to any specific set of universal extrinsic parameters. These identified extrinsic parameters are also not specifically transferrable to different minerals, even those that share the same crystal symmetry due to the contribution of intrinsic parameters. Thus, even if naturally occurring sample data were available to construct Figure 4.17 there would still be overlap in slip-system regions between Figures 4.16 and 4.17, where CPO has been activated in one mineral and not another. These regions of slip-system overlap could potentially lend towards the use of multiple mineral slip-systems to better refine deformation parameters, if the extrinsic parameter values were properly quantified for the sample (unlike the nakhlites presented here). Note that for Figure 4.17 there is currently not enough existing data regarding the effect of water content on clinopyroxene slip-system signatures to realistically discuss this intrinsic parameter for the here presented nakhlites. Thus, the presented results will only be discussed in terms of the external parameters: temperature and strain.

Variation between identified high and low deformation regions within the nakhlites identified from GROD angle maps suggest localisation of deformation within the nakhlites (*e.g.*, Fig. 4.5). The identification and localisation of mechanical twinning within identified high deformation regions suggest that the high deformation bands are related to shock deformation. This interpretation is in line with observed mIPF slip-system patterns (discussed below) and previous analysis of the nakhlites where shock levels were calculated to range between 5-20 GPa (Fritz, Artemieva, et al., 2005).

4.6.2.1 Impact deformation regime from mIPF slip-system patterns

Similarities between whole section and high deformation region compared to low deformation region mIPF slip-system patterns suggest that the localised high deformation regions are more prevalent in the nakhlites than the low deformation region deformation source. Out of the nine identified groups five express slip-system patterns more related to low temperatures and high strain, while the other three (Groups V–VII, and IX) appear to be more dominated by higher temperature deformation Figs 4.14, 4.16, and 4.17).

Within the mineral olivine the direction of slip along the {010} lattice plane tends to respond the most significantly to temperature, whilst slip associated with either the {100} or {001} lattice plane appear to respond more readily to changes in strain (Fig. 4.16). For the nakhlites three of the six most commonly observed slip-system patterns are associated with strain. Comparison between whole section, high deformation, and low deformation region results show that these specific slip-systems, the most significant being {hk0}[001], is observed to increase in intensity in the high deformation regions (Figs. 4.4, 4.14, and 4.15; Table 4.2).

Augite within the nakhlites is observed to deform preferentially in the direction of <001> and <010> (Fig. 4.2). These preferences result in the commonly observed (100)[001]:(001)[100] slip-system patterns (Fig. 4.2) identified at most Earth relevant temperature, pressure, stress, and strain conditions (Fig. 4.17). This preferential occurrence in (100)[001]:(001)[100] slip-system mIPF pattern matches observed crystallographic preferred orientation (CPO) patterns from naturally occurring samples, where high levels of compression for <010> and perpendicular alignment to the principal strain axis for <001> is observed (Frets et al., 2012; Mauler et al., 2000). Experimental studies have shown the amount of (001)[100] slip present in a given sample is observed to increase in response to greater amounts of strain at low temperatures (Fig. 4.17). Between whole and high section mIPF results a slight increase in (001)[100] is observed within some of the samples (*e.g.*, Fig. 4.12). Both groups I and II, encompassing eight of the 16 analysed stones, exhibit mIPF patterns that relate increased proportions of (001)[100] slip within the (100)[001] : (001)[100] pairing (Fig 4.14). When comparing between the high deformation and low deformation regions, for all nakhlites exhibiting augite (100)[001]:(001)[100] mIPF slip-system patterns, the intensity of (001)[100] is observed to decrease in the low deformation mIPF plots (Fig. 4.15; Table 4.2). This indicates an increase in low temperature high strain deformation being present within high deformation regions within the nakhlites.

Assessment of mIPF slip-system patterns suggest that impact deformation within the nakhlites is typically expressed as {hk0}[001] slip in olivine and increased proportions of (001)[100] within the (100)[001] : (001)[100] slip system pairing in augite (Figs 4.14 and 4.15). However, it should be noted that the expression of impact induced deformation is not solely restricted to the high GROD angle regions within a given nakhlite sample. Many of the low deformation region mIPF slip-system patterns observed within the nakhlites still express remnants of the low temperature, high strain slip (Fig. 4.15, Table 4.2).

4.6.2.2 Emplacement, low finite strain from mIPF slip-system pattern signatures

The occurrence of high deformation bands within the nakhlites in conjunction with their observed slip-system mIPF patterns indicating deformation related impact, suggests that the low deformation regions may provide evidence for emplacement deformation. Out of the 16 analysed nakhlites, only four stones showed evidence for high temperature deformation within the high deformation regions [Y 000749 (group V), MIL 090030 (group VI), MIL 090136 (Group VII), and Y 000593 (127-A; group IX); Figs 4.9–4.11, and 4.13, respectively]. The high temperature slip-

system patterns observed in these regions were only seen to intensify in MUD values within the low deformation regions mIPF plots (Figs. 4.14, 4.15). For augite slip in these groups is observed to occur along the {110} lattice or along multiple slip planes (Fig. 4.2, 4.15, and 4.17) and for olivine slip is predominantly observed to incorporate (010)[100] (Fig. 4.1, 4.14, and 4.16). It should be noted that the samples attributed to groups V–VII, and IX all exhibited low detected GROD angles within the map areas (Figs. 4.9–4.11, and 4.13). For identified groups I–IV, and VIII which all exhibit impact related slip-system patterns had at least one analysed section within the group that exhibited identifiable shifts in mIPF slip-system patterns between high and low deformation regions (Table 4.2). Assessment of the low deformation regions express mIPF slip-system patterns for those sections show shifts that emphasise patterns related to (010)[001] or (001)[100]/(100)[001] in olivine and (100)[001] in augite (Fig 4.15). (010)[100] slip is a common slip-system observed in mantle olivine's on Earth (Fig. 16; (Bernard et al., 2019; Girard et al., 2013; Ohuchi et al., 2011; Yao et al., 2019). The presence of (100)[001] slip in augite is also commonly observed within nearly all naturally forming Earth samples (Bascou, Tommasi, et al., 2002; Godard & van Roermund, 1995). Ultimately the slip-system patterns observed within these samples are typically associated with relatively low-moderate temperatures and low strain conditions (Figs. 4.16 and 4.17) indicating that they are indeed remnants of emplacement deformation within the nakhlites that have been subsequently overprinted by shock deformation.

4.6.2.3 Dominant clinopyroxene slip-systems

From the two analysed minerals augite shows the least diversity in mIPF slip-system patterns (Table 4.2). Laboratory experiments have shown that clinopyroxene slip-systems are strongly influenced by crystal orientation relative to the principal strain axis for the activation of specific slip-systems (Avé Lallemant, 1978; Bascou, Tommasi, et al., 2002; Kollé & Blacic, 1982). Clinopyroxenes, including augite, have one of the lowest forms of crystal symmetry (monoclinic, 2/m). The relationship between augite's crystallographic axes ($\alpha = 107°$, $\beta = 90°$, and $\gamma = 90°$), where the crystallographic length of $<c> > <a>$, for augite's unit cell, will often require either specific orientation and/or higher strain for activation of slip-systems other than (100)[001] : (001)[100], such as {h0l} to form. Laboratory studies have also shown that even when such specific conditions are met to activate another of augite's slip-systems, (100)[001] : (001)[100] slip-systems will also often be observed within the sample (Avé Lallemant, 1978; Kollé & Blacic, 1983; Philippot & van Roermund, 1992).

For any geological sample, a variety of observed different slip-systems within a single sample would be expected. The expectation of variable slip-systems is in part due to the variation in alignment of crystals within a given rock and each crystal's local petrological context and surrounding mineral assemblage. For igneous samples, >50 % crystal alignment is considered as strong CPO (Bunge, 1982; Vollmer, 1990). In the nakhlites, augite exhibits S- to LS-type CPO where crystal alignment ranges from 8–26 % (Griffin et al., 2022). The higher percentage of random crystal orientations within any given sample coupled with a high dependence on crystal orientation for the

activation of slip-system signatures will naturally result in multiple slip-system development between crystals. However, just like shape preferred orientation (SPO) and CPO within a rock, in order to assess representative deformation across a given sample several crystals preferentially on a similar level for statistical relevance (*i.e.,* ≥100–150 crystals) would need to be assessed (Skemer et al., 2005; Vollmer, 1990). Overall, despite the low crystal symmetry and higher slip-system activation criteria in clinopyroxenes, differences between certain extrinsic conditions, *e.g.,* low temperature and high pressure, high temperature low pressure, high temperature and pressure *etc.* can be observed (Fig. 4.17). However, studies so far indicate for most Earth relevant conditions the changes in slip-systems will be more subtle and be predominantly focused on shifts within the (100)[001]:(001)[100] slip-system pairing. Although clinopyroxene slip-systems have been identified to associate with specific conditions, there is a lot more work to be done. In particular, more information is needed addressing natural formation conditions and the effect of water content, before clinopyroxene slip-systems can be definitively used with the same level of certainty as geologists currently use olivine.

4.6.3 Implications for the nakhlites' time on Mars

Across the 16 analysed nakhlite meteorites nine distinct mIPF slip-system pattern combinations for whole section data are observed (Fig. 4.4) that reflect high strain deformation (Fig. 4.14). These mIPF slip-systems, when separated into respective high and low deformation regions (Figs, 4.14 and 4.15, Table 4.2), indicate signatures that most likely reflect differences in shock deformation, agreeing with previously petrologically identified shock features (Fritz, Artemieva, et al., 2005). Even low deformation regions within the analysed nakhlites show a strong influence of high strain deformation (*e.g.,* shock) over low strain deformation signatures (*e.g.,* mantle). Hence the extrinsic parameters presented in Figures 4.16 and 4.17 will not be applicable to the nakhlites but the relationship between the different slip-systems can be applied. On this basis, the presented data show several different high-strain deformation environments from within the nakhlite source indicating heterogenous sampling (spallation zone depth and distance from impactite) of the ejection crater (Bowling et al., 2020).

Comparison between whole section, high deformation, and low deformation region slip-system patterns across the 21 analysed sections show an increase in the slip-system patterns of {hk0}[001] in olivine and an increased (001)[100] component within the dominant augite (100)[001]:(001)[100] signature in high deformation regions. These particular slip-systems have been shown in mantle rocks to indicate increase strain at low temperatures (Figs. 4.16 and 4.17; Cordier, 2002; Katayama et al., 2004; Kollé & Blacic, 1983; Mainprice et al., 2005; Mauler et al., 2000), which suggests that this particular olivine-augite slip-system combination often expresses as the dominant or secondary slip-system pattern within the identified nakhlite groups, particularly groups I–IV and VIII (Figs. 4.5–4.9, 4.12–4.14, Table 4.2), could be indicative of shock-induced deformation. Our hypothesis can be tested through shock recovery experiments on olivine and pyroxene to assess the shock-induced activation of specific slip-systems.

The establishment of olivine slip-systems under low-strain extrinsic parameters are well constrained where the influences of the extrinsic parameters are an ongoing and active field of research (Bernard et al., 2019). The relationship of augite to extrinsic parameters, on the other hand, has not been as consistently studied olivine but has gained serious momentum over the last decade [*e.g.*, Bascou et al. (2011), Tedonkenfack et al. (2021), and Van der Werf et al. (2017)]. Presented in this study is the first attempt to collate existing clinopyroxene slip-system data to begin thinking about clinopyroxene slip-systems in a similar manner to olivine with respect to extrinsic parameters. Through comparing observed clinopyroxene (in this instance augite) MIPF slip-system patterns against published experimental data and the more-established olivine slip-system extrinsic parameters to ascertain patterns and commonalities (due to the data pertaining to low strain parameters), rough implications with respect to the nakhlites can be drawn. All of the identified groups apart from groups V–VII, and IX (Figs. 4.9–4.11, and 4.13, respectively; Table 4.2) exhibit slip-system patterns that are highly influenced by high strain deformation (Fig. 4.14, Table 4.2). Groups V–VII and IX express slip-system patterns commonly associated in mantle rocks with high temperature deformation the difference being group V exhibiting patterns indicative of higher strain and group IX indicating mIPF slip-system patterns potentially related to annealing processes (Figs. 4.9, 4.13, 4.16 and 4.17).

Separation of the high and low deformation regions within the nakhlites show that interpretation of mantle derived parameters is more complex than just assessing regions of low deformation within the samples. Despite the nakhlites being described as relatively low shock samples [5–20 GPa (Fritz, Artemieva, et al., 2005; Fritz, Greshake, et al., 2005)], mIPF slip-system patterns even within the low deformation regions still exhibit weakened high deformation region signatures, most likely formed as the result of shock deformation (Fig. 4.15). This finding could support the hypothesis of the nakhlite ejecta crater being positioned on the extremity of an older crater (Daly, Lee, et al., 2019). Out of all the analysed samples only 9 of the 21 sections showed significant shifts in either olivine and/or augite major mIPF slip-system patterns between separated high and low deformation regions (Table 4. 2, Figs. 4.14 and 4.15). In these particular samples, an increase in the MUD is observed within less dominant mIPF slip-systems patterns and a weakening of the MUD for olivine {hk0}[001] and augite (001)[100] is typically observed. The implications of these observations indicate that there is potential for the minor slip-systems observed to increase in MUD intensity within the mIPF low deformation region plots could indicate nakhlite mantle related deformation. However, further investigation is required before any interpretations could be made.

The current groupings presented in Figures 4.4, 4.14, 4.15, and Table 2 indicate samples that share similar extrinsic parameters related to high strain deformation. This could be interpreted as samples exposed to similar conditions within the ejecta crater during launch. These groupings do not indicate that the samples are sourced from the same magmatic body as is evidence by samples MIL 03346 and NWA 817 within identified group II that show different slip-system patterns within their low deformation region mIPF plots despite sharing the same whole section and high deformation slip-system signatures (Table 4.2, Figs. 4.14 and 4.15). The same observation can be applied to the

proposed ‘paired’ Yamato and Miller Range nakhlites were different mIPF slip-system patters are observed for both whole section (Fig. 4.4) and identified low and high deformation regions (Figs. 4.14 and 4.15, Table 4.2).

For the Yamato nakhlites, here categorised into groups I, V, VIII, and IX (Figs. 4.9, 4.12, and 4.13, Table 4.2) mIPF slip-system patterns express temperature differences that could not be resolved if they were located in the same position within the nakhlite ejecta crater and formed from the same magma body on Mars (Figs. 4.16 and 4.17). For the Miller Range nakhlites samples such as MIL 03346 and MIL 090032 could be related based off observed slip-system patterns (Figs. 4. 6, 4.14, and 4.15, Table 4.2). However, both MIL 090030 (Fig. 4.10) and MIL 090030 (Fig. 4.11) exhibit mIPF slip-system patterns whose extrinsic parameters do not support pairing with any of the Miller Range nakhlites (Figs. 4.4, 4.14, and 4.15, Table 4.2).

Apart from the two Y 000593 sections, discussed above, each of the different Miller Range and Yamato samples are sourced from separate stones that were found in a similar location in Antarctica (Treiman, 2005). These locations are known glacial fields that are fed from a large catchment area. The variation observed in mIPF slip-system patterns between these ‘paired’ stones implies different deformation parameters for the separate meteorites, which could indicate either a range of deformation environments with each meteorite being sourced from a different section within the same igneous body or could suggest that each individual meteorite represents its own separate flow/intrusion. From rudimentary modelling of the nakhlite emplacement parameters, magma body unit thicknesses greater than ten meters were suggested for the Miller Range nakhlites, while the Yamato nakhlites were suggested to have magma body unit thicknesses less than ten meters (Griffin et al., n.d.). The smaller modelled unit thicknesses in conjunction with the observed differences in crystallographic deformation, similar recovery position, and geochronological dating (Cohen et al., 2017), currently supports the hypothesis that the Yamato individual nakhlites formed as individual igneous units that were located in close proximity to one another on Mars while the larger unit thicknesses, current geochronological dating in combination with presented crystallographic slip-systems would suggest that the Miller Range nakhlites could represent different regions (or lobes) from a single igneous event (Griffin et al., n.d.). Overall, variation in slip-system patterns observed from presented data, suggests that the suite of nakhlites meteorites heterogeneously sample different areas from within their launch crater on Mars, sampling a variety of different igneous units.

4.7 Conclusions

Observed slip-system patterns can be used to discern between samples exposed to varying extrinsic parameters. However, more work (both natural samples and laboratory based) needs to be undertaken to further constrain slip-system signature extrinsic parameters, particularly regarding the effects of high strain and water content. In addition, EBSD has the potential to become a powerful technique to constrain extrinsic parameters associated with deformation (*i.e.*, pressure, temperature, strain, water content) of Martian magmas and other meteorites when combined with analysis of naturally occurring samples and laboratory experiments regarding slip-system activations.

Combined olivine and clinopyroxene mIPF slip-system patterns identified nine different slip-system pattern combinations within the nakhlites five of which were associated with high strain deformation interpreted as shock deformation. This shock (high strain) deformation is observed as increased proportions of (001)[100] in augite and {hk0}[001] in olivine. Investigation of slip-system patterns between identified high and low deformation regions within the data indicate high strain deformation to be prevalent through the sample, including within the low deformation regions. Less dominant slip-system patterns identified to increase in MUD intensity within the low deformation slip-system patterns could have the potential to represent low strain (mantle related) deformation. However, further work investigating the contributions of shock metamorphism and the exact relationship between high strain slip-system extrinsic parameters is required.

4.7.1 Acknowledgments, specimens, and data

The authors are grateful to the following curational facilities for providing the samples used in this stud: NHM London (Governador Valadares), Japanese Antarctic Meteorite Research Centre (NIPR; Y 000593, Y 000749, Y 000802), Macovich Collection, The Museum of Western Australia(Nakhla WAM 12965), Centre Européen de Recherche et d'Enseignemet de Géosciences de l'Environment (CEREGE; Caleta el Cobre 022), the Institute of Meteoritics University of New Mexico (NWA 10153, NWA 12542), Smithsonian National museum of Natural History (Lafayette, Nakhla USNM 426-1), and ANSMET (MIL 03346, MIL 090030, MIL 090032, and MIL 090136). US Antarctic meteorite samples are recovered by the Antarctic Search for Meteorites (ANSMET) program, which has been funded by the NSF and NASA, and characterised and curated by the department of Mineral Sciences, of the Smithsonian Institution and Astromaterials Acquisition and Curation Office at NASA Johnson Space Centre. The authors thank the editor Laurent Montési, our two anonymous reviewers as well as David Prior and Iain Neill for their helpful comments which significantly enhanced our manuscript. This work was funded by the Science and Technology Facilities Council through grants ST/N000846/1 and ST/H002960/1 to M.R.L). All data are available at Griffin et al. (2021).

5 Final summary

The nakhlites are a constantly expanding class of Martian meteorites increasing from eight meteorites in 2001 to seventeen meteorites in 2017 (when this thesis began), to twenty-six specimens in 2021 (The Meteoritical Society, 2021). The unprecedented addition of new nakhlite samples over the last decade has enabled larger studies, *e.g.,* Day et al. (2018), Udry & Day (2018), and this thesis to be undertaken. It is from these larger studies that the increase of diversity within the nakhlites can be fully appreciated and used to interrogate larger scale processes on Mars. Additionally the hypothesised trends and relationships previously reported for the group can be reconsidered and tested to a level that was not feasible prior to ~2010 *e.g.,* Treiman (2005) and references therein, due to the limited number of specimens available for study.

Previous geochemical investigations of eleven nakhlites by Day et al., (2018), has shown the class evolved from the same (unknown) magmatic plumbing system on Mars, most likely related to the periphery of a mantle plume. The paired studies of Day et al. (2018) and Udry & Day (2018) laid the geochemical groundwork which when assessed with the results of Cohen et al. (2017) enabled the nakhlites analysed here to be assumed as being related to a common parental melt but representing different igneous units. There have been many other geochemical studies presented also confirming the nakhlites common parental source, however the larger studies of Day et al. (2018) and Udry & Day (2018) were the first to present a large number of samples all analysed in the same way within the same lab. In the geochemical analysis of meteorites, where the allotment of sample is often significantly less than would be considered robust for Terrestrial studies, the distinction of datasets that can be interrogated outwith of instrumental bias is important and should not be over-looked.

Individual magmatic events sourced from a singular magma plumbing system on Earth are often shown to be similar in terms of major element chemistry and mineralogy—and yet also subtly distinct and diverse in terms of micro-structure and trace element geochemistry (Németh et al., 2003). The ability to discern between individual igneous units is often reliant on an understanding of the sample's 'field-context' to recognise said subtle shifts in analysed data. However, until Mars sample return is completed, the applicability of field-context for contextualising physical Martian specimens is unavailable thus other means must be investigated.

5.1 EBSD as a tool to distinguish different igneous units

The crystallographic technique of EBSD is a powerful tool that enables high spatial resolution data with a 3D reference frame, via the crystallographic axis. to be discerned from a flat 2D plane of a given sample (*e.g.,* thick/thin sections). The ability to use the crystallographic axis as a common reference frame between samples, makes the technique of EBSD advantageous over other forms of microscopy. The use of an internal reference frame versus an external reference frame enables micro-structures to be consistently assessed across multiple meteorite specimens, which typically lack any form of identifiable external reference frame. Technological advancements in both computer processing, computer memory, detector ability, and beam stability have enabled larger areas of a

sample to be mapped at increasingly higher spatial resolutions over reduced time periods. These advancements have enabled the collection of EBSD datasets which contain statistically relevant numbers of grains to be quantitatively assessed. An important consideration when the specimen being analysed is limited. It is important to note for meteorite specimens, that lower gravity conditions should theoretically inadvertently increase the data sizes required for robust quantitative analysis, simply by the lowered amount of external strain contribution towards developed SPO intensity within the sample (Rowland et al., 2004). Lower expected SPO intensities alongside limited sample availability highlight the importance of collecting and working with representative datasets such as was attempted in this thesis. Advancement in EBSD technology has now enabled maps to be collected in the order of several centimetres squared, *i.e.*, the equivalent of a standard petrological thin/thick section. Enabling the micro-structural assessment of equivalent size datasets to what was previously restricted to standard SEM or optical microscopy, which can be considered representative of samples with low intensity SPO. More importantly within groups such as the nakhlites, analysis of larger available sections can provide approximate lower limit criterion for representative dataset collection in rarer samples.

High spatial resolution stitched area EBSD mapping opens the potential for new avenues of crystallographic investigation such as investigating intra-crystalline misorientations (used to infer slip-systems) such as the data presented in chapter 4 or investigations related to microstructures in the mesostasis regions (not presented here) at a comparable scale and rigour to SPO investigations (such as is presented in Chapter 3). These features are important in understanding how an igneous unit is emplaced. However, these data and machine-time expensive experiments are not without trade-offs compared to the traditional method of coarser large maps with targeted higher spatial resolution crystals/areas. These include but are not limited to; significantly increased experimental time required for the collection of EBSD datasets, the potential generation of false micro-structures from overlapping stitched-map regions, the increased machine-time costs, storage and access to the collected data, and the additional skillsets required to analyse multiple large data sets.

The ability to correctly identify and distinguish micro-structures associated with different igneous units requires collected data to 1) be representative of the igneous unit, 2) have a way to consistently compare data between samples, and 3) have an understanding of the sample's igneous formation and emplacement conditions. EBSD if used correctly can provide information to all three points as evidenced from this thesis further detailed below:

1) Mapped EBSD experiments run at a resolution above the smallest grainsize (for SPO or inter-crystalline CPO) or ≤4 μm (intra-crystalline misorientation CPO) has the capability to generate datasets equivalent to whole thin/thick section analysis. This is equivalent to established microscopic petrological studies entailing and can ensure reasonable grain counts (~300 grains minimum for the nakhlites, Chapter 3) to be collected and assessed.
2) EBSD datasets can be assessed against either the crystallographic reference frame of the mineral of interest or the reference frame of the sample. Ideally, studies will use both reference frames. For the study of meteorites, the crystallographic reference frame can be

used as the common reference between individual samples. Identification of common SPO/CPO features, such as the augite [001] girdle CPO in all of the nakhlites (Chapter 3), can then provide a means to which all of the data may be eventually assessed against and even rotated against. The latter point has not been solved in this thesis but is noted as future work for the samples.

3) SPO and CPO provide important information relating to an igneous sample's physical emplacement. EBSD can provide CPO data and can leverage CPO to infer SPO using strategic crystallographic axes (as was shown in Chapters 2 and 3). Inter-crystalline CPO investigations can provide information relating to emplacement (Chapters 2 and 3), while intra-crystalline misorientation CPO investigations can provide information relating to plastic deformation within the samples (Chapters 2 and 4). While the work presented in Chapter 4 is merely qualitative, additional quantitative investigations of internal grain boundary relationships and weighted burgess vector calculations applied to the existing datasets shows that EBSD collected data can be used to quantitatively assess igneous formation and emplacement conditions of igneous units lacking geological contexts.

Overall, this thesis has shown that EBSD as a technique can be used to identify different micro-structural features within the nakhlite meteorites. However, additional supporting work is required before such data could be used to accurately distinguish an uncontextualised igneous unit from another. Firstly, more experimental crystallographic work is required to better constrain how different intra-crystalline misorientation patterns relate to crystallographic slip-systems. Not only for olivine and augite (as presented in chapter 4) but for other common mafic minerals. In particular focus needs to be placed on high pressure deformation to understand the shock component common for all meteorite studies. Secondly, leveraging common physical principles and processes known for magmatic systems to interrogate CPO data. The model calculations used in Chapter 3 provides a pilot study for future modelling-EBSD investigations. This avenue of interrogating EBSD data may provide the framework to computationally test best-fit geological contexts for achondritic planetary samples that are constrained and bespoke to the samples of interest.

5.2 The nakhlites emplacement on Mars and what it means for their source volcano

The micro-structural work presented here expands on the EBSD work presented by (Daly, Lee, et al. (2019) and Daly, Piazolo, et al. (2019). This thesis presents SPO and CPO datasets for 16 different nakhlites (including the reprocessed datasets of the aforementioned studies) making the presented data the largest known individual study of the nakhlites to date. The use of high spatial resolution EBSD mapping has enabled both inter-crystalline and intra-crystalline CPO to be assessed from the same dataset in a manner and at a scale that is currently unprecedented for meteoritical analyses.

Large scale studies provide the ability to identify trends across a given suite of rocks. The identification of such trends can impart important information about the history of the magmatic

source through time as well as information relating to the emplacement of its magmatic units. Low intensity CPO is consistent for all analysed samples. This lower intensity requires larger datasets to discern CPO and SPO. In the case of the nakhlites ~300 crystals were required for CPO results to deviate ≤2%, *i.e.*, considered to be statistically stable (Skemer et al., 2005). Lower intensity SPO and CPO on Earth is commonly associated with lower energy environments *e.g.*, stagnant lava ponds and plutonic intrusions such as large xenoliths and/or sills. However, it cannot be discounted the impact lower gravity should theoretically have on planetary bodies, such as the Moon and Mars in terms of SPO and CPO development within surficial flows (Rowland et al., 2004). Assessment of intra-crystalline misorientation strain within the samples exhibit point/lineation signatures (see appendix Figs 9.2–9.4), indicating directionality to the overriding expressed strain. These point signatures become stronger when investigating the lower deformation regions of the samples, indicating that the directional strain is most likely related to emplacement rather than the subsequent hypervelocity impact.

Calculated nakhlite CPO strength best agrees with weak-moderate plutonic strength values on Earth. If the environments between Earth and Mars were directly comparable (which in reality they are not), then this result alone would disprove the nakhlites formation as surficial flows. However, there is currently not enough work assessing the effect of lower gravity on CPO values to be able to use calculated index CPO values as an effective determinant on its own. Daly, Piazolo, et al. (2019) identified CPO in four nakhlites (whose datasets were included and reprocessed in this thesis). From their results they hypothesised nakhlite formation in two different environments: pure crystal settling (foliation CPO only) and hyperbolic flow (foliation with lineation CPO). This thesis has shown lineation to be a common feature in nearly all samples (Chapter 3), albeit weak and at lower intensity than the persistent and more dominant [001] foliation CPO. Pure foliation CPO was only identified in two of the sixteen analysed meteorites (Caleta el Cobre 022 and Lafayette, Chapter 3). The identification of weak lineation with direction strain in the samples, microstructurally disproves the nakhlites formation as large cumulate body, while the geochemical relationship (previously analysed by Day et al. (2018) recognised between the group, makes it improbable for the Caleta el Cobre 022 and Lafayette to have formed as cumulates either. However, further assessment of the data is required to confirm this hypothesis.

Further investigations into the lineation component of the CPO identified [100] axis preference for nearly all samples with only one sample, Y 000593, exhibiting a [010] axis preference (Chapters 2 and 3) which also shows signs of annealing (Chapter 2). On Earth lineation is typically observed in the [010] axis of clinopyroxene (as it is the perpendicular axis to the [001]). The preference of the [100] axis in conjunction with the direction strain misorientation CPO suggests that almost all lineation CPO in the nakhlites is remnant of the magmatic body's initial intrusion into the shallow Martian crust, which was then overprinted by the foliation CPO which formed during the igneous body's final stages of crystallisation once emplaced.

Augite residence times calculated by Udry & Day (2018) and used in this thesis to assist computational investigations into the nakhlite's emplacement mechanism (Chapter 3) showed

variable growth times across the samples. These variable growth times in conjunction with at least four distinct crystallisation ages identified for the nakhlites (Cohen et al., 2017), indicate that emplacement of the nakhlites had to have occurred over several different events despite CPO identified from this thesis suggesting a common emplacement style. What this means for the nakhlites source volcano is a consistency in emplacement type through time. Identified rims that are primarily located and geochemically match mesostasis compositions indicate majority of the augite phenocrystic growth occurred pre-emplacement of the magma body. The basic calculations assessing the three different emplacement cooling mechanisms (thermal diffusion, crystal settling, and crystal convection) indicate that both crystal settling and crystal convection would be required for majority of the samples, with crystal settling being the more dominant component of the two. The results for the Yamato nakhlites however, indicated a higher level of thermal diffusion than crystal convection, indicating faster final stage cooling than the rest of the nakhlites despite their crystal size distributions suggesting longer phenocryst growth times (Chapter 2). The next step in the assessment of emplacement would be to conduct similar analysis of the mesostasis material.

Investigation into the relationship between CPO and calculated emplacement through time, revealed a random nature to the nakhlites' emplacement on Mars. This finding is not unusual when investigating related igneous events on Earth. However, what this result does highlight for planetary studies is the danger of interpreting, then widely applying trends to a system based off limited data. It is an acknowledged fact within the Planetary community that limited resources will often result in studies not necessarily reaching or using the same standards as equivalent Terrestrial studies. However, it should not be used as an excuse to justify over-interpreting data, lack of scientific rigor, or relying solely on the instrumental error as a sign that your data is representative and robust without considering the wider context of the sample and how the collected results relate. Lack of geological context in combination with limited sample does make it difficult to interpret results, however, there are other methods that can be used to validate experimental results such as using correlative techniques to gain multiple perspectives (*e.g.*, Chapter 2) or leveraging computational models to test various hypotheses (*e.g.*, the preliminary calculations in Chapter 3). However, conducting studies involving multiple specimens in combination with correlative techniques and modelling could be considered an ideal choice, wherever possible.

Cosmogenic exposure ages indicate that the nakhlites ejected from Mars at 10.7 ± 0.8 Ma (Cohen et al., 2017) through a hypervelocity impact event hypothesised (due to the geochemical and isotopic relationships of the nakhlites) to be related to a single (yet to be confirmed) ejection crater . Intra-crystalline misorientation patterns indicate that the nakhlites represent a heterogenous sampling of the impact crater's spallation zone (Chapter 4). Micro-structures in the form of intra-crystalline misorientations indicate eight distinct deformation patterns. These patterns indirectly correspond to crystallographic plastic deformation (slip-systems) recording emplacement and subsequent shock metamorphism events. In all of the analysed samples apart from Y 000593 (127-A), which exhibits patterns indicative of creep and recrystallisation, indicate shock deformation as the dominant CPO signature within identified high and low deformation regions (Chapter 4). Emplacement intra-

crystalline misorientation patterns are discernible from the dominant shock patterns signatures within nine of the sixteen analysed meteorites. These hypothesised emplacement signatures range from lower temperature/moderate-high strain through to high temperatures and strain. However, what is of greater interest is that some of the samples which exhibit similar whole section misorientation patterns have different identifiable emplacement patterns which indicates variation in both emplacement and shock throughout the group. I will note that these patterns have yet to be fully quantified, and as they currently sit can only be interpreted in a qualitative manner.

For the assessment of mantle mafic rocks, intra-crystalline misorientation patterns olivine is typically the default primary indicator used to assess the recorded extrinsic parameters. The use of orthopyroxene (another orthorhombic mineral) is typically used as a secondary measure (if at all). However, within the nakhlites, olivine does not occur in high enough proportions (~10 vol.%, Chapter 3) to be considered an effective indicator mineral and orthopyroxene is largely restricted to the mesostasis. Thus Chapter 4, presents summarised extrinsic parameters for clinopyroxene slip-systems. These extrinsic parameters are based on observed experimental activation criteria for mantle processes (*i.e.*, low strain), however, the activation relationships (*i.e.*, higher, and lower relative temperature) are still applicable to the observed high strain slip-systems inferred for the nakhlites. Until more high-strain/high pressure experiments are conducted that assess shock and deep mantle related plastic deformation the exact parameter values (Temperature, stress, and strain) for the inferred slip-systems cannot yet be extracted and directly applied to the nakhlites or any other meteorites using the methods of Chapter 4. Additionally for the results presented in Chapter 4 additional quantitative assessment (*i.e.*, weighted burgess vector and/or intragrain boundary misorientation studies) would need to be undertaken. However, the presented data can be utilised to separate and group the individual meteorites into sub-groups. As such, a cautious approach was applied to the nakhlites' intra-crystalline misorientation pattern interpretations, in recognition of the identified future work required and the suitability of current experimental results (aimed at studying mantle processes *i.e.*, high temperature low strain) for hypervelocity generated slip-systems (low temperature, high strain).

Interpretation of the observed micro-structural variability across the nakhlites reveals several sub-groupings. These subgroups indicate the nakhlites to represent variable (most likely intrusive) igneous bodies heterogeneously located within spallation zone of an ejecta crater on Mars. The igneous bodies through the microstructural work presented in this thesis are hypothesised to represent at least eight different units. The increase from the chronologically reported four crystallisation events is not surprising considering only six nakhlites were dated using the high resolution $^{40}Ar/^{39}Ar$ geochronology by Cohen et al. (2017), compared to the sixteen nakhlites studied by EBSD in this thesis. These events based on the presented data are most likely to represent a series of variable sized shallow intrusions (sills and dykes) that may or may not have evolved into lava pools at the surface rather than surficial flows as was initially hypothesised (Day et al., 2006; Friedman Lentz et al., 1999; Imae et al., 2005; Richter et al., 2016; Treiman, 2005; Treiman & Irving, 2008).

If this presented hypothesis of the nakhlites being formed from predominantly intrusive activity is correct, then the location of the nakhlite magmatic source may not in fact be limited to an established volcano on the surface of Mars exhibiting Amazonian-aged, impacted surface lava flows. Instead, the source location could be located along one of the fissures within the known Amazonian volcanic fields on Mars. Another hypothesis stemming from the nakhlites being plutonic, is that volcanic activity on Mars would be predominantly intrusive in nature, where like Earth, a significant proportion of produced igneous material does not completely make it to the surface.

6 Conclusions

- EBSD is a technique capable of identifying differences within Martian meteorites. Distinct igneous units can be identified within the Nakhlites. However, in order to collect relevant and robust results the experimental parameters need to be fully considered.
- When attributing characteristics to a rock it is essential to make sure that the dataset is statistically representative. Whenever possible it is good practice to assess the data via other techniques. This practice becomes even more essential in the case of meteorites, when the sample sizes are lower than what is ideal and where the geological context for the sample is either vague or missing completely.
- The nakhlites represent a diverse set of igneous bodies (at least 8 different units) which although geochemically related, represent different emplacement environments. The group show a consistent dominant emplacement mechanism (low intensity weak-moderate foliation with a weak flow component). The emplacement mechanism of the nakhlites show crystal settling to dominate with the identification of two distinct groups reflecting different contributions of crystal convection and thermal diffusion within the units.
- The nakhlites represent a heterogeneous sampling of the launch crater spallation zone, where related micro-structures to the hypervelocity event are pervasive throughout the entire sample but at variable intensity. Identified internal misorientation patterns identify a distinct shift between high and low deformation regions, which has here been hypothesised as shock overprinting. However, further work is required to fully quantify the findings.

6.1 Summary of scientific contributions

- Two modern quantitative micros-structural techniques (EBSD and CSD) were compared, highlighting their strengths and weaknesses to understand how generated results from each technique could differ when investigating the same sample. Chapter two highlights the strengths of each technique and explains how the techniques can be used and applied.
- Confirmed that the dominant CPO across the nakhlites is low intensity foliation with a lower component of lineation. The identification of lineation within the sample in combination with the direction strain observed across all samples, disproves the former hypothesis of the nakhlites forming as a large cumulate pile on Mars. Instead, CPO results indicate a diverse emplacement environment for the samples such as a network of sills and dykes.
- Highlighted the random micro-structural nature of the nakhlites, which supports their treatment as individual units.
- Identified distinct intra-crystalline misorientation patterns within the nakhlites, indicating variable strain and temperature conditions across the group. These results highlight the danger of paring found meteorites located in a similar region and determining slip-systems based of limited crystal datasets.

- Showed that even low deformation regions of the samples still primarily exhibit shock deformation signatures. These results indicate that shock deformation, and how it interacts with crystals is a region of research that needs to be expanded upon before intra-crystalline deformation can be utilised to understand formation conditions of planetary bodies, outside of Earth.

7 Future work

The work presented in this thesis highlights the importance of large scale meteoritical studies. The key findings of this thesis (summarised above) only scratch the surface in terms of understanding the nakhlites and their magmatic source, opening more questions for future investigation.

The micro-structures presented in this thesis only assesses the phenocryst crystals. However, microstructures relating to the mesostasis material has yet to be discerned. The understanding of the mesostasis material's CPO, SPO, microstructures, and growth rates would provide more accurate time scales in terms of emplacement crystallisation, the effect of aqueous alteration (as this is where most is located), as well as the relationship between phenocryst and mesostasis regions which would provide better insight into the nakhlites CPO development.

Inter-crystalline CPO investigations presented here were carried out in a quantified way. However, the intra-crystalline misorientation CPO presented were only qualitative. In order to quantify the intra-crystalline misorientation CPO within the presented samples further analysis in terms of either grain boundary orientation investigations or weighted burgess vector calculations would need to be undertaken. Ideally a combination of both presented options should be applied.

Further investigations of the mesostasis material should involve intra-crystalline misorientation investigations including weighted burgess distribution calculations and/or grain boundary disorientation studies to determine deformation strain and temperature parameters more quantitatively. Investigations into the matrices of chondrites has shown that majority of the deformation within meteorites is generally accommodated within the finer-crystallised regions (Forman et al., 2016). From the grain reference orientation distribution (GROD) angle maps (aka mis2mean, presented in chapter 4) regions of high deformation are observed to coincide with mesostasis regions.

Investigations into the crystallographic intra-crystalline misorientations (Chapter 4) indicate that the majority of the intra-crystalline misorientation pattern signatures observed within the nakhlites are associated with impact deformation. To properly quantify this observation, investigations into terrestrial analogues such as naturally occurring basaltic impact craters and anthropogenic craters (*e.g.*, Danny Boy nuclear test site crater) should be undertaken. These analogues, due to their known location, and in the case of Danny Boy known strength of impact and availability of unshocked samples, would enable the formation of high strain misorientation patterns with respect to pre-existing CPO microstructures to be investigated.

Calculations of potential emplacement mechanisms for the nakhlites (Chapter 3) gave some upper and lower bound constraints for potential thicknesses of the nakhlite emplacement units. This work can be substantially expanded upon to better refine the current model by mixing and changing the proportions of the three currently calculated endmember scenarios. By comparing modelling results from mixed proportions of the different emplacement mechanism against analytical data will further refine the emplacement criteria for each nakhlite to reflect a more realistic geological setting. Depth of emplacement for each sample is another factor to build into the models to test whether

analytical results best fit shallow intrusions or surficial flow criteria. Understanding whether these samples were formed as intrusions, surficial flows, or a combination of the two is critical for locating the nakhlite ejection crater on Mars, as well as furthering the understanding of the nakhlites formation and Amazonian igneous activity on Mars.

This thesis utilised four different EBSD instruments. Out of these four instruments only one had the latest EBSD detector (symmetry) installed (Curtin University). This detector enabled samples to be run at a fraction of the time at a higher resolution, resulting in most of the larger datasets presented in this thesis. Larger thick sections were taken to Curtin University to be run as the processing software available at the other facilities could not handle the analysis. In order to be collecting larger representative datasets at a high enough spatial resolution for internal deformation studies, these newer detectors and associated processing software are necessary. In order to properly quantify mesostasis material higher spatial resolution studies would also need to be run, this would be pushing the current resolution limits for EBSD. Transmission Kikuchi diffraction (TKD) analysis, not used in this thesis, could provide a solution for the resolution and the ability to index phases more likely to amorphise. However, this technique is limited to the size of the transmission electron microscope (TEM) grid. TEM grids tend to be ~3 mm in diameter, which would limit the size of the dataset available for study. Thus, multiple grids would need to be analysed to reach an equivalent sized region accessible by EBSD. Creation of TEM grids are also a time and cost expensive procedure, where the loss of the grid can be quite high.

Currently use of EBSD has been restricted to 2D planar surfaces of a given sample in most laboratories. However, the use of EBSD combined with computer tomography (CT) scanning is available in larger synchrotron facilities. This combination enables full 3D imagery not only at the surface of the sample but also at increased depths. As technology has improved the combination of EBSD and CT, currently marketed as lab DCT, is becoming more readily available for purchase from commercial developers (*e.g.*, Oxford Instruments) as laboratory scale instruments. The spatial resolution of lab DCT is currently suitable for assessing CPO but not slip-system resolution micro-structural analysis. However, in the context of meteorite (or other material) investigations the ability to determine CPO within a given samples and assess CPO from more than the top ~50 nm could provide vital information for not only more reliable SPO interpretation but also better thin/thick section placement for traditional EBSD investigations.

8 Appendices

8.1 Chapter II specific appendices

8.1.1 EBSD

Table 8.1. *EBSD and additional EDS map analysis SEM settings*

	Y 000593		**Y 000749**		**Y 000802**
	106-A	*127-A*	*64-A*	*72-A*	*36-A*
Area (mm²)	41	31	54	48	35
Section analysed	Whole	Partial	Partial	Whole	Partial
Step size (µm)	3	3.5	3.5	3	5
Tilt (°)	70	70	70	70	70
Accelerating voltage (keV)	20	20	20	20	20
Aperture (µm)	120	120	120	120	120
Beam Exposure (ms/ EBSP)	29	26	26	30	24
Beam Current (nA)	4.1	4.1	4.1	4.1	4.1
Pressure (Pa)	3.5×10^{-4}	3.5×10^{-4}	3.5×10^{-4}	3.5×10^{-4}	3.5×10^{-4}
MAD	0.57	0.51	0.72	0.72	0.67
Mean BS	62.74	95.28	50.63	50.63	52.72
Mean BC	79.55	99.14	53.11	53.11	53.11
Bin criteria	4 x 4	4 x 4	4 x 4	4 x 4	4 x 4
EDS collected	Yes	Yes	Yes	Yes	Yes
SEM settings for additional EDS maps					
Additional EDS map		Yes	Yes		Yes
Field of view (mm per frame)		0.6 x 0.8	0.6 x 0.8		0.6 x 0.8
WD (mm)		8.5	8.5		8.5
Tilt (°)		0	0		0
Accelerating voltage (keV)		20	20		20
Beam Current (nA)		4.1	4.1		4.1

EBSP = electron backscatter patterns a.k.a. Kikuchi diffraction patterns
MAD = Mean angular deviation
BS = Back scatter
BC = Back contrast
EDS = electron dispersive spectroscopy
WD = working distance

Table 8.2. *EBSD augite statistics (crystals >0.3 mm shape diameter).*

		Y 000593		**Y 000749**		**Y 000802**
		106-A	*127-A*	*64-A*	*72-A*	*36-A*
Augite indexed (%)		54.6	53.2	44.7	29.2	62.4
N (all data)		1035	395	7450	2478	670
N (OPPG)		93	109	197	111	138
N (MTEX)		287	299	508	303	383
Diameter (mm)						
Av.		0.44	0.35	0.44	0.42	0.43
SD		0.13	0.14	0.12	0.88	0.14
Aspect ratio						
A-axis						
Av.		-	-	1.63	3.51	1.65
N_A		0	0	4	2	5
SD		-	-	0.45	0.08	0.68
B-axis						
Av.		-	-	1.4	-	-
N_B		0	0	1	0	0
SD		-	-	-	-	-
C-axis						
Av.		1.86	1.24	2.11	2.36	2.11
N_C		4	2	6	7	11
SD		0.79	0.2	0.95	0.72	2.21
All axes						
Av.		1.86	1.24	1.91	2.62	2.02
N_T		4	2	10	9	16
SD		0.79	0.2	0.8	0.81	1.91
Percentage of elongate crystals		4.3	1.8	5.1	8.1	11.6
GOS (°)		4.36–6.26	2.64–6.78	4.44–8.54	1.42–6.26	2.84–35.95
Av.		5.42	4.61	6.15	3.64	13.36
SD		0.84	2.00	1.13	1.52	11.61
MOS (°)		0.42–3.17	0.37–1.07	0.52–2.13	0.19–0.98	0.45–3.12
Av.		1.13	0.58	0.90	0.48	1.24
SD		1.36	0.33	0.53	0.25	1.16
CPO						
M-Index		0.03	0.03	0.04	0.04	0.02
J-Index		3.55 ± 0.71	4.76 ± 0.23	2.92 ± 0.14	3.79 ± 0.18	2.76 ± 0.14
Eigenvalue						
Point (P)	<100>	0.04	0.06	0.07	0.13	0.12
	<010>	0.13	0.14	0.14	0.08	0.08
	<001>	0.17	0.10	0.11	0.18	0.15
Girdle (G)	<100>	0.19	0.11	0.04	0.02	0.15
	<010>	0.09	0.08	0.16	0.24	0.05
	<001>	0.27	0.41	0.44	0.38	0.19
Random (R)	<100>	0.78	0.78	0.89	0.84	0.73
	<010>	0.78	0.79	0.71	0.68	0.87
	<001>	0.56	0.49	0.45	0.44	0.65
M.U.D. $_{max-min}$		0.23–5.92	0.26–2.91	0.46–2.22	0.22–4.78	0.59–2.26

N = number of crystals
OPPG = one point per grain
Av. = average
SD = standard deviation
CPO = crystal preferred orientation
MOS = mean orientation spread
NA = number of crystals in subset A
NB = number of crystals in subset B
NC = number of crystals in subset C
NT = total number of crystals with any axis parallel (± 5°) to the plane of the sample
GOS = grain (*i.e.*, crystal) orientation spread
MUD = multiples of uniform density
LS index = assessment of lineation (L=1) and foliation (S=0) CPO between <010> and <001> eigenvalue results from equation 2.1
BA index = assessment crystallographic preference between <010> (B=1) and <100> (A=0) from equation 2.2

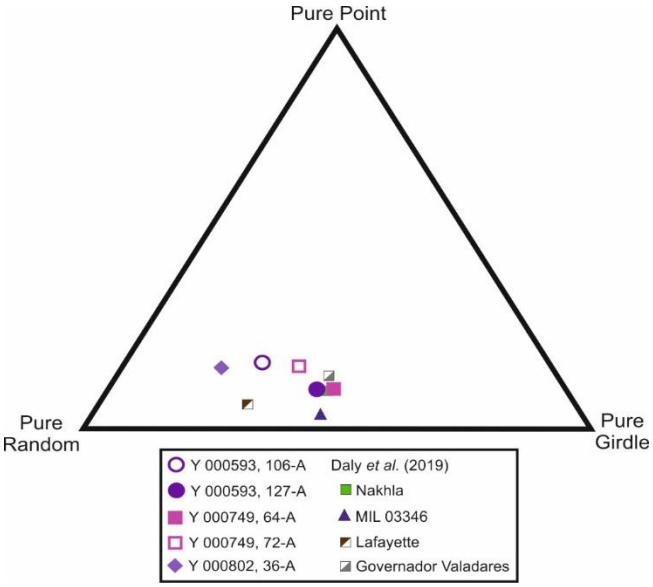

Figure 8.1. *Yamato nakhlite Eigenvalue CPO ternary <c> axis idenitifying individual nakhlites. This is a fully coloured version of Figure 9 in-text.*

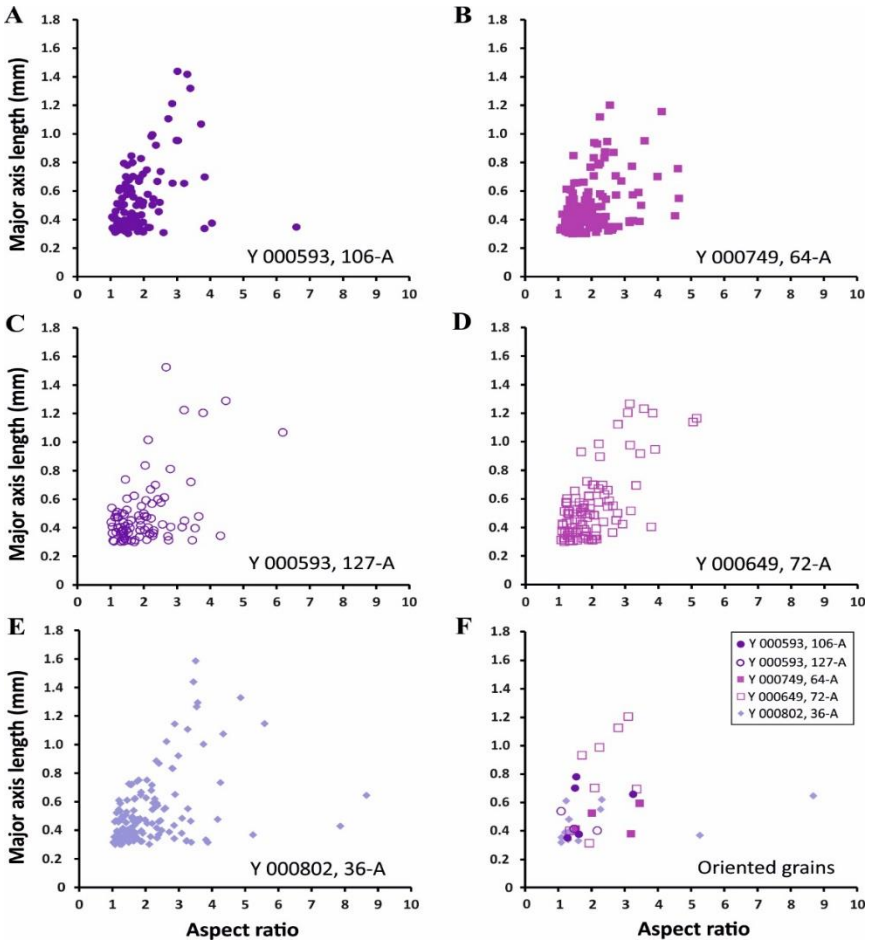

Figure 8.2. *Major axis length vs. aspect ratio of Yamato nakhlites for crystals with >0.3 mm. A) Y 000593 106-A; B) Y 000593, 127-A; C) Y 000749 64-A; D) Y 000749, 72-A; E) Y 000802 36-A; F) shape diameter of augite with <c> axis parallel to the plane of the analysed section (i.e., long shape-axis ±5° in the plane of the section).*

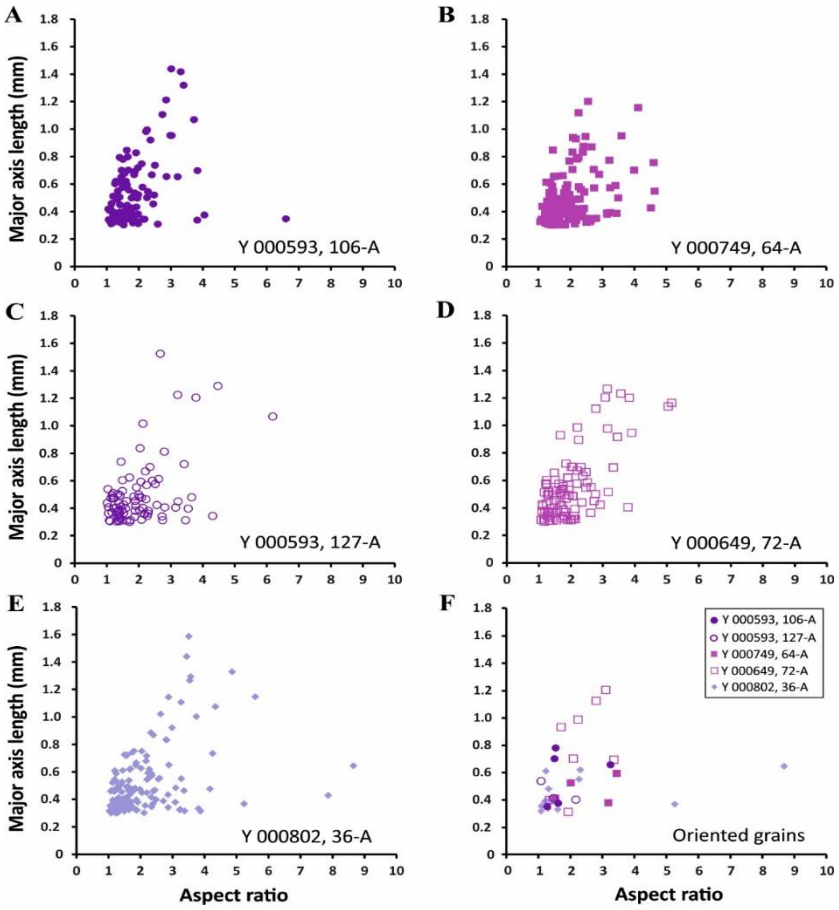

Figure 8.3. *Major axis length vs. aspect ratio of Yamato nakhlites for crystals with >0.3 mm. A) Y 000593 106-A; B) Y 000593, 127-A; C) Y 000749 64-A; D) Y 000749, 72-A; E) Y 000802 36-A; F) shape diameter of all augite with <c> axis parallel to the plane of the analysed section (i.e., long shape-axis ±5° in the plane of the section).*

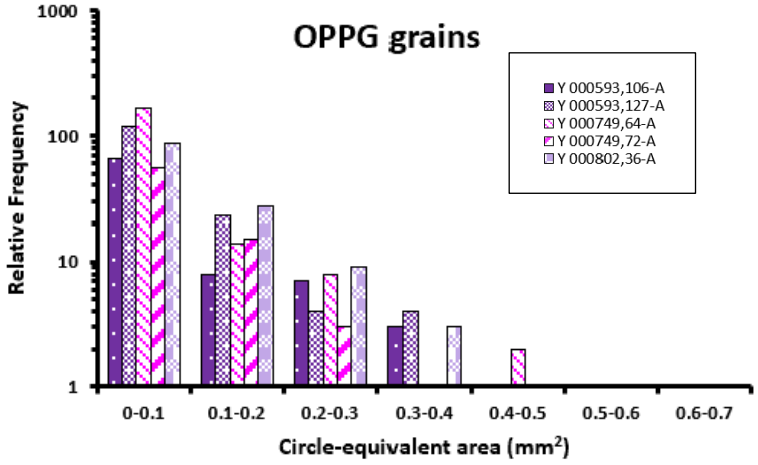

Figure 8.4*. EBSD circle equivalent area (OPPG).*

Table 8.3. *EBSD circle equivalent area (OPPG)*

Crystal Area (mm²)					
rel. abundance	**Y 000593** 106-A	**Y 000593** 127-A	**Y 000749** 64-A	**Y 000749** 72-A	**Y 000802** 36-A
0-0.1	66	119	168	56	87
0.1-0.2	8	23	14	15	27
0.2-0.3	7	4	8	3	9
0.3-0.4	3	4	1	1	3
0.4-0.5	1		2		1
0.5-0.6		1			
0.6-0.7		1			

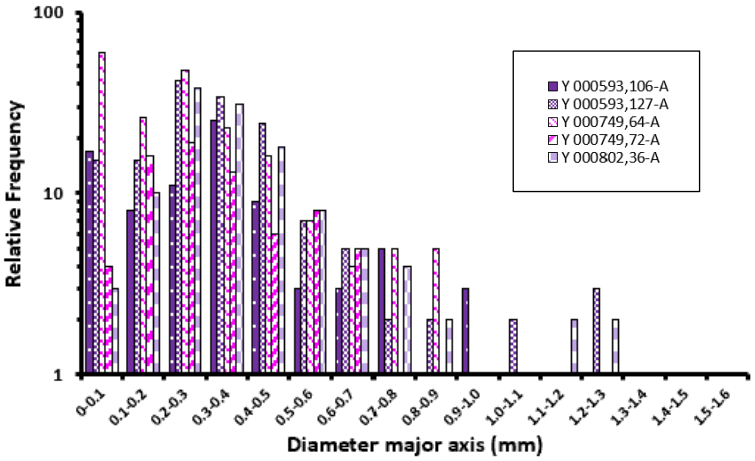

Figure 8.5. *EBSD major axis diameter of calculated ellipse (OPPG).*

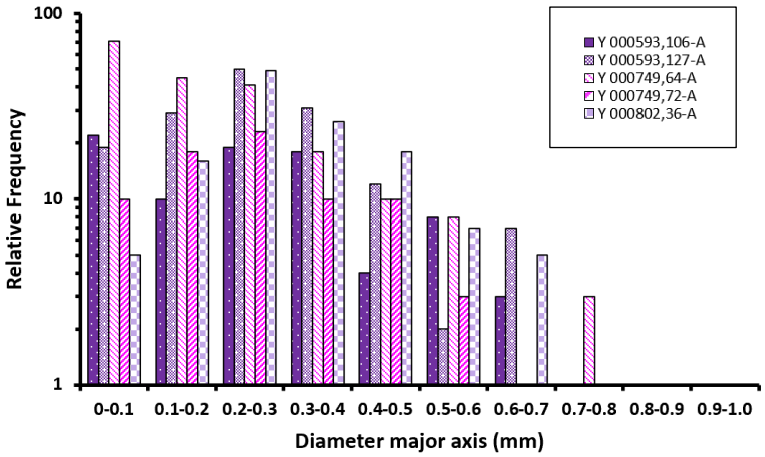

Figure 8.6. *EBSD long shape diameter of augite (OPPG).*

Table 8.4. *EBSD fitted slope major axis (OPPG)*

Diameter (mm)					
rel. abundance	**Y 000593** 106-A	**Y 000593** 127-A	**Y 000749** 64-A	**Y 000749** 72-A	**Y 000802** 36-A
0-0.1	17	15	60	4	3
0.1-0.2	8	15	26	16	10
0.2-0.3	11	42	48	19	38
0.3-0.4	25	34	23	13	31
0.4-0.5	9	24	16	6	18
0.5-0.6	3	7	7	8	8
0.6-0.7	3	5	4	5	5
0.7-0.8	5	2	5	1	4
0.8-0.9		2	5		2
0.9-1.0	3			1	1
1.0-1.1		2			1
1.1-1.2			1	1	2
1.2-1.3		3	1	1	2
1.3-1.4					1
1.4-1.5	1				1
1.5-1.6		1			

Table 8.5. *EBSD circle equivalent area (OPPG augite orientated to polished section surface).*

Crystal Area (mm²)					
rel. abundance	**Y 000593** 106-A	**Y 000593** 127-A	**Y 000749** 64-A	**Y 000749** 72-A	**Y 000802** 36-A
0-0.1	3	7	11	3	8
0.1-0.2					2
0.2-0.3	1				
0.3-0.4	1				
0.4-0.5					
0.5-0.6					
0.6-0.7					

Table 8.6. *EBSD length long shape-axis (OPPG)*

	Diameter (mm)				
rel. abundance	**Y 000593** 106-A	**Y 000593** 127-A	**Y 000749** 64-A	**Y 000749** 72-A	**Y 000802** 36-A
0-0.1	22	19	71	10	5
0.1-0.2	10	29	45	18	16
0.2-0.3	19	50	41	23	49
0.3-0.4	18	31	18	10	26
0.4-0.5	4	12	10	10	18
0.5-0.6	8	2	8	3	7
0.6-0.7	3	7		1	5
0.7-0.8	1		3		1
0.8-0.9		1			
0.9-1.0		1			

Table 8.7. *EBSD fitted slope major axis (OPPG augite orientated to polished section surface).*

	Diameter (mm)				
rel. abundance	**Y 000593** 106-A	**Y 000593** 127-A	**Y 000749** 64-A	**Y 000749** 72-A	**Y 000802** 36-A
0-0.1	1	2	5		
0.1-0.2		1	1		2
0.2-0.3	1	2	1	2	1
0.3-0.4	1		1		5
0.4-0.5		2	1		2
0.5-0.6			2		
0.6-0.7					
0.7-0.8	2				
0.8-0.9					
0.9-1.0					
1.0-1.1					
1.1-1.2					
1.2-1.3				1	

Table 8.8. *EBSD length long shape-axis (OPPG augite orientated to polished section surface).*

	Diameter (mm)				
rel. abundance	**Y 000593** 106-A	**Y 000593** 127-A	**Y 000749** 64-A	**Y 000749** 72-A	**Y 000802** 36-A
0-0.1	1	2	5	1	
0.1-0.2		2	3	1	2
0.2-0.3	1	1		1	3
0.3-0.4	1	1	3		5
0.4-0.5					1
0.5-0.6	1				
0.6-0.7	1				

Table 8.9. *EBSD circle equivalent area (All augite).*

	Crystal Area (mm²)				
rel. abundance	**Y 000593** 106-A	**Y 000593** 127-A	**Y 000749** 64-A	**Y 000749** 72-A	**Y 000802** 36-A
0-0.1	2707	435	8858	2347	800
0.1-0.2	36	24	24	34	39
0.2-0.3	14	5	15	10	17
0.3-0.4	7	4	3	4	4
0.4-0.5	3		2	2	1
0.5-0.6	1	1			1
0.6-0.7		1			

Table 8.10. *EBSD length long shape-axis (All augite).*

	Diameter (mm)				
rel. abundance	**Y 000593** 106-A	**Y 000593** 127-A	**Y 000749** 64-A	**Y 000749** 72-A	**Y 000802** 36-A
0-0.1	2554	306	8491	2168	614
0.1-0.2	77	56	224	104	75
0.2-0.3	44	62	106	55	95
0.3-0.4	43	31	50	32	48
0.4-0.5	14	13	17	22	25
0.5-0.6	15	3	15	9	15
0.6-0.7	7	7	3	5	6
0.7-0.8	3		3	2	1
0.8-0.9	1	1			1
0.9-1.0		1			

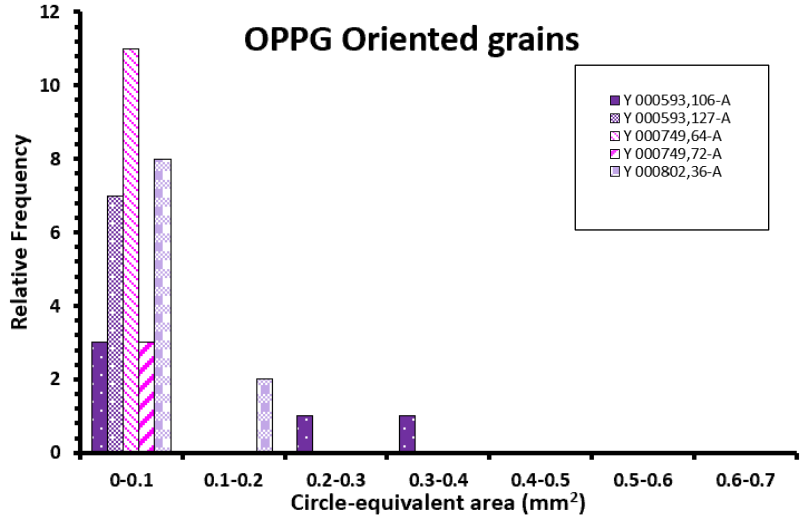

Figure 8.7. *EBSD circle equivalent area (OPPG augite orientated ±5° to polished section surface).*

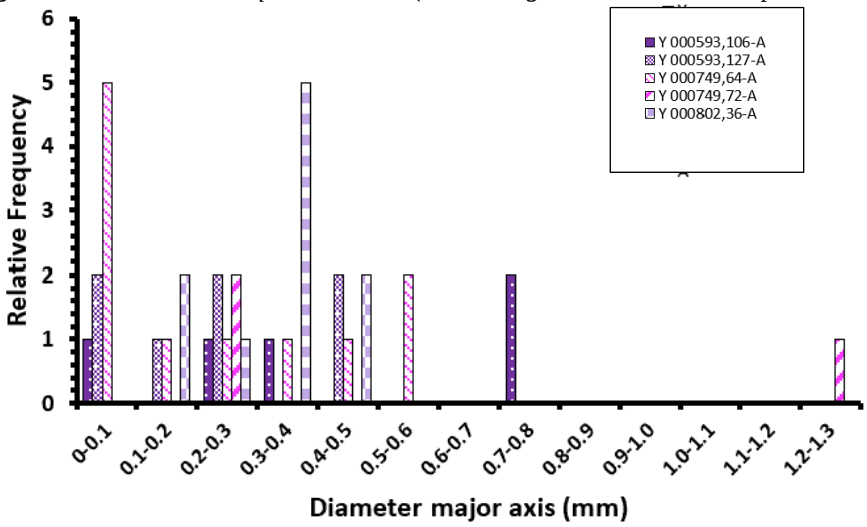

Figure 8.8. *EBSD major axis diameter of calculated ellipse (OPPG augite orientated ±5° to polished section surface).*

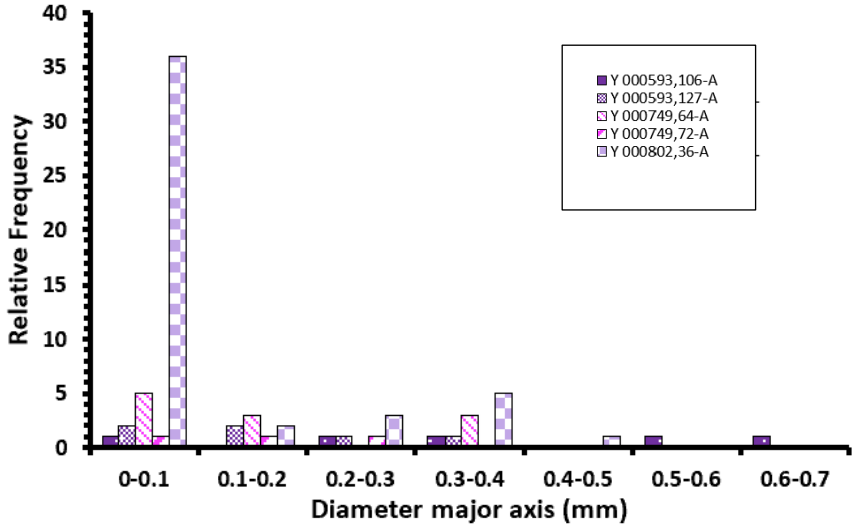

Figure 8.9. *EBSD long shape diameter of augite (OPPG augite orientated ±5° to polished section surface).*

Table 8.11. *EBSD fitted slope major axis (All augite).*

	Diameter (mm)				
rel. abundance	**Y 000593** 106-A	**Y 000593** 127-A	**Y 000749** 64-A	**Y 000749** 72-A	**Y 000802** 36-A
0-0.1	2501	276	8329	2086	576
0.1-0.2	92	57	288	143	80
0.2-0.3	51	59	147	69	76
0.3-0.4	51	39	65	36	64
0.4-0.5	16	25	37	18	34
0.5-0.6	14	8	16	19	15
0.6-0.7	12	6	6	12	11
0.7-0.8	8	2	8	1	8
0.8-0.9	2	2	6	1	4
0.9-1.0	5		4	5	1
1.0-1.1	1	2			3
1.1-1.2	1		2	3	3
1.2-1.3	1	3	1	4	2
1.3-1.4	1				1
1.4-1.5	2				1
1.5-1.6		1			1

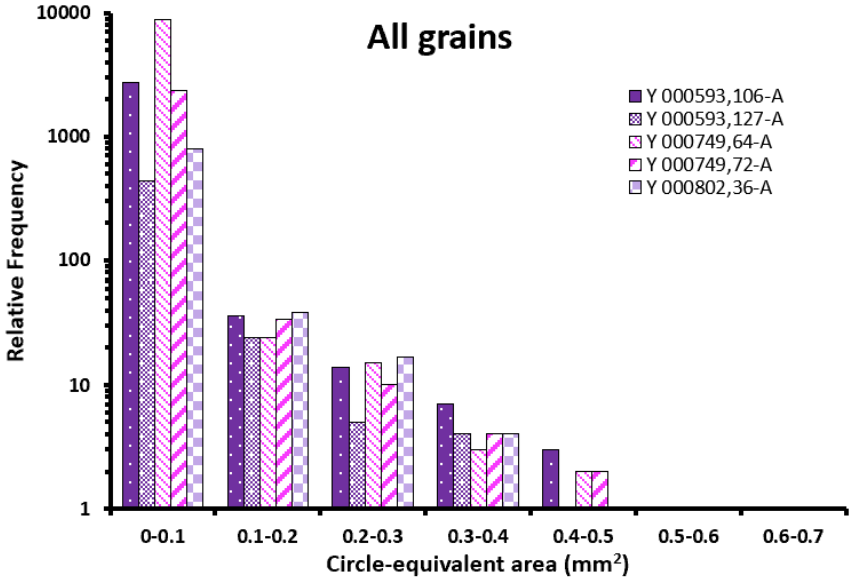

Figure 8.10. *EBSD circle equivalent area (All augite).*

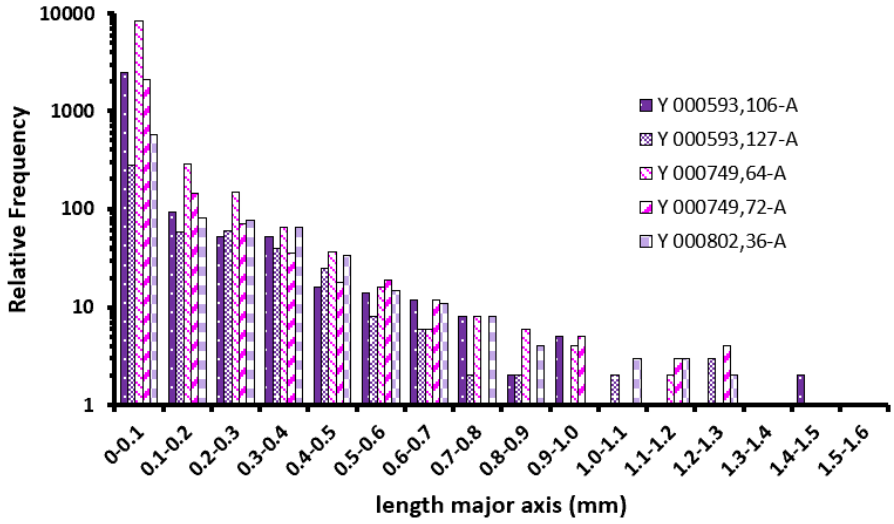

Figure 8.11. *EBSD major axis diameter of calculated ellipse (All augite).*

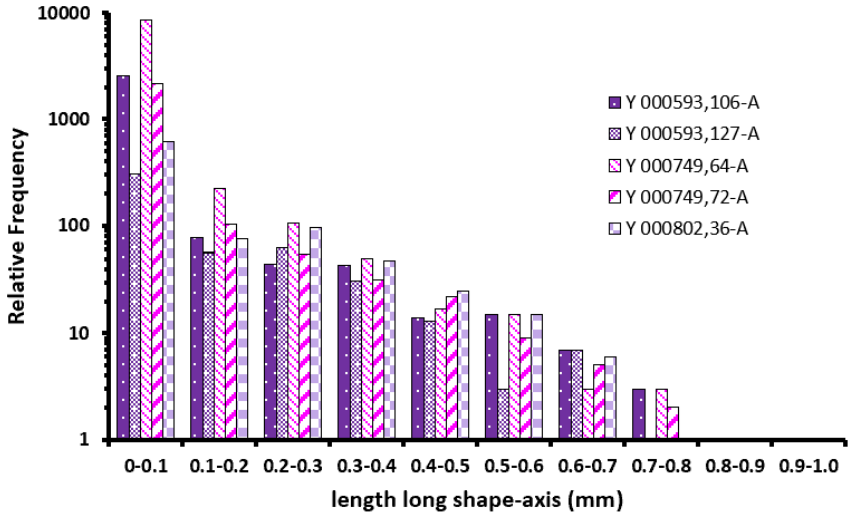

Figure 8.12. *EBSD long shape diameter of augite (All augite).*

Table 8.12. *EBSD circle equivalent area (augite orientated to polished section surface).*

Crystal Area (mm²)					
	Y 000593	**Y 000593**	**Y 000749**	**Y 000749**	**Y 000802**
rel. abundance	106-A	127-A	64-A	72-A	36-A
0-0.1	108	29	675	225	84
0.1-0.2	1			2	4
0.2-0.3	1	1			1
0.3-0.4	1			2	
0.4-0.5				1	
0.5-0.6					
0.6-0.7					

Table 8.13. *EBSD fitted slope major axis (augite orientated to polished section surface).*

Diameter (mm)					
	Y 000593	**Y 000593**	**Y 000749**	**Y 000749**	**Y 000802**
rel. abundance	106-A	127-A	64-A	72-A	36-A
0-0.1	98	23	649	208	134
0.1-0.2	5	3	15	7	7
0.2-0.3	3	2	6	7	6
0.3-0.4	2		2	2	8
0.4-0.5		2	1		2
0.5-0.6	1		2		1
0.6-0.7	1			2	3
0.7-0.8	2				
0.8-0.9					
0.9-1.0				2	
1.0-1.1					
1.1-1.2				1	
1.2-1.3				1	

Table 8.14. *EBSD length long shape-axis (augite orientated to polished section surface).*

Diameter (mm)					
	Y 000593	**Y 000593**	**Y 000749**	**Y 000749**	**Y 000802**
rel. abundance	106-A	127-A	64-A	72-A	36-A
0-0.1	99	25	658	212	62
0.1-0.2	6	2	11	6	12
0.2-0.3	3	1	3	6	6
0.3-0.4	2	1	3	2	5
0.4-0.5				1	2
0.5-0.6	1	1		2	1
0.6-0.7	1				
0.7-0.8				1	

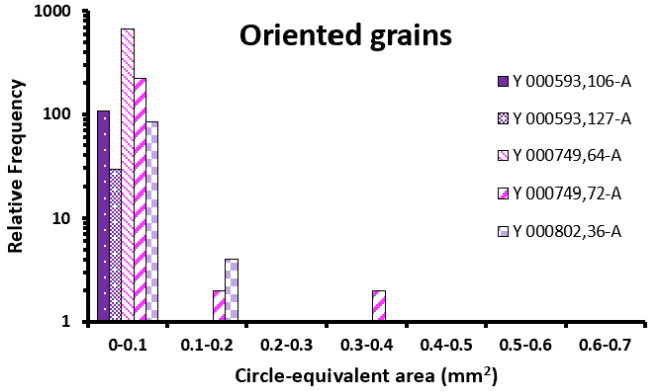

Figure 8.13. *EBSD circle equivalent area (all augite orientated ±5° to polished section surface).*

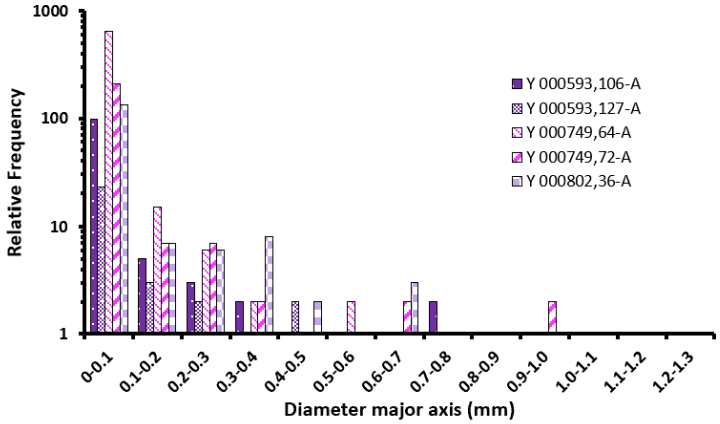

Figure 8.14. *EBSD major axis diameter of calculated ellipse (all augite orientated ±5° to polished section surface).*

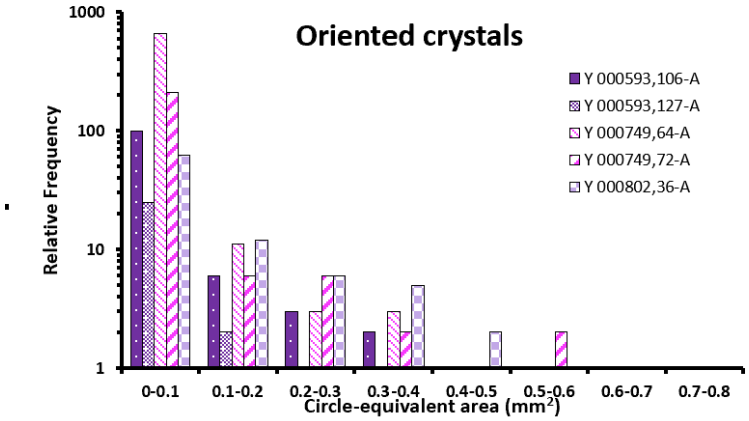

Figure 8.15. *EBSD long shape diameter of augite (orientated ±5° to polished section surface).*

Table 8.15 *EBSD Phase distribution within the nakhlites*

Sample	*Section*	**Px**	**Ol**	**Mss**
Y 000593	*106-A*	53.71	9.30	36.99
	127-A	52.64	12.30	35.06
Y 000749	*64-A*	44.72	3.54	51.74
	72-A	31.91	2.04	66.05
Y 000802	*36-A*	61.31	6.80	31.89

Table continued

CPx	**Opx**	**Ol**	**Plag**	**Chromite**	**Fe-oxides**	**Sulphides**	**Glass**	**Silicates**	**Alt**
53.70	0.01	9.30	1.18	0.00	0.39	0.18	0.00	0.54	0.02
52.60	0.04	12.30	0.21	0.00	1.40	0.00	0.00	0.01	0.00
44.70	0.02	3.54	0.01	0.00	0.60	0.00	0.00	0.00	0.00
31.80	0.11	2.04	0.01	0.00	0.10	0.00	0.00	0.04	0.01
61.30	0.01	6.80	0.10	0.00	1.04	0.00	0.00	0.02	0.00

8.1.2 CSD

Table 8.16. *CSD statistical data of the Nakhlites. Orange cells indicate the data discussed in this study. Dark orange cells indicate new data from this study all other data is sourced from Udry and Day (2018).*

Sample	No. of crystals	Total Area (mm^2)	R^2	Shape	Alignment factor	Big R	Orientation	Average size (mm)	1 SD
NWA 10645	134	100	0.76	1.00:1.20:3.60	0.13	1.48	Length	1.00	0.50
							Width	0.66	0.21
NWA 10645 corrected	134	100	0.76	1.00:1.20:1.60	0.13	1.48	Length	1.00	0.50
							Width	0.66	0.21
NWA 11013	532	93	0.86	1.00:1.25:1.80	0.07	1.29	Length	0.40	0.27
							Width	0.22	0.10
MIL 03346, 98	856	139	0.91	1.00:1.15:1.50	0.19	1.41	Length	0.45	0.38
							Width	0.26	0.12
MIL 090030, 21	382	61	0.91	1.00:1.20:1.40	0.19	1.47	Length	0.42	0.25
							Width	0.25	0.10
MIL 090032, 21	713	101	0.89	1.00:1.25:1.40	0.20	1.46	Length	0.43	0.26
							Width	0.25	0.10
MIL 090136, 5	673	100	0.89	1.00:1.20:1.40	0.10	1.45	Length	0.41	0.22
							Width	0.25	0.11
NWA 817	1477	242	0.89	1.00:1.25:1.40	0.16	1.35	Length	0.4	0.24
							Width	0.24	0.10
Y 000593, 127A	419	69	0.8985	1.00:1.15:1.60	0.17	1.43	Length	0.45	0.27
							Width	0.27	0.11
Y 000749, 64A	446	86	0.8688	1.00:1.30:2.00	0.12	1.39	Length	0.51	0.29
							Width	0.29	0.12
Y 000802, 36-A	227	40	0.8815	1.00:1.20:1.70	0.17	1.41	Length	0.46	0.31
							Width	0.27	0.11
Y 000593, 106A	118	22	0.84	1.00:1.25:1.90	0.10	1.44	Length	0.47	0.27
							Width	0.27	0.12
Y 000749, 72 A	193	34	0.84	1.00:1.30:1.80	0.12	1.36	Length	0.45	0.33
							Width	0.25	0.15
Y combined	311	60	0.9	1.00:1.30:1.90	0.11	X	Length	0.46	0.31
							Width	0.26	0.14
Nakhla, USNM 5891-2	1126	91	0.85	1.00:1.25:1.60	0.13	1.41	Length	0.32	0.18
							Width	0.19	0.08
Governador Valadares	382	38	0.89	1.00:1.15:1.50	0.25	1.47	Length	0.35	0.21
							Width	0.22	0.09
Lafayette, USNM 1805-8	756	19	0.85	1.00:1.30:1.70	0.12	1.43	Length	0.29	0.17
							Width	0.17	0.07
NWA 998	1471	128	0.88	1.00:1.25:1.90	0.05	1.45	Length	0.32	0.23
							Width	0.23	0.09
Caleta el Cobre 022*	2103	160	0.88	1.00:1.25:1.80	0.02	1.28	Length	0.27	0.18
							Width	0.15	0.07

Table continued

Sample	Max	Min	Slope (mm^{-1})	Intercept	T (years)[a] 10^{-9}	T (years)[a] 10^{-10}	Slope	Intercept	residence times	
NWA 10645	3.92	0.08	-0.77 ± 0.05	0.26 ± 0.19	41	411	-0.77	0.26	41	412
	0.08	0.04	-1.46 ± 0.14	2.07 ± 0.29	22	217	-1.46	2.07	22	217
NWA 10645 corrected	3.92	0.08	-1.72 ± 0.12	1.57 ± 0.20	18	184	-1.72	1.57	18	184
	0.08	0.04	-3.32 ± 0.34	3.54 ± 0.32	10	96	-3.32	3.54	10	96
NWA 11013	1.99	0.07	-3.55 ± 0.12	4.60 ± 0.10	9	89	-3.55	4.60	9	89
	0.58	0.05	-6.89 ± 0.32	6.70 ± 0.15	5	46	-6.89	6.70	5	46
MIL 03346, 98	1.96	0.05	-3.60 ± 0.10	4.45 ± 0.08	9	89	-3.56	4.45	9	89
	1.03	0.05	-6.01 ± 0.27	6.03 ± 0.14	5	53	-6.01	6.03	5	53
MIL 090030, 21	2.08	0.08	-4.48 ± 0.19	4.97 ± 0.12	7	71	-4.48	4.97	7	71
	0.72	0.04	-6.91 ± 0.48	6.43 ± 0.21	5	46	-6.91	6.43	5	46
MIL 090032, 21	1.85	0.08	-4.66 ± 0.15	5.13 ± 0.09	7	68	-4.68	5.13	7	68
	0.6	0.04	-6.53 ± 0.35	6.36 ± 0.15	5	49	-6.53	6.36	5	49
MIL 090136, 5	1.47	0.06	-4.70 ± 0.16	5.15 ± 0.10	7	67	-4.70	5.15	7	67
	0.75	0.04	-7.47 ± 0.33	6.37 ± 0.14	4	42	-7.487	6.37	4	42
NWA 817	2.43	0.06	-4.79 ± 0.10	5.09 ± 0.06	7	66	-4.79	5.09	7	66
	0.75	0.04	-7.82 ± 0.24	6.78 ± 0.10	4	41	-7.82	6.78	4	41
Y 000593, 127A	1.779	0.04	-3.45 ± 0.14	4.43 ± 0.2	9	92	-3.45	4.43	9	92
	0.66	0.03	-5.21 ± 0.33	5.67 ± 0.18	6	61	-5.21	5.67	6	61
Y 000749, 64A	2.66	0.11	-2.90 ± 0.12	4.04 ± 0.11	11	109	-2.90	4.04	11	109
	0.77	0.06	-4.26 ± 0.23	5.37 ± 0.17	7	74	-4.26	5.37	7	74
Y 000802, 36-A	2.87	0.12	-3.43 ± 0.21	4.39 ± 0.17	9	92	-3.43	4.39	9	92
	0.7	0.08	-4.90 ± 0.46	5.56 ± 0.26	6	65	-4.90	5.56	6	65
Y 000593, 106A	1.46	0.09	-2.86 ± 0.25	3.94 ± 0.23	11	111	-2.86	3.94	11	111
	0.84	0.04	-3.74 ± 0.57	5.03 ± 0.39	8	85	-3.74	5.03	8	85
Y 000749, 72 A	2.34	0.08	-3.03 ± 0.19	3.86 ± 0.16	10	105	-3.03	3.86	10	105
	0.82	0.03	-3.85 ± 0.35	4.67 ± 0.23	8	82	-3.85	4.67	8	82
Y combined	4.4	0.26	-2.82 ± 0.14	3.79 ± 0.13	11	112	-2.82	3.79	11	112
Nakhla, USNM 5891-2	1.92	0.03	-3.76 ± 0.29	4.76 ± 0.20	8	84	-3.76	4.76	8	84
	1.54	0.08	-5.43 ± 0.15	6.09 ± 0.08	6	58	-5.43	6.09	6	58
Governador Valadares	0.52	0.03	-7.65 ± 0.30	7.28 ± 0.12	4	41	-7.65	7.28	4	41
	2.41	0.04	-4.70 ± 0.21	5.58 ± 0.13	7	67	-4.70	5.58	7	67
Lafayette, USNM 1805-8	0.65	0.03	-8.01 ± 2.54	6.64 ± 1.23	4	40	-8.01	6.64	4	40
	1.11	0.07	-5.68 ± 0.30	6.35 ± 0.15	6	56	-5.68	6.35	6	56
NWA 998	0.57	0.05	-8.61 ± 0.55	7.80 ± 0.20	4	37	-8.61	7.80	4	37
	2.69	0.03	-3.25 ± 0.35	4.66 ± 0.52	10	98	-3.25	4.66	10	98
Caleta el Cobre 022*	0.60	0.03	-6.45 ± 0.80	6.41 ± 0.44	5	49	-6.45	6.41	5	49
	2.11	0.04	-5.31 ± 0.09	6.01 ± 0.05	6	60	-5.31	6.01	6	60
	0.65	0.03	-8.07 ± 0.22	7.33 ± 0.08	4	40	-8.07	7.33	4	39

a. T in years using growth rates of 10-9 mm/s and (Cashman and Marsh, 1988; Jerram et al., 2003) and 10-10 mm/s (Leu et al., 2010)

*From Krämer Ruggiu 2020

Table 8.17. *Summarised CSD statistical data of the Nakhlites. Orange cells indicate the data discussed in this study. Dark orange cells indicate new data from this study all other data is sourced from Udry and Day (2018)*

Sample	No. of crystals	Total Area (mm^2)	R^2	Shape	Average ol length (mm)	Big R	Orientation	Average px length (mm)	1 SD	Max	Min	Slope (mm^{-1})
NWA 10645	134	100	0.76	1.00:1.20:3.60	0.87	1.475	Length	1.00	0.50	3.92	0.08	-0.77 ± 0.05
NWA 10645 corrected	134	100	0.76	1.00:1.20:1.60	0.87	1.475	Length	1.00	0.50	3.92	0.08	-1.72 ± 0.12
NWA 11013	532	93	0.86	1.00:1.25:1.80	3.00	1.291	Length	0.40	0.27	1.99	0.07	-3.55 ± 0.12
MIL 03346, 98	856	136	0.91	1.00:1.15:1.50	1.90	1.410	Length	0.45	0.38	1.96	0.05	-3.59 ± 0.10
MIL 090030, 21	382	61	0.91	1.00:1.20:1.40	0.58	1.469	Length	0.42	0.25	2.08	0.08	-4.48 ± 0.19
MIL 090032, 21	713	101	0.90	1.00:1.25:1.40	0.89	1.459	Length	0.43	0.25	1.91	0.08	-4.68 ± 0.15
MIL 090136, 5	673	97	0.89	1.00:1.20:1.40	0.72	1.446	Length	0.41	0.22	1.47	0.06	-4.70 ± 0.16
NWA 817	1477	242	0.89	1.00:1.25:1.40	0.53	1.354	Length	0.40	0.24	2.43	0.06	-4.79 ± 0.10
Y 000593, 127A	419	69	0.90	1.00:1.15:1.60	0.64	1.430	Length	0.45	0.27	1.78	0.04	-3.45 ± 0.14
Y 000749, 64A	446	86	0.87	1.00:1.30:2.00	0.56	1.393	Length	0.51	0.29	2.66	0.11	-2.90 ± 0.12
Y 000802, 36-A	227	40	0.88	1.00:1.20:1.70	0.63	1.412	Length	0.46	0.31	2.87	0.12	-3.43 ± 0.21
Y 000593, 106A	118	22	0.84	1.00:1.25:1.90	0.61	1.441	Length	0.47	0.27	1.46	0.09	-2.85 ± 0.25
Y 000749, 72 A	193	34	0.84	1.00:1.30:1.80	0.41	1.355	Length	0.45	0.33	2.34	0.08	-3.03 ± 0.19
Y combined Nakhla,	311	60	0.9	1.00:1.30:1.90	0.51	X	Length	0.50	0.31	4.4	0.26	-2.82 ± 0.14
USNM 5891-2	1126	91	0.85	1.00:1.25:1.60	0.58	1.413	Length	0.32	0.18	1.54	0.08	-5.43 ± 0.15
Governador Valadares	382	38	0.89	1.00:1.15:1.50	0.65	1.470	Length	0.35	0.21	2.41	0.04	-4.70 ± 0.21
Lafayette, USNM 1805-8	756	19	0.85	1.00:1.30:1.70	0.31	1.431	Length	0.29	0.17	1.11	0.07	-5.68 ± 0.30
NWA 998	1471	128	0.88	1.00:1.25:1.90	0.38	1.453	Length	0.32	0.23	2.69	0.03	-3.25 ± 0.35
NWA 5790 a								0.30				-4.00
NWA 5790 b								0.28				-5.30
Caleta el Cobre 022	2103	160	0.88	1.00:1.25:1.80	0.02	1.28	Length	0.27	0.18	2.11	0.04	-5.31 ± 0.09

Table continued

Intercept	Pyroxene %	Alignment factor	T (years) [a] 10^{-9}	T (years) [a] 10^{-10}		Slope	Intercept	residence times		*error* ±	vv	Slope/intercept
0.26 ± 0.19	61.8	0.13	41	411	NWA 10645	-0.72	0.08	44	440		0.02	-9.00
1.57 ± 0.20	61.8	0.13	18	184	NWA 10645 corrected	-1.61	1.41	20	197		0.05	-1.14
4.60 ± 0.10	55.0	0.07	9	89	NWA 11013	-2.92	3.95	11	109		0.09	-0.74
4.46 ± 0.08	69.1	0.19	9	88	MIL 03346, 98	-3.28	4.19	10	97		0.10	-0.78
4.97 ± 0.12	73.5	0.19	7	71	MIL 090030, 21	-3.73	4.41	8	85		0.12	-0.85
5.16 ± 0.09	66.9	0.20	7	68	MIL 090032, 21	-4.18	4.79	8	76		0.13	-0.87
5.18 ± 0.10	72.1	0.10	7	67	MIL 090136, 5	-4.66	5.15	7	68		0.15	-0.90
5.09 ± 0.06	63.1	0.16	7	66	NWA 817	-4.18	4.64	8	76		0.13	-0.90
4.43 ± 0.20	67.2	0.17	9	92	Y 000593	-3.61	4.61	9	88	*4*	0.11	-0.78
4.04 ± 0.11	70.4	0.12	11	109	Y 000749	-3.03	4.18	10	105	*4*	0.10	-0.72
4.39 ± 0.17	66.8	0.17	9	92	Y 000802	-3.43	4.39	9	88	*6*	0.11	-0.78
3.89 ± 0.23	72.1	0.10	11	111	Y000593, 106A	-2.72	3.77	12	117		0.09	-0.72
3.86 ± 0.16	68.8	0.12	10	105	Y 000749, 72 A	-2.84	3.70	11	112		0.09	-0.77
3.79 ± 0.13	70.5	0.11	11	112	Y combined	-2.76	3.71	11	115		0.09	-0.74
6.09 ± 0.08	77.1	0.13	6	58	Nakhla, USNM 5891-2	-5.51	6.15	6	58		0.17	-0.90
5.58 ± 0.13	73.9	0.25	7	67	Governador Valadares	-3.54	4.52	9	89		0.11	-0.78
6.35 ± 0.15	76.1	0.12	6	56	Lafayette, USNM 1805-8	-4.85	5.71	7	65		0.15	-0.85
4.66 ± 0.52	71.7	0.05	10	98	NWA 998	-2.48	3.83	13	128		0.08	-0.65
	53.1				NWA 5790 a	-4.00	3.10	8	79		0.13	-1.29
	53.1				NWA 5790 b	-5.30	4.15	6	60		0.17	-1.28
6.01 ± 0.05					Caleta el Cobre 022	-5.31	6.01	6	60		0.17	-0.88

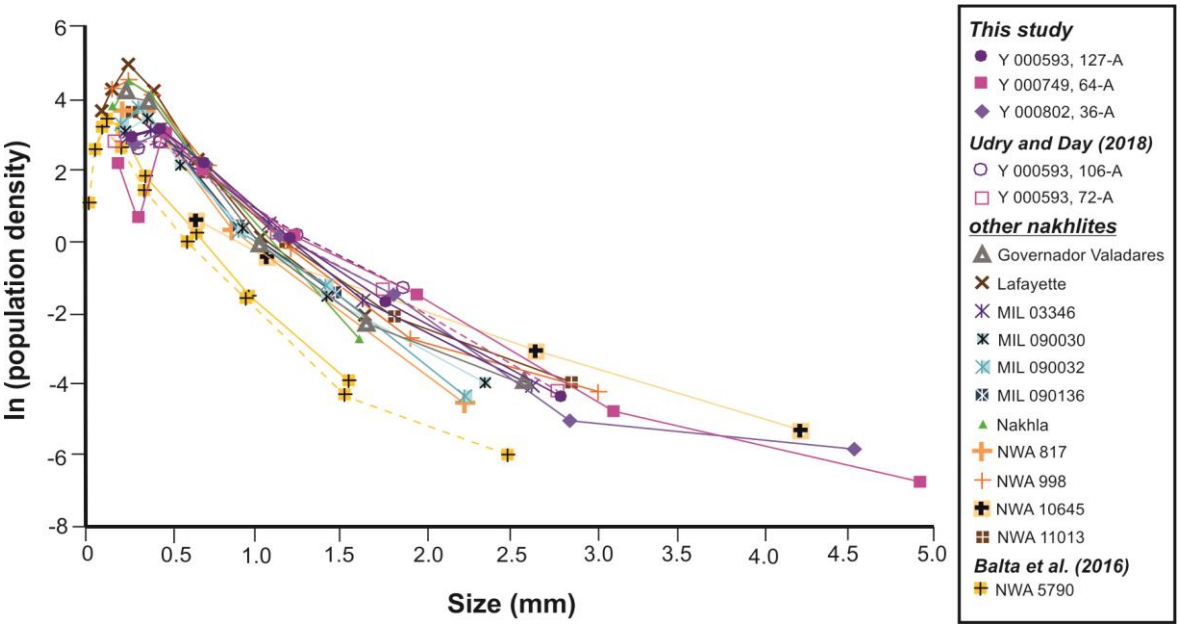

Figure 8.16. *CSD slopes of all nakhlites. This figure is a fully coloured version of figure 2.3 in-text.*

Table 8.18. *CSD slope data for the nakhlites. Orange heading refer to the Yamato nakhlites discussed in this study. Dark orange cells indicate new data, all other data is sourced from Udry and Day (2018).*

This study

Y 000593 (127-A)

Length Thick section					Width Thick section				
Size	**Population**	**Min**	**max**	**Vol%**	**Size**	**Population**	**Min**	**max**	**Vol%**
2.80	-4.36	-5.22	-3.91	16.23	1.28	-2.20	-2.89	-1.80	6.19
1.77	-1.72	-2.01	-1.50	35.98	0.81	1.23	1.08	1.37	30.37
1.12	0.21	0.05	0.35	39.58	0.51	3.31	3.22	3.39	38.31
0.70	2.15	2.05	2.24	43.45	0.32	3.73	3.60	3.84	9.25
0.44	3.02	2.92	3.11	16.41	0.20	3.05	2.55	3.39	0.75
0.28	2.89	2.68	3.06	2.29	0.13				
0.18					0.08				
0.11					0.05				
0.07									

Y 000749 (64-A)

Length Thick section					Width Thick section				
Size	**Population**	**Min**	**max**	**Vol%**	**Size**	**Population**	**Min**	**max**	**Vol%**
4.91	-6.75	#NAME?	-6.06	10.13	1.60	-2.34	-2.87	-2.00	9.49
3.10	-4.76	-5.67	-4.30	11.74	1.01	0.98	0.85	1.10	41.67
1.95	-1.52	-1.72	-1.35	47.68	0.64	2.86	2.78	2.93	43.27
1.23	0.12	-0.02	0.25	39.12	0.40	3.32	3.20	3.42	10.85
0.78	1.89	1.80	1.97	36.11	0.25				
0.49	2.72	2.62	2.81	13.12	0.16				
0.31	0.55	#NAME?	1.26	0.24	0.10				
0.20	2.15	1.77	2.42	0.19					

Y 000802 (36-A)

Length Thick section					Width Thick section				
Size	**Population**	**Min**	**max**	**Vol%**	**Size**	**Population**	**Min**	**max**	**Vol%**
4.52	-5.85	#NAME?	-5.15	23.02	1.36	-3.12	#NAME?	-2.43	2.90
2.85	-5.03	#NAME?	-4.29	8.24	0.86	1.16	0.95	1.33	33.33
1.80	-1.53	-1.88	-1.28	43.24	0.54	3.09	2.97	3.20	36.51
1.14	0.16	-0.06	0.35	37.36	0.34	3.71	3.55	3.84	10.66
0.72	1.94	1.80	2.06	35.05	0.22				
0.45	3.02	2.89	3.14	16.37	0.14				
0.29	2.67	2.31	2.94	1.83					
0.18									

Udry and Day (2018)

Y 000593 (106-A)

Length Thick section					Width Thick section				
Size	**Population**	**Min**	**max**	**Vol%**	**Size**	**Population**	**Min**	**max**	**Vol%**
1.93	-1.42	-1.86	-1.12	53.56	1.52	-2.66	infinity	-1.97	5.97
1.22	0.27	-0.01	0.49	46.06	0.96	1.25	0.99	1.45	47.18
0.77	1.78	1.57	1.95	32.89	0.61	2.98	2.82	3.13	42.54
0.49	2.70	2.48	2.87	13.07	0.38	3.25	2.97	3.47	8.80
0.31	2.74	2.32	3.03	2.16	0.24				
0.19					0.15				
0.12					0.10				

Y 000749 (72-A)

Length Thick section					Width Thick section				
Size	**Population**	**Min**	**max**	**Vol%**	**Size**	**Population**	**Min**	**max**	**Vol%**
2.79	-4.11	-5.33	-3.57	18.36	1.44	-1.72	-2.41	-1.32	14.30
1.76	-1.33	-1.66	-1.08	46.75	0.91	1.13	0.91	1.30	39.05
1.11	0.24	0.01	0.43	35.73	0.57	2.74	2.58	2.87	30.98
0.70	1.64	1.46	1.80	22.93	0.36	3.06	2.82	3.26	6.81
0.44	2.75	2.59	2.90	11.03	0.23	3.43	3.05	3.70	1.55
0.28	2.86	2.56	3.09	1.95	0.14	3.55	2.70	4.01	0.28
0.18	2.76	2.02	3.18	0.28	0.09				
0.11					0.06				
0.07					0.04				
0.04									

Table 8.19. *Augite spatial distribution pattern data.*

Px	Section	% Melt CSD corr	Big R	Phase ab CSD corr
From Udry and Day (2018)				
NWA 10645		40.69	1.48	59.31
NWA 11013	B	45.13	1.29	54.87
MIL 03346	98	32.27	1.41	67.73
MIL 090030	21	40.09	1.47	59.91
MIL 090032	21	31.23	1.46	68.77
MIL 090136	5	36.83	1.45	63.17
NWA 817		43.18	1.36	56.82
Y 000593	106-A	31.2	1.44	68.8
Y 000749	72-A	37.32	1.36	62.68
Nakhla	USNM 5891-2	29.58	1.41	70.42
Governador Valadares		29.48	1.47	70.52
Lafayette	USNM 1805-8	30.98	1.43	69.02
NWA 998		35.19	1.45	64.81
This study				
Y 000593	127-A	33.43	1.43	66.57
Y 000749	64-A	29.68	1.39	70.32
Y 000802	36-A	33.35	1.41	66.65

Table 8.20. *Modal abundances (%) calculated using CSD data. Orange cells refer to the Yamato nakhlites.*

	Section	Px	Ol	Mss	CPx	Ol	Glass	Plagioclase	Opx	Chromite	Fe-oxides
Udry and Day (2018)											
NWA 10645		61.8	1.7	36.5	61.8	1.7	0.0	33.5	0.0	0.0	3.0
NWA 11013	B	55.0	11.7	33.4	55.0	11.7	0	32.4	0.0	0.0	1.0
MIL 03346	98	69.1	7.3	23.6	69.1	7.3	19.1	0.0	0.0	0.0	4.5
MIL 090030	21	73.5	3.9	22.6	73.5	3.9	18.6	0.0	0.0	0.0	4.0
MIL 090032	21	66.9	9.3	23.7	66.9	9.3	19.2	0.0	0.0	0.0	4.5
MIL 090136	5	72.1	7.4	20.5	72.1	7.4	16.4	0.0	0.0	0.0	4.1
NWA 817		63.1	12.3	24.5	63.1	12.3	24.5	0.0	0.0	0.0	2.6
Nakhla	USNM 5891-2	77.1	11.0	11.9	77.1	11.0	0.0	10.4	0.0	0.0	1.5
Governador Valadares		73.9	12.9	13.2	73.9	12.9	12.2	0.0	0.0	0.0	1.0
Lafayette	USNM 1805-8	76.1	10.1	13.8	76.1	10.1	8.9	3.6	0.0	0.0	1.3
NWA 998		71.7	12.0	16.3	71.7	12.0	0.0	10.5	4.2	0.0	1.2
Y 000593	106-A	72.1	14.9	12.9	72.1	14.9	0.0	9.2	0.0	0.0	3.7
Y 000749	72-A	68.8	10.8	20.3	68.8	10.8	0.0	16.3	0.0	0.0	4.0
Chassigny		1.7	91.4	6.9	0.0	91.4	0.0	5.7	1.7	1.2	0.0
NWA 2737		2.0	90.7	7.3	0.0	90.7	0.0	4.6	2.0	2.7	0.0
This Study											
Y 000593	127-A	67.2	15.8	17.0	67.2	15.8	0.0	16.2	0.0	0.0	0.8
Y 000749	64-A	70.4	10.8	18.8	70.4	10.8	0.0	17.9	0.0	0.0	0.9
Y 000802	36-A	66.3	15.6	18.1	66.3	15.6	0.0	16.2	0.0	0.0	1.9

8.2 MTEX code

Nakhlite input parameters

8.2.1 Nakhlite Thickness Calculation variables

Caleta el Cobre 022 (CEREGE)

```
rhoS       = 3048;   % Density of solid [g/m^3];
rhoM       = 2693;   % Density of melt [g/m^3];
muDry      = 326;    % dry melt viscosity [g/ms];
muWet      = 297;    % wet melt viscosity [g/ms];
MapArea    = 81831573;    % scan area [µm²]
TE         = 0.0000217;    % Thermal expansivity coefficient from EBSD mineralogy
RT         = 189216000;    % Residence time [s]
```

Governador Valadares (BM.1975,M16, P8469)

```
rhoS       = 3235;   % Density of solid [g/m^3];
rhoM       = 2784;   % Density of melt [g/m^3];
muDry      = 270;    % dry melt viscosity [g/ms];
muWet      = 250;    % wet melt viscosity [g/ms];
MapArea    = 15478668;    % scan area [µm²]
TE         = 0.000024;    % Thermal expansivity coefficient from EBSD mineralogy
RT         = 220752000;    % Residence time [s]
```

Governador Valadares (BM.1975,M16, P19783)

```
rhoS       = 3149;   % Density of solid [g/m^3];
rhoM       = 2722;   % Density of melt [g/m^3];
muDry      = 336;    % dry melt viscosity [g/ms];
muWet      = 301;    % wet melt viscosity [g/ms];
MapArea    = 21027600;    % scan area [µm²]
TE         = 0.0000228;    % Thermal expansivity coefficient from EBSD mineralogy
RT         = 220752000;    % Residence time [s]
```

Lafayette (USNM 1505-5)

```
rhoS       = 3196;   % Density of solid [g/m^3];
rhoM       = 2757;   % Density of melt [g/m^3];
muDry      = 294;    % dry melt viscosity [g/ms];
muWet      = 270;    % wet melt viscosity [g/ms];
MapArea    = 73556688;    % scan area [µm²]
TE         = 0.0000236;    % Thermal expansivity coefficient from EBSD mineralogy
RT         = 189216000;    % Residence time [s]
```

MIL 03346 (118)

```
rhoS       = 3096;   % Density of solid [g/m^3];
rhoM       = 2710;   % Density of melt [g/m^3];
muDry      = 335;    % dry melt viscosity [g/ms];
muWet      = 306;    % wet melt viscosity [g/ms];
MapArea    = 106457520;    % scan area [µm²]
TE         = 0.000022;    % Thermal expansivity coefficient from EBSD mineralogy
RT         = 283824000;    % Residence time [s]
```

MIL 090030 (62)

```
rhoS       = 3092;   % Density of solid [g/m^3];
rhoM       = 2710;   % Density of melt [g/m^3];
muDry      = 324;    % dry melt viscosity [g/ms];
muWet      = 298;    % wet melt viscosity [g/ms];
MapArea    = 79637733;    % scan area [µm²]
TE         = 0.0000238;    % Thermal expansivity coefficient from EBSD mineralogy
RT         = 220752000;    % Residence time [s]
```

MIL 090032 (108)

```
rhoS       = 3208;   % Density of solid [g/m^3];
rhoM       = 2788;   % Density of melt [g/m^3];
muDry      = 242;    % dry melt viscosity [g/ms];
muWet      = 227;    % wet melt viscosity [g/ms];
MapArea    = 14685300;    % scan area [µm²]
TE         = 0.000024;    % Thermal expansivity coefficient from EBSD mineralogy
RT         = 220752000;    % Residence time [s]
```

MIL 090136 (50)

rhoS = 3080; % Density of solid [g/m^3];
rhoM = 2701; % Density of melt [g/m^3];
muDry = 336; % dry melt viscosity [g/ms];
muWet = 308; % wet melt viscosity [g/ms];
MapArea = 43170379.7; % scan area [µm²]
TE = 0.0000225; % Thermal expansivity coefficient from EBSD mineralogy
RT = 220752000; % Residence time [s]

Nakhla (USNM 426-1)

rhoS = 3151; % Density of solid [g/m^3];
rhoM = 2721; % Density of melt [g/m^3];
muDry = 342; % dry melt viscosity [g/ms];
muWet = 308; % wet melt viscosity [g/ms];
MapArea = 209570940; % scan area [µm²]
TE = 0.000023; % Thermal expansivity coefficient from EBSD mineralogy
RT = 189216000; % Residence time [s]

Nakhla (WAM 12965)

rhoS = 3150; % Density of solid [g/m^3];
rhoM = 2723; % Density of melt [g/m^3];
muDry = 338; % dry melt viscosity [g/ms];
muWet = 303; % wet melt viscosity [g/ms];
MapArea = 13376250; % scan area [µm²]
TE = 0.0000228; % Thermal expansivity coefficient from EBSD mineralogy
RT = 189216000; % Residence time [s]

NWA 817 (N8-1)

rhoS = 3057; % Density of solid [g/m^3];
rhoM = 2677; % Density of melt [g/m^3];
muDry = 282; % dry melt viscosity [g/ms];
muWet = 257; % wet melt viscosity [g/ms];
MapArea = 7598940.5; % scan area [µm²]
TE = 0.0000239; % Thermal expansivity coefficient from EBSD mineralogy
RT = 220752000; % Residence time [s]

NWA 998 (T1)

rhoS = 3110; % Density of solid [g/m^3];
rhoM = 2716; % Density of melt [g/m^3];
muDry = 317; % dry melt viscosity [g/ms];
muWet = 288; % wet melt viscosity [g/ms];
MapArea = 9864462.5; % scan area [µm²]
TE = 0.0000226; % Thermal expansivity coefficient from EBSD mineralogy
RT = 315360000; % Residence time [s]

NWA 998 (UG-1)

rhoS = 3210; % Density of solid [g/m^3];
rhoM = 2771; % Density of melt [g/m^3];
muDry = 261; % dry melt viscosity [g/ms];
muWet = 243; % wet melt viscosity [g/ms];
MapArea = 36143739; % scan area [µm²]
TE = 0.000024; % Thermal expansivity coefficient from EBSD mineralogy
RT = 315360000; % Residence time [s]

NWA 10153 SH65 (T-2_2)

rhoS = 3021; % Density of solid [g/m^3];
rhoM = 2680; % Density of melt [g/m^3];
muDry = 445; % dry melt viscosity [g/ms];
muWet = 393; % wet melt viscosity [g/ms];
MapArea = 112838265; % scan area [µm²]
TE = 0.0000235; % Thermal expansivity coefficient from EBSD mineralogy
RT = 283824000; % Residence time [s]

NWA 11013 (UG-1)

rhoS = 3029; % Density of solid [g/m^3];
rhoM = 2675; % Density of melt [g/m^3];
muDry = 355; % dry melt viscosity [g/ms];
muWet = 323; % wet melt viscosity [g/ms];
MapArea = 37009563; % scan area [µm²]

TE = 0.000022; % Thermal expansivity coefficient from EBSD mineralogy
RT = 283824000; % Residence time [s]
NWA 12542 (F83-1)
rhoS = 3196; % Density of solid [g/m^3];
rhoM = 2769; % Density of melt [g/m^3];
muDry = 269; % dry melt viscosity [g/ms];
muWet = 250; % wet melt viscosity [g/ms];
MapArea = 113650290; % scan area [µm²]
TE = 0.0000242; % Thermal expansivity coefficient from EBSD mineralogy
RT = 220752000; % Residence time [s]
Y 000593 (106-A)
rhoS = 3236; % Density of solid [g/m^3];
rhoM = 2786; % Density of melt [g/m^3];
muDry = 273; % dry melt viscosity [g/ms];
muWet = 252; % wet melt viscosity [g/ms];
MapArea = 36090252; % scan area [µm²]
TE = 0.0000234; % Thermal expansivity coefficient from EBSD mineralogy
RT = 346896000; % Residence time [s]
Y 000593 (127-A)
rhoS = 3228; % Density of solid [g/m^3];
rhoM = 2781; % Density of melt [g/m^3];
muDry = 271; % dry melt viscosity [g/ms];
muWet = 252; % wet melt viscosity [g/ms];
MapArea = 23782540.3; % scan area [µm²]
TE = 0.0000243; % Thermal expansivity coefficient from EBSD mineralogy
RT = 283824000; % Residence time [s]
Y 000749 (64-A)
rhoS = 3196; % Density of solid [g/m^3];
rhoM = 2763; % Density of melt [g/m^3];
muDry = 293; % dry melt viscosity [g/ms];
muWet = 270; % wet melt viscosity [g/ms];
MapArea = 64558010.9; % scan area [µm²]
TE = 0.0000228; % Thermal expansivity coefficient from EBSD mineralogy
RT = 346896000; % Residence time [s]
Y 000749 (72-A)
rhoS = 3172; % Density of solid [g/m^3];
rhoM = 2750; % Density of melt [g/m^3];
muDry = 301; % dry melt viscosity [g/ms];
muWet = 276; % wet melt viscosity [g/ms];
MapArea = 49922028; % scan area [µm²]
TE = 0.0000227; % Thermal expansivity coefficient from EBSD mineralogy
RT = 315360000; % Residence time [s]
Y 000802 (36-A)
rhoS = 3181; % Density of solid [g/m^3];
rhoM = 2754; % Density of melt [g/m^3];
muDry = 300; % dry melt viscosity [g/ms];
muWet = 270; % wet melt viscosity [g/ms];
MapArea = 35860550; % scan area [µm²]
TE = 0.0000235; % Thermal expansivity coefficient from EBSD mineralogy
RT = 283824000; % Residence time [s]

8.2.2 Magma body thickness code

Augite

CS_aug = crystalSymmetry ('12/m1', [9.7381 8.8822 5.2821], [90,106.23,90] * degree, 'X| |a*', 'Y| |b*', 'Z| |c', 'mineral', 'Augite')
disregard non-indexed data
ebsd = ebsd('indexed');
calculate grains
[grains, ebsd, grainID] = calcGrains(ebsd, 'boundary', 'tight', 'angle', 10*degree);
To remove single pixel grains (*i.e.* noise) we create a condition to check for grains <= 10 pixels (or any parameter of your choice) which we then delete from the grain dataset. (equivalent to wildspike)

```
cond = grains.grainSize <=10;
nnz(cond);
grains(cond) = [];
check data and set condition boundary
plot(grains)
histogram(diameter(grains('Augite')))
[nAug, edges]   = histcounts(diameter(grains('Augite')));
Separate mesostasis and phenocryst grains (number refers to pixels per grain) n.b. this separates all phases
cond1 = grains.diameter <=200;
nnz(cond1);
MesGrain = nnz(cond1);
cond2 = grains.diameter >=200;
nnz(cond2);
PhenGrain = nnz(cond2);
```

Estimating Sample thickness

use parameters from NakhliteVariables_ThicknessCalculation.mlx
Import accompanying *Griffin_NakhlitePetrofabrics.csv* filepath

```
filename      = 'Griffin_NakhlitePetrofabrics.csv';
delimiterIn   = ' ';
headerlinesIn = 1,2;
param         = importdata(filename,delimiterIn,headerlinesIn);
rhoS          =  3171995.655;   % Density of solid [g/m^3];
rhoM          =  2750378.353;   % Density of melt [g/m^3];
muDry         =  0.00109091;    % dry melt viscosity [m^2/s];
muWet         =  0.00101818;    % wet melt viscosity [m^2/s];
MapArea       =  49922028;    % scan area [µm²]
TE            =  0.0000227;    % Thermal expansivity coefficient from EBSD mineralogy
RT            =  315360000;    % Residence time [s]
```

Input parameters

```
kT      = 7.5e-7;  % Thermal diffusivity basalt [m^2/s]
sGR     = 1e-12;   % Silicate growth rate [m/s] Cashman and Marsh (1988) and Jerram et al. (2003)
cGR     = 1e-13;   % clinopyroxene growth rate [m/s] Leu (2010)
rhoSb   = 3370; % Density of solid (basalt) [g/m^3]
rhoMb   = 2860; % Density of melt (basalt) [g/m^3]
gravityM = 3.72;    % Mars gravity [m/s]
aPhen   = mean(area(PhenGrain('Augite')));   % average size of phenocryst grains classed as >200 pixels
[µm²]
aMes    = mean(area(MesGrain('Augite'))); %mean(area(MesGrain('Augite')));    % average size of
mesostasis grains >=10, <200 pixels [µm²]
theta   = 0.1;      % crystal volume fraction # as cumulate cannot use the difference between phen and map
```

Thermal Diffusion

```
Ddiff = sqrt(kT * RT)
```

Crystal growth = Crystal settling

```
LsettPhen = ((rhoS-rhoM)/muDry) * gravityM * (aPhen*1e-12) * (1-theta)^4 *RT
LsettMes = ((rhoS-rhoM)/muDry) * gravityM * (aMes*1e-12) * (1-theta)^4 *RT
```

Crystal settling with convection

```
Lconv = muDry/(RT*theta*(rhoS-rhoM)*gravityM)
```

8.2.3 CPO code

MTEX code for quantitative analysis of nakhlite CPO

adapted from Daly L., Piazolo S., Lee M. R., Griffin S., Chung P., Campanale F., Cohen B. E., Hallis L. J., Trimby P. W., Baumgartner R., Forman L. V., and Benedix G. K. (2019) Understanding the emplacement of Martian volcanic rocks using petrofabrics of the nakhlite meteorites., *Sci. Adv*. 5, 1–11.

Set up MTEX within MATLAB

Import data

```
startup_mtex;
```

1. click on import EBSD data hyperlink from the MTEX menu
2. add the .csc or .ctf file of choice (+ button on the right-hand side)
3. import relevant phases and orientations
4. hit run (button in top ribbon of MATLAB)
5. save file as .m fille
6. copy relevant crystallographic information from the script window into the command window:

or alternatively

```
ebsd = EBSD.load('fname')
```

where fname refers to the name of your file.

Crystallographic information used in this study:

Augite

```
CS_aug = crystalSymmetry ('12/m1', [9.7381 8.8822 5.2821], [90,106.23,90] * degree, 'X| |a*', 'Y| |b*', 'Z| |c', 'mineral', 'Augite');
```

and

Forsterite

```
CS_fors = crystalSymmetry ('mmm', [4.756 10.207 5.98], 'mineral', 'Forsterite')
```

For the code below we have used CS_aug remember to substitute the following terms

- 'Augite' for the name of your desired phase *e.g.*, 'Augite'
- aug for an abrreviated name of your chosen phase *e.g.*, aug
- 'point group' for the crystallographic space group description *e.g.*, 12/m1

Exact terms will be sourced from the crystallographic information generated during file input above

Assess data set

```
plot(ebsd, ebsd.orientations)
```

This will produce an IPF |z| map

Denoising data

For raw exported data that has not undergone noise reduction using a commercial programme we first need to clean the data and remove any known twin boundaries

To identify grains and create a separate list

```
[grains, ebsd, grainID] = calcGrains(ebsd, 'boundary', 'tight')
```

To remove single pixel grains (*i.e.*, noise) we create a condition to check for grains <= 2 pixels (or any parameter of your choice) which we then delete from the grain dataset. (equivalent to wildspike)

```
cond = grains.grainsize <=2;
mnz(cond)
ebsd(grains(cond)) = [];
```

Visually assess the data

```
plot(ebsd, ebsd.orientations)
hold on
plot(grains.boundary)
hold off
```

For any remaining pixels repeat lines 5-11

Plot grains

Input grain boundary conditions

```
[grains, ebsd.grainId, ebsd.mis2mean] = calcGrains(ebsd,'angle',10*degree);
```

plot grains

```
plot(grains)

cs = ebsd('Augite').CS;
ck = ipfHSVKey(cs);
ck.inversePoleFigureDirection = zvector;
```

```
plot(grains('Augite'),ck.orientation2color(grains('Augite').meanOrientation))
```
Smooth grain boundaries
```
F = halfQuadraticFilter;
F.alpha = 0.5;
grains = smooth(grains, F, 'fill');
```
Separate mesostasis and phenocryst grains
```
cond1 = grains.grainsize <=200;
mnz(cond1)
ebsd(grains(cond1)) = grains.mes;

cond2 = grains.grainsize >=200;
mnz(cond2)
ebsd(grains(cond2)) = grains.phen;
```
Where 200 refers to 200 pixels

Infill missing pixels

Visually check and select phase for infilling
```
ebsd('Augite');
ebsd('Augite').orientations;

plot(ebsd('Augite'),ebsd('Augite').orientations);
hold on
plot(grains.boundary,'linewidth',1.5)
hold off
```
Input fill parameters
```
F = halfQuadraticFilter;
F.alpha = 0.5;
```
Interpolate missing data
```
ebsd_aug_filled = smooth(ebsd('Augite'),F,'fill',grains('Augite'));
ebsd_aug_filled = ebsd_aug_filled('indexed');
```
Plot data to visually check
```
plot(ebsd_aug_filled('indexed'),ebsd_aug_filled.orientations)

hold on
plot(grains('Augite').boundary,'linewidth',1.5)
hold off
```

Identification and accounting for twin boundaries

define grain boundaries as a separate variable and isolate twin boundary
```
gB = grains.boundary;
gB_aug_aug = gB('Augite','Augite');
```
To identify the regions where twinning in present (*i.e.,* boundary conditions exceeding 10 degrees) we first visualise the grain boundaries
```
plot(gB_aug_aug, gB_aug_aug.misorientation.angle./degree,'linewidth',2)
mtexColorbar;
```
Plot the misorientation distribution
```
histogram(gB_aug_aug.misorientation.angle./degree,180)
xlabel('misorientation angle (degree)')
```
From the histogram we can further analyse the identified misorientation peaks as clusters,
where 180 refers to the misorientation degree
```
ind = gB_aug_aug.misorientation.angle>180*degree & gB_aug_aug.misorientation.angle<=180*degree;
mori = gB_aug_aug.misorientation(ind);
scatter(mori);
```
From the cluster we can determine the mean and whether there is a special relationship to the orientation, which will output the parameters to define our twin boundary
```
mori_mean = mean(mori,'robust');
round2Miller(mori_mean);
```
e.g., output for Augite
mori_mean = misorientation (show methods, plot)
size: 1 x 1
crystal symmetry : Augite (12/m1, X||a, Y||b, Z||c)*
crystal symmetry : Augite (12/m1, X||a, Y||b, Z||c)*
antipodal: true
Bunge Euler angles in degree

phi1 Phi phi2 Inv.
123.98 0.347742 55.5556 0
round2Miller(mori_mean);
(10-1) || (00-1) [0-10] || [010] error: 1.1°
From the generated output we can then define our misorientation boundaries

```
twinning = orientation.map(Miller(1,0,-1, CS_aug),Miller(0,0,-1, CS_aug),...
Miller(0,-1,0, CS_aug),Miller(0,1,0, CS_aug));
```

Check the misorientation rotation axis and angle

```
round(twinning.axis);
twinning.angle / degree;
```

e.g., output for augite
ans = Miller (show methods, plot)
size: 1 x 1
mineral: Augite (121, X||a, Y||b, Z||c)*
h -1
k 0
l 2
ans = 180
Visually Check each boundary segment against twinning boundary

```
isTwinning = angle(gB_aug_aug.misorientation,twinning) < 5*degree;
twinBoundary = gB_aug_aug(isTwinning);

plot(grains('Augite'),grains('Augite').meanOrientation);
hold on
plot(twinBoundary,'linecolor','w','linewidth',4,'displayName','twin boundary')
hold off;
```

Merge Twin grains
merge along twin boundary to form parent and child grains

```
[mergedGrains,parentId] = merge(grains,twinBoundary);

hold on
plot(mergedGrains.boundary,'linecolor','k','linewidth',2.5,'linestyle','-',...
'displayName','merged grains')
hold off
```

For quantitative metrics we need to update grain orientation within the merged child grains to a single crystallographic orientation to produce a single coherent parent grain. This needs to be done for every individual merged grain. To identify the parent grain ID, you click on the grain within the above generated map
For Augite we assign one of the daughter grains as the parent grain orientation in order to account for simple twinning (180 degrees rotation within the grain)

```
childs = grains(parentId == mergedGrains(#).id);

plot(childs,grains.prop.index)
histogram(childs.orientations)

childGOS_aug   = grains('Augite').GOS;
childArea_aug' = grains('Augite').area;

mergedGrains.prop.GOS = accumarray(parentId,1:length(grains),size(mergedGrains),...
nanmeanWeights(childGOS_aug,childArea_aug));
```

Update grain ID of merged grains

```
ebsd_merged = ebsd;

ebsd_merged('indexed').grainId = parentId(grains.id2ind(ebsd('indexed').grainId))
```

Smooth out internal grain orientation

```
F2 = meanFilter;
F2.numNeighbours = 1;
```

Where numNeighbours refers to the neighbouring pixel orientations averaged
Smooth the data

```
ebsdS = smooth(ebsd,F2);
ebsdS = ebsdS('grains');
```

To visually check data before undertaking quantitative metrics we can assess both phase and IPF maps

plot phase map of data with grain boundaries

```
plot(ebsdS);
hold on
plot(grains.boundary,'color','k','linewidth',1.5)
hold off;
```

Plot IPF of selected mineral with detected grain boundaries

```
plot(ebsd('Augite'),ebsd('Augite').orientations)

hold on
plot(grains.boundary,'linewidth',1.5)
hold off;
```

J-Index

The scale for J-Index goes from 0 - infinity ; For igneous rocks CPO values are:

- Random CPO <1.40
- weak CPO 1.40 - 1.80
- weak-medium CPO 1.80 - 2.40
- medium CPO 2.40 - 5.00
- medium to strong CPO 5.00 - 12.00
- strong CPO >12.00

```
odf_aug = calcDensity (grains.phen('Augite').orientations) ;
J_aug   = textureindex (odf_aug)
```

M-Index

M-Tex values range from 0 - 1. Where 0 is completely random and 1 is a single crystal. For igneous rocks values typically range from x-z

note M-index values for Augite (high-Ca clinopyroxene) will present anomolously low values (on the range of 0.01) which are uncoupled from the standard M-Index range.

```
[density_uniform, ~] = calcAngleDistribution(grains.phen(CS_aug)) ;
density_uniform      = density_uniform / sum(density_uniform) ;
mdf                  = calcMDF(grains.phen(odf_aug)) ;
[density_MDF, ~]     = calcAngleDistribution(mdf,'resolution', 1*degree) ;
density_MDF          = density_MDF / sum (density_MDF) ;
M_index              = (sum((abs(density_MDF-density_uniform)) / 2) )
```

Eigenvalue PGR-Index

Eigenvalue analysis assesses CPO along each crystallographic axis on the basis of point (P), girdle (G), and random (R). Calculated values range from 0 - 1, where the total sum for each for PGR calculation will always equal 1.

R values:

- Random CPO > 0.9

P and G values:

- No CPO < 0.1
- Weak CPO 0.1 - 0.3
- Moderate CPO 0.3 - 0.5
- Strong CPO > 0.5

establish orientation

```
o = (grains.phen('Augite').orientations) ;
```

establish co-ordinate frame

```
[x,y,z]         = double(v) ;
OT              = 1. / numel(x) * [x,y,z]' * [x,y,z] ;
[Vec, Diagonal] = eig(OT) ;
value           = diag(Diagonal) ;
[value, index]  = sort(value, 'descend') ;
vec1(1:3)       = Vec(:, index(1)) ;
vec2(1:3)       = Vec(:, index(2)) ;
vec3(1:3)       = Vec(:, index(3)) ;
NORM            = value(1) + value(2) + value(3) ;
```

PGR Miller (100)

establish Milles indices

```
v = o * Miller(1, 0, 0, grains.phen(CS_aug, 'Augite', 'point group')) ;
```

Output PGR values

```
calculate P(100) value
P100       = (value(1) - value(2)) / NORM ;
calculate G(100) value
G100       = (2.0 * (value(2) - value(3))) / NORM ;
Calculate R(100) value
R100       = (3.0 * value(3)) / NORM ;
Sum PGR values (PGR = 1)
PGR        = P100 + G100 + R100 ;
```

PGR Miller (010)

```
establish Milles indices
v = o * Miller (0, 1, 0, grains.phen(CS_aug, 'Augite', 'point group')) ;
```

Output PGR values

```
calculate P (010) value
 P010       = (value(1) - value(2)) / NORM ;
calculate G (010) value
 G010       = (2.0 * (value(2) - value(3))) / NORM ;
Calculate R (010) value
 R010       = (3.0 * value(3)) / NORM ;
Sum PGR values (PGR = 1)
 PGR        = P010 + G010 + R010 ;
```

PGR Miller (001)

```
establish Miller indices
 v = o * Miller (0, 0, 1, grains.phen(CS_aug, 'Augite', 'point group')) ;
```

Output PGR values

```
calculate P(001) value
 P001       = (value(1) - value(2)) / NORM ;
calculate G(001) value
 G001       = (2.0 * (value(2) - value(3))) / NORM ;
Calculate R(001) value
 R001       = (3.0 * value(3)) / NORM ;
Sum PGR values (PGR = 1)
 PGR        = P001 + G001 + R001 ;
```

8.3 EBSD Data

Modal mineralogy

	Caleta el Cobre 022	**Governador Valadares**		**Lafayette**	**MIL 03346**	**MIL 090030**	**MIL 090032**	**MIL 090136**	**Nakhla**		**NWA 817**
	CEREGE	*BM.1975, M16, P8469*	*BM.1975, M16, P19783*	*USNM 1505-5*	*118*	*62*	*108*	*50*	*USNM 426-1*	*WAM 12965*	*N8-1*
Scan Area (mm²)	112.83	15.48	21.03	73.56	106.4	79.64	14.69	43.17	209.57	13.3	7.6
% Crystalline	13	38	42	30	14	11	52	12	15	28	9
% Mesostasis	60	14	44	27	40	40	17	33	31	34	35
% melt/void space	27	48	13	42	46	49	31	56	54	37	56
Vol. %											
Augite	46.7	40.9	79.5	52.1	58.5	45.2	55.8	43.2	44.6	66.0	31.7
Enstatite	0.3			0.3	0.1	0.1			0.1		
Forsterite	4.2	12.1	9.1	9.3	0.3	8.4	12.7	2.5	5.0	7.2	9.1
Plagioclase	9.3	2.3	1.9	0.3					0.1	1.7	
Titanomagnetite	1.0	0.1	0.3	0.4	0.2	0.8	1.0	0.1	0.2	0.2	0.6
Apatite	0.3										
Alteration			0.1							0.1	0.9

	NWA 998		**NWA 10153**	**NWA 11013**	**NWA 12542**	**Y 000593**		**Y 000749**		**Y 000802**
	T1	*UG-1*	*SH65 T-2*	*UG-1*	*F83-1*	*106-A*	*36-A*	*64-A*	*72-A*	*36-A*
Scan Area (mm²)	9.86	36.14	37.01	37.01	113.65	36.09	35.86	64.56	48.92	35.86
% Crystalline	25	16	14	16	27	20	38	15	11	38
% Mesostasis	30	34	39	23	46	42	34	28	25	34
% melt/void space	46	50	48	61	26	38	28	57	64	28
Vol. %										
Augite	48.3	44.5	42.8	44.4	59.1	54.6	62.4	44.7	29.2	62.4
Enstatite		0.1	0.1		0.8				0.1	
Forsterite	4.9	10.2	11.6	0.3	14.0	9.7	10.2	3.5	2.2	10.2
Plagioclase	2.7	0.1	4.2	1.1	0.3	1.8				
Titanomagnetite	0.4	0.6	0.3	0.6	1.7	0.6	0.6	0.6	0.1	0.6
Apatite	0.1		0.1							
Alteration			0.1							

Table 8.21. *Nakhlite augite crystal statistics*

	Caleta el Cobre 022	Governador Valadares		Lafayette	MIL 03346	MIL 090030
	CERGE	*BM.1975, M16, P8469*	*BM.1975, M16, P19783*	*USNM 1505-5*	*118*	*108*
Augite indexed (%)	46.7	40.9	79.5	52.1	58.5	55.8
N (all data)	48844	1215	355	4572	5675	620
N (OPPG; >200 µm)	276	93	137	156	301	104
N (MTEX; >200 µm)	1789	134	326	899	984	126
Diameter (µm)						
Av.	86.23	37.837	204.2	57.6	59.09	65.88
SD	95.78	70.57	124.31	81.30	97.21	112.99
Aspect ratio						
A-axis						
Av.	1.83	2.65	2.12	1.87	2.05	2.09
N_A	1788	10	10	244	331	75
SD	0.64	2.26	0.92	0.7	0.92	1.03
B-axis						
Av.	1.83	2.17	2.09	1.92	2.13	1.94
N_B	146	58	3	37	10	9
SD	0.63	0.94	0.30	0.91	0.61	0.87
C-axis						
Av.	1.86	2.30	2.26	1.86	1.90	1.63
N_C	1954	22	10	178	165	19
SD	0.72	1.88	1.03	0.66	0.71	0.54
All axes						
Av.	1.84	2.34	1.97	1.87	2.00	2.01
N_T	3888	90	23	459	506	103
SD	0.69	1.71	0.77	0.69	0.86	0.97
Elongate crystals (%)	7.96	7.41	6.48	10.04	8.92	16.61
GOS (°)	0.14–45.29	0.56–57.39	0.41–20.46	1.93–31.00	0.45–46.51	0.55–16.11
Av.	5.33	7.41	3.72	7.12	6.71	4.66
SD	4.51	6.16	2.93	3.94	4.74	2.9
MOS (°)	0.09–14.19	0.22–11.02	0.24–6.31	0.35–6.01	0.25–10.19	0.27–4.07
Av.	1.53	2.09	0.93	1.07	1.98	0.94
SD	1.14	1.68	0.86	0.77	1.36	0.46
CPO						
M-Index	0.01 ± 0.0002	0.04 ± 0.011	0.03 ± 0.010	0.01 ± 0.004	0.02 ± 0.006	0.03 ± 0.009
J-Index	1.37 ± 0.07	4.35 ± 0.65	2.57 ± 0.13	2.27 ± 0.11	2.05 ± 0.10	5.33 ± 0.80
Eigenvalue						
Point (P) <100>	0.08	0.10	0.15	0.05	0.17	0.16
<010>	0.05	0.09	0.08	0.08	0.05	0.10
<001>	0.05	0.14	0.13	0.07	0.03	0.15
Girdle (G) <100>	0.07	0.07	0.07	0.05	0.04	0.05
<010>	0.04	0.26	0.17	0.12	0.56	0.08
<001>	0.27	0.37	0.42	0.29	0.45	0.21
Random (R) <100>	0.86	0.83	0.79	0.90	0.79	0.80
<010>	0.92	0.66	0.75	0.81	0.90	0.81
<001>	0.68	0.49	0.45	0.64	0.52	0.64
LS index	0.31	0.51	0.46	0.40	0.30	0.43
BA index	0.50	0.66	0.69	0.56	0.67	0.60
$MUD_{max-min}$	0.06–2.54	0.00–3.96	0.00–2.64	0.06–2.29	0.04–2.97	0.00–3.85

N = number of crystals
OPPG = one point per grain
Av. = average
SD = standard deviation
NA = number of crystals in subset A
NB = number of crystals in subset B
NC = number of crystals in subset C
NT = total number of crystals with any axis parallel to the plane of the sample
CPO = crystal preferred orientation
MUD = multiples of uniform density
GOS = grain orientation spread
MOS = mean orientation spread

(See supplementary materials for spreadsheet format)

	MIL 090032	**MIL 090136**	**Nakhla**		**NWA 817**	**NWA 998**		**NWA 10153**
	108	*50*	*USNM 426-1*	*WAM 12965*	*N8-1*	*T1*	*UG-1*	*SH65 T-2, 2*
Augite indexed (%)	55.8	43.2	44.6	66	31.7	48.3	44.5	42.8
N (all data)	620	1567	23824	304	4282	998	1888	19759
N (OPPG; >200 µm)	104	267	1093	138	50	68	135	385
N (MTEX; >200 µm)	126	355	2492	234	43	110	356	849
Diameter (µm)								
Av.	65.88	69.31	34.44	148.34	6.6	38.31	59.08	24.27
SD	112.99	99.69	58.62	90.55	26.61	66.44	78.58	45.87
Aspect ratio								
A-axis								
Av.	2.09	1.75	1.8	1.66	1.99	1.7	1.79	1.76
N_A	75	102	1177	23	72	49	84	687
SD	1.03	0.59	0.57	0.43	0.68	0.48	0.55	0.57
B-axis								
Av.	1.94	1.66	1.76	1.14	2.07	1.74	2.25	1.74
N_B	9	8	166	1	4	8	7	69
SD	0.87	0.57	0.55	n.d.	1.01	0.45	0.87	0.46
C-axis								
Av.	1.63	1.80	1.78	1.51	2.25	1.81	1.79	1.80
N_C	19	25	638	5	64	36	54	797
SD	0.54	0.54	0.55	0.28	1.02	0.67	0.55	0.76
All axes								
Av.	2.01	1.76	1.78	1.63	2.11	1.75	1.81	1.78
N_T	103	135	1981	29	140	93	145	1553
SD	0.97	0.58	0.55	0.41	0.86	0.55	0.57	0.67
Elongate crystals (%)	16.61	8.62	8.32	9.54	3.27	9.32	7.68	7.86
GOS (°)	0.55–16.11	0.41–9.78	0.13–32.6	0.61–19.00	0.10–25.35	0.30–19.73	0.00–29.47	0.06–46.65
Av.	4.66	3.31	3.60	5.45	2.31	4.1	4.79	4.96
SD	2.9	1.37	3.06	3.34	2.41	3.51	3.56	4.47
MOS (°)	0.27–4.07	0.13–3.53	0.07–9.16	0.28–5.86	0.05–5.29	0.24–8.38	0.00–6.78	0.01–10.41
Av.	0.94	0.63	1.23	1.46	0.79	1.13	1.28	1.80
SD	0.46	0.31	0.79	1.00	0.58	0.86	0.83	1.16
CPO								
M-Index	0.03 ± 0.009	0.02 ± 0.007	0.02 ± 0.0004	0.02 ± 0.006	0.08 ± 0.049	0.03 ± 0.013	0.02 ± 0.007	0.01 ± 0.0003
J-Index	5.33 ± 0.80	3.14 ± 0.16	1.5 ± 0.08	2.85 ± 0.14	14.42 ± 8.65	4.97 ± 0.74	2.78 ± 0.14	1.78 ± 0.09
Eigenvalue								
Point (P)								
<100>	0.16	0.13	0.13	0.12	0.26	0.09	0.04	0.15
<010>	0.10	0.06	0.08	0.08	0.11	0.10	0.09	0.03
<001>	0.15	0.08	0.01	0.04	0.24	0.10	0.01	0.06
Girdle (G)								
<100>	0.05	0.16	0.04	0.14	0.24	0.08	0.10	0.08
<010>	0.08	0.10	0.03	0.06	0.34	0.11	0.18	0.01
<001>	0.21	0.33	0.48	0.47	0.29	0.37	0.38	0.32
Random (R)								
<100>	0.80	0.71	0.83	0.7.9	0.50	0.83	0.86	0.77
<010>	0.81	0.84	0.90	0.87	0.55	0.79	0.73	0.96
<001>	0.64	0.59	0.51	0.49	0.47	0.53	0.62	0.63
LS index	0.43	0.42	0.16	0.25	0.60	0.37	0.35	0.23
BA index	0.60	0.55	0.53	0.44	0.64	0.53	0.50	0.48
$MUD_{max-min}$	0.00–3.85	0.08–3.01	0.14–2.19	0.00–3.87	0.00–4.68	0.00–4.42	0.00–3.23	0.08–2.52

	NWA 11013	NWA 12542	Y 000593		Y 000749		Y 000802
	UG-1	*F83-1*	*106-A*	*127-A*	*64-A*	*72-A*	*36-A*
Augite indexed (%)	44.4	59.1	54.6	53.2	44.7	29.2	62.4
N (all data)	8922	9964	1035	395	7450	2478	670
N (OPPG; >200 µm)	177	963	93	109	197	111	138
N (MTEX; >200 µm)	273	1081	241	219	447	281	341
Diameter (µm)							
Av.	23.37	46.32	71.04	227.86	33.76	32.46	132.19
SD	38.17	79.95	132.94	144.54	59.36	113.90	154.33
Aspect ratio							
A-axis							
Av.	1.81	2.05	2.36	1.85	1.968	1.88	2.02
N_A	214	400	13	5	287	66	42
SD	0.6	0.93	1.30	0.92	0.65	0.72	0.88
B-axis							
Av.	1.85	1.88	1.90	5.33	2.09	1.84	2.01
N_B	10	27	21	2	60	52	14
SD	0.57	0.67	0.70	1.19	0.65	0.52	1.04
C-axis							
Av.	1.95	2.10	2.04	1.59	1.96	2.35	1.98
N_C	338	138	27	3	84	25	22
SD	0.81	0.97	0.88	0.63	0.68	1.09	1.27
All axes							
Av.	1.91	2.05	2.07	2.47	1.97	1.95	1.98
N_T	562	565	66	10	556	149	78
SD	0.74	0.93	0.94	1.70	0.66	0.76	1.11
Elongate crystals (%)	6.30	5.67	6.38	2.53	7.46	6.01	11.64
GOS (°)	0.55–16.11	0.45–37.69	0.43–45.96	0.46–35.95	0.25–10.75	0.40–31.24	0.23–9.61
Av.	4.66	6.26	7.25	5.83	2.44	2.00	1.46
SD	2.9	4.48	4.99	4.96	1.92	1.43	1.22
MOS (°)	0.27–4.07	0.12–9.10	0.20–10.37	0.29–8.78	0.13–3.94	0.23–6.97	0.11–2.50
Av.	0.946.31	2.09	1.51	1.77	0.44	0.66	0.41
SD	0.4617.76	1.23	1.06	1.39	0.32	0.32	0.22
CPO							
M-Index	0.02 ± 0.006	0.02 ± 0.0003	0.03 ± 0.008	0.03 ± 0.007	0.03 ± 0.009	0.04 ± 0.011	0.02 ± 0.006
J-Index	3.33 ± 0.17	1.54 ± 0.08	3.41 ± 0.17	4.62 ± 0.23	2.66 ± 0.13	3.61 ± 0.18	2.67 ± 0.13
Eigenvalue							
Point (P) <100>	0.18	0.12	0.04	0.06	0.13	0.13	0.12
<010>	0.04	0.06	0.01	0.14	0.07	0.08	0.08
<001>	0.07	0.06	0.17	0.10	0.10	0.16	0.15
Girdle (G) <100>	0.09	0.07	0.18	0.11	0.03	0.02	0.15
<010>	0.15	0.05	0.09	0.08	0.15	0.20	0.05
<001>	0.37	0.40	0.27	0.41	0.42	0.37	0.19
Random (R) <100>	0.74	0.81	0.78	0.83	0.90	0.87	0.73
<010>	0.81	0.90	0.78	0.78	0.72	0.72	0.87
<001>	0.56	0.54	0.56	0.49	0.46	0.50	0.65
LS index	0.48	0.28	0.38	0.29	0.44	0.54	0.41
BA index	0.73	0.54	0.27	0.37	0.74	0.79	0.42
$MUD_{max-min}$	0.02–4.00	0.03–2.37	0.23–5.92	0.26–2.91	0.46–2.22	0.22–4.78	0.59–2.26

Table 8.22. Nakhlite olivine (forsterite) crystal statistics.

	Caleta el Cobre 022	**Governador Valadares**		**Lafayette**	**MIL 03346**	**MIL 090030**	**MIL 090032**
	CEREGE	*BM.1975, M16, P8469*	*BM.1975, M16, P19783*	*USNM 1505-5*	*118*	*62*	*108*
Augite indexed (%)	4.2	12.1	9.1	9.3	0.3	8.4	12.6
N (all data)	6653	140	16	1014	134	1614	319
N (OPPG; >200 µm)	14	9	8	88	18	39	9
N (MTEX; >200 µm)	10	9	12	94	71	88	1
Diameter (µm)							
Av.	31.17	51.89	330.82	49.24	22.37	31.77	24.26
SD	69.01	117.53	227.59	14.27	18.33	62.81	79.4
Aspect ratio							
A-axis							
Av.	1.70	1.87	1.66	1.91	1.81	1.82	2.04
N_A	446	47	2	93	8	20	11
SD	0.51	0.62	0.56	0.65	0.31	0.53	0.38
B-axis							
Av.	1.74	1.6	n.d.	1.75	n.d.	n.d.	1.81
N_B	20	2	0	9	0	0	5
SD	0.52	0.67	n.d.	0.59	n.d.	n.d.	0.65
C-axis							
Av.	1.70	2.10	2.05	1.76	2.20	1.86	1.41
N_C	104	6	1	71	3	31	2
SD	0.55	0.70		0.47	0.66	0.63	0.00
All axes							
Av.	1.70	1.88	1.79	1.84	1.92	1.86	1.93
N_T	570	55	3	173	11	51	18
SD	0.52	0.63	0.46	0.58	0.43	0.62	0.47
Elongate crystals (%)	8.57	39.29	18.75	17.06	8.21	3.16	5.64
GOS (°)	0.06-6.65	0.04-2.80	0.25-61.41	0.37-4.76	0.20-5.03	0.10-4.25	0.28-3.28
Av.	1.44	1.08	0.66	1.24	1.07	0.90	1.04
SD	0.99	0.59	0.29	0.79	0.54	0.49	0.56
MOS (°)	0.08-25.59	0.80-21.53	0.58-10.08	2.00-24.04	0.50-9.27	0.18-15.15	0.54-11.09
Av.	4.69	5.24	3.77	7.8	2.46	2.34	2.44
SD	4.86	4.7	2.66	4.35	1.34	2.06	1.60
CPO							
M-Index	0.37 ± 0.36	0.10 ± 0.10	0.12 ± 0.12	0.13 ± 0.01	0.07 ± 0.01	0.05 ± 0.01	0.87 ± 0.86
J-Index	45.68 ± 36.55	18.08 ± 14.46	21.70 ± 16.28	5.23 ± 1.31	5.48 ± 2.74	6.72 ± 2.01	127.60 ± 126.32
Eigenvalue							
Point (P) <100>	0.32	0.27	0.26	0.1	0.13	0.13	0.97
<010>	0.29	0.29	0.12	0.09	0.16	0.05	0.97
<001>	0.78	0.07	0.22	0.06	0.09	0.17	0.97
Girdle (G) <100>	0.66	0.5	0.49	0.12	0.2	0.21	0.02
<010>	0.57	0.36	0.48	0.04	0.4	0.17	0.01
<001>	0.2	0.22	0.06	0.29	0.37	0.25	0.01
Random (R) <100>	0.02	0.23	0.25	0.78	0.68	0.66	0.02
<010>	0.15	0.36	0.37	0.87	0.44	0.78	0.2
<001>	0.02	0.71	0.72	0.66	0.55	0.58	0.02
M.U.D. $_{max-min}$	0.00-11.78	0.00-18.52	0.00-28.23	0.00-3.94	0.00-18.59	0.00-5.87	0.00-39.02

N = number of crystals
Av. = average
SD = standard deviation
OPPG = one point per grain
GOS = grain orientation spread
MOS = maximum orientation spread from the mean orientation spread
N_A = number of crystals in subset A
N_B = number of crystals in subset B
N_C = number of crystals in subset C
N_T = total number of crystals with any axis parallel to the plane of the sample
CPO = crystal preferred orientation
M.U.D. = multiples of uniform density

Table continued

	MIL 090136	**Nakhla**		**NWA 817**	**NWA 998**		**NWA 10153**
	50	*USNM 426-1*	*WAM 12965*	*N8-1*	*T1*	*UG-1*	*SH65 T-2*
Augite indexed (%)	2.5	5	7.2	9.1	4.9	10.2	11.6
N (all data)	110	1900	21	5508	74	299	3438
N (OPPG; >200 µm)	13	46	6	32	8	29	16
N (MTEX; >200 µm)	7	68	10	4	7	35	43
Diameter (µm)							
Av.	47.81	32.56	211.9	4.61	49.38	66.77	27
SD	96.63	76.02	154.99	12.22	76.65	101.24	62.82
Aspect ratio							
A-axis							
Av.	1.84	1.85	n.d.	2.02	1.95	1.67	1.69
N_A	1	65	0	295	21	11	226
SD	n.d.	0.64	n.d.	0.84	0.51	0.42	0.52
B-axis							
Av.	n.d.	1.96	n.d.	n.d.	n.d.	1.9	1.81
N_B	0	3	0	0	0	10	2
SD	n.d.	0.56	n.d.	n.d.	n.d.	0.53	0.02
C-axis							
Av.	1.84	1.84	2.66	2.04	1.62	1.86	1.54
N_C	9	110	6	132	4	18	27
SD	0.43	0.57	0.53	0.87	0.42	0.91	0.48
All axes							
Av.	1.88	1.83	2.66	2.02	1.90	1.82	1.97
N_T	10	178	6	427	25	39	255
SD	0.43	0.59	0.53	0.84	0.50	0.72	0.51
Elongate crystals (%)	9.09	9.37	28.57	7.75	33.78	13.04	7.42
GOS (°)	0.65-1.43	0.10-6.14	0.42-2.94	0.07-6.57	0.25-6.97	0.29-4.77	0.13-6.85
Av.	1.03	0.74	0.96	1.03	1.19	1.14	1.35
SD	0.40	0.44	0.61	0.62	1.16	0.94	0.94
MOS (°)	3.29-9.51	0.13-24.77	0.95-16.93	0.16-22.94	0.88-13.99	0.72-18.43	0.15-37.54
Av.	5.57	1.94	5.13	2.91	4.33	5.63	3.24
SD	2.55	1.89	4.13	2.15	2.96	3.89	3.02
CPO							
M-Index	0.15 ± 0.14	0.09 ± 0.09	0.12 ± 0.05	0.27 ± 0.27	0.15 ± 0.14	0.12 ± 0.07	0.15 ± 0.07
J-Index	24.99 ± 21.24	5.88 ± 4.71	15.82 ± 8.70	35.71 ± 33.92	19.01 ± 16.16	13.54 ± 8.80	22.52 ± 13.51
Eigenvalue							
Point (P)							
<100>	0.24	0.15	0.31	0.22	0.29	0.36	0.11
<010>	0.3	0.15	0.07	0.31	0.25	0.2	0.31
<001>	0.17	0.26	0.32	0.17	0.21	0.26	0.39
Girdle (G)							
<100>	0.23	0.31	0.18	0.16	0.27	0.23	0.58
<010>	0.42	0.17	0.41	0.6	0.35	0.16	0.51
<001>	0.47	0.45	0.45	0.75	0.42	0.39	0.34
Random (R)							
<100>	0.53	0.55	0.51	0.63	0.44	0.41	0.31
<010>	0.28	0.67	0.52	0.09	0.41	0.65	0.31
<001>	0.36	0.29	0.22	0.09	0.35	0.35	0.38
M.U.D. $_{max-min}$	0.00-15.75	0.00-5.38	0.00-16.24	0.00-5.82	0.00-15.91	0.00-7.70	0.00-14.38

Table continued

	NWA 11013	**NWA 12542**	**Y 000593**		**Y 000749**		**Y 000802**
	UG-1	*F83-1*	*106-A*	*127-A*	*64-A*	*72-A*	*36-A*
Forsterite indexed (%)	0.3	14	9.7	14.9	2.2	3.5	10.2
N (all data)	189	3466	633	102	1614	336	148
N (OPPG; >200 µm)	3	136	11	32	19	9	23
N (MTEX; >200 µm)	2	129	15	31	24	10	26
Diameter (µm)							
Av.	16.39	31.62	33.63	141.476	23.81	27.68	105.01
SD	9.20	66.86	74.65	155.9	28.98	60.59	150.84
Aspect ratio							
A-axis							
Av.	n.d.	1.77	1.58	1.69	1.90	1.68	1.62
N_A	0	143	1	4	436	1	7
SD	n.d.	0.56	n.d.	0.59	0.64	n.d.	0.35
B-axis							
Av.	n.d.	1.57	n.d.	n.d.	n.d.	n.d.	1.68
N_B	0	8	0	0	0	0	3
SD	n.d.	0.42	n.d.	n.d.	n.d.	n.d.	0.21
C-axis							
Av.	1.85	1.87	1.46	1.81	1.91	1.61	2.33
N_C	43	215	3	8	157	0.2	4
SD	0.59	0.84	0.21	0.67	0.62	0.63	0.76
All axes							
Av.	1.85	1.82	1.49	1.82	1.90	1.61	1.88
N_T	43	366	4	12	593	1.2	14
SD	0.59	0.73	0.18	0.62	0.63	0.20	0.44
Elongate crystals (%)	22.75	10.56	0.63	11.76	36.74	0.36	9.46
MOS (degree)	0.06-5.99	0.23-9.47	0.19-3.40	0.15-2.41	0.14-2.59	0.09-1.17	0.29-2.10
Av.	1.80	1.76	0.85	0.45	0.44	0.39	0.75
SD	1.20	1.27	0.46	0.37	0.17	0.18	0.36
GOS (degree)	0.19-19.47	0.39-48.06	0.34-13.20	0.35-6.85	0.21-8.61	0.09-4.77	0.59-16.75
Av.	4.95	6.14	2.41	2.38	1.14	1.13	3.55
SD	3.41	5.24	1.84	1.66	0.77	0.68	2.76
CPO							
M-Index	0.05 ± 0.05	0.04 ± 0.002	0.23 ± 0.22	0.07 ± 0.03	0.04 ± 0.04	0.17 ± 0.17	0.06 ± 0.05
J-Index	4.44 ± 4.35	4.20 ± 0.63	37.58 ± 28.18	8.52 ± 5.54	6.33 ± 4.43	22.32 ± 17.86	9.18 ± 6.42
Eigenvalue							
Point (P)							
<100>	0.27	0.18	0.46	0.11	0.06	0.23	0.12
<010>	0.01	0.07	0.35	0.21	0.11	0.84	0.12
<001>	0.06	0.1	0.29	0.11	0.28	0.43	0.11
Girdle (G)							
<100>	0.07	0.15	0.08	0.35	0.17	0.49	0.05
<010>	0.34	0.09	0.25	0.14	0.61	0.23	0.74
<001>	0.3	0.4	0.46	0.46	0.57	0.47	0.81
Random (R)							
<100>	0.66	0.67	0.54	0.54	0.77	0.28	0.83
<010>	0.65	0.85	0.65	0.65	0.11	0.28	0.16
<001>	0.64	0.49	0.43	0.43	0.32	0.45	0.07
M.U.D. $_{max-min}$	0.00-27.89	0.00-3.28	0.00-16.98	0.00-7.28	0.00-12.85	0.00-19.84	0.00-9.02

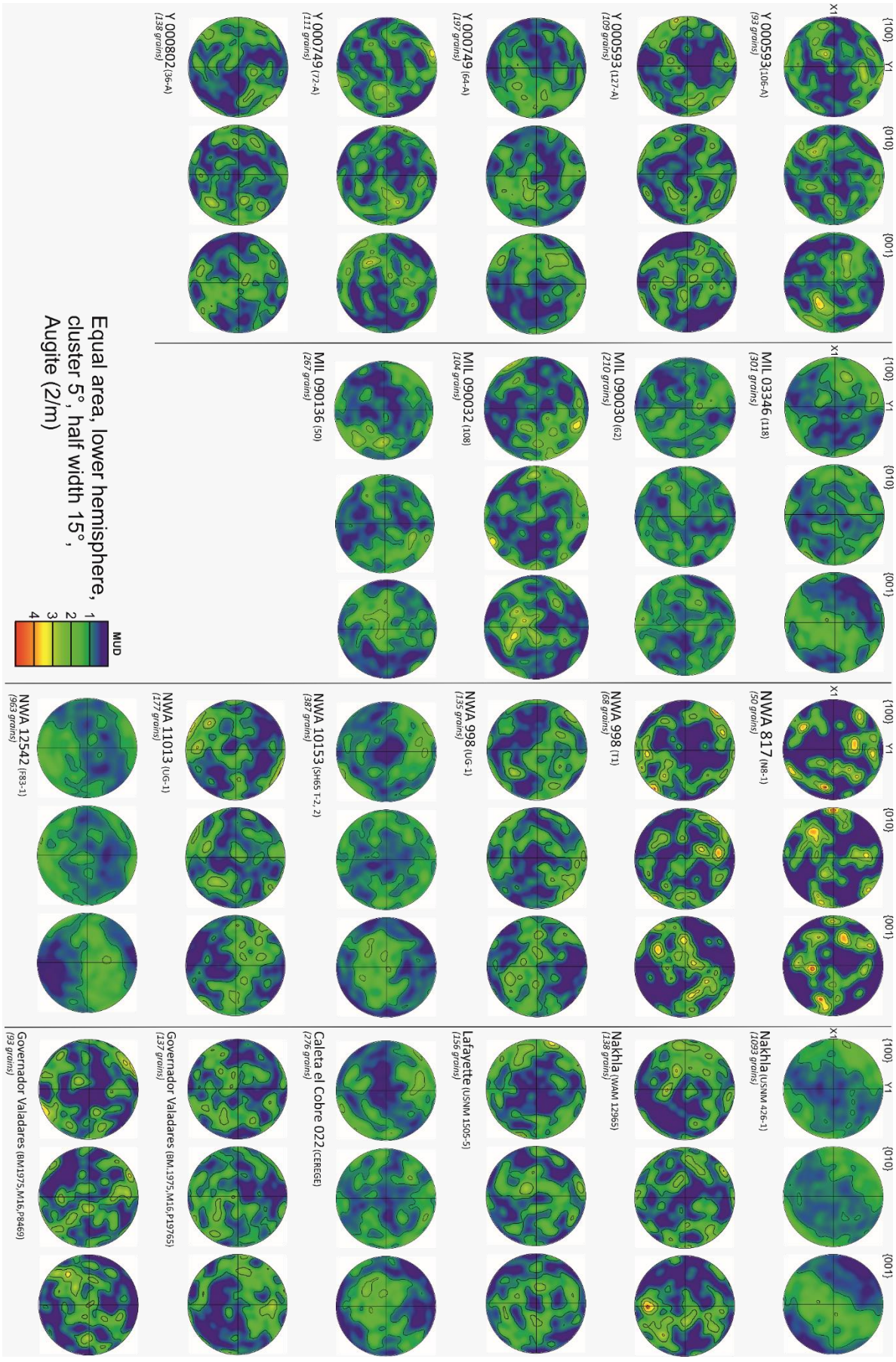

Figure 8.17. *Nakhlite augite CPO plots for all crystallographic axes.*

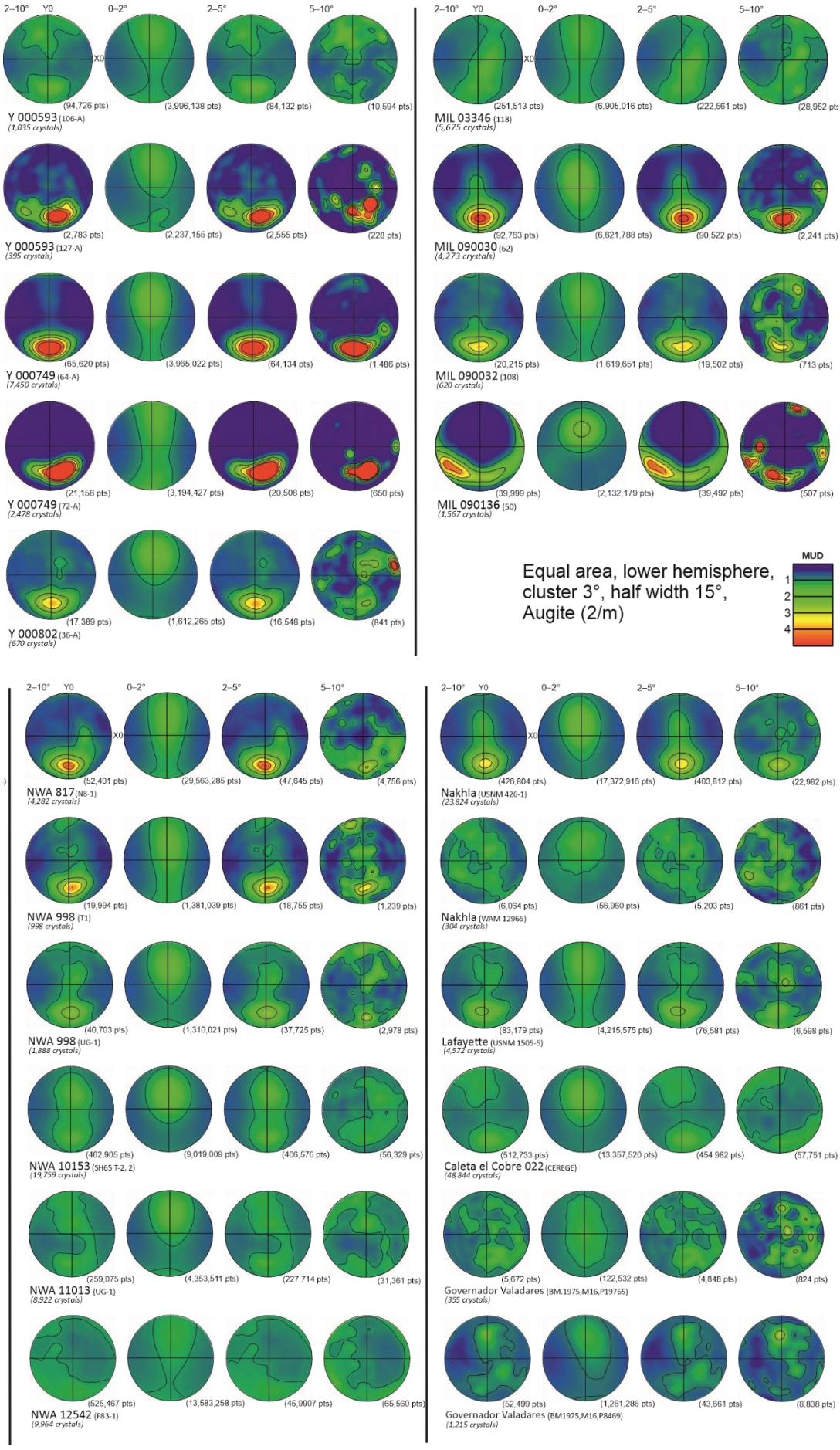

***Figure 8.18**. Nakhlite sample reference augite CPO misorientation (whole sample data).*

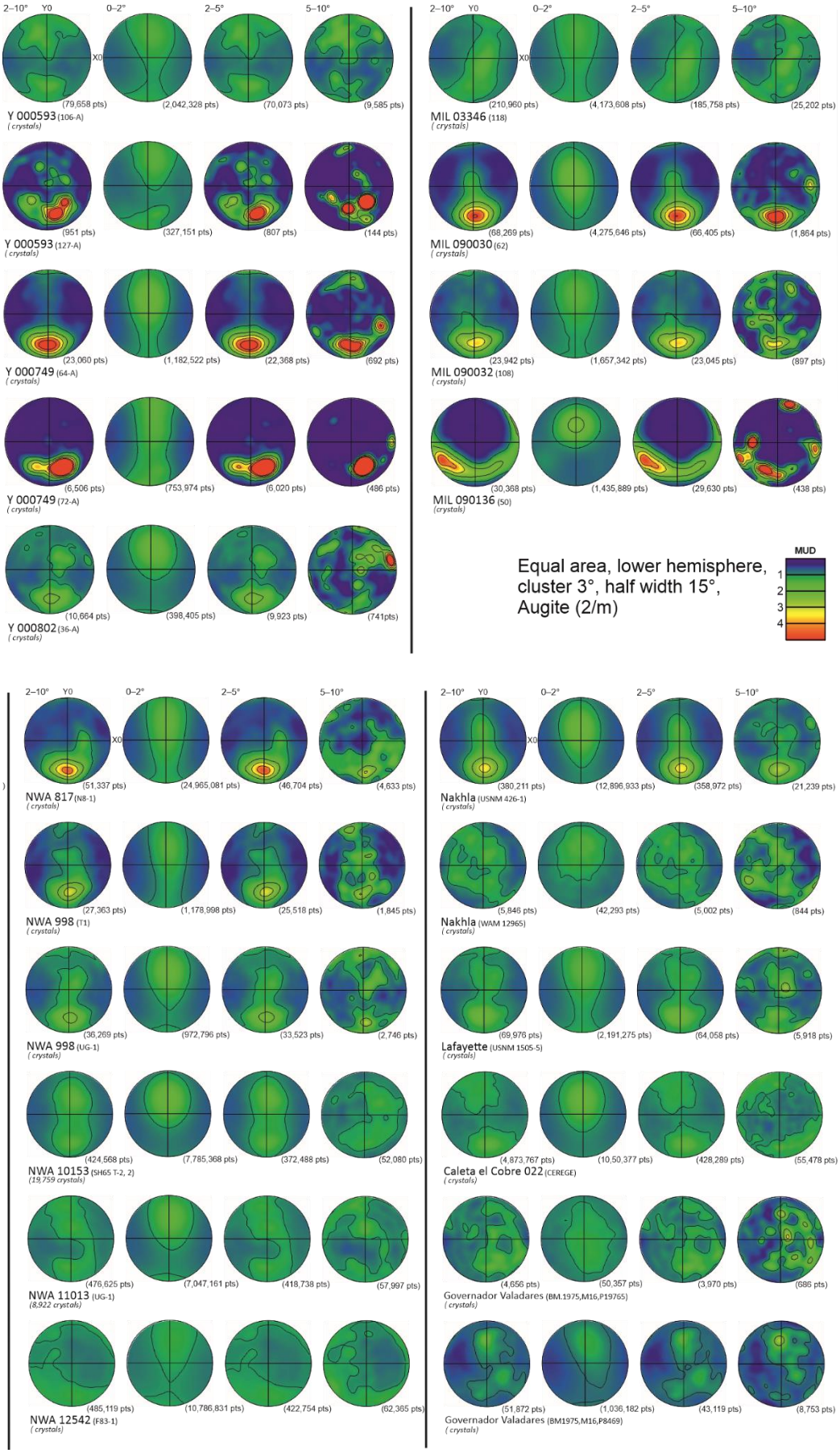

Figure 8.19: *Nakhlite sample reference augite CPO misorientation (high deformation region data).*

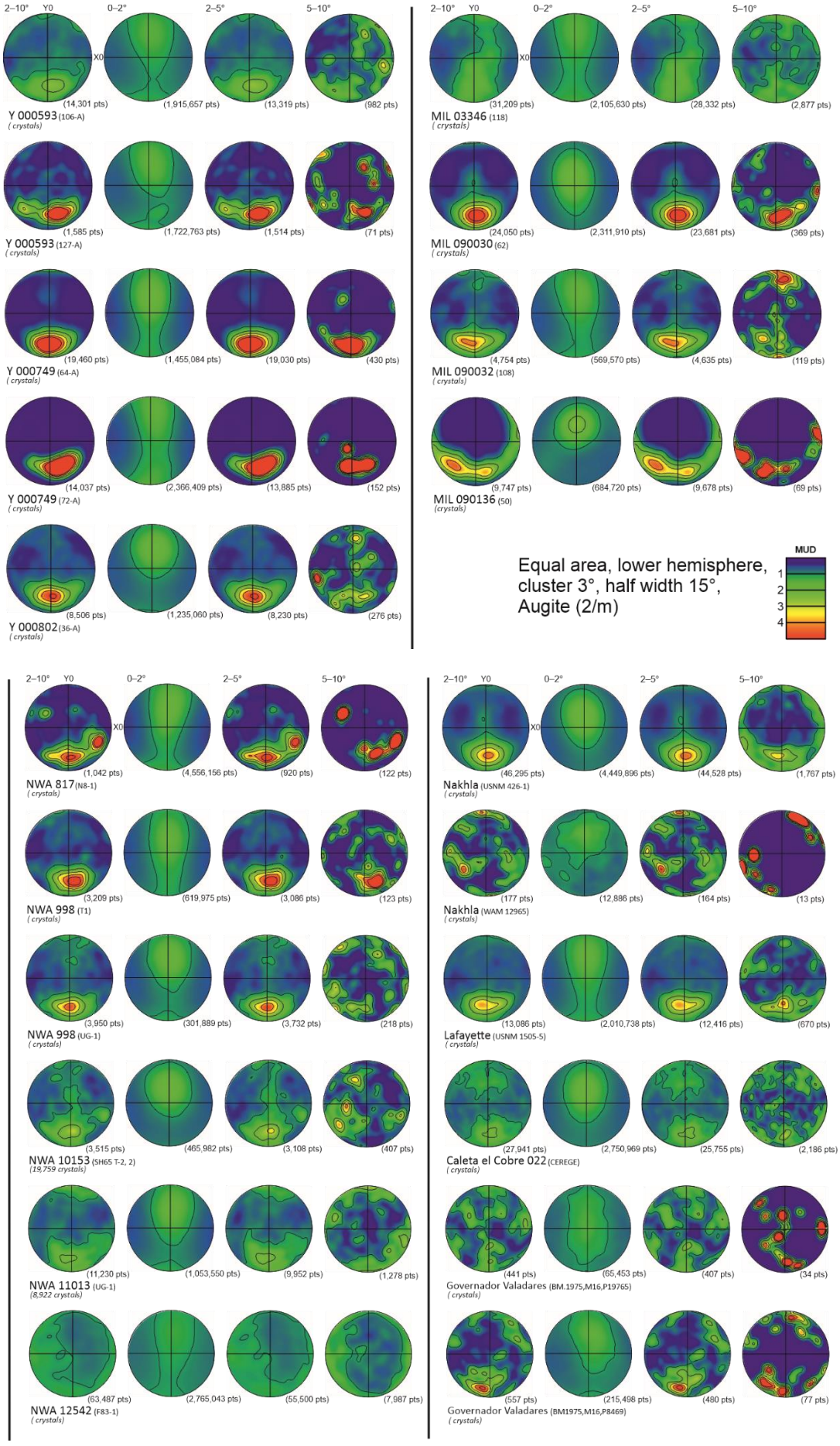

Figure 8.20. *Nakhlite sample reference augite CPO misorientation (low deformation region data).*

8.4 EDS data

Table 8.23. CIPW norm results from EDS analyses

	Caleta el Cobre 022	Governador Valadares		Lafayette	MIL 03346	MIL 090030	MIL 090032	MIL 090136
	CEREGE	*BM.1975, M16, P8469*	*BM.1975, M16, P19783*	*USNM 1505-5*	*118*	*62*	*108*	*50*
EDS spectra [wt %]								
SiO_2	28.22	23.84	29.26	28.28	27.55	27.79	26.88	28.73
TiO_2	4.48	0.19	3.97	3.83	4.21	4.61	3.85	4.38
Al_2O_3	9.54	1.41	7.11	6.96	8.1	8.98	7.66	8.67
Fe_2O_3	21.18	19.15	20.52	22.41	19.61	20.99	26.24	20.05
FeO								
MnO	2.11	0.5	2.29	2.27	2.25	2.48	2.26	2.33
MgO	7.02	7.15	9.24	9.26	7.18	7.96	7.88	7.53
CaO	10.34	10.43	13.11	13.17	12.55	10.72	11.24	12.53
Na_2O	3.67	0.6	2.46	2.35	3.01	3.28	2.74	3.29
K_2O	2.39	0.15	2.12	1.96	2.18	2.37	2.04	2.25
P_2O_5	10.35	0.04	9.5	9.11	9.61	10.58	8.81	9.93
S	0.07	0.01	0.09	0.03	0.05	0.05	0.11	0.06
Cl	0.06	0.07	0.08	0.05	0.06	0.06	0.05	0.05
Cr	0.11	0.24	0.19	0.28	0.21	0.15	0.24	0.19
CIPW Normalised values [wt. %]								
SiO_2	55.45	55.71	58.77	56.74	56.95	56.44	52.75	56.84
TiO_2	0.65	0.35	0.36	0.38	0.74	0.75	0.65	0.77
Al_2O_3	11.36	4.85	4.95	5.20	8.39	9.44	8.12	9.29
Fe_2O_3	1.85	2.39	1.83	2.09	1.78	1.88	2.53	1.73
FeO	12.18	15.79	12.10	13.78	11.75	12.40	16.72	11.44
MnO	0.34	0.47	0.39	0.42	0.34	0.36	0.46	0.33
MgO	5.90	8.64	8.76	8.85	6.54	7.24	7.15	6.58
CaO	8.31	10.63	11.29	11.39	11.13	8.99	9.34	10.56
Na_2O	2.34	0.79	0.85	0.79	1.67	1.79	1.42	1.91
K_2O	0.26	0.12	0.19	0.11	0.22	0.22	0.23	0.21
P_2O_5	1.33	0.23	0.45	0.23	0.44	0.46	0.57	0.30
S	0.02	0.00	0.03	0.01	0.02	0.02	0.04	0.02
Cl	0.02	0.03	0.03	0.02	0.02	0.02	0.02	0.02
Cr	0.00	0.00	0.00	0.00	0.00	0.00	0.00	0.00
Total	100.00	100.00	100.00	100.00	100.00	100.00	100.00	100.00
Calculated model input parameters								
Density, solid [g/m³]	3048	3235	3149	3196	3096	3092	3208	3080
Density, liquid [g/m³]	2693	2784	2722	2757	2710	2710	2788	2701
Viscosity, dry [g/m.s]	326	270	336	294	335	324	242	336
Viscosity, wet [g/m.s]	297	250	302	270	306	298	227	308
liquidus temp [°C]	1114	1109	1053	1090	1086	1096	1163	1088
H_2O content [wt. %]	0.88	0.91	1.31	1.04	1.06	1.00	0.60	

1.05

McBirney A.R. 1993, Igneous Petrology 2nd edition, Appendix B, in Jones and Bartlett, Publishers, Boston, 508P

Nakhla		**NWA 817**	**NWA 998**		**NWA 10153**	**NWA 11013**	**NWA 12542**	**Y 000593**		**Y 000749**		**Y 000802**
USNM 426-1	*WAM 12965*	*N8-1*	*T1*	*UG-1*	*SH65 T-2,2*	*UG-1*	*F83-1*	*106-A*	*127-A*	*64-A*	*72-A*	*36-A*
28.34	29.25	24.83	29.34	27.7	27.89	29.71	27.02	27.38	27.18	28.02	28.26	27.81
4.33	3.98	5.49	3.79	3.87	4.64	4.34	4.1	3.89	3.98	3.87	4.02	4.01
7.57	7.12	10.06	7.81	7.26	9.02	9.04	7.61	6.84	7.11	7.19	7.37	7.46
19.94	20.48	18.39	21.14	23.93	21.85	19.56	24.21	25.1	24.69	23.84	23	23.18
2.45	2.3	2.84	2.23	2.29	2.42	2.24	2.34	2.35	2.35	2.28	2.28	2.33
9.35	9.2	8.57	8.46	9.21	7.06	6.47	8.26	8.32	8.58	8.27	8.19	8.28
12.6	13.26	9.13	12.63	11.77	10.34	12.36	11.49	12.1	11.78	12.42	12.47	12.2
2.57	2.47	4.62	2.94	2.58	3.51	3.66	2.79	2.43	2.56	2.57	2.36	2.68
2.2	2.08	2.84	2.09	1.99	2.40	2.52	2.11	1.96	2.03	2.02	2.04	2.13
10.38	9.54	13.03	9.1	9.15	10.51	9.68	9.51	9.16	9.38	9.15	9.27	9.47
0	0.02	0	0.04	0	0.16	0.21	0.07	0.22	0.01	0.2	0.02	0.07
0.03	0.06	0.04	0.21	0.04	0.07	0.07	0.06	0.03	0.03	0.1	0.02	0.01
0.22	0.2	0.17	0.22	0.23	0.13	0.18	0.21	0.23	0.22	0.23	0.23	0.22
59.26	58.85	55.30	56.54	55.04	59.01	56.81	54.85	55.67	55.64	56.32	56.39	56.36
0.36	0.37	0.74	0.36	0.41	0.96	0.91	0.59	0.44	0.43	0.39	0.60	0.43
4.91	4.90	9.68	7.92	6.09	10.38	10.73	6.77	4.82	5.25	5.82	6.27	6.19
1.80	1.83	1.60	1.85	2.26	2.08	1.62	2.34	2.46	2.42	2.27	2.15	2.19
11.86	12.07	10.58	12.22	14.91	13.72	10.71	15.44	16.26	15.98	14.97	14.19	14.48
0.38	0.38	0.29	0.38	0.44	0.36	0.29	0.42	0.50	0.46	0.43	0.41	0.42
9.22	8.72	8.70	7.57	9.32	0.64	5.17	7.78	7.88	8.23	7.71	7.54	7.75
11.24	11.46	8.03	10.38	9.93	8.96	10.00	9.86	10.50	10.24	10.67	10.63	10.55
0.77	0.84	3.63	1.61	1.10	2.28	2.42	1.35	0.90	1.03	1.08	1.18	1.17
0.11	0.15	0.25	0.22	0.14	0.28	0.45	0.18	0.11	0.13	0.15	0.16	0.19
0.09	0.41	1.18	0.87	0.34	1.26	0.80	0.39	0.38	0.17	0.17	0.48	0.24
0.00	0.00	0.00	0.01	0.00	0.06	0.07	0.02	0.08	0.00	0.01	0.00	0.02
0.01	0.02	0.02	0.07	0.02	0.02	0.03	0.02	0.00	0.01	0.01	0.01	0.01
0.00	0.00	0.00	0.00	0.00	0.00	0.00	0.00	0.00	0.00	0.00	0.00	0.00
100.00	100.00	100.00	100.00	100.00	100.00	100.00	100.00	100.00	100.00	100.00	100.00	100.00
3151	3150	3057	3110	3210	3021	3029	3196	3236	3228	3196	3172	3181
2721	2723	2677	2716	2771	2680	2676	2769	2786	2781	2763	2750	2754
342	338	282	317	261	445	355	269	273	272	293	301	297
308	303	257	288	243	393	323	250	252	252	270	276	273
1044	1051	1116	1094	1121	1048	1089	1125	1110	1110	1098	1096	1097
1.38	1.32	0.86	1.02	0.83	1.35	1.05	0.81	0.91	0.90	0.98	0.99	0.99

*

8.5 EBSD maps

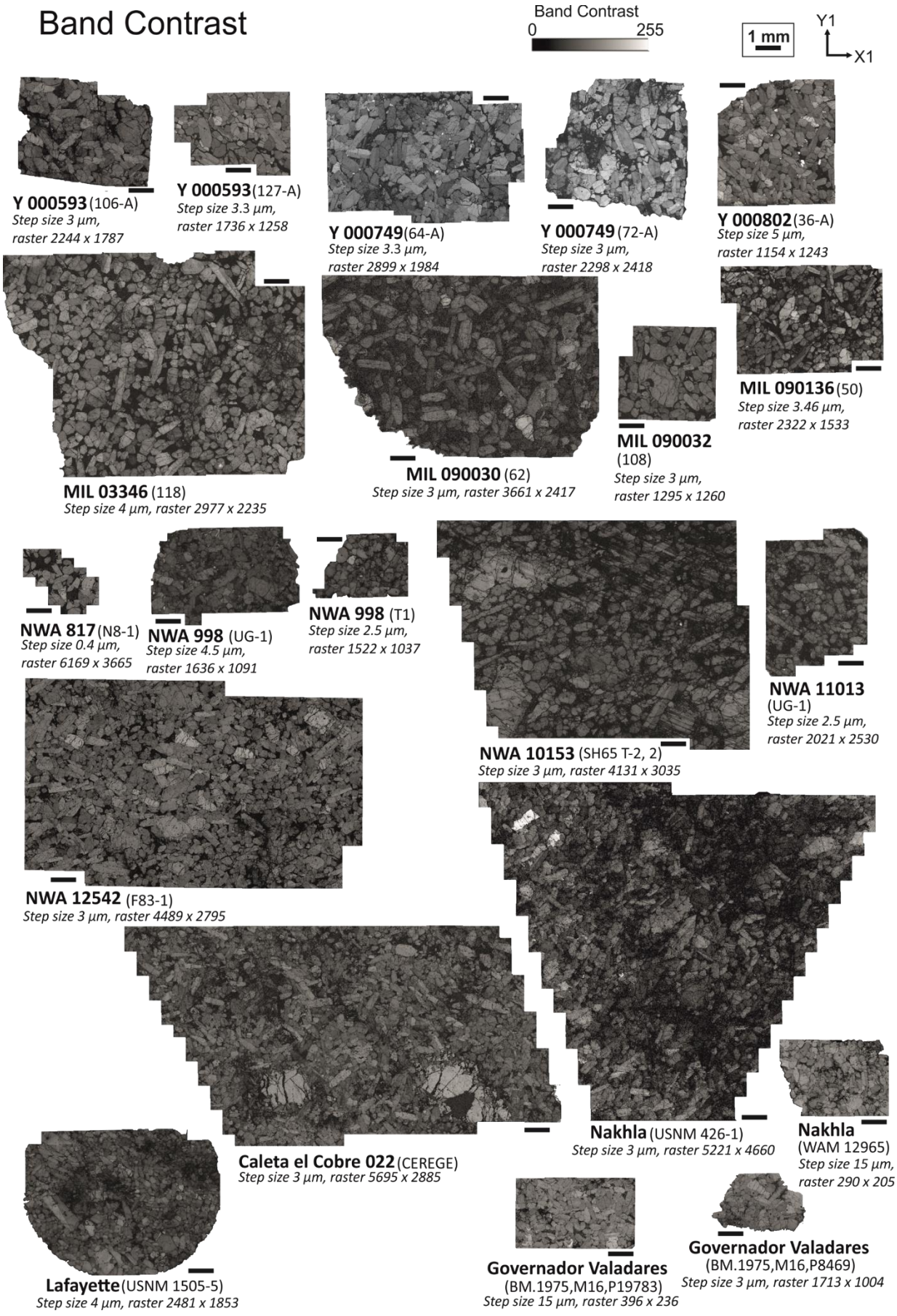

Figure 8.21. *Nakhlite band contrast maps.*

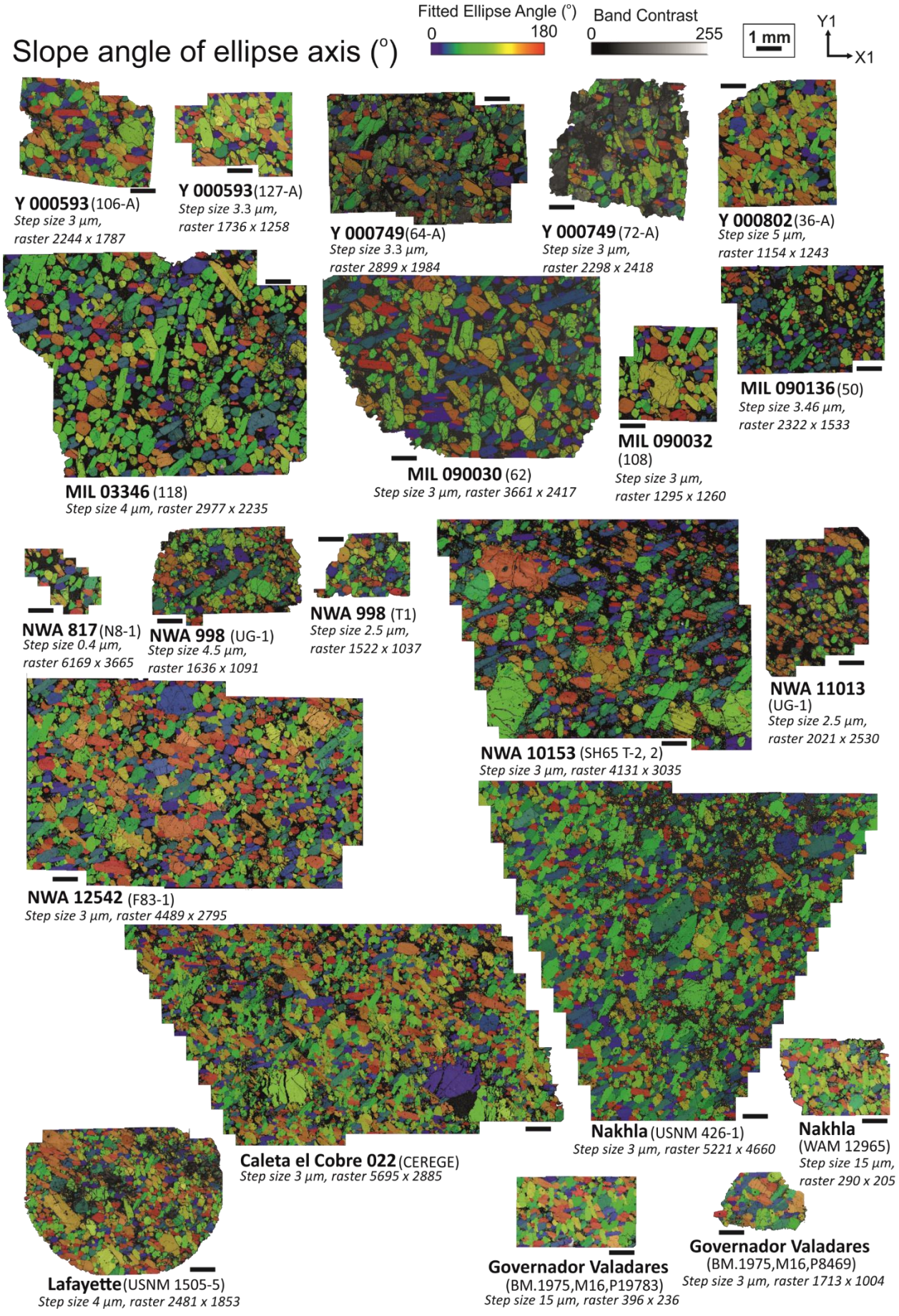

Figure 8.22. *Nakhlite best-fit ellipse axis slope angle.*

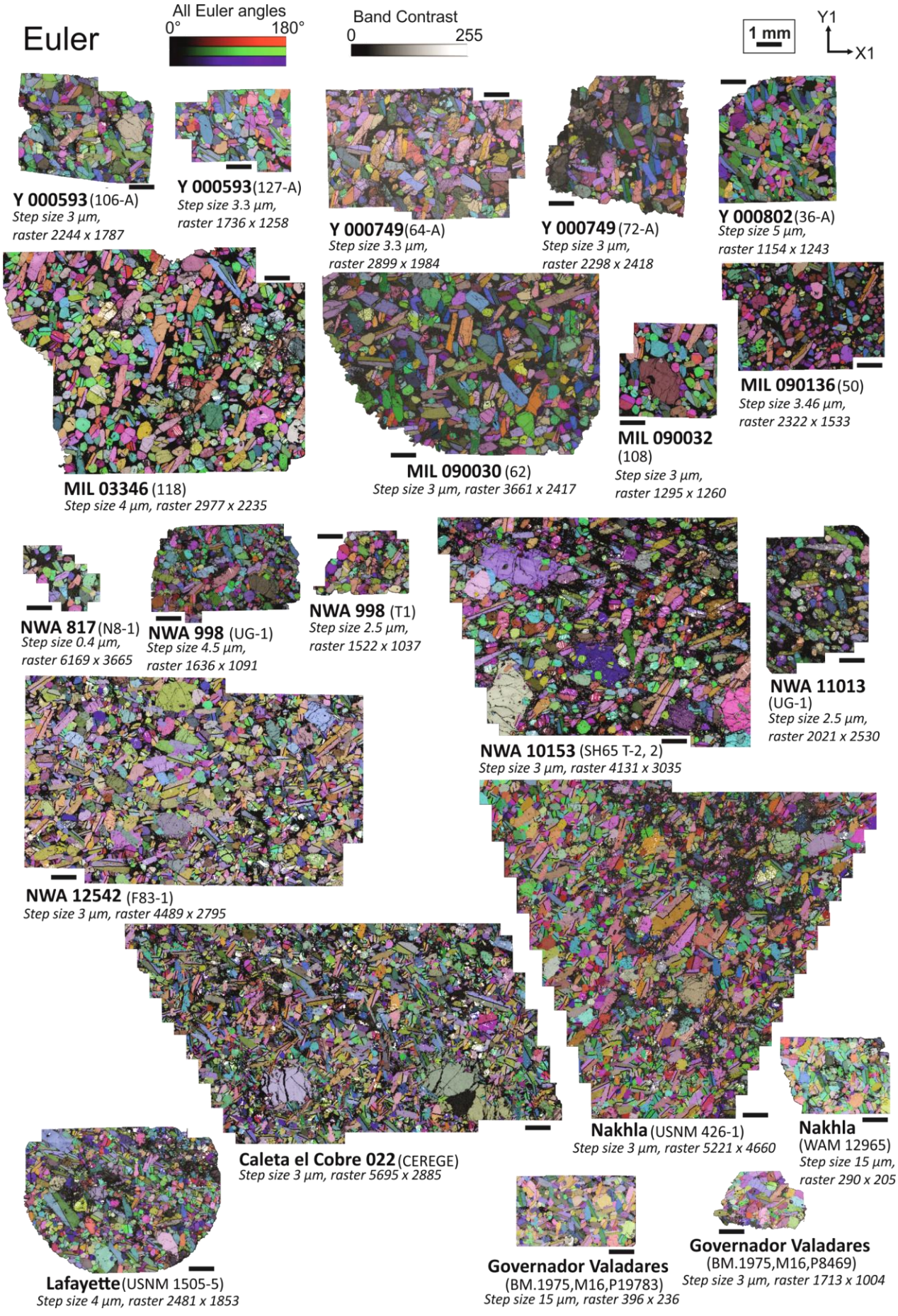

Figure 8.23. *Nakhlite combined Euler angle maps.*

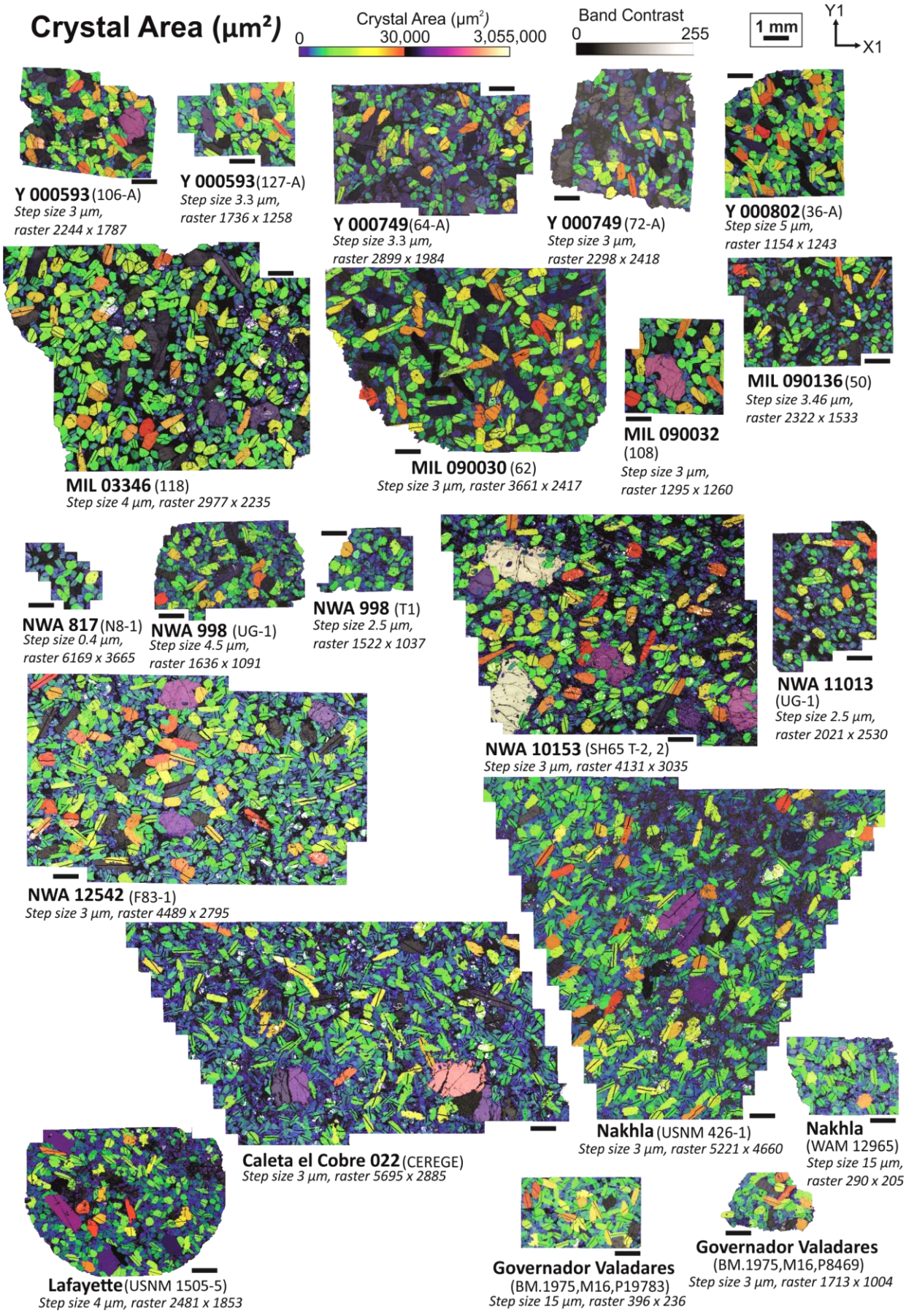

Figure 8.24. *Nakhlite crystal size maps.*

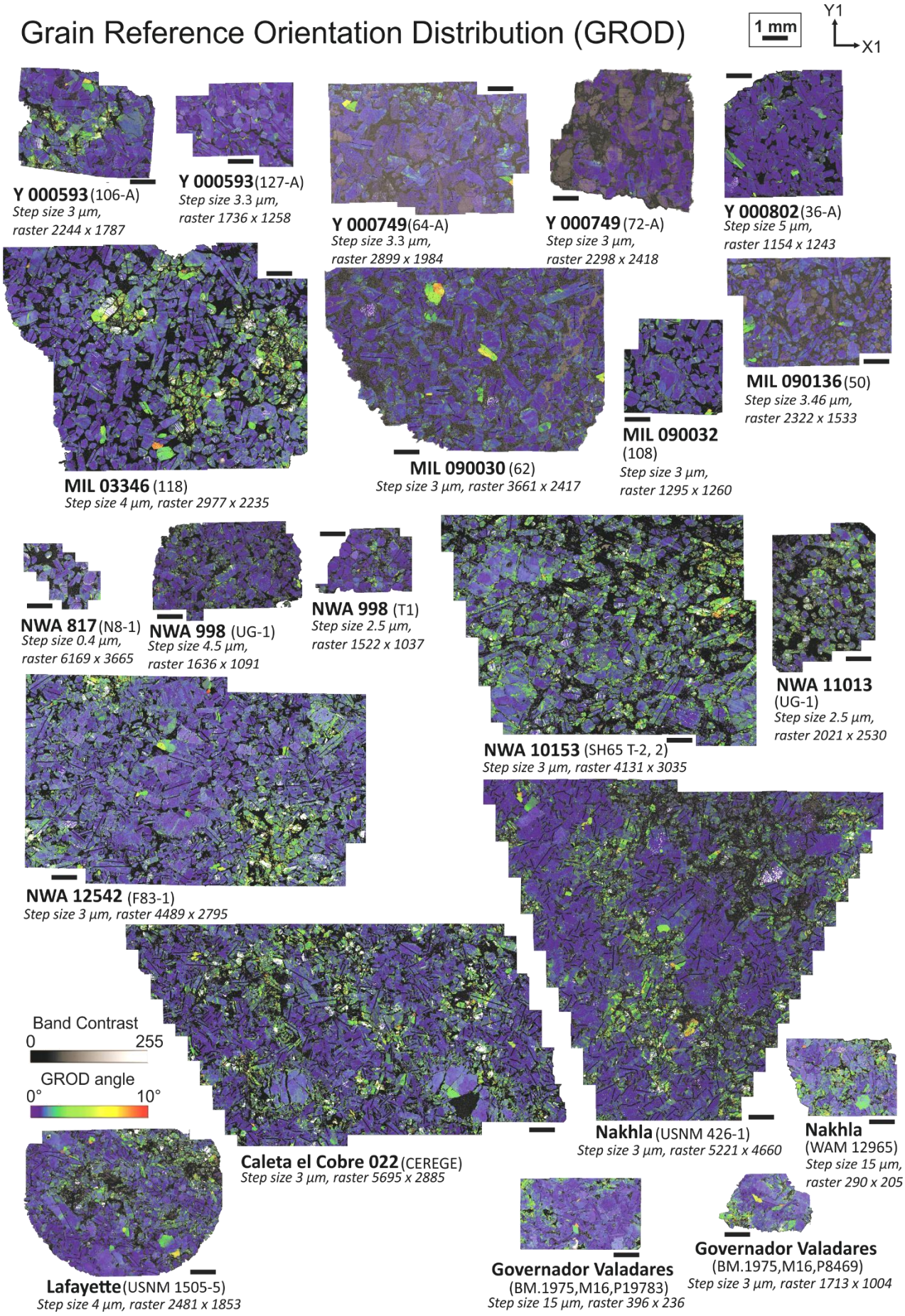

Figure 8.25. *Nakhlite grain reference orientation (GROD) angle maps.*

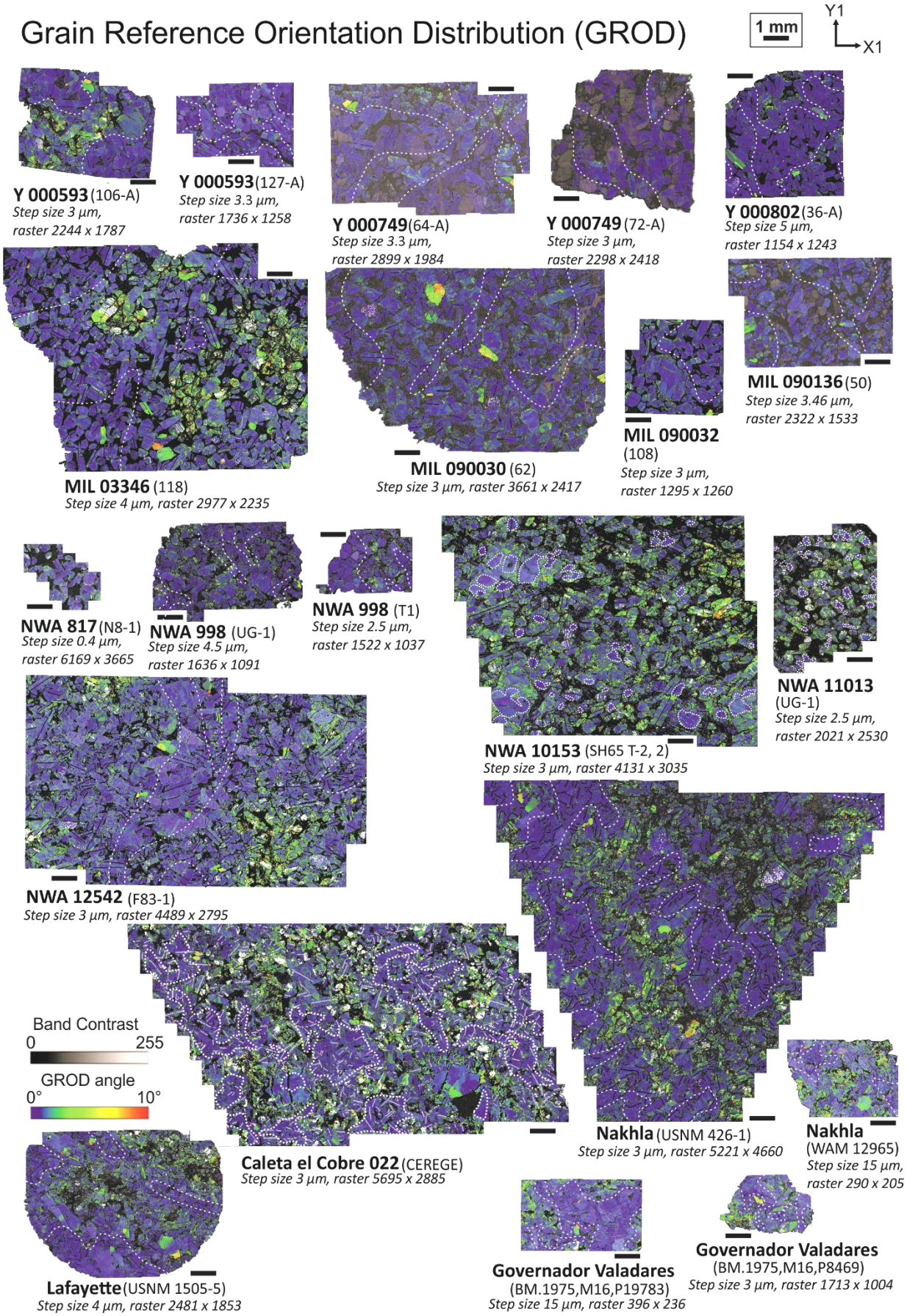

Figure 8.26. *Nakhlite grain reference orientation (GROD) angle maps depicting high deformation and low deformation regions used for slip-system analysis (Chapter IV).*

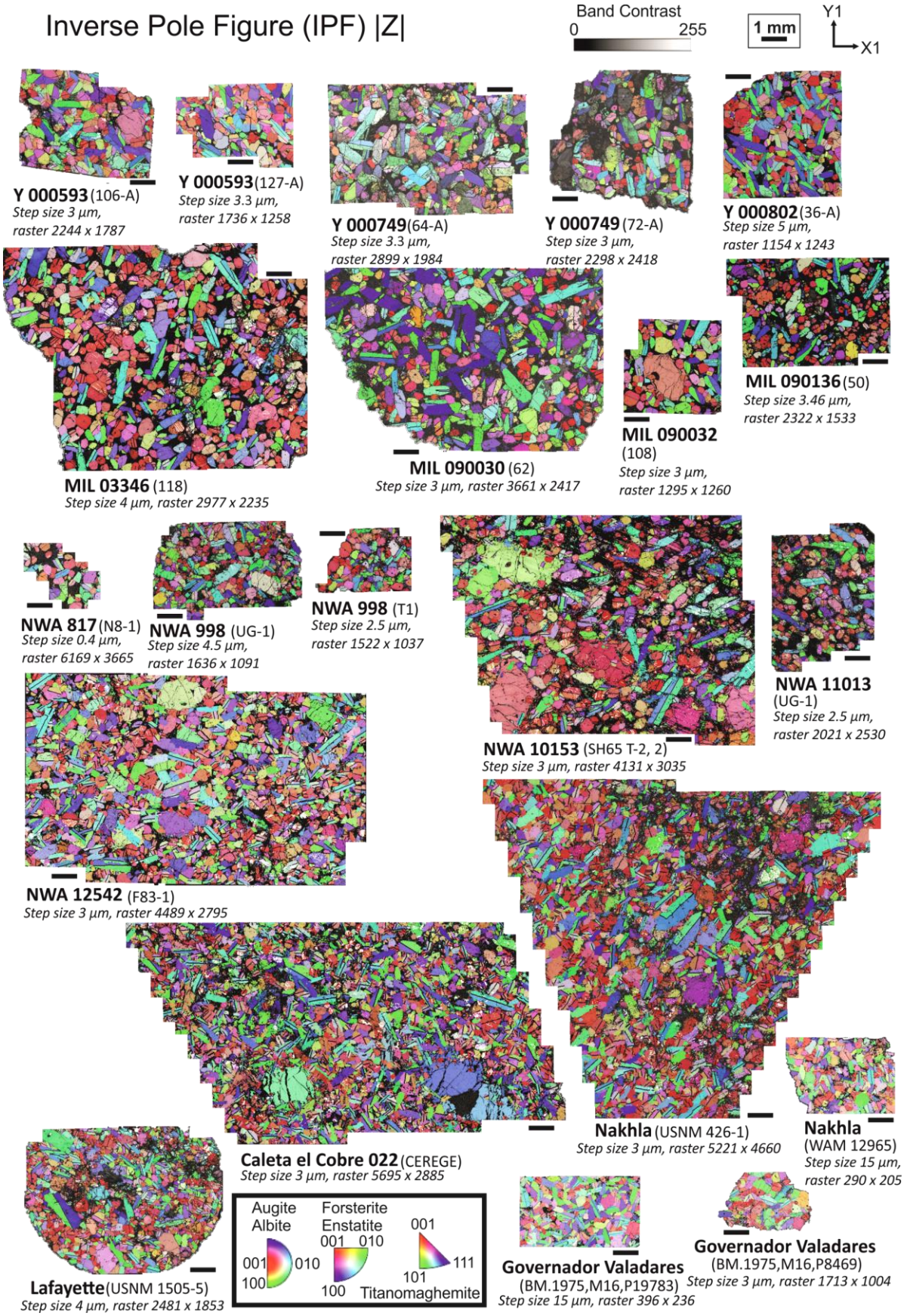

Figure 8.27. *Nakhlite inverse pole figure (IPF) |Z| maps.*

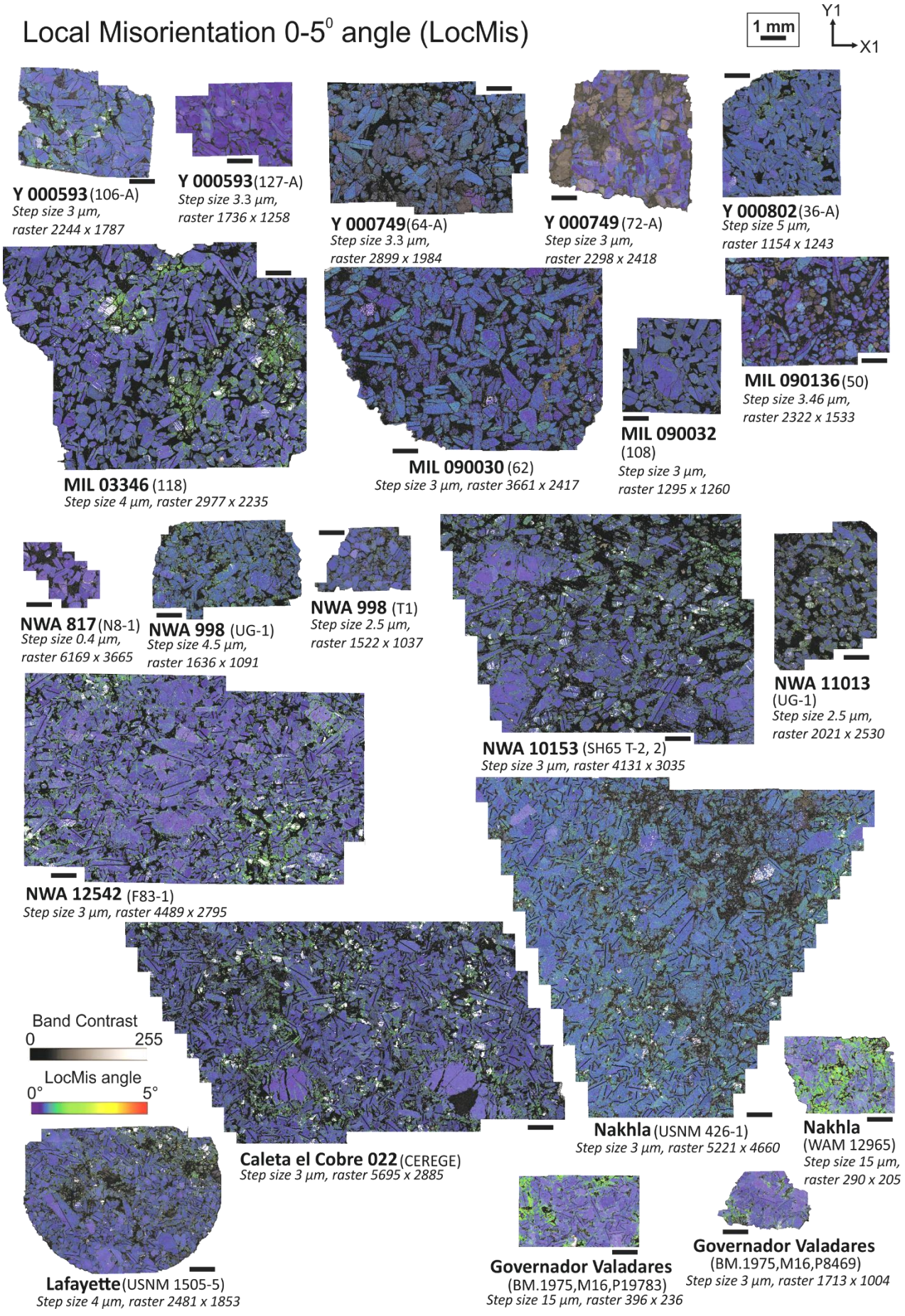

Figure 8.28. *Nakhlite local misorientation maps.*

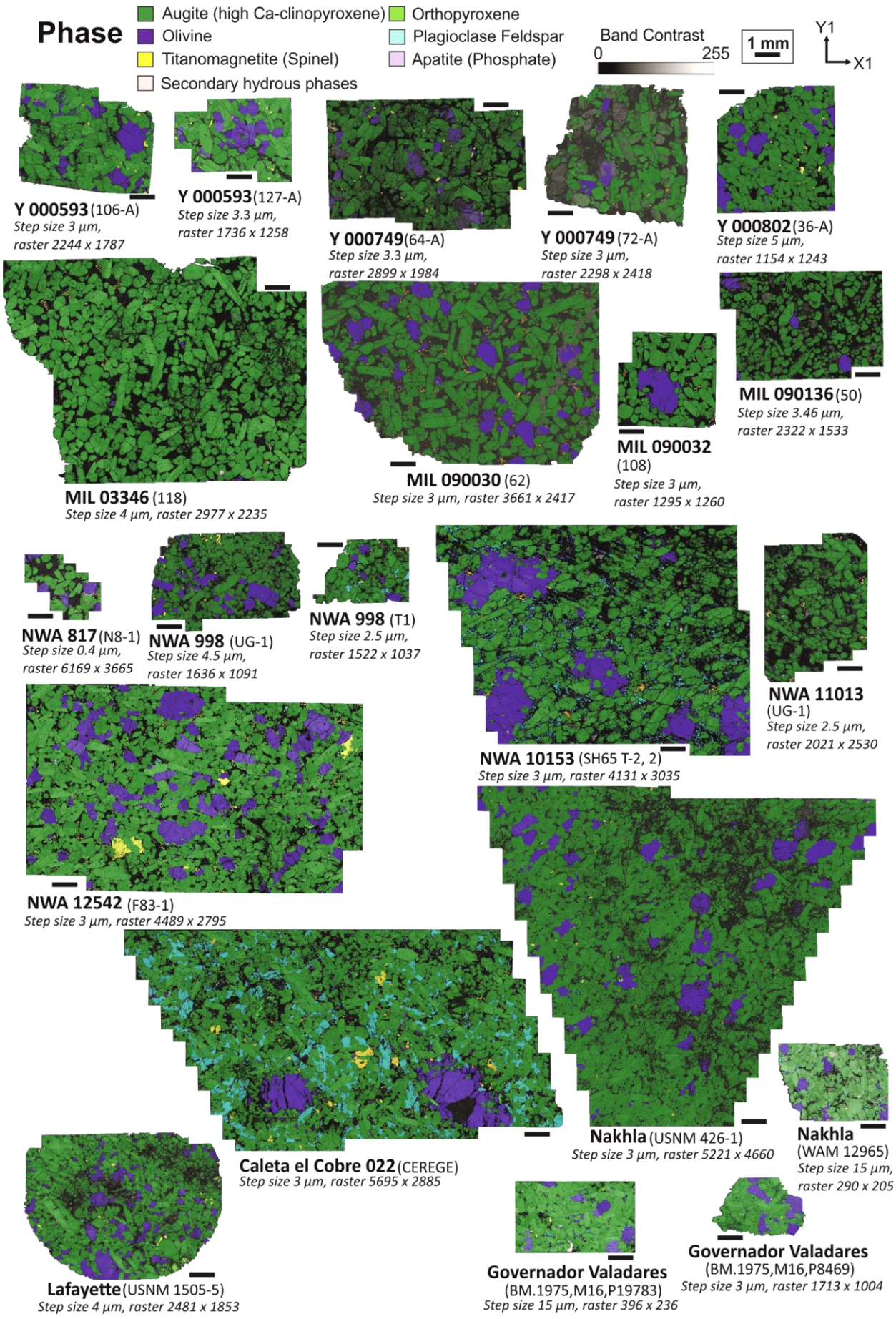

Figure 8.29. *Nakhlite indexed phase maps.*

8.6 Intra-crystalline misorientation/slip-system diagrams

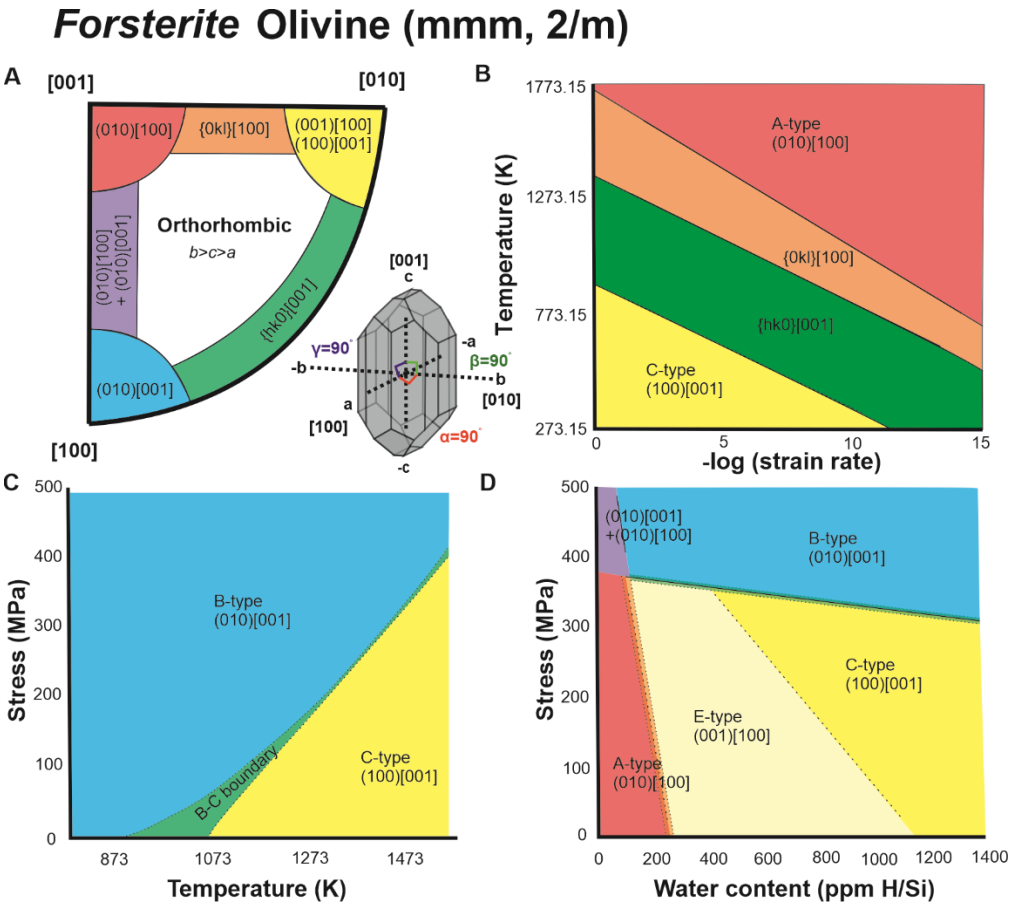

Figure 8.30. *Olivine slip-system regions.*

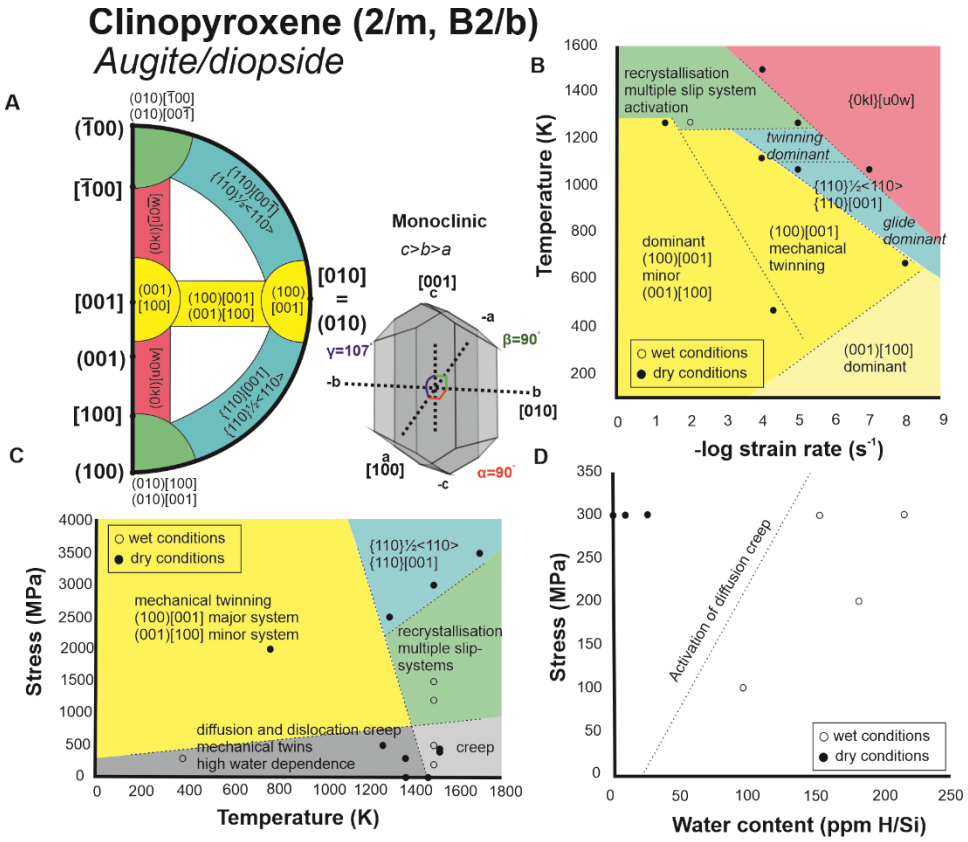

Figure 8.31. Clinopyroxene slip-system regions with literature data.

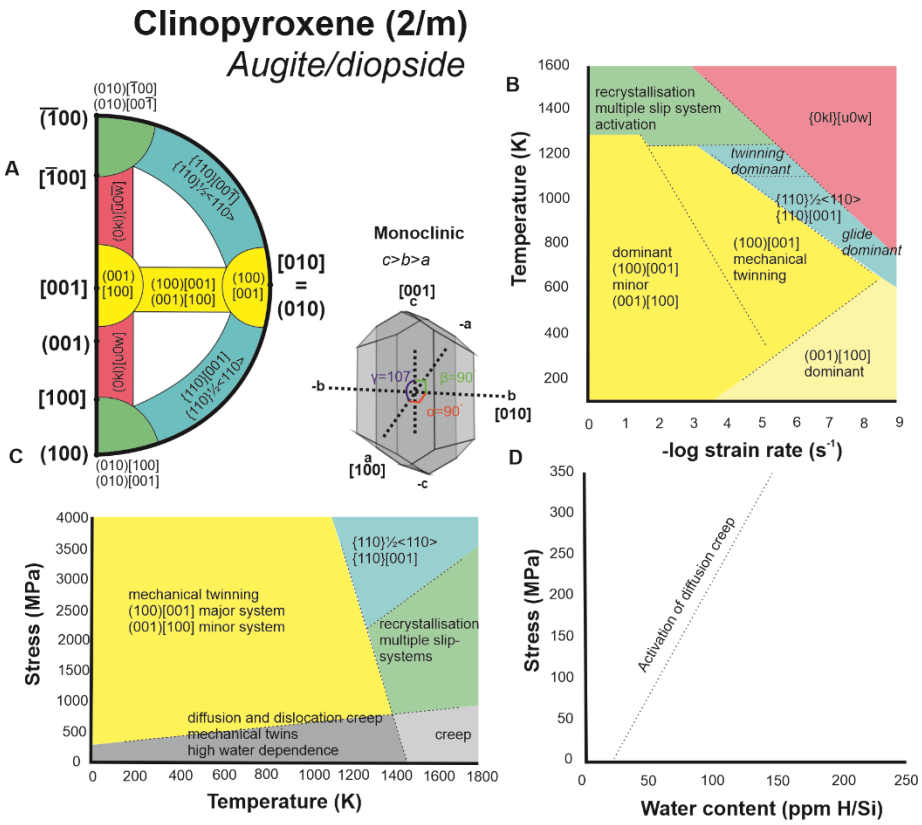

Figure 8.32. Clinopyroxene slip-system regions.

8.7 Additional publications

8.7.1 Research papers

Daly, L.; Lee, M.R.; Bagot, P.; Halpin, J.; Smith, W.; Mcfadzean, S.; O'Brien, A.C.; **Griffin, S**: Hallis, L.J.; BE Cohen (2020). Exploring Mars at the nanoscale: Applications of transmission electron microscopy and atom probe tomography in planetary exploration. *IOP Conference Series: Materials Science and Engineering, 891.*

Daly, L.; Piazolo, S.; Lee, M.R.; **Griffin, S.**; Chung, P; Fabrizio, C.; Cohen, B.E.; Hallis, L.J.; Trimby, P.W.; Baumgartner, R.; Forman, L.V.; Benedix, G.K. (2019). Understanding the emplacement of Martian volcanic rocks using petrofabrics of the nakhlite meteorites. *Earth and Planetary Science Letters, 520,* 220-230.

Daly, L.; Lee, M.R.; Piazolo, S.; **Griffin, S.**; Bazargan, M.; Campanale, F.; Chung, P.; Cohen, B.E., Hallis, L.J.; Trimby, P.W.; Baumgartner, R.; Forman, L.V.; Benedix, G.K. (2019). Boom Boom Pow: shock-facilitated aqueous alteration and evidence for two shock events in the Martian nakhlite meteorites. *Science Advances, 5*, 1-11.

Lee, M.R.; Daly, L.; Cohen, B.E.; Hallis, L.J.; **Griffin, S.**; Trimby, P.; Boyce, A; Mark, D.F. (2018). Aqueous alteration of the martian meteorite Northwest Africa 817: Probing fluid-rock interaction at the nakhlite launch site. *Meteoritics and Planetary Science, 53,* 2395-2412.

8.7.2 Conference abstracts

Griffin, S.; Daly, L.; Lee, M.R.; Piazolo, S.; Bazargan, M.; Chung, P.; Cohen, B.E.; Campanale, F.; Pickersgill, A. E.; Hallis, L. J.; Trimby, P.W.; Baumgartner, R.; Forman, L.V.; Benedix, G.K. (2020). Implications of shock-facilitated alteration on Mars from EBSD and EDS analysis of the nakhlites. *51st Lunar and Planetary Science Conference*, The Woodlands, Texas, U.S.A., 16-20 March 2020.

Griffin, S; Daly, L.; Udry, A.; lee, M. R.; Cohen, B. E. (2020) Assessing the relationship between crystal orientation and shock in the Yamato nakhlites. *2nd meeting of the British Planetary Science Congress*, Oxford, UK, 13-15 January 2020.

Griffin, S; Daly, L.; Lee, M.R.; Cohen, B.E. (2019). The Yamato Nakhlites: A case study for three-dimensional analysis. *82nd Annual meeting of the Meteoritical Society*, Sapporo, Japan, 7-12 July 2019.

Griffin, S.; Daly, L.; Lee, M.R.; Piazolo, S.; Trimby, P.W.; Forman, L.V.; Chung, P.; Cohen, B.E.; Baumgartner, R.; Benedix, G.K. (2019). New insights into the magmatic and shock history of the nakhlite meteorites from Electron Backscatter Diffraction. *50th Lunar and Planetary Science Conference*, The Woodlands, Texas, U.S.A., 18-22 March 2019.

Griffin, S.; Daly, L.; Lee, M.R.; Cohen, B.E. (2018). Characterising shock deformation of the martian crust by Electron Backscatter Diffraction (EBSD) analysis of the nakhlite meteorites Governador Valadares and NWA 998. *15th European Workshop on Modern Developments and Applications in Microbeam Analysis (EMAS2018).* Bristol, U.K., 4-7 September 2018.

Forman, L.V.; Daly, L.; Bland, P.A.; Corrigan, C.M.; McCoy, T.J.; Hoskin, J.; Anders, C.; Polley, G.; Trimby, P.W.; Piazolo, S. **Griffin, S.**; Pickersgill, A.E.; O'Brien, A.C. (2019). Macroscale and microscale fabric analysis of Allende. *82nd Annual meeting of the Meteoritical Society*, Sapporo, Japan, 7-12 July 2019.

Daly, L.; Lee, M.R.; Bagot, P.; Halpin, J.; Smith, W.; McFadzean, S.; O'Brien, A.C.; **Griffin, S.**; Cohen, B.E. (2019). Exploring Mars at the nanoscale: Applications of Transmission Electron Microscopy and Atom Probe Tomography in planetary exploration. *16th European Workshop on Modern Developments and Applications in Microbeam Analysis (EMAS2019)*. Trondheim, Norway, 19-23 May 2019. (Accepted Publication).

Cohen, B.E.; Mark, D.F.; Lee, M.R.; Cassata, W.S.; **Griffin, S.**; Smith, C.L.; Tomkinson, T. (2018). The nakhlites sample multiple igneous units: evidence from $^{40}Ar/^{39}Ar$ chronology and geochemistry. *49th Lunar and Planetary Science Conference 2018*, The Woodlands, Texas, U.S.A.

Griffin, S.; Lee, M.R.; Cohen, B.E.; Daly, L. (2019). Crystallisation and alteration of the Yamato nakhlites. *82nd Annual meeting of the Meteoritical Society*, Sapporo, Japan, 7-12 July 2019.

Griffin, S.; Daly, L.; Lee, M.R.; Piazolo, S.; Trimby, P.W.; Forman, L.V.; Chung, P.; Cohen, B.E.; Baumgartner, R.; Benedix, G.K. (2019). Nakhlite meteorite petrofabrics revealed by Electron Backscatter Diffraction. *50th Lunar and Planetary Science Conference*, The Woodlands, Texas, U.S.A., 18-22 March 2019.

Griffin, S.; Cohen, B.E.; Lee, M.R.; Kirby, S. (2017). Reassessing the geochemical evolution of the nakhlite meteorites as multiple martian lava flows. *1st British Planetary Science Congress*, Glasgow, U.K., 3-5 Dec 2017.

9 List of References

Adams, B. L., & Field, D. P. (2009). Electron Backscatter Diffraction in Materials Science. In A. J. Schwartz, M. Kumar, B. L. Adams, & D. P. Field (Eds.), *Electron Backscatter Diffraction in Materials Science* (Second, pp. i–xxii). https://doi.org/10.1007/978-0-387-88136-2

Anderson, D. L. (1981). Hotspots, basalts, and the evolution of the mantle. *Science (New York, N.Y.)*, *213*(4503), 82–9. https://doi.org/10.1126/science.213.4503.82

Artemieva, N. A., & Ivanov, B. A. (2004). Launch of martian meteorites in oblique impacts. *Icarus*, *171*(1), 84–101. https://doi.org/10.1016/j.icarus.2004.05.003

Ashby, M. F. (1970). The deformation of plastically non-homogeneous materials. *Philosophical Magazine*, *21*(170), 399–424. https://doi.org/10.1080/14786437008238426

Ashby, M. F. (1983). *Mechanisms of Deformation and Fracture*. *Advances in Applied Mechanics* (Vol. 23).

Avé Lallemant, H. G. (1978). Experimental deformation of diopside and websterite. *Tectonophysics*, *48*(1–2), 1–27. https://doi.org/https://doi.org/10.1016/0040-1951(78)90083-5

Bachmann, F., Hielscher, R., Jupp, P. E., Pantleon, W., Schaeben, H., & Wegert, E. (2010). Inferential statistics of electron backscatter diffraction data from within individual crystalline grains. *Journal of Applied Crystallography*, *43*(6), 1338–1355. https://doi.org/10.1107/S002188981003027X

Bachmann, F., Hielscher, R., & Schaeben, H. (2011). Grain detection from 2d and 3d EBSD data-Specification of the MTEX algorithm. *Ultramicroscopy*, *111*(12), 1720–1733. https://doi.org/10.1016/j.ultramic.2011.08.002

Bacon, C. R., Sison, T. W., & Mazdab, F. K. (2007). Young cumulate complex beneath Veniaminof caldera, Aleutian arc, dated by zircon in erupted plutonic blocks. *Geology*, *35*(6), 491–494. https://doi.org/10.1130/G23446A.1

Balta, J. B., Sanborn, M. E., Mayne, R. G., Wadhwa, M., McSween, H. Y., & Crossley, S. D. (2017). Northwest Africa 5790: A previously unsampled portion of the upper part of the nakhlite pile. *Meteoritics and Planetary Science*, *52*(1), 36–59. https://doi.org/https://doi.org/10.1111/maps.12744

Barber, D. J., Wenk, H. R., Hirth, G., & Kohlstedt, D. L. (2010). *Chapter 95 Dislocations in Minerals*. *Dislocations in Solids* (Vol. 16). Elsevier. https://doi.org/10.1016/S1572-4859(09)01604-0

Barsdell, M. (1988). Petrology and petrogenesis of clinopyroxene-rich tholeiitic lavas, Merelava Volcano, Vanuatu. *Journal of Petrology*, *29*(5), 927–964. https://doi.org/https://doi.org/10.1093/petrology/29.5.927

Bascou, J., Tommansi, A., Mainprice, D., Tommasi, A., & Mainprice, D. (2002). Plastic deformation and development of clinopyroxene lattice preferred orientations in eclogites. *Journal of Structural Geology*, *24*(2002), 43603. https://doi.org/10.1016/S0191-8141(01)00137-7

Bascou, J., Tommasi, A., & Mainprice, D. (2002). Plastic deformation and development of clinopyroxene lattice preferred orientations in eclogites. *Journal of Structural Geology*, *24*(8), 1357–1368. https://doi.org/10.1016/S0191-8141(01)00137-7

Bascou, J., Doucet, L. S., Saumet, S., Ionov, D. A., Ashchepkov, I. V., & Golovin, A. V. (2011). Seismic velocities, anisotropy and deformation in Siberian cratonic mantle: EBSD data on xenoliths from the Udachnaya kimberlite. *Earth and Planetary Science Letters*, *304*(1–2), 71–84. https://doi.org/10.1016/j.epsl.2011.01.016

Baumgartner, R. J., Baratoux, D., Gaillard, F., & Fiorentini, M. L. (2017). Numerical modelling of erosion and assimilation of sulfur-rich substrate by martian lava flows: Implications for the genesis of massive sulfide mineralization on Mars. *Icarus*, *296*, 257–274. https://doi.org/10.1016/j.icarus.2017.06.016

Becker, T. E. (2011). *Preferred orientations of pyroxene in the Zagami shergottite: Implications for magmatic emplacement*. Colby College.

Belleguic, V., Lognonné, P., & Wieczorek, M. (2005). Constraints on the Martian lithosphere from gravity and topography data. *Journal of Geophysical Research E: Planets*, *110*(11), 1–22. https://doi.org/10.1029/2005JE002437

Berkley, J. L., Keil, K., & Prinz, M. (1980). Comparative petrology and origin of Governador Valadares and other nakhlites. In *Proceedings of Lunar and Planetary Science* (Vol. 11, pp. 1089–1102). Retrieved from https://adsabs.harvard.edu/pdf/1980LPSC...11.1089B

Bernard, R. E., Behr, W. M., Becker, T. W., Young, D. J., & Young, David, J. (2019). Relationships Between Olivine CPO and Deformation Parameters in Naturally Deformed Rocks and Implications for Mantle Seismic Anisotropy. *Geochemistry, Geophysics, Geosystems*, *20*(7), 3469–3494. https://doi.org/10.1029/2019GC008289

Bertolett, E. M., Prior, D. J., Gravley, D. M., Hampton, S. J., & Kennedy, B. M. (2019). Compacted cumulates revealed by electron backscatter diffraction analysis of plutonic lithics. *Geology*, *47*(5), 445–448. https://doi.org/https://doi.org/10.1130/G45616.1

Bestmann, M., & Prior, D. J. (2003). Intragranular dynamic recrystallization in naturally deformed calcite marble: Diffusion accommodated grain boundary sliding as a result of subgrain rotation recrystallization. *Journal of Structural Geology*, *25*(10), 1597–1613. https://doi.org/https:/doi.org/10.1016/S0191-8141(03)00006-3

Bhattacharyya, D. S. (1966). Orientation of mineral lineation along the flow direction in rocks. *Tectonophysics*, *3*(1), 29–33. https://doi.org/10.1016/0040-1951(66)90023-0

Bickel, C. E. (1979). The CIPW Normative Calculation. *Journal of Geological Education*, *27*(2), 80–82. https://doi.org/10.5408/0022-1368-27.2.80

Blamey, N. J. F., Parnell, J., McMahon, S., Mark, D. F., Tomkinson, T., Lee, M. R., et al. (2015). Evidence for methane in Martian meteorites. *Nature Communications*, *6*(May), 7399. https://doi.org/10.1038/ncomms8399

Bogard, D. D., & Johnson, P. (1983). Martian Gases in an Antarctic Meteorite? *Science*, *1228*(4611), 651–655. https://doi.org/https://doi.org/10.1126/science.221.4611.651

Boneh, Y., & Skemer, P. (2014). The effect of deformation history on the evolution of olivine CPO. *Earth and Planetary Science Letters*, *406*, 213–222. https://doi.org/10.1016/j.epsl.2014.09.018

Borg, L. E., & Drake, M. J. (2005). A review of meteorite evidence for the timing of magmatism and of surface or near-surface liquid water on Mars. *Journal of Geophysical Research: Planets*, *110*(12), 1–10. https://doi.org/https://doi.org/10.1029/2005JE002402

Bowling, T. J., Johnson, B. C., Wiggins, S. E., Walton, E. L., Melosh, H. J., & Sharp, T. G. (2020). Dwell time at high pressure of meteorites during impact ejection from Mars. *Icarus*, *343*(February), 113689. https://doi.org/10.1016/j.icarus.2020.113689

Bridges, J. C., & Grady, M. M. (1999). A halite-siderite-anhydrite-chlorapatite assemblage in Nakhla: Mineralogical evidence for evaporites on Mars. *Meteoritics & Planetary Science*, *34*(3), 407–415. https://doi.org/10.1111/j.1945-5100.1999.tb01349.x

Bridges, J. C., & Grady, M. M. (2000). Evaporite mineral assemblages in the nakhlite (martian) meteorites. *Earth and Planetary Science Letters*, *176*(3–4), 267–279. https://doi.org/10.1016/S0012-821X(00)00019-4

Bridges, J. C., & Schwenzer, S. P. (2012). The nakhlite hydrothermal brine on Mars. *Earth and Planetary Science Letters*, *359–360*, 117–123. https://doi.org/10.1016/j.epsl.2012.09.044

Bridges, J. C., Catling, D. C., Saxton, J. M., Swindle, T. D., Lyon, I. C., & Grady, M. M. (2001). Alteration assemblages in Martian meteorites : implications for near-surface processes. *Space Science Reviews*, *96*(1–4), 365–392. https://doi.org/10.1023/A

Britton, T. Ben, Jiang, J., Guo, Y., Vilalta-Clemente, A., Wallis, D., Hansen, L. N., et al. (2016). Tutorial: Crystal orientations and EBSD - Or which way is up? *Materials Characterization*, *117*, 113–126. https://doi.org/10.1016/j.matchar.2016.04.008

Brož, P., Hauber, E., Platz, T., & Balme, M. (2015). Evidence for Amazonian highly viscous lavas in the southern highlands on Mars. *Earth and Planetary Science Letters*, *415*, 200–212. https://doi.org/10.1016/j.epsl.2015.01.033

Brož, P., Hauber, E., Wray, J. J., & Michael, G. (2017). Amazonian volcanism inside Valles Marineris on Mars. *Earth and Planetary Science Letters*, *473*, 122–130. https://doi.org/10.1016/j.epsl.2017.06.003

Bunch, T. E., & Reid, A. M. (1975). The Nakhlites. Part I: Petrography and mineral chemistry. *Meteoritics*, *10*, 303–315.

Bunge, H.-J. (1982). *Texture analysis in materials science: Mathematical methods*. (H.-J. Bunge, Ed.) (Paperback). Cuvillier Verlag, Gottingen. https://doi.org/10.7312/chi-18840-001

Burbine, T. H., McCoy, T. J., Meibom, A., Gladman, B., & Keil, K. (2002). Meteoritic parent bodies: Their number and identification. In W. F. Bottke, A. Cellino, Paolicchi, & R. P. Binzel (Eds.), *Asteroids III* (pp. 653–667). Tucson: University of Arizona Press. https://doi.org/10.1080/23744235.2017.1384957

Bystricky, M., & Mackwell, S. (2001). Creep of dry clinopyroxene aggregates with deformation in the dislocation creep. *Journal of Geophysical Research*, *106*, 13443–13454.

Callot, J. P., & Guichet, X. (2003). Rock texture and magnetic lineation in dykes: A simple analytical model. *Tectonophysics*, *366*(3–4), 207–222. https://doi.org/10.1016/S0040-1951(03)00096-9

Carr, M. H., & Head, J. W. (2010). Geologic history of Mars. *Earth and Planetary Science Letters*, *294*(3–4), 185–203. https://doi.org/10.1016/j.epsl.2009.06.042

Carr, M. H., Masursky, H., & Saunders, R. S. (1973). A generalized geologic map of Mars. *J Geophys Res*, *78*(20), 4031–4036. https://doi.org/10.1029/JB078i020p04031

Cartwright, J. A., Gilmour, J. D., & Burgess, R. (2013). Martian fluid and Martian weathering signatures identified in Nakhla, NWA 998 and MIL 03346 by halogen and noble gas analysis. *Geochimica et Cosmochimica Acta*, *105*, 255–293. https://doi.org/10.1016/j.gca.2012.11.046

Cashman, K. V., & Marsh, B. D. (1988). Crystal size distribution (CSD) in rocks and the kinetics and dynamics of crystallization II: Makaopuhi lava lake. *Contributions to Mineralogy and Petrology*, *99*(3), 292–305. https://doi.org/https://doi.org/10.1007/BF00375363

Cavosie, A. J., Erickson, T. M., & Timms, N. E. (2015). Nanoscale records of ancient shock deformation: Reidite (ZrSiO4) in sandstone at the Ordovician Rock Elm impact crater. *Geology*, *43*(4), 315–318. https://doi.org/10.1130/G36489.1

Chamberlain, T. E., Cole, H. L., Dutton, R. G., Greene, G. C., & Tillman, J. E. (1976). Atmopspheric Measurements on Mars: the Viking Meteorology Experiment. *Bulletin of the American Meteorological Society*, *57*(9), 1094–1104. https://doi.org/10.1175/1520-0477(1976)057<1094:amomtv>2.0.co;2

Changela, H. G., & Bridges, J. C. (2011). Alteration assemblages in the nakhlites: Variation with depth on

Mars. *Meteoritics and Planetary Science*, *45*(12), 1847–1867. https://doi.org/10.1111/j.1945-5100.2010.01123.x

Chin, E. J., Soustelle, V., & Liu, Y. (2020). An SPO-induced CPO in composite mantle xenoliths correlated with increasing melt-rock interaction. *Geochimica et Cosmochimica Acta*, *278*, 199–218. https://doi.org/10.1016/j.gca.2019.10.002

Cohen, B. E., Mark, D. F., Cassata, W. S., Lee, M. R., Tomkinson, T., Smith, C. L., et al. (2017). Taking the pulse of Mars via dating of a plume-fed volcano. *Nature Communications*, *8*(1), 640. https://doi.org/10.1038/s41467-017-00513-8

Cordier, P. (2002). Dislocations and slip systems of mantle minerals. *Reviews in Mineralogy and Geochemistry*, *51*. https://doi.org/10.2138/gsrmg.51.1.137

Corrigan, C. M., Velbel, M. A., & Vicenzi, E. P. (2015). Modal abundances of pyroxene, olivine, and mesostasis in nakhlites: Heterogeneity, variation, and implications for nakhlite emplacement. *Meteoritics and Planetary Science*, *50*(9), 1497–1511. https://doi.org/https://doi.org/10.1111/maps.12492

Cousin, A., Sautter, V., Payré, V., Forni, O., Mangold, N., Gasnault, O., et al. (2017). Classification of igneous rocks analyzed by ChemCam at Gale crater, Mars. *Icarus*, *288*, 265–283. https://doi.org/10.1016/j.icarus.2017.01.014

Cox, M. A., Cavosie, A. J., Bland, P. A., Miljković, K., & Wingate, M. T. D. (2019). Microstructural dynamics of central uplifts: Reidite offset by zircon twins at the Woodleigh impact structure, Australia. *Geology*, *47*(5), e465–e465. https://doi.org/10.1130/G46155C.1

Cox, M. A., Erickson, T. M., Schmieder, M., Christoffersen, R., Ross, D. K., Cavosie, A. J., et al. (2020). High-Resolution Microstructural and Compositional Analyses of Shock Deformed Apatite from the Peak Ring of the Chicxulub Impact Crater. *Meteoritics and Planetary Science, Accepted*, 1–19. https://doi.org/10.1111/maps.13541

Daly, L., Bland, P. A., Dyl, K. A., Forman, L. V., Saxey, D. W., Reddy, S. M., et al. (2016). Crystallography of refractory metal nuggets in carbonaceous chondrites: A transmission Kikuchi diffraction approach. *Geochimica et Cosmochimica Acta*. https://doi.org/10.1016/j.gca.2017.03.037

Daly, L., Lee, M. R., Piazolo, S., Griffin, S., Bazargan, M., Campanale, F., et al. (2019). Boom Boom Pow: shock-facilitated aqueous alteration and evidence for two shock events in the Martian nakhlite meteorites. *Science Advances*, *5*(9), 1–11. https://doi.org/DOI: 10.1126/sciadv.aaw5549

Daly, L., Piazolo, S., Lee, M. R., Griffin, S., Chung, P., Campanale, F., et al. (2019). Understanding the emplacement of Martian volcanic rocks using petrofabrics of the nakhlite meteorites. *Earth and Planetary Science Letters*, *520*, 220–230. https://doi.org/10.1016/j.epsl.2019.05.050

Darling, J. R., Moser, D. E., Barker, I. R., Tait, K. T., Chamberlain, K. R., Schmitt, A. K., & Hyde, B. C. (2016). Variable microstructural response of baddeleyite to shock metamorphism in young basaltic shergottite NWA 5298 and improved U-Pb dating of Solar System events. *Earth and Planetary Science Letters*, *444*, 1–12. https://doi.org/10.1016/j.epsl.2016.03.032

Darling, J. R., White, L. F., Kizovski, T., Černok, A., Moser, D. E., Tait, K. T., et al. (2021). The shocking state of apatite and merrillite in shergottite Northwest Africa 5298 and extreme nanoscale chlorine isotope variability revealed by atom probe tomography. *Geochimica et Cosmochimica Acta*, *293*, 422–437. https://doi.org/10.1016/j.gca.2020.11.007

Day, J. M. D., Taylor, L. A., Floss, C., & McSween, H. Y. (2006). Petrology and chemistry of MIL 03346 and its significance in understanding the petrogenesis of nakhlites on Mars. *Meteoritics & Planetary Science*, *41*(4), 581–606. https://doi.org/10.1111/j.1945-5100.2006.tb00484.x

Day, J. M. D., Tait, K. T., Udry, A., Moynier, F., Liu, Y., & Neal, C. R. (2018a). Martian magmatism from plume metasomatized mantle. *Nature Communications*, *9*(1), 4799. https://doi.org/10.1038/s41467-018-07191-0

Day, J. M. D., Tait, K. T., Udry, A., Moynier, F., Liu, Y., & Neal, C. R. (2018b). Rejuvenated magmatism on Mars. In *49th Lunar amd Planetary Science Conference* (p. A1014).

Devillepoix, H. A. R., Cupák, M., Bland, P. A., Sansom, E. K., Towner, M. C., Howie, R. M., et al. (2020). A Global Fireball Observatory. *Planetary and Space Science*, *191*(July). https://doi.org/10.1016/j.pss.2020.105036

Dingley, D. J., & Wright, S. I. (2009). Phase identification through symmetry determination in EBSD patterns. In A. J. Schwartz, M. Kumar, B. L. Adams, & D. P. Field (Eds.), *Electron Backscatter Diffraction in Materials Science* (Second, pp. 97–107). https://doi.org/10.1007/978-0-387-88136-2

Donohue, P. H., & Neal, C. R. (2015). Quantitative textural analysis of ilmenite in Apollo 17 high-titanium mare basalts. *Geochimica et Cosmochimica Acta*, *149*, 115–130. https://doi.org/10.1016/j.gca.2014.11.002

Donohue, P. H., & Neal, C. R. (2018). Textural and mineral chemical evidence for the cumulate origin and evolution of high-titanium basalt fragment 71597. *American Mineralogist*, *103*(2), 284–297. https://doi.org/10.2138/am-2018-6173

Durham, W. B., Mirkovich, V. V., & Heard, H. C. (1987). Thermal diffusivity of igneous rocks at elevated pressure and temperature. *Journal of Geophysical Research: Solid Earth*, *92*(B11), 11615–11634. https://doi.org/10.1029/jb092ib11p11615

Dyck, B., & Holness, M. B. (2022). Microstructural evidence for convection in high-silica granite. *Geology*, *50*(3), 295–299. https://doi.org/10.1130/g49431.1

Eigenbrode, J. L., Summons, R. E., Steele, A., Freissinet, C., Millan, M., Navarro-González, R., et al. (2018). Organic matter preserved in 3-billion-year-old mudstones at Gale crater, Mars. *Science*, (June), 1–6. https://doi.org/10.1126/science.aas9185

Einsle, J. F., Eggeman, A. S., Martineau, B. H., Saghi, Z., Collins, S. M., & Blukis, R. (2018). Nanomagnetic properties of the meteorite cloudy zone. *PNAS*, *115*(49), 1–10. https://doi.org/10.1073/pnas.1809378115

Erickson, T. M., Cavosie, A. J., Moser, D. E., Barker, I. R., & Radovan, H. A. (2013). Correlating planar microstructures in shocked zircon from the Vredefort Dome at multiple scales: Crystallographic modeling, external and internal imaging, and EBSD structural analysis. *American Mineralogist*, *98*(1), 53–65. https://doi.org/10.2138/am.2013.4165

Farla, R. J. M., Kokkonen, H., Gerald, J. D. F., Barnhoorn, A., Faul, U. H., & Jackson, I. (2011). Dislocation recovery in fine-grained polycrystalline olivine. *Physics and Chemistry of Minerals*, *38*(5), 363–377. https://doi.org/10.1007/s00269-010-0410-3

Farley, K. A., Williford, K. H., Stack, K. M., Bhartia, R., Chen, A., de la Torre, M., et al. (2020). Mars 2020 Mission Overview. *Space Science Reviews*, *216*(8). https://doi.org/10.1007/s11214-020-00762-y

Fei, H., Hegoda, C., Yamazaki, D., Wiedenbeck, M., Yurimoto, H., Shcheka, S., & Katsura, T. (2012). High silicon self-diffusion coefficient in dry forsterite. *Earth and Planetary Science Letters*, *345–348*, 95–103. https://doi.org/10.1016/j.epsl.2012.06.044

Fenton, C. R., Poreda, R. J., Nash, B. P., Webb, R. H., & Cerling, T. E. (2004). Geochemical Discrimination of Five Pleistocene Lava-Dam Outburst-Flood Deposits, Western Grand Canyon, Arizona. *The Journal of Geology*, *112*(1), 91–110. https://doi.org/10.1086/379694

Fleck, N. A., Muller, G. M., Ashby, M. F., & Hutchinson, J. W. (1994). Strain gradient plasticity: theory and experiment. *Acta Metal Material*, *42*(2), 475–487.

Forman, L. V., Bland, P. A., Timms, N. E., Collins, G. S., Davison, T. M., Ciesla, F. J., et al. (2016). Hidden secrets of deformation: Impact-induced compaction within a CV chondrite. *Earth and Planetary Science Letters*, *452*, 133–145. https://doi.org/10.1016/j.epsl.2016.07.050

Forman, L. V., Bland, P. A., Timms, N. E., Daly, L., Benedix, G. K., Trimby, P. W., et al. (2017). Defining the mechanism for compaction of the CV chondrite parent body. *Geology*, *45*(6), 559–562. https://doi.org/10.1130/G38864.1

Forman, L. V., Timms, N. E., Bland, P. A., Daly, L., Benedix, G. K., & Trimby, P. W. (2019). A morphologic and crystallographic comparison of CV chondrite matrices. *Meteoritics & Planetary Science*, *2651*(11), 2633–2651. https://doi.org/10.1111/maps.13380

Frets, E., Tommasi, A., Garrido, C. J., Padrón-Navarta, J. A., Amri, I., & Targuisti, K. (2012). Deformation processes and rheology of pyroxenites under lithospheric mantle conditions. *Journal of Structural Geology*, *39*, 138–157. https://doi.org/10.1016/j.jsg.2012.02.019

Friedman Lentz, R. C., Taylor, G. J., & Treiman, A. H. (1999). Formation of a martian pyroxenite: A comparative study of the nakhlite meteorites and Theo's Flow. *Meteoritics & Planetary Science*, *34*(6), 919–932. https://doi.org/10.1111/j.1945-5100.1999.tb01410.x

Friedman Lentz, R. C., McCoy, T. J., Collins, L. E., Corrigan, C. M., & Benedix, G. K. (2011). Theo's Flow, Ontario, Canada: A terrestrial analog for Martian meteorites. *The Geological Society of America*, *Special Pa*(483), 263–277. https://doi.org/10.1130/2011.2483(17)

Friedrich, J. M., Ruzicka, A., Macke, R. J., Thostenson, J. O., Rudolph, R. A., Rivers, M. L., & Ebel, D. S. (2017). Relationships among physical properties as indicators of high temperature deformation or post-shock thermal annealing in ordinary chondrites. *Geochimica et Cosmochimica Acta*, *203*, 157–174. https://doi.org/10.1016/j.gca.2016.12.039

Fritz, J., Artemieva, N. A., & Greshake, A. (2005). Ejection of Martian meteorites. *Meteoritics & Planetary Science*, *40*(9–10), 1393–1411. https://doi.org/10.1111/j.1945-5100.2005.tb00409.x

Fritz, J., Greshake, A., & Stöffler, D. (2005). Micro-Ramen spectroscopy of plagioclase and maskelynite in Martian meteorites: Evidence of progressive shock metamorphism. *Antarctic Meteorite Research*, *18*, 96–116. https://doi.org/2005ASMR....18...96F

Gamble, J. A., Wood, C. P., Price, R. C., Smith, I. E. M., Stewart, R. B., & Waight, T. (1999). A fifty year perspective of magmatic evolution on Ruapehu Volcano, New Zealand: Verification of open system behaviour in an arc volcano. *Earth and Planetary Science Letters*, *170*(3), 301–314. https://doi.org/10.1016/S0012-821X(99)00106-5

Gerth, D., & Schwarzer, R. A. (1993). Graphical Representation of Grain and Hillock Orientations in Annealed Al–1%Si Films. *Textures and Microstructures*, *21*(2–3), 177–193. https://doi.org/10.1155/tsm.21.177

Gibb, F. G. F., & Henderson, C. M. B. (1992). Convection and crystalisation in sills. *Contrib. Mineral. Petrol.*, *109*, 538–545. https://doi.org/10.1007/BF00306555

Gillet, P., Barrat, J.-A., Deloule, E., Wadhwa, M., Jambon, A., Sautter, V., et al. (2002). Aqueous alteration in the Northwest Africa 817 (NWA 817) Martian meteorite. *Earth and Planetary Science Letters*, *203*(1), 431–444. https://doi.org/10.1016/S0012-821X(02)00835-X

Girard, J., Chen, J., Raterron, P., & Holyoke, C. W. (2013). Hydrolytic weakening of olivine at mantle pressure: Evidence of [100](010) slip system softening from single-crystal deformation experiments. *Physics of the Earth and Planetary Interiors*, *216*, 12–20. https://doi.org/10.1016/j.pepi.2012.10.009

Godard, G., & van Roermund, H. L. M. (1995). Deformation-induced clinopyroxene fabrics from eclogites. *Journal of Structural Geology*, *17*(10), 1425–1443. https://doi.org/10.1016/0191-8141(95)00038-F

Goldstein, J. I., & Michael, J. R. (2006). The formation of plessite in meteoritic metal. *Meteoritics and Planetary Science*, *41*(4), 553–570. https://doi.org/10.1111/j.1945-5100.2006.tb00482.x

Goldstein, Joseph I. (2012). *Practical scanning and electron microscopy: electron and ion microprobe analysis*. (Joseph I. Goldstein, Ed.). Springer Science & Business Media.

Goldstein, Joseph I., Newbury, D. E., Michael, J. R., Ritchie, N. W. M., Scott, J. H. J., & Joy, D. C. (2017). *Scanning electron microscopy and X-ray microanalysis*. (Joseph I. Goldstein, D. E. Newbury, & P. Schlin, Eds.). Springer US.

Goode, A. D. T. (1976). Small scale primary cumulus igneous layering in the kalka layered intrusion, giles complex, central Australia. *Journal of Petrology*, *17*(3), 379–397. https://doi.org/10.1093/petrology/17.3.379

Goswami, S., Mamtani, M. A., & Rana, V. (2018). Quartz CPO and kinematic analysis in deformed rocks devoid of visible stretching lineations: An integrated AMS and EBSD investigation. *Journal of Structural Geology*, *115*(March), 270–283. https://doi.org/10.1016/j.jsg.2018.04.008

Greeley, R., & Guest, J. E. (1987). *Geologic map of the eastern equatorial region of Mars*. *Arcadia*. U.S. Geological Survey. Retrieved from http://astrogeology.usgs.gov/Projects/PlanetaryMapping/DIGGEOL/mars/marseast/me.pdf

Greeley, R., & Spudis, P. D. (1981). Volcanism on Mars. *Reviews of Geophysics and Space Physics*, *19*(1), 13–41. https://doi.org/10.1029/RG019i001p00013

Greshake, A., Fritz, J., Böttger, U., & Goran, D. (2013). Shear-induced ringwoodite formation in the Martian shergottite Dar al Gani 670. *Earth and Planetary Science Letters*, *375*, 383–394. https://doi.org/10.1016/j.epsl.2013.06.002

Griffin, S., Keller, T., Daly, L., Lee, M. R., Cohen, B. E., Forman, L. V., et al. (n.d.). *Emplacement of Amazonian nakhlite ignenous rocks and implications for their source volcano on Mars*.

Griffin, S., Daly, L., Keller, T., Piazolo, S., Forman, L. V., Lee, M. R., et al. (2021). Constraints on the emplacement of Martian nakhlite igneous rocks and their source volcano from advanced micro-petrofabric analysis (Version MTEX 5.7.0, MATLAB 2021a) [Data set]. Zenodo. Retrieved from https://doi.org/10.5281/ZENODO.5545821

Grott, M., Baratoux, D., Hauber, E., Sautter, V., Mustard, J., Gasnault, O., et al. (2013). Long-term evolution of the martian crust-mantle system. *Space Science Reviews*, *174*(1–4), 49–111. https://doi.org/10.1007/s11214-012-9948-3

Groves, G. W., & Kelly, A. (1963). Independent slip systems in crystals. *Philosophical Magazine*, *8*(89), 877–887. https://doi.org/10.1080/14786436308213843

Gueguen, Y., & Nicolas, A. (1980). Deformation of mantle rocks. *Annual Review of Earth and Planetary Sciences*, *8*, 119–144.

Halfpenny, A. (2010). Some important practical issues for the collection and manipulation of electron backscatter diffraction (EBSD) data from geological samples. *Journal of the Virtual Explorer*, *35*, 1–18. https://doi.org/10.3809/jvirtex.2011.00272

Halfpenny, A., Prior, D. J., & Wheeler, J. (2012). Electron backscatter diffraction analysis to determine the mechanisms that operated during dynamic recrystallisation of quartz-rich rocks. *Journal of Structural Geology*, *36*, 2–15. https://doi.org/10.1016/j.jsg.2012.01.001

Hallis, L. J., & Taylor, G. J. (2011). Comparisons of the four Miller Range nakhlites, MIL 03346, 090030, 090032 and 090136: Textural and compositional observations of primary and secondary mineral assemblages. *Meteoritics and Planetary Science*, *46*(12), 1787–1803. https://doi.org/10.1111/j.1945-5100.2011.01293.x

Hammer, J. E., Sharp, T. G., & Wessel, P. (2010). Heterogeneous nucleation and epitaxial crystal growth of magmatic minerals. *Geology*, *38*(4), 367–370. https://doi.org/10.1130/G30601.1

Hansen, L. N., Zhao, Y. H., Zimmerman, M. E., & Kohlstedt, D. L. (2014). Protracted fabric evolution in olivine: Implications for the relationship among strain, crystallographic fabric, and seismic anisotropy. *Earth and Planetary Science Letters*, *387*, 157–168. https://doi.org/10.1016/j.epsl.2013.11.009

Harrison, K. P., & Grimm, R. E. (2005). Groundwater-controlled valley networks and the decline of surface runoff on early Mars. *Journal of Geophysical Research E: Planets*, *110*(12), 1–17. https://doi.org/10.1029/2005JE002455

Harvey, R. P., & McSween, H. Y. (1992). The parent magma of the nakhlite meteorites: Clues from melt inclusions. *Earth and Planetary Science Letters*, *111*(2–4), 467–482. https://doi.org/10.1016/0012-821X(92)90197-4

Hauber, E., Brož, P., Jagert, F., Jodowski, P., & Platz, T. (2011). Very recent and wide-spread basaltic volcanism on Mars. *Geophysical Research Letters*, *38*(10), 1–5. https://doi.org/10.1029/2011GL047310

Head, J. N., Melosh, H. J., & Ivanov, B. A. (2002). Martian meteorite launch: High-speed ejecta from small

craters. *Science*, *298*(5599), 1752–1756. https://doi.org/10.1126/science.1077483
Helmstaedt, H., Anderson, O. L., & Gavasci, A. T. (1972). Petrofabric studies of eclogite, spinel-Websterite, and spinel-lherzolite Xenoliths from kimberlite-bearing breccia pipes in southeastern Utah and northeastern Arizona. *Journal of Geophysical Research*, *77*(23), 4350–4365. https://doi.org/10.1029/JB077i023p04350
Henry, H., Tilhac, R., Griffin, W. L., O'Reilly, S. Y., Satsukawa, T., Kaczmarek, M.-A., et al. (2017). Deformation of mantle pyroxenites provides clues to geodynamic processes in subduction zones: Case study of the Cabo Ortegal Complex, Spain. *Earth and Planetary Science Letters*, *472*, 174–185. https://doi.org/10.1016/j.epsl.2017.05.028
Henry, H., Kaczmarek, M. A., Ceuleneer, G., Tilhac, R., Griffin, W. L., O'Reilly, S. Y., et al. (2021). The microstructure of layered ultramafic cumulates: Case study of the Bear Creek intrusion, Trinity ophiolite, California, USA. *Lithos*, *388–389*. https://doi.org/10.1016/j.lithos.2021.106047
Hepburn, A. J., Ng, F. S. L., Holt, T. O., & Hubbard, B. (2020). Late Amazonian Ice Survival in Kasei Valles, Mars. *Journal of Geophysical Research: Planets*, *125*(11). https://doi.org/10.1029/2020JE006531
Hicks, L. J., Bridges, J. C., & Gurman, S. J. (2014). Ferric saponite and serpentine in the nakhlite martian meteorites. *Geochimica et Cosmochimica Acta*, *136*(April), 194–210. https://doi.org/10.1016/j.gca.2014.04.010
Hidas, K., Garrido, C. J., Booth-Rea, G., Marchesi, C., Bodinier, J. L., Dautria, J. M., et al. (2019). Lithosphere tearing along STEP faults and synkinematic formation of lherzolite and wehrlite in the shallow subcontinental mantle. *Solid Earth*, *10*(4), 1099–1121. https://doi.org/10.5194/se-10-1099-2019
Hier-Majumder, S., Mei, S., & Kohlstedt, D. L. (2005). Water weakening of clinopyroxenite in diffusion creep. *Journal of Geophysical Research: Solid Earth*, *110*(7), 1–12. https://doi.org/10.1029/2004JB003414
Higgins, M. D. (2000). Measurement of crystal size distributions. *American Mineralogist*, *85*(9), 1105–1116. https://doi.org/10.2138/am-2000-8-901
Higgins, M. D. (2006). *Quantitative textural measurements in igneous and metamorphic petrology* (1st ed., Vol. 1). New York: Cambridge University Press.
Hirt, C., Claessens, S. J., Kuhn, M., & Featherstone, W. E. (2012). Kilometer-resolution gravity field of Mars: MGM2011. *Planetary and Space Science*, *67*(1), 147–154. https://doi.org/10.1016/j.pss.2012.02.006
Holness, M. B. (2007). Textural immaturity of cumulates as an indicator of magma chamber processes: Infiltration and crystal accumulation in the Rum Eastern Layered Intrusion. *Journal of the Geological Society*, *164*(3), 529–539. https://doi.org/10.1144/0016-76492006-021
Holness, M. B., Cheadle, M. J., & McKenzie, D. (2005). On the use of changes in dihedral angle to decode late-stage textural evolution in cumulates. *Journal of Petrology*, *46*(8), 1565–1583. https://doi.org/10.1093/petrology/egi026
Holness, M. B., Tegner, C., Nielsen, T. F. D., Stripp, G., & Morse, S. A. (2007). A textural record of solidification and cooling in the skaergaard intrusion, East Greenland. *Journal of Petrology*, *48*(12), 2359–2377. https://doi.org/10.1093/petrology/egm064
Holness, M. B., Nielsen, T. F. D., & Tegner, C. (2007). Textural maturity of cumulates: A record of chamber filling, liquidus assemblage, cooling rate and large-scale convection in mafic layered intrusions. *Journal of Petrology*, *48*(1), 141–157. https://doi.org/10.1093/petrology/egl057
Holness, M. B., Stripp, G., Humphreys, M. C. S., Veksler, I. V., Nielsen, T. F. D., & Tegner, C. (2011). Silicate liquid immiscibility within the crystal mush: late-stage magmatic microstructures in the skaergaard intrusion, east greenland. *Journal of Petrology*, *52*(1), 175–222. https://doi.org/10.1093/petrology/egq077
Holness, M. B., Sides, R., Prior, D. J., Cheadle, M. J., & Upton, B. G. J. (2012). The peridotite plugs of Rum: Crystal settling and fabric development in magma conduits. *Lithos*, *134–135*, 23–40. https://doi.org/10.1016/j.lithos.2011.11.024
Holness, M. B., Vukmanovic, Z., & Mariani, E. (2017). Assessing the role of compaction in the formation of adcumulates: A microstructural perspective. *Journal of Petrology*, *58*(4), 643–674. https://doi.org/10.1093/petrology/egx037
Holness, M. B., Nielsen, T. F. D., & Tegner, C. (2017). The skaergaard intrusion of east Greenland: Paradigms, problems and new perspectives. *Elements*, *13*(6), 391–396. https://doi.org/10.2138/gselements.13.6.391
Horsman, E., Tikoff, B., & Morgan, S. (2005). Emplacement-related fabric and multiple sheets in the Maiden Creek sill, Henry Mountains, Utah, USA. *Journal of Structural Geology*, *27*(8), 1426–1444. https://doi.org/10.1016/j.jsg.2005.03.003
Horvath, D. G., Moitra, P., Hamilton, C. W., Craddock, R. A., & Andrews-Hanna, J. C. (2021). Evidence for geologically recent explosive volcanism in Elysium Planitia, Mars. *Icarus*, *365*(August 2020), 114499. https://doi.org/10.1016/j.icarus.2021.114499
Hunter, R. H. (1996). Texture Development in Cumulate Rocks. *Developments in Petrology*, *15*(C), 77–101.

https://doi.org/10.1016/S0167-2894(96)80005-4
Iezzi, G., & Ventura, G. (2002). Crystal fabric evolution in lava flows: Results from numerical simulations. *Earth and Planetary Science Letters*, *200*(1–2), 33–46. https://doi.org/10.1016/S0012-821X(02)00617-9
Ikeda, Y. (1994). Petrography and petrology of the ALH-77005 shergottite. *Proceedings of the NIPR Symposium on Antarctic Meteorites*, *7*, 9–29. Retrieved from https://adsabs.harvard.edu/pdf/1994AMR.....7....9I
Ildefonse, B., Sokoutis, D., & Mancktelow, N. S. (1992). Mechanical interactions between rigid particles in a deforming ductile matrix. Analogue experiments in simple shear flow. *Journal of Structural Geology*, *14*(10), 1253–1266. https://doi.org/10.1016/0191-8141(92)90074-7
Imae, N., & Ikeda, Y. (2007). Petrology of the Miller Range 03346 nakhlite in comparison with the Yamato-000593 nakhlite. *Meteoritics & Planetary Science*, *42*(2), 171–184. https://doi.org/10.1111/j.1945-5100.2007.tb00225.x
Imae, N., Ikeda, Y., Shinoda, K., Kojima, H., & Iwata, N. (2003). Yamato nakhlites: Petrography and mineralogy. *Antarctic Meteorite Research*, *16*, 13–33. Retrieved from https://adsabs.harvard.edu/pdf/2003AMR....16...13I
Imae, N., Ikeda, Y., & Kojima, H. (2005). Petrology of the Yamato nakhlites. *Meteoritics and Planetary Science*, *40*(11), 1581–1598. https://doi.org/10.1111/j.1945-5100.2005.tb00133.x
Ingrin, J., Doukhan, N., & Doukhan, J. C. (1991). High-Temperature Deformation of Diopside Single-Crystal .2. Transmission Electron-Microscopy Investigation Of The Defect Microstructures. *Journal Of Geophysical Research-Solid Earth And Planets*, *96*(B9), 14287–14297. https://doi.org/10.1029/91JB01233
Irvine, T. N. (1982). Terminology for layered intrusions. *Journal of Petrology*, *23*(2), 127–162. https://doi.org/10.1093/petrology/23.2.127-a
Irving, A. J., Kuehner, S. M., Rumble III, D., Carlson, R. W., Hupe, A. C., & Hupe, G. M. (2002). Petrology and isotopic composition of orthopyroxene-bearing nakhlite NWA 998. In *The Meteoritical Society* (p. A70).
Isherwood, R. J., Jozwiak, L. M., Jansen, J. C., & Andrews-Hanna, J. C. (2013). The volcanic history of Olympus Mons from paleo-topography and flexural modeling. *Earth and Planetary Science Letters*, *363*, 88–96. https://doi.org/10.1016/j.epsl.2012.12.020
Ismaïl, W. Ben, & Mainprice, D. (1998). An olivine fabric database: An overview of upper mantle fabrics and seismic anisotropy. *Tectonophysics*, *296*(1–2), 145–157. https://doi.org/10.1016/S0040-1951(98)00141-3
Jackson, R. S., Wiens, R. C., Vaniman, D. T., Beegle, L. W., Gasnault, O., Newsom, H. E., et al. (2016). ChemCam investigation of the John Klein and Cumberland drill holes and tailings, Gale crater, Mars. *Icarus*, *277*, 330–341. https://doi.org/10.1016/j.icarus.2016.04.026
Jambon, A., Sautter, V., Barrat, J.-A., Gattacceca, J., Rochette, P., Boudouma, O., et al. (2016). Northwest Africa 5790: Revisiting nakhlite petrogenesis. *Geochimica et Cosmochimica Acta*, *190*(January), 191–212. https://doi.org/10.1016/j.gca.2016.06.032
Jankovics, M. É., Harangi, S., Kiss, B., & Ntaflos, T. (2012). Open-system evolution of the Füzes-tó alkaline basaltic magma, western Pannonian Basin: Constraints from mineral textures and compositions. *Lithos*, *140–141*, 25–37. https://doi.org/10.1016/j.lithos.2012.01.020
Jaoul, O., & Raterron, P. (1994). High-temperature deformation of diopside crystal 3. Influences of pO2 and SiO2 precipitation. *Journal of Geophysical Research*, *99*(B5), 9423–9439. https://doi.org/10.1029/93JB03363
Jenniskens, P., Gabadirwe, M., Yin, Q., Proyer, A., Moses, O., Kohout, T., et al. (2021). The impact and recovery of asteroid 2018 LA. *Meteoritics & Planetary Science*, *50*, 1–50. https://doi.org/10.1111/maps.13653
Jerram, D. A. (2003). Quantifying the Building Blocks of Igneous Rocks: Are Clustered Crystal Frameworks the Foundation? *Journal of Petrology*, *44*(11), 2033–2051. https://doi.org/10.1093/petrology/egg069
Jerram, D. A., Cheadle, M. J., Hunter, R. H., & Elliott, M. T. (1996). The spatial distribution of grains and crystals in rocks. *Contributions to Mineralogy and Petrology*, *125*(1), 60–74. https://doi.org/10.1007/s004100050206
Jerram, D. A., Dobson, K. J., Morgan, D. J., & Pankhurst, M. J. (2018). The petrogenesis of magmatic systems: Using igneous textures to understand magmatic processes. In S. Burchardt (Ed.), *Volcanic and Igneous Plumbing Systems: Understanding Magma Transport, Storage, and Evolution in the Earth's Crust* (pp. 191–229). Amsterdam, Netherlands: Elsevier. https://doi.org/10.1016/B978-0-12-809749-6.00008-X
Jung, H., Katayama, I., Jiang, Z., Hiraga, T., & Karato, S.-I. (2006). Effect of water and stress on the lattice-preferred orientation of olivine. *Tectonophysics*, *421*(1–2), 1–22. https://doi.org/10.1016/j.tecto.2006.02.011
Jung, Haemyeong, Mo, W., & Green, H. W. (2009). Upper mantle seismic anisotropy resulting from pressure-induced slip transition in olivine. *Nature Geoscience*, *2*(1), 73–77. https://doi.org/10.1038/ngeo389

Kaboli, S., Burnley, P. C., Xia, G., & Green, H. W. (2017). Pressure Dependence of Creep in Forsterite Olivine: Comparison of Measurements From the D-DIA and Griggs Apparatus. *Geophysical Research Letters*, *44*(21), 10,939-10,947. https://doi.org/10.1002/2017GL075177

Kalidindi, S. R., Knezevic, M., Niezgoda, S., & Shaffer, J. (2009). Representation of the orientation distribution function and computation of first-order elastic properties closures using discrete Fourier transforms. *Acta Materialia*, *57*(13), 3916–3923. https://doi.org/10.1016/j.actamat.2009.04.055

Karato, S., Jung, H., Katayama, I., & Skemer, P. (2008). Geodynamic Significance of Seismic Anisotropy of the Upper Mantle: New Insights from Laboratory Studies. *Annual Review of Earth and Planetary Sciences*, *36*(1), 59–95. https://doi.org/10.1146/annurev.earth.36.031207.124120

Katayama, I., & Karato, S. ichiro. (2006). Effect of temperature on the B- to C-type olivine fabric transition and implication for flow pattern in subduction zones. *Physics of the Earth and Planetary Interiors*, *157*(1–2), 33–45. https://doi.org/10.1016/j.pepi.2006.03.005

Katayama, I., Jung, H., & Karato, S. I. (2004). New type of olivine fabric from deformation experiments at modest water content and low stress. *Geology*, *32*(12), 1045–1048. https://doi.org/10.1130/G20805.1

Katayama, I., Karato, S. I., & Brandon, M. (2005). Evidence of high water content in the deep upper mantle inferred from deformation microstructures. *Geology*, *33*(7), 613–616. https://doi.org/10.1130/G21332.1

Kelly, A., & Knowles, K. M. (2020). *Crystallography and Crystal Defects*. (A. Kelly, Ed.) (Third). Wiley.

Kenny, G. G., Karlsson, A., Schmieder, M., Whitehouse, M. J., Nemchin, A. A., & Bellucci, J. J. (2020). Recrystallization and chemical changes in apatite in response to hypervelocity impact. *Geology*, *48*(1), 19–23. https://doi.org/10.1130/G46575.1

Keppler, R. (2018). Crystallographic preferred orientations in eclogites – A review. *Journal of Structural Geology*, *115*(April), 284–296. https://doi.org/10.1016/j.jsg.2018.04.003

Kereszturi, A., & Chatzitheodoridis, E. (2016). Searching for the Source Crater of Nakhlite Meteorites. *Origins of Life and Evolution of Biospheres*, *46*(4), 455–471. https://doi.org/10.1007/s11084-016-9498-x

Kizovski, T. V., Izawa, M. R. M., Tait, K. T., Moser, D. E., Day, J. M. D., Hyde, B. C., et al. (2020). Petrogenesis, alteration, and shock history of intermediate shergottite Northwest Africa 7042: Evidence for hydrous magmatism on Mars? *Geochimica et Cosmochimica Acta*, *283*, 103–123. https://doi.org/10.1016/j.gca.2020.05.030

Kollé, J. J., & Blacic, J. D. (1982). Deformation of single-crystal clinopyroxenes: 1. Mechanical twinning in diopside and hedenbergite. *Journal of Geophysical Research*, *87*(B5), 4019–4034.

Kollé, J. J., & Blacic, J. D. (1983). Deformation of single-crystal clinopyroxenes: 2. Dislocation- controlled flow processes in hedenbergite. *Journal of Geophysical Research*, *88*(B3), 2381–2393. https://doi.org/10.1029/JB088iB03p02381

Komar, P. D. (1972). Interactions of Phenocrysts and Flow Differentiation of Igneous Dikes and Sills. *Geological Society of America Bulletin*, *83*, 973–988. https://doi.org/10.1130/0016-7606(1972)83[973:MIOPAF]2.0.CO;2

Korochantseva, E. V., Schwenzer, S. P., Buikin, A. I., Hopp, J., Ott, U., & Trieloff, M. (2011). 40Ar-39Ar and cosmic-ray exposure ages of nakhlites-Nakhla, Lafayette, Governador Valadares-and Chassigny. *Meteoritics and Planetary Science*, *46*(9), 1397–1417. https://doi.org/10.1111/j.1945-5100.2011.01240.x

Kouchi, A., Tsuchiyama, A., & Sunagawa, I. (1986). Effect of stirring on crystallization kinetics of basalt: texture and element partitioning. *Contributions to Mineralogy and Petrology*, *93*(4), 429–438. https://doi.org/10.1007/BF00371713

Krämer Ruggiu, L., Gattacceca, J., Bevouard, B., Udry, A., Debaille, V., Rochette, P., et al. (2020). Caleta el Cobre 022 martian meteorite: increasing nakhlite diversity. *Meteoritics and Planetary Science*, *25*, 1–25. https://doi.org/10.1111/maps.13534

Kuebler, K. E. (2013). A comparison of the iddingsite alteration products in two terrestrial basalts and the Allan Hills 77005 martian meteorite using Raman spectroscopy and electron microprobe analyses. *Journal of Geophysical Research: Planets*, *118*(4), 803–830. https://doi.org/10.1029/2012JE004243

Kurokawa, H., Sato, M., Ushioda, M., Matsuyama, T., Moriwaki, R., Dohm, J. M., & Usui, T. (2014). Evolution of water reservoirs on Mars: Constraints from hydrogen isotopes in martian meteorites. *Earth and Planetary Science Letters*, *394*, 179–185. https://doi.org/10.1016/j.epsl.2014.03.027

Lapen, Thomas J., Righter, M., Andreasen, R., Irving, A. J., Satkoski, A. M., Beard, B. L., et al. (2017). Two billion years of magmatism recorded from a single Mars meteorite ejection site. *Science Advances*, *3*(2), 1–7. https://doi.org/10.1126/sciadv.1600922

Lapen, Thomas John, Righter, M., Brandon, A. D., Debaille, V., Beard, B. L., Shafer, J. T., & Peslier, A. H. (2010). A younger age for ALH 84001 and its geochemical link to shergottite sources in Mars. *Science*, *328*(April), 347–352. https://doi.org/10.1126/science.1185395

Law, R. D. (1990). Crystallographic fabrics: a selective review of their applications to research in structural geology. *Deformation Mechanisms, Rheology and Tectonics. Geological Society Special Publication*, *54*(54), 352–355. https://doi.org/10.1144/GSL.SP.1990.054.01.30

Lee, M. R., Tomkinson, T., Mark, D. F., Stuart, F. M., & Smith, C. L. (2013). Evidence for silicate dissolution on Mars from the Nakhla meteorite. *Meteoritics and Planetary Science*, *48*(2), 224–240.

https://doi.org/10.1111/maps.12053
Lee, M. R., Tomkinson, T., Hallis, L. J., & Mark, D. F. (2015). Formation of iddingsite veins in the martian crust by centripetal replacement of olivine: Evidence from the nakhlite meteorite Lafayette. *Geochimica et Cosmochimica Acta*, *154*, 49–65. https://doi.org/10.1016/j.gca.2015.01.022
Lee, M. R., Maclaren, I., Andersson, S. M. L., Kovács, A., Tomkinson, T., Mark, D. F., & Smith, C. L. (2015). Opal-A in the Nakhla meteorite: A tracer of ephemeral liquid water in the Amazonian crust of Mars. *Meteoritics and Planetary Science*, *50*(8), 1362–1377. https://doi.org/10.1111/maps.12471
Lee, M. R., Daly, L., Cohen, B. E., Hallis, L. J., Griffin, S., Boyce, A. J., & Mark, D. F. (2018). Aqueous alteration of the Martian meteorite Northwest Africa 817 : Probing fluid – rock interaction at the nakhlite launch site. *Meteoritics & Planetary Science*, *53*(11), 2395–2412. https://doi.org/10.1111/maps.13136
Leroux, H. (2001). Microstructural shock signatures of major minerals in meteorites. *European Journal of Mineralogy*, *13*(2), 253–272. https://doi.org/10.1127/0935-1221/01/0013-0253
Leu, A. R. (2010). Clinopyroxene growth rate in mafic melts. *2010 GSA Denver Annual Meeting*, *5*, 100.
Li, Z. Y., Wen, D. P., Wang, Y. F., & Liu, X. (2020). An Investigation of Dislocation in Olivine Phenocrysts from the Hawaiian Basalts. *Journal of Earth Science*, *31*(6), 1183–1189. https://doi.org/10.1007/s12583-020-1338-2
Liu, S., Tommasi, A., Vauchez, A., & Mazzucchelli, M. (2019). Deformation, Annealing, Melt-Rock Interaction, and Seismic Properties of an Old Domain of the Equatorial Atlantic Lithospheric Mantle. *Tectonics*, *38*(4), 1164–1188. https://doi.org/10.1029/2018TC005373
Liu, Y., Fischer, W. W., Ma, C., Beckett, J. R., Tschauner, O., Guan, Y., et al. (2021). Manganese oxides in Martian meteorites Northwest Africa (NWA) 7034 and 7533. *Icarus*, *364*(February), 114471. https://doi.org/10.1016/j.icarus.2021.114471
Lodders, K. (1998). A survey of shergottite, nakhlite and chassigny meteorites whole-rock compositions. *Meteoritics & Planetary Science*, *33*, A183–A190.
Lofgren, G. E. (1983). Effect of heterogeneous nucleation on basaltic textures: a dynamic crystallization study. *Journal of Petrology*, *24*(3), 229–255. https://doi.org/10.1093/petrology/24.3.229
Longhi, J. (1991). Complex Magmatic Processes on Mars: Inferences from the SNC Meteorites. In *Lunar and Planetary Science XXI* (Vol. 21, pp. A91-42332 17–19). Houston, TX: Lunar and Planetary Institute. Retrieved from http://adsabs.harvard.edu/full/1991LPSC...21..695L
M, M. K. B., & Annavarapu, R. N. (2020). Assessment of Efficiency , Impact Factor , Impact of Probe Mass , Probe Life Expectancy , and Reliability of Mars Missions. In *AIAA Propulsion and Energy 2020 Forum* (pp. 1–14).
Ma, C., & Rossman, G. R. (2009). Tistarite, ti203, a new refractory mineral from the allende meteorite. *American Mineralogist*, *94*(5–6), 841–844. https://doi.org/10.2138/am.2009.3203
Ma, C., Simon, S. B., Rossman, G. R., & Grossman, L. (2009). Calcium Tschermak's pyroxene, CaAlAlSiO6, from the Allende and Murray meteorites: EBSD and micro-Raman characterizations. *American Mineralogist*, *94*(10), 1483–1486. https://doi.org/10.2138/am.2009.3231
Ma, C., Tschauner, O., Beckett, J. R., Rossman, G. R., & Liu, W. (2012). Allende meteorite : Synchrotron micro-diffraction and EBSD. *American Mineralogist*, *97*, 1219–1225.
Ma, C., Tschauner, O., Beckett, J. R., Liu, Y., Rossman, G. R., Zhuravlev, K., et al. (2015). Tissintite, (Ca,Na, ⊕)AlSi2O6, a highly-defective, shock-induced, high-pressure clinopyroxene in the Tissint martian meteorite. *Earth and Planetary Science Letters*, *422*, 194–205. https://doi.org/10.1016/j.epsl.2015.03.057
Ma, C., Tschauner, O., Beckett, J. R., Liu, Y., Rossman, G. R., Sinogeikin, S. V., et al. (2016). Ahrensite, γ-Fe2SiO4, a new shock-metamorphic mineral from the Tissint meteorite: Implications for the Tissint shock event on Mars. *Geochimica et Cosmochimica Acta*, *184*, 240–256. https://doi.org/10.1016/j.gca.2016.04.042
Ma, C., Lin, C., Bindi, L., & Steinhardt, P. J. (2017). Hollisterite (Al3Fe), kryachkoite (Al,Cu)6(Fe,Cu), and stolperite (AlCu): Three new minerals from the Khatyrka CV3 carbonaceous chondrite. *American Mineralogist*, *102*(3), 690–693. https://doi.org/10.2138/am-2017-5991
Ma, C., Tschauner, O., Beckett, J. R., Rossman, G. R., Prescher, C., Prakapenka, V. B., et al. (2018). Liebermannite, KAlSi3O8, a new shock-metamorphic, high-pressure mineral from the Zagami Martian meteorite. *Meteoritics and Planetary Science*, *53*(1), 50–61. https://doi.org/10.1111/maps.13000
Ma, C., Tschauner, O., Beckett, J. R., Liu, Y., Greenberg, E., & Prakapenka, V. B. (2019). Chenmingite, FeCr2 O4 in the CaFe2 O4-type structure, a shock-induced, high-pressure mineral in the Tissint martian meteorite. *American Mineralogist*, *104*(October), 1521–1525.
Magrassi, F., Rocco, E., Barberis, S., Gallo, M., & Del Borghi, A. (2019). Hybrid solar power system versus photovoltaic plant: A comparative analysis through a life cycle approach. *Renewable Energy*, *130*, 290–304. https://doi.org/10.1016/j.renene.2018.06.072
Mainprice, D., Tommasi, A., Couvy, H., Cordier, P., & Frost, D. J. (2005). Pressure sensitivity of olivine slip systems and seismic anisotropy of Earth's upper mantle. *Nature*, *433*(7027), 731–733. https://doi.org/10.1038/nature03266
Mainprice, D., Bachmann, F., Hielscher, R., Schaeben, H., & Lloyd, G. E. (2015). Calculating anisotropic

piezoelectric properties from texture data using the MTEX open source package. In D. R. Faulkner, E. Mariani, & J. Mecklenburgh (Eds.), *Rock deformation from field, experiments and theory: A volume in honour of Ernie Rutter* (Vol. 409, pp. 223–249).

Mainprice, D., Bachmann, F., Hielscher, R., & Schaeben, H. (2015). Descriptive tools for the analysis of texture projects with large datasets using MTEX: Strength, symmetry and components. *Geological Society Special Publication*, *409*(1), 251–271. https://doi.org/10.1144/SP409.8

Malaya Kumar Biswal, M., & Annavarapu, R. N. (2020). Mars missions failure report assortment review and conspectus. In *AIAA Propulsion and Energy 2020 Forum* (pp. 1–15). https://doi.org/10.2514/6.2020-3541

Malaya Kumar Biswal, M., & Annavarapu, R. N. (2021). A study on mars probe failures. *AIAA Scitech 2021 Forum*, (January), 1–18. https://doi.org/10.2514/6.2021-1158

Mangold, N., Roach, L., Milliken, R., Le Mouélic, S., Ansan, V., Bibring, J.-P., et al. (2010). A Late Amazonian alteration layer related to local volcanism on Mars. *Icarus*, *207*(1), 265–276. https://doi.org/10.1016/j.icarus.2009.10.015

Marsh, B. D. (1988). Crystal size distribution (CSD) in rocks and the kinetics and dynamics of crystallization - I. Theory. *Contributions to Mineralogy and Petrology*, *99*(3), 277–291. https://doi.org/10.1007/BF00375362

Marsh, B. D. (1996). Solidification fronts and magmatic evolution. *Mineralogical Magazine*, *60*(398), 5–40. https://doi.org/10.1180/minmag.1996.060.398.03

Marsh, B. D. (1998). Crystal capture, sorting, and retention in convecting magma. *Special Paper of the Geological Society of America*, *253*(November), 399–416. https://doi.org/10.1130/SPE253-p399

Marsh, B. D. (2013). On some fundamentals of igneous petrology. *Contributions to Mineralogy and Petrology*, *166*(3), 665–690. https://doi.org/10.1007/s00410-013-0892-3

Mason, J. K., & Schuh, C. A. (2009). Representations of texture. In A. J. Schwartz, M. Kumar, B. L. Adams, & D. P. Field (Eds.), *Electron Backscatter Diffraction in Materials Science* (Second, pp. 1–403). https://doi.org/10.1007/978-0-387-88136-2

Mauler, A., Bystricky, M., Kunze, K., & Mackwell, S. (2000). Microstructures and lattice preferred orientations in experimentally deformed clinopyroxene aggregates. *Journal of Structural Geology*, *22*, 1633–1648. https://doi.org/10.1016/S0191-8141(00)00073-0

McBirney, A. R. (1993). *Igneous Petrology* (2nd ed.). Jones and Barltett Publishers.

McCubbin, F. M., Smirnov, A., Nekvasil, H., Wang, J., Hauri, E., & Lindsley, D. H. (2010). Hydrous magmatism on Mars: A source of water for the surface and subsurface during the Amazonian. *Earth and Planetary Science Letters*, *292*(1–2), 132–138. https://doi.org/10.1016/j.epsl.2010.01.028

McCubbin, F. M., Boyce, J. W., Novák-Szabó, T., Santos, A. R., Tartèse, R., Muttik, N., et al. (2015). Geologic history of Martian regolith breccia Northwest Africa 7034: Evidence for hydrothermal activity and lithologic diversity in the Martian crust. *Journal of Geophysical Research: Planets*, *121*, 495–514. https://doi.org/10.1002/2014JE004737.Received

McEwen, A. S., Preblich, B. S., Turtle, E. P., Artemieva, N. A., Golombek, M. P., Hurst, M., et al. (2005). The rayed crater Zunil and interpretations of small impact craters on Mars. *Icarus*, *176*(2), 351–381. https://doi.org/10.1016/j.icarus.2005.02.009

McKenzie, D., Barnett, D. N., & Yuan, D. N. (2002). The relationship between Martian gravity and topography. *Earth and Planetary Science Letters*, *195*(1–2), 1–16. https://doi.org/10.1016/S0012-821X(01)00555-6

McSween, H. Y. (1994). What We Have Learned About Mars from SNC Meteorites. *Meteoritics*, *29*(6), 757–779. https://doi.org/10.1111/j.1945-5100.1994.tb01092.x

McSween, H. Y. (2002). The rocks of Mars, from far and near. *Meteoritics & Planetary Science*, *37*, 7–25.

McSween, H. Y., & Treiman, A. H. (1998). Martian Meteroties. In J. J. Papike (Ed.), *Planetary Materials. Reviews in mineralogy* (Vol. 36, pp. 1–53). Washington, DC: Mineralogical Society America.

McSween, H. Y., Grove, T. L., Friedman Lentz, R. C., Dann, J. C., Holzheid, A. H., Riciputi, L. R., & Ryan, J. G. (2001). Geochemical evidence for magmatic water within mars from pyroxenes in the shergotty meteorite. *Nature*, *409*(6819), 487–490. https://doi.org/10.1038/35054011

Mei, S., & Kohlstedt, D. L. (2000). Influence of water on plastic deformation of olivine aggregates 2. Dislocation creep regime. *Journal of Geophysical Research: Solid Earth*, *105*(B9), 21471–21481. https://doi.org/10.1029/2000jb900180

Melosh, H. J. (1984). Impact ejection, spallation, and the origin of meteorites. *Icarus*, *59*(2), 234–260. https://doi.org/10.1016/0019-1035(84)90026-5

Merkle, R. K. W., & Wallmach, T. (1997). Ultramafic rocks in the centre of the Vredefort structure (South Africa): Geochemical affinity to Bushveld rocks. *Chemical Geology*, *143*(1–2), 43–64. https://doi.org/10.1016/S0009-2541(97)00099-5

Merle, O. (1998). Internal strain within lava flows from analogue modelling. *Journal of Volcanology and Geothermal Research*, *81*(3–4), 189–206. https://doi.org/10.1016/S0377-0273(98)00009-2

Mikouchi, T., & Kurihara, T. (2008). Mineralogy and petrology of paired lherzolitic shergottites Yamato 000027, Yamato 000047, and Yamato 000097: Another fragment from a Martian “lherzolite” block. *Polar Science*, *2*(3), 175–194. https://doi.org/10.1016/j.polar.2008.06.003

Mikouchi, T., Righter, M., Ziegler, K., & Irving, A. J. (2016). Petrology, Mineralogy and oxygen isotopic composition of the Northwest Africa 10153 nakhlite: A sample from a different flow from other nakhlites? In *79th Annual Meeting of the Meteoritical Society* (p. A6396). https://doi.org/10.1111/maps.12934

Misawa, K., Kojima, H., Imae, N., & Nakamura, N. (2003). The Yamato nahklite consortium. *Antarctic Meteorite Research*, *16*, 1–12.

Mohammed, A., & Abdullah, A. (2018). Scanning Electron Microscopy (SEM): A Review. *International Conference on Hydraulics and Pneumatics*, *7*(January), 1–9. Retrieved from https://www.researchgate.net/publication/330168803

Van de Moortèle, B., Reynard, B., Rochette, P., Jackson, M., Beck, P., Gillet, P., et al. (2007). Shock-induced metallic iron nanoparticles in olivine-rich Martian meteorites. *Earth and Planetary Science Letters*, *262*(1–2), 37–49. https://doi.org/10.1016/j.epsl.2007.07.002

Morgan, D. J., & Jerram, D. A. (2006). On estimating crystal shape for crystal size distribution analysis. *Journal of Volcanology and Geothermal Research*, *154*(1–2), 1–7. https://doi.org/10.1016/j.jvolgeores.2005.09.016

Morgan, J. W., & Anders, E. (1979). Chemical composition of Mars. *Geochimica et Cosmochimica Acta*, *43*(10), 1601–1610. https://doi.org/10.1016/0016-7037(79)90180-7

Morimoto, N., Fabries, J., Ferguson, A. K., Ginzburg, I. V., Ross, M., Seifert, F. A., et al. (1988). Petrology Nomenclature of Pyroxenes. *Reviews in Mineralogy*, *39*, 55–76. Retrieved from https://doi.org/10.1007/BF01226262

Moser, D. E., Cupelli, C. L., Barker, I. R., Flowers, R. M., Bowman, J. R., Wooden, J., & Hart, J. R. (2011). New zircon shock phenomena and their use for dating and reconstruction of large impact structures revealed by electron nanobeam (EBSD, CL, EDS) and isotopic U-Pb and (U-Th)/he analysis of the vredefort dome. *Canadian Journal of Earth Sciences*, *48*(2), 117–139. https://doi.org/10.1139/E11-011

Moser, D. E., Chamberlain, K. R., Tait, K. T., Schmitt, A. K., Darling, J. R., Barker, I. R., & Hyde, B. C. (2013). Solving the Martian meteorite age conundrum using micro-baddeleyite and launch-generated zircon. *Nature*, *499*(7459), 454–457. https://doi.org/10.1038/nature12341

Müller, W. F., Walte, N., & Miyajima, N. (2008). Experimental deformation of ordered natural omphacite: a study by transmission electron microscopy. *European Journal of Mineralogy*, *20*, 835–844. https://doi.org/10.1127/0935-1221/2008/0020-1851

Muto, J., Hirth, G., Heilbronner, R., & Tullis, J. (2011). Plastic anisotropy and fabric evolution in sheared and recrystallized quartz single crystals. *Journal of Geophysical Research: Solid Earth*, *116*(2), 1–18. https://doi.org/10.1029/2010JB007891

Nagaya, T., Wallis, S. R., Kobayashi, H., Michibayashi, K., Mizukami, T., Seto, Y., et al. (2014). Dehydration breakdown of antigorite and the formation of B-type olivine CPO. *Earth and Planetary Science Letters*, *387*, 67–76. https://doi.org/10.1016/j.epsl.2013.11.025

Nazari-Sharabian, M., Aghababaei, M., Karakouzian, M., & Karami, M. (2020). Water on Mars-A Literature Review. *Galaxies*, *8*(40), 1–45. https://doi.org/10.3390/galaxies8020040

Németh, K., White, J. D. L., Reay, A., & Martin, U. (2003). Compositional variation during monogenetic volcano growth and its implications for magma supply to continental volcanic fields. *Journal of the Geological Society*, *160*(4), 523–530. https://doi.org/10.1144/0016-764902-131

Nichols, C. I. O., Krakow, R., Herrero-Albillos, J., Kronast, F., Northwood-Smith, G., & Harrison, R. J. (2018). Microstructural and paleomagnetic insight into the cooling history of the IAB parent body. *Geochimica et Cosmochimica Acta*, *229*, 1–19. https://doi.org/10.1016/j.gca.2018.03.009

Nicolas, A. (1992). Kinematics in magmatic rocks with special reference to gabbros. *Journal of Petrology*, *33*(4), 891–915. https://doi.org/10.1093/petrology/33.4.891

Niu, R., & Pang, M. (2020). Numerical study on the effect of gravity levels on apparent viscosity of bubbly suspensions. *Microgravity Science and Technology*, *32*(4), 555–577. https://doi.org/10.1007/s12217-020-09792-1

Noguchi, T., Nakamura, T., Misawa, K., Imae, N., Aoki, T., & Toh, S. (2009). Laihunite and jarosite in the Yamato 00 nakhlites: Alteration products on Mars? *Journal of Geophysical Research: Planets*, *114*(10), 1–13. https://doi.org/10.1029/2009JE003364

Nolze, G., Geist, V., Saliwan Neumann, R., & Buchheim, M. (2005). Investigation of orientation relationships by EBSD and EDS on the example of the Watson iron meteorite. *Crystal Research and Technology*, *40*(8), 791–804. https://doi.org/10.1002/crat.200410434

Nolze, Gert, Geist, V., Saliwan Neumann, R., & Buchheim, M. (2005). Investigation of orientation relationships by EBSD and EDS on the example of the Watson iron meteorite. *Crystal Research and Technology*, *40*(8), 791–804. https://doi.org/10.1002/crat.200410434

Nyquist, L. E., Bogard, D. D., Shih, C. Y., Greshake, A., Stöffler, D., & Eugster, O. (2001). Ages and geologic histories of Martian meteorites. In R. Kallenbach, J. Geiss, & W. K. Hartmann (Eds.), *Chronology and Evolution of Mars. Space Sciences Series of ISSI* (Vol. 12, pp. 105–164). Dordrecht: Springer. https://doi.org/https://doi.org/10.1007/978-94-017-1035-0_5

Ohuchi, T., Kawazoe, T., Nishihara, Y., Nishiyama, N., & Irifune, T. (2011). High pressure and temperature fabric transitions in olivine and variations in upper mantle seismic anisotropy. *Earth and Planetary*

Science Letters, *304*(1–2), 55–63. https://doi.org/10.1016/j.epsl.2011.01.015

Okazaki, R., Keisuke, N., Imae, N., & Kojima, H. (2003). Noble gas signatures of Antarctic nakhlites, Yamato (Y) 000593, Y000749, and Y000802. *Antarctic Meteorite Research*, *16*, 58–79. Retrieved from http://adsabs.harvard.edu/full/2003AMR....16...58O

Papike, J. J., Burger, P. V., Bell, A. S., Shearer, C. K., Le, L., Jones, J., & Provencio, P. (2014). Valence state partitioning of V between pyroxene and melt for martian melt compositions Y 980459 and QUE 94201: The effect of pyroxene composition and crystal structure. *American Mineralogist*, *99*(5–6), 1175–1178. https://doi.org/10.2138/am.2014.4788

Park, J., Garrison, D. H., & Bogard, D. D. (2009). 39Ar-40Ar ages of martian nakhlites. *Geochimica et Cosmochimica Acta*, *73*(7), 2177–2189. https://doi.org/10.1016/j.gca.2008.12.027

Park, J., Nyquist, L. E., Herzog, G. F., Turrin, B. D., Linsay, F. N., Delaney, J. S., & Swisher III, C. C. (2016). 40Ar/39Ar ages of nakhlites Miller Range (MIL) 090030, 090032 and 090136. In *Lunar and Planetary Science Conference XCVII* (pp. 1821–1822). https://doi.org/10.1029/2009GC003013

Paterson, S. R., Fowler, T. K., Schmidt, K. L., Yoshinobu, A. S., Yuan, E. S., & Miller, R. B. (1998). Interpreting magmatic fabric patterns in plutons. *Lithos*, *44*(1–2), 53–82. https://doi.org/10.1016/S0024-4937(98)00022-X

Perugini, D., Busà, T., Poli, G., & Nazzareni, S. (2003). The role of chaotic dynamics and flow fields in the development of disequilibrium textures in volcanic rocks. *Journal of Petrology*, *44*(4), 733–756. https://doi.org/10.1093/petrology/44.4.733

Peslier, A. H., Hervig, R., Yang, S., Humayun, M., Barnes, J. J., Irving, A. J., & Brandon, A. D. (2019). Determination of the water content and D/H ratio of the martian mantle by unraveling degassing and crystallization effects in nakhlites. *Geochimica et Cosmochimica Acta*, *266*, 382–415. https://doi.org/10.1016/j.gca.2019.04.023

Philippot, P., & van Roermund, H. L. M. (1992). Deformation processes in eclogitic rocks: evidence for the rheological delamination of the oceanic crust in deeper levels of subduction zones. *Journal of Structural Geology*, *14*(8/9), 1059–1077. https://doi.org/10.1016/0191-8141(92)90036-V

Piazolo, S., Bons, P. D., & Passchier, C. W. (2002). The influence of matrix rheology and vorticity on fabric development of populations of rigid objects during plane strain deformation. *Tectonophysics*, *351*(4), 315–329. https://doi.org/10.1016/S0040-1951(02)00220-2

Poirier, J.-P. (1975). On the Slip Systems of Olivine. *Journal of Geophysical Research*, *80*(29), 4059–4061.

Poirier, J.-P. (1982). On transformation plasticity. *Journal of Geophysical Research*, *87*(B8), 6791–6797.

Poirier, J.-P. (1985). *Creep of crystals: High-temperature deformation processes in Metals, ceramics and minerals*. Cambridge University Press.

Poirier, J.-P. (1995). Mineral physics and. In T. J. Ahrens (Ed.), *Mineral physics and crystallography: a handbook of physical constants* (pp. 245–252). American Geophysical Union. https://doi.org/10.4324/9780203121146-35

Poirier, J.-P., & Nicolas, A. (1975). Deformation-Induced Recrystallization Due to Progressive Misorientation of Subgrains, with Special Reference to Mantle Peridotites. *The Journal of Geology*, *83*(6), 707–720. https://doi.org/10.1086/628163

Prasannakumar, V., & Lloyd, G. E. (2010). Application of SEM-EBSD to regional scale shear zone analysis: A case study of the bhavani shear Zone, South India. *Journal of the Geological Society of India*, *75*(1), 183–201. https://doi.org/10.1007/s12594-010-0007-y

Précigout, J., & Hirth, G. (2014). B-type olivine fabric induced by grain boundary sliding. *Earth and Planetary Science Letters*, *395*, 231–240. https://doi.org/10.1016/j.epsl.2014.03.052

Prior, D. J., Boyle, A. P., Brenker, F. E., Cheadle, M. C., Day, A. P., Lopez, G. G., et al. (1999). The application of electron backscatter diffraction and orientation constrast imaging in the SEM to textural problems in rocks. *American Mineralogist*, *84*(11–12), 1741–1759. https://doi.org/10.2138/am-1999-11-1204

Prior, D. J., Mariani, E., & Wheeler, J. (2009). EBSD in the Earth Sciences: Applications, common practice and challenges. In A. J. Schwartz, M. Kumar, B. L. Adams, & D. P. Field (Eds.), *Electron Backscatter Diffraction in Materials Science* (second, pp. 1–403). Boston, MA.: Springer. https://doi.org/10.1007/978-0-387-88136-2

Pruseth, K. L. (2009). Calculation of the CIPW norm: New formulas. *Journal of Earth System Science*, *118*(1), 101–113. https://doi.org/10.1007/s12040-009-0010-0

Qi, C., Hansen, L. N., Wallis, D., Holtzman, B. K., & Kohlstedt, D. L. (2018). Crystallographic Preferred Orientation of Olivine in Sheared Partially Molten Rocks: The Source of the "a-c Switch." *Geochemistry, Geophysics, Geosystems*, *19*(2), 316–336. https://doi.org/10.1002/2017GC007309

Rahib, R. R., Udry, A., Howarth, G. H., Gross, J., Paquet, M., Combs, L. M., et al. (2019). Mantle source to near-surface emplacement of enriched and intermediate poikilitic shergottites in Mars. *Geochimica et Cosmochimica Acta*, *266*, 463–496. https://doi.org/10.1016/j.gca.2019.07.034

Raleigh, C. B. (1967). Plastic Deformation of Upper Mantle Silicate Minerals. *Geophysical Journal of the Royal Astronomical Society*, *14*, 45–49. https://doi.org/10.1111/j.1365-246X.1967.tb06220.x

Raterron, P., Doukhan, N., Jaoul, O., & Doukhan, J. C. (1994). High temperature deformation of diopside IV: predominance of {110} glide above 1000°C. *Physics of the Earth and Planetary Interiors*, *82*, 209–

222. https://doi.org/10.1016/0031-9201(94)90073-6
Raterron, Paul, & Jaoul, O. (1991). High-temperature deformation of diopside single crystal: 1. Mechanical data. *Journal of Geophysical Research: Solid Earth*, *96*(B9), 14277–14286. https://doi.org/10.1029/91JB01205
Raterron, Paul, Chen, J., Geenen, T., & Girard, J. (2011). Pressure effect on forsterite dislocation slip systems: Implications for upper-mantle LPO and low viscosity zone. *Physics of the Earth and Planetary Interiors*, *188*(1–2), 26–36. https://doi.org/10.1016/j.pepi.2011.06.009
Richter, F., Chaussidon, M., Mendybaev, R., & Kite, E. (2016). Reassessing the cooling rate and geologic setting of Martian meteorites MIL 03346 and NWA 817. *Geochimica et Cosmochimica Acta*, *186*, 357–359. https://doi.org/10.1016/j.gca.2016.05.016
van Roermund, H. L. M., & Boland, J. N. (1981). The dislocation substructures of naturally deformed omphacites. *Tectonophysics*, *78*, 403–418.
Roszjar, J., Moser, D. E., Hyde, B. C., Chanmuang, C., & Tait, K. (2017). Comparing chemical microstructures of some early Solar System zircon from differentiated asteroids,Mars and Earth. In Desmond E. Moser, F. Corfu, J. D. Darling, S. M. Reddy, & K. Tait (Eds.), *Microstructural Geochronology: Planetary Records Down to Atom Scale* (1st ed., pp. 113–135). John Wiley & Sons, Inc. https://doi.org/10.1002/9781119227250.ch5
Rowland, S. K., Harris, A. J. L., & Garbeil, H. (2004). Effects of Martian conditions on numerically modeled, cooling-limited, channelized lava flows. *Journal of Geophysical Research E: Planets*, *109*(10), 1–16. https://doi.org/10.1029/2004JE002288
Rudge, J. F., Holness, M. B., & Smith, G. C. (2008). Quantitative textural analysis of packings of elongate crystals. *Contributions to Mineralogy and Petrology*, *156*(4), 413–429. https://doi.org/10.1007/s00410-008-0293-1
Ruggles, T. J., & Fullwood, D. T. (2013). Estimations of bulk geometrically necessary dislocation density using high resolution EBSD. *Ultramicroscopy*, *133*, 8–15. https://doi.org/10.1016/j.ultramic.2013.04.011
Ruzicka, A. M., & Hugo, R. C. (2018). Electron backscatter diffraction (EBSD) study of seven heavily metamorphosed chondrites: Deformation systematics and variations in pre-shock temperature and post-shock annealing. *Geochimica et Cosmochimica Acta*, *234*, 115–147. https://doi.org/10.1016/j.gca.2018.05.014
Santos, A. R., Agee, C. B., McCubbin, F. M., Shearer, C. K., Burger, P. V., Tartèse, R., & Anand, M. (2015). Petrology of igneous clasts in Northwest Africa 7034: Implications for the petrologic diversity of the martian crust. *Geochimica et Cosmochimica Acta*, *157*, 56–85. https://doi.org/10.1016/j.gca.2015.02.023
Satsukawa, T., & Michibayashi, K. (2009). Determination of slip system in olivine based on crystallographic preferred orientation and subgrain-rotation axis: examples from Ichinomegata peridotite xenoliths, Oga peninsula, Akita prefecture. *The Journal of the Geological Society of Japan*, *115*(6), 288–291. https://doi.org/10.5575/geosoc.115.288
Sautter, V., Barrat, J.-A., Jambon, A., Lorand, J. P., Gillet, P., Javoy, M., et al. (2002). A new Martian meteorite from Morocco: The nakhlite North West Africa 817. *Earth and Planetary Science Letters*, *195*(3–4), 223–238. https://doi.org/10.1016/S0012-821X(01)00591-X
Sautter, V., Toplis, M. J., Lorand, J. P., & Macri, M. (2012). Melt inclusions in augite from the nakhlite meteorites: A reassessment of nakhlite parental melt and implications for petrogenesis. *Meteoritics and Planetary Science*, *47*(3), 330–344. https://doi.org/10.1111/j.1945-5100.2012.01332.x
Schneider, C. A., Rasband, W. S., & Eliceiri, K. W. (2012). NIH Image to ImageJ: 25 years of image analysis. *Nature Methods*, *9*(7), 671–675. https://doi.org/10.1038/nmeth.2089
Schwartz, A. J., Kumar, M., Adams, B. L., & Field, D. P. (Eds.). (2000). *Electron Backscatter Diffraction in Materials Science* (second edi). Kluwer Academic, Plenum Publishers. https://doi.org/10.1007/978-0-387-88136-2 Library
Sciences, P. (1978). The mechanisms of creep in olivine. *Philosophical Transactions of the Royal Society of London. Series A, Mathematical and Physical Sciences*, *288*(1350), 99–119. https://doi.org/10.1098/rsta.1978.0008
Scott, D. H., Tanaka, K. L., & Geology, P. (1986). Geologic map of the western equatorial region of Mars, Scale 1:15,000,000, . *U.S. Geol. Survey Map I-1802-A*. Retrieved from http://astrogeology.usgs.gov/Projects/PlanetaryMapping/DIGGEOL/mars/marswest/mw.pdf%5Cnpapers3://publication/uuid/9DE8930B-BC79-41A2-98E9-42D39A4380EF
Settle, M. (1979). Lava Rheology: Thermal buffering produced by the latent heat of crystallisation. In *Lunar and Planetary Science X* (pp. 1107–1109). Retrieved from http://adsabs.harvard.edu/full/1979LPI....10.1107S
Shearer, C. K., Burger, P. V., Papike, J. J., McCubbin, F. M., & Bell, A. S. (2015). Crystal chemistry of merrillite from Martian meteorites: Mineralogical recorders of magmatic processes and planetary differentiation. In *Meteoritics and Planetary Science* (Vol. 50, pp. 649–673). https://doi.org/10.1111/maps.12355
Shelley, D. (1985). Determining paleo-flow directions from groundmass fabrics in the Lyttelton radial dykes,

New Zealand. *Journal of Volcanology and Geothermal Research*, *25*, 69–75185. https://doi.org/10.1111/ane.12608

Shelley, D. (1988). Radial dikes of lyttelton volcano — their structure, form, and petrography. *New Zealand Journal of Geology and Geophysics*, *31*(1), 65–75. https://doi.org/10.1080/00288306.1988.10417810

Skemer, P., Katayama, I., Jiang, Z., & Karato, S. I. (2005). The misorientation index: Development of a new method for calculating the strength of lattice-preferred orientation. *Tectonophysics*, *411*(1–4), 157–167. https://doi.org/10.1016/j.tecto.2005.08.023

Skrotzki, W. (1994). Defect structure and deformation mechanisms in naturally deformed augite and enstatite. *Tectonophysics*, *229*(1–2), 43–68. https://doi.org/10.1016/0040-1951(94)90005-1

Smith, D. E., Zuber, M. T., Solomon, S. C., Phillips, R. J., Head, J. W., Garvin, J. B., et al. (1999). The global topography of Mars and implications for surface evolution. *Science*, *284*(5419), 1495–1503. https://doi.org/10.1126/science.284.5419.1495

Smith, D. E., Sjogren, W. L., Tylter, G. L., Balmino, G., Lemoine, F. G., & Konopliv, A. S. (1999). The gravity field of Mars: Results from Mars global surveyor. *Science*, *286*(5437), 94–97. https://doi.org/10.1126/science.286.5437.94

Smith, J. V. (2002). Structural analysis of flow-related textures in lavas. *Earth-Science Reviews*, *57*(3–4), 279–297. https://doi.org/10.1016/S0012-8252(01)00081-2

Sneddon, G. C., Trimby, P. W., & Cairney, J. M. (2016). Transmission Kikuchi diffraction in a scanning electron microscope: A review. *Materials Science and Engineering R: Reports*, *110*, 1–12. https://doi.org/10.1016/j.mser.2016.10.001

Soustelle, V., & Manthilake, G. (2017). Deformation of olivine-orthopyroxene aggregates at high pressure and temperature: Implications for the seismic properties of the asthenosphere. *Tectonophysics*, *694*, 385–399. https://doi.org/10.1016/j.tecto.2016.11.020

Stocker, R. L., & Ashby, M. F. (1973). On the rheology of the upper mantle. *Reviews of Geophysics and Space Physics*, *11*(2), 391–426.

Stöffler, D., Hamann, C., & Metzler, K. (2018). Shock metamorphism of planetary silicate rocks and sediments: Proposal for an updated classification system. *Meteoritics and Planetary Science*, *53*(1), 5–49. https://doi.org/10.1111/maps.12912

Stopar, J. D., Taylor, G. J., Velbel, M. A., Norman, M. D., Vicenzi, E. P., & Hallis, L. J. (2013). Element abundances, patterns, and mobility in Nakhlite Miller Range 03346 and implications for aqueous alteration. *Geochimica et Cosmochimica Acta*, *112*, 208–225. https://doi.org/10.1016/j.gca.2013.02.024

Suavet, C., Alexandre, A., Franchi, I. A., Gattacceca, J., Sonzogni, C., Greenwood, R. C., et al. (2010). Identification of the parent bodies of micrometeorites with high-precision oxygen isotope ratios. *Earth and Planetary Science Letters*, *293*(3–4), 313–320. https://doi.org/10.1016/j.epsl.2010.02.046

Sundberg, M., & Cooper, R. F. (2008). Crystallographic preferred orientation produced by diffusional creep of harzburgite: Effects of chemical interactions among phases during plastic flow. *Journal of Geophysical Research: Solid Earth*, *113*(12), 1–16. https://doi.org/10.1029/2008JB005618

Tanaka, K. L., Robbins, S. J., Fortezzo, C. M., Skinner, J. A., & Hare, T. M. (2014). The digital global geologic map of Mars: Chronostratigraphic ages, topographic and crater morphologic characteristics, and updated resurfacing history. *Planetary and Space Science*, *95*, 11–24. https://doi.org/10.1016/j.pss.2013.03.006

Tanaka, Kenneth L. (1986). The stratigraphy of Mars. *Journal of Geophysical Research*, *91*(B13), 139–158. https://doi.org/10.1029/JB091iB13p0E139

Tasaka, M., Michibayashi, K., & Mainprice, D. (2008). B-type olivine fabrics developed in the fore-arc side of the mantle wedge along a subducting slab. *Earth and Planetary Science Letters*, *272*(3–4), 747–757. https://doi.org/10.1016/j.epsl.2008.06.014

Taylor, G. J. (2013). The bulk composition of Mars. *Chemie Der Erde - Geochemistry*, *73*(4), 401–420. https://doi.org/10.1016/j.chemer.2013.09.006

Tedonkenfack, S. S. T., Puziewicz, J., Aulbach, S., Ntaflos, T., Kaczmarek, M. A., Matusiak-Małek, M., et al. (2021). Lithospheric mantle refertilization by DMM-derived melts beneath the Cameroon Volcanic Line—a case study of the Befang xenolith suite (Oku Volcanic Group, Cameroon). *Contributions to Mineralogy and Petrology*, *176*(5), 1–18. https://doi.org/10.1007/s00410-021-01796-3

Tegner, C., Thy, P., Holness, M. B., Jakobsen, J. K., & Lesher, C. E. (2009). Differentiation and compaction in the Skaergaard intrusion. *Journal of Petrology*, *50*(5), 813–840. https://doi.org/10.1093/petrology/egp020

The Meteoritical Society. (2021). Meteoritical Bulletin Database. *Meteoritical Bulletin Database*. The Meteoritical Society. Retrieved from https://www.lpi.usra.edu/meteor/

Tielke, J., Mecklenburgh, J., Mariani, E., & Wheeler, J. (2019). The Influence of Water on the Strength of Olivine Dislocation Slip Systems. *Journal of Geophysical Research: Solid Earth*, *124*(7), 6542–6559. https://doi.org/10.1029/2019JB017436

Tkalcec, B. J., & Brenker, F. E. (2019). Absence of olivine orientation fabric in highly shocked Martian dunite. *Meteoritics and Planetary Science*, *54*(2), 267–279. https://doi.org/10.1111/maps.13204

Tomkinson, T., Lee, M. R., Mark, D. F., & Smith, C. L. (2013). Sequestration of Martian CO2 by mineral carbonation. *Nature Communications*, *4*, 1–6. https://doi.org/10.1038/ncomms3662

Tomkinson, T., Lee, M. R., Mark, D. F., Dobson, K. J., & Franchi, I. A. (2015a). The Northwest Africa (NWA) 5790 meteorite: A mesostasis-rich nakhlite with little or no Martian aqueous alteration. *Meteoritics & Planetary Science*, *50*(2), 287–304. https://doi.org/10.1111/maps.12424

Tomkinson, T., Lee, M. R., Mark, D. F., Dobson, K. J., & Franchi, I. A. (2015b). The Northwest Africa (NWA) 5790 meteorite: A mesostasis-rich nakhlite with little or no Martian aqueous alteration. *Meteoritics and Planetary Science*, *50*(2), 287–304. https://doi.org/10.1111/maps.12424

Tornabene, L. L., Moersch, J. E., McSween, H. Y., McEwen, A. S., Piatek, J. L., Milam, K. A., & Christensen, P. R. (2006). Identification of large (2-10 km) rayed craters on Mars in THEMIS thermal infrared images: Implications for possible Martian meteorite source regions. *Journal of Geophysical Research*, *111*(10), 1–25. https://doi.org/10.1029/2005JE002600

Tredoux, M., Hart, R. J., Carlson, R. W., & Shirey, S. B. (1999). Ultramafic rocks at the center of the Vredefort structure: Further evidence for the crust on edge model. *Geology*, *27*(10), 923–926. https://doi.org/10.1130/0091-7613(1999)027<0923:URATCO>2.3.CO;2

Treiman, A. H. (2005). The nakhlite meteorites: Augite-rich igneous rocks from Mars. *Chemie Der Erde - Geochemistry*, *65*(3), 203–270. https://doi.org/10.1016/j.chemer.2005.01.004

Treiman, A. H., & Gooding, J. L. (1991). Iddingsite in the Nakhla meteorite: TEM study of mineralogy and texture of pre-terrestrial (Martian?) alterations. *Meteoritical Society: Abstracts*, *26*, 402.

Treiman, A. H., & Irving, A. J. (2008). Petrology of Martian meteorite Northwest Africa 998. *Meteoritics & Planetary Science*, *43*(5), 829–854. https://doi.org/10.1111/j.1945-5100.2008.tb01085.x

Treiman, A. H., & Lindstrom, D. J. (1997). Trace element geochemistry of Martian iddingsite in the Lafayette meteorite. *Journal of Geophysical Research*, *102*(E4), 9153–9163.

Treiman, A. H., Barrett, R. A., & Gooding, J. L. (1993). Preterrestrial aqueous alteration of the Lafayette (SNC) meteorite. *Meteoritics*, *28*, 86–97.

Trimby, P., Daly, L., & Piazolo, S. (2018). The Use of High Speed, High Resolution EBSD to Unlock Hidden Secrets of the Allende Meteorite. *Microscopy and Microanalysis*, *24*(S1), 2082–2083. https://doi.org/10.1017/s1431927618010899

Trimby, P. W. (2012). Orientation mapping of nanostructured materials using transmission Kikuchi diffraction in the scanning electron microscope. *Ultramicroscopy*, *120*, 16–24. https://doi.org/10.1016/j.ultramic.2012.06.004

Udry, A., & Day, J. M. D. (2018). 1.34 billion-year-old magmatism on Mars evaluated from the co-genetic nakhlite and chassignite meteorites. *Geochimica et Cosmochimica Acta*, *238*, 292–315. https://doi.org/10.1016/J.GCA.2018.07.006

Udry, A., McSween, H. Y., Lecumberri-Sanchez, P., & Bodnar, R. J. (2012). Paired nakhlites MIL 090030, 090032, 090136, and 03346: Insights into the Miller Range parent meteorite. *Meteoritics and Planetary Science*, *47*(10), 1575–1589. https://doi.org/10.1111/j.1945-5100.2012.01420.x

Udry, A., Howarth, G. H., Herd, C., Day, J. M. D., Lapen, T. J., & Filiberto, J. (2020). What martian meteorites reveal about the interior and surface of Mars. *Journal of Geophysical Research: Planets*, *125*, e2020JE006523. https://doi.org/10.1029/2020JE006523

Ulrich, S., & Mainprice, D. (2005). Does cation ordering in omphacite influence development of lattice-preferred orientation? *Journal of Structural Geology*, *27*(3), 419–431. https://doi.org/10.1016/j.jsg.2004.11.003

Velbel, M. A. (2012). Aqueous alteration in Martian meteorites: Comparing mineral relations in igneous-rock weathering of Martian meteorites and in the sedimentary cycle of Mars. *Sedimentary Geology of Mars*, (102), 97–117. https://doi.org/10.2110/pec.12.102.0097

Vetere, F., Murri, M., Alvaro, M., Domeneghetti, M. C., Rossi, S., Pisello, A., et al. (2019). Viscosity of Pyroxenite Melt and Its Evolution During Cooling. *Journal of Geophysical Research: Planets*, *124*(5), 1451–1469. https://doi.org/10.1029/2018JE005851

Vollmer, F. W. (1990). An application of eigenvalue methods to structural domain analysis. *Bulletin of the Geological Society of America*, *102*(6), 786–791. https://doi.org/10.1130/0016-7606(1990)102<0786:AAOEMT>2.3.CO;2

Vukmanovic, Z., Holness, M. B., & Veksler, I. (2021). Microstructural constraints on the origin and evolution of the UG2 chromitite layer of the Bushveld Complex , South Africa. *Journal of Petrology*.

de Waal, S. A., Graham, I. T., & Armstrong, R. A. (2006). The Lindeques Drift and Heidelberg Intrusions and the Roodekraal Complex, Vredefort, South Africa: Comagmatic plutonic and volcanic products of a 2055 Ma ferrobasaltic magma. *South African Journal of Geology*, *109*(3), 279–300. https://doi.org/10.2113/gssajg.109.3.279

Watt, L. E., Bland, P. A., Prior, D. J., & Russell, S. S. (2006). Fabric analysis of Allende matrix using EBSD. *Meteoritics and Planetary Science*, *41*(7), 989–1001. https://doi.org/10.1111/j.1945-5100.2006.tb00499.x

Wenk, H. R., & Tomé, C. N. (1999). Modeling dynamic recrystallization of olivine aggregates deformed in simple shear. *Journal of Geophysical Research: Solid Earth*, *104*(B11), 25513–25527. https://doi.org/10.1029/1999jb900261

Van Der Werf, T., Chatzaras, V., Marcel Kriegsman, L., Kronenberg, A., Tikoff, B., & Drury, M. R. (2017). Constraints on the rheology of the lower crust in a strike-slip plate boundary: Evidence from the San

Quintín xenoliths, Baja California, Mexico. *Solid Earth*, *8*(6), 1211–1239. https://doi.org/10.5194/se-8-1211-2017

Werner, S. C. (2009). The global martian volcanic evolutionary history. *Icarus*, *201*(1), 44–68. https://doi.org/10.1016/j.icarus.2008.12.019

Winiarski, B., Gholinia, A., Mingard, K., Gee, M., Thompson, G., & Withers, P. J. (2021). Correction of artefacts associated with large area EBSD. *Ultramicroscopy*, *226*(March), 113315. https://doi.org/10.1016/j.ultramic.2021.113315

Winter, J. D. (2013). *Principles of Igneous and Metamorphic Petrology* (New Intern). Pearson. Retrieved from https://books.google.be/books?id=HBWpBwAAQBAJ

Woodward, C. (2005). Plasticity at the Atomic Scale: Parametric, Atomistic, and Electronic Structure Methods. *Handbook of Materials Modeling*, 2865–2869. https://doi.org/10.1007/978-1-4020-3286-8_171

Yao, Z., Qin, K., Wang, Q., & Xue, S. (2019). Weak B-Type Olivine Fabric Induced by Fast Compaction of Crystal Mush in a Crustal Magma Reservoir. *Journal of Geophysical Research: Solid Earth*, *124*(4), 3530–3556. https://doi.org/10.1029/2018JB016728

Zhang, J., & Green, H. W. (2007). Experimental investigation of eclogite rheology and its fabrics at high temperature and pressure. *Journal of Metamorphic Geology*, *25*, 97–115. https://doi.org/10.1111/j.1525-1314.2006.00684.x

Zhang, J., Green II, H. W., & Bozhilov, K. N. (2006). Rheology of omphacite at high temperature and pressure and significance of its lattice preferred orientations. *Earth and Planetary Science Letters*, *246*, 432–443. https://doi.org/10.1016/j.epsl.2006.04.006

Zhou, W., Apkarian, R., Wang, Z. L., & Joy, D. (2007). Fundamentals of scanning electron microscopy (SEM). *Scanning Microscopy for Nanotechnology: Techniques and Applications*, 1–40. https://doi.org/10.1007/978-0-387-39620-0_1

Zieg, M. J., & Marsh, B. D. (2002). Crystal Size Distributions and Scaling Laws in the Quantification of Igneous Textures. *Journal of Petrology*, *43*(1), 85–101. https://doi.org/10.1093/petrology/43.1.85

Zolensky, M. E., Gounelle, M., Mikouchi, T., Ohsumi, K., Le, L., Hagiya, K., & Tachikawa, O. (2008). Andreyivanovite: A second new phosphide from the Kaidun meteorite. *American Mineralogist*, *93*(8–9), 1295–1299. https://doi.org/10.2138/am.2008.2614

Zuber, M. T. (2001). The crust and mantle of Mars. *Nature*, *412*(6843), 220–227. https://doi.org/10.1038/35084163